SCHOLARLY PUBLICATIONS

A CURRENT AWARENESS BULLETIN
OF RESEARCH OUTPUT

@DTU

(78th Edition)

JUNE 2019

BY: CENTRAL LIBRARY

DELHI TECHNOLOGICAL UNIVERSITY

(FORMERLY *DELHI COLLEGE OF ENGINEERING*)
GOVT. OF N.C.T. OF DELHI
SHAHBAD DAULATPUR, MAIN BAWANA ROAD
DELHI 110042

PREFACE

This is the **Seventy eight** Issue of Current Awareness Bulletin started by Delhi Technological University, Central Library. The aim of the bulletin is to compile, preserve and disseminate information published by the faculty, students and alumni for mutual benefits. The bulletin also aims to propagate the intellectual contribution of Delhi Technological University (DTU) as a whole to the academia.

The bulletin contains information resources available in the internet in the form of articles, reports, presentations published in international journals, websites, etc. by the faculty and students of DTU. The publications of faculty and student which are not covered in this bulletin may be because of the reason that the full text either was not accessible or could not be searched by the search engine used by the library for this purpose.

The learned faculty and students are requested to provide their uncovered publications to the library either through email or in CD, etc. to make the bulletin more comprehensive.

This issue contains the information published during **June, 2019**. The arrangement of the contents is alphabetical. The full text of the article which is either subscribed by the university or available in the web is provided in this bulletin.

Central Library

CONTENTS

11. Observational constraints on viscous Ricci dark energymodel, *3.C.P. Singh[1]* and *6.Amit Kumar[2]*, [1]Mathematics and [2]Physics, DTU

12. Optimal users based secure data transmission on the internet of healthcare things (IoHT) with lightweight block ciphers, S. Sheeba Rani, Jafar A. Alzubi, S. K. Lakshmanaprabu, *7.1.Deepak Gupta* and Ramachandran Manikandan, CSE, DTU

13. Preliminary Assessment for the Potential of Citrus Limetta Peel Waste for Bioethanol Production under Indian Conditions, *7.Vinay Prabhakar* and *3.SK Singh*, Environmental, DTU

14. SNAP-BATNET: Cascading Author Profiling and Social Network Graphs for Suicide Ideation Detection on Social Media, *8.Rohan Mishra*, *8.Pradyumna Prakhar Sinha*, Ramit Sawhney, Debanjan Mahata, Puneet Mathur and Rajiv Ratn Shah, IT, DTU

15. Study of the influence of friction stir processing on tungsten inert gas welding of different aluminum alloy, *6.Husain Mehdi* and *3.R. S. Mishra,* Mechanical, DTU

16. THE SHARP BOUNDS OF THE SECOND AND THIRD HANKEL DETERMINANTS FOR THE CLASS SL, *6.SHAGUN BANGA* AND *3.S. SIVAPRASAD KUMAR*, Applied Mathematics, DTU

17. Toward Zero Energy: Active and passive design strategies to achieve net zero Energy Building, *6.Shambalid Ahady*, *3.Nirendra Dev* and *3.Anubha Mandal*, Civil, DTU

1. *Chancellor*
2. *Pro Vice Chancellor*   *2.1. Ex Pro Vice Chancellor*
3. *Faculty*   *3.1. Ex Faculty*
4. *Teaching-cum-Research Fellow*   *4.1.Asst. Librarian*
5. *Alumni*
6. *Research Scholar*   *6.1. Ex Research Scholar*
7. *PG Scholar*   *7.1. Ex PG Scholar*
8. *Undergraduate Student*   *8.1. Ex Undergraduate Student*

Check for
updates

Certain Class of Starlike Functions Associated with Modified Sigmoid Function

Priyanka Goel[1] · S. Sivaprasad Kumar[1]

Abstract

Let $\mathcal{S}^*_{SG} = \{f \in \mathcal{A} : zf'(z)/f(z) \prec 2/(1 + e^{-z})\}$. For this class, several radius estimates and coefficient bounds are obtained as well as structural formula, growth theorem, distortion theorem and inclusion relations are established. Further, let p be an analytic function such that $p(0) = 1$. Sharp bounds on $\beta \in \mathbb{R}$ are determined for various first-order differential subordinations such as $1 + \beta zp'(z)/p^k(z)$, $p(z) + \beta zp'(z)/p^k(z) \prec 2/(1 + e^{-z})$ to imply that $p(z) \prec (1 + Az)/(1 + Bz)$, where $-1 \leq B < A \leq 1$ or $\sqrt{1 + z}$ and also when the position of dominants is interchanged. Moreover, these results are extended by considering β to be a complex number.

Keywords Starlike functions · Sigmoid function · Subordination · Radius problems · Coefficient estimates

Mathematics Subject Classification 30C45 · 30C50 · 30C80

1 Introduction

Let $\mathcal{H} = \mathcal{H}(\mathbb{D})$ be the class of functions analytic in $\mathbb{D} := \mathbb{D}_1$, where $\mathbb{D}_r := \{z \in \mathbb{C} : |z| < r\}$. For a positive integer n and $a \in \mathbb{C}$, let

$$\mathcal{H}[a, n] := \{f \in \mathcal{H} : f(z) = a + a_n z^n + a_{n+1} z^{n+1} + a_{n+2} z^{n+2} + \ldots\}.$$

✉ S. Sivaprasad Kumar
  spkumar@dce.ac.in

  Priyanka Goel
  priyanka.goel0707@gmail.com

[1] Department of Applied Mathematics, Delhi Technological University, Delhi 110042, India

🖄 Springer

We denote by $\mathcal{A}_n$ the class of functions $f(z)$ of the form

$$f(z) = z + a_{n+1}z^{n+1} + a_{n+2}z^{n+2} + \ldots$$

which are analytic in $\mathbb{D}$ and $\mathcal{A} := \mathcal{A}_1$. The subclass of $\mathcal{A}$ consisting of univalent functions is denoted by $\mathcal{S}$. Let f and F be members of $\mathcal{H}$, we say that f is subordinate to F, written as $f \prec F$, if there exists a Schwartz function ω which is analytic in $\mathbb{D}$ satisfying $\omega(0) = 0$ and $|\omega(z)| < 1$ such that $f(z) = F(\omega(z))$. Further, if F is univalent, then $f \prec F$ if and only if $f(0) = F(0)$ and $f(\mathbb{D}) \subset F(\mathbb{D})$. Let $f(z) = \sum_{n=0}^{\infty} a_n z^n$ and $g(z) = \sum_{n=0}^{\infty} b_n z^n$ be in $\mathcal{H}$, then the convolution of f and g is given by $(f * g)(z) = \sum_{n=0}^{\infty} a_n b_n z^n$. In 1989, Shanmugam [15] considered the classes

$$\mathcal{S}_g^*(h) = \left\{ f \in \mathcal{A} : \frac{z(f*g)'(z)}{(f*g)(z)} \prec h(z) \right\} \quad \text{such that} \quad \frac{(f*g)(z)}{z} \neq 0$$

and

$$\mathcal{C}_g(h) = \left\{ f \in \mathcal{A} : 1 + \frac{z(f*g)''(z)}{(f*g)'(z)} \prec h(z) \right\} \quad \text{such that} \quad (f*g)'(z) \neq 0,$$

where h is a convex univalent function with $h(0) = 0$ and $\operatorname{Re} h(z) > 0$ $(z \in \mathbb{D})$. Later, in 1992, using subordination Ma and Minda [8] gave a general form of various subclasses of starlike and convex functions for which the respective quantities $zf'(z)/f(z)$ and $1 + zf''(z)/f'(z)$ are subordinate to a function with special properties. These subclasses are defined as:

$$\mathcal{S}^*(\varphi) = \left\{ f \in \mathcal{S} : \frac{zf'(z)}{f(z)} \prec \varphi(z) \right\} \quad \text{and} \quad \mathcal{C}(\varphi) = \left\{ f \in \mathcal{S} : 1 + \frac{zf''(z)}{f'(z)} \prec \varphi(z) \right\},$$

where φ is an analytic function having positive real part, $\varphi(\mathbb{D})$ is starlike with respect to $\varphi(0) = 1$, $\varphi(\mathbb{D})$ is symmetric about the real axis and $\varphi'(0) > 0$. Several well-known classes can be obtained by specializing φ such as the Janowski starlike class given by $\mathcal{S}^*[A, B] := \mathcal{S}^*((1 + Az)/(1 + Bz))$, where $B < A$ and $A, B \in [-1, 1]$ (see [4]), the class $\mathcal{S}^*(\alpha)$ of starlike functions of order α defined by taking $\varphi = ((1 + (1 - 2\alpha)z))/(1 - z))$, where $0 \leq \alpha < 1$. In the similar manner, the class of Janowski convex functions denoted by $\mathcal{C}[A, B] := \mathcal{C}((1 + Az)/(1 + Bz))$ and the class of convex functions of order α denoted by $\mathcal{C}(\alpha) := \mathcal{C}((1 + (1 - 2\alpha)z))/(1 - z))$ can also be obtained by setting ϕ accordingly. The classes $\mathcal{S}^* := \mathcal{S}^*(0)$ and $\mathcal{C} := \mathcal{C}(0)$ are the classes of starlike and convex functions, respectively. Note that by taking $\phi(z) = 1 + 2/\pi^2 (\log((1 + \sqrt{z})/(1 - \sqrt{z})))^2$, we obtain the class $\mathcal{S}_P$ of parabolic starlike functions, introduced by Rønning [14] and correspondingly, the class UCV of uniformly convex functions, introduced by Goodman [3]. If $\phi(z) = \sqrt{1 + z}$, then the class $\mathcal{S}^*(\phi)$ reduces to the class $\mathcal{S}_L^* := \mathcal{S}^*(\sqrt{1 + z})$, introduced by Sokół and Stankiewicz [17]. In geometrical sense, a function $f \in \mathcal{S}_L^*$ if and only if $zf'(z)/f(z)$ lies in the region bounded by the right lemniscate of Bernoulli defined by $|w^2 - 1| < 1$.

Therefore, $\mathcal{S}_L^* := \{f \in \mathcal{A} : |(zf'(z)/f(z))^2 - 1| < 1\}$. In order to prove our results, we need to recall various subclasses of $\mathcal{S}$, namely $\mathcal{S}^*(\alpha)$ $(0 \leq \alpha < 1)$, the class of starlike functions of order α characterized by the condition $\text{Re}(zf'(z)/f(z)) > \alpha$, the class of strongly starlike functions of order β denoted by $\mathcal{SS}^*(\beta)$ $(0 < \beta \leq 1)$ whose characterization is given by $|\arg(zf'(z)/f(z))| < \beta\pi/2$. One more interesting class studied by Uralegaddi et al. [20] is $\mathcal{M}(\beta)$ $(\beta > 1)$, characterized by $\text{Re}(zf'(z)/f(z)) < \beta$. A closely related class studied by Ravichandran and Kumar [12] is the class of starlike functions of reciprocal order α $(0 \leq \alpha < 1)$, denoted by $\mathcal{RS}^*(\alpha)$ and characterized by the condition $\text{Re}(f(z)/zf'(z)) > \alpha$. In 1999, the class $k - \mathcal{ST}$ of k-starlike functions $(k \geq 0)$ was introduced by Kanas and Wiśniowska [5] and defined by the condition $\text{Re}(zf'(z)/f(z)) > k|zf'(z)/f(z) - 1|$. Further, this class has been generalized by Kanas and Răducanu by adding a parameter α. This class is denoted by $\mathcal{ST}(k, \alpha)$ and is characterized by the condition $\text{Re}(zf'(z)/f(z)) > k|zf'(z)/f(z) - 1| + \alpha$. Geometrically, the boundary of the domain $\Omega_{k,\alpha} = \{w \in \mathbb{C} : \text{Re } w > k|w - 1| + \alpha\}$ represents an ellipse for $k > 1$, a parabola for $k = 1$ and a hyperbola for $0 < k < 1$. Consider the sigmoid function given by $g(z) = 1/(1 + e^{-z})$. In order to obtain the normalized form of $g(z)$, we define the modified sigmoid function as $G(z) = 2/(1 + e^{-z})$. The modified sigmoid function maps $\mathbb{D}$ onto a domain $\Delta_{SG} := \{w \in \mathbb{C} : |\log(w/(2 - w))| < 1\}$, which is symmetric about the real axis. Moreover, $G(z)$ is a convex and hence starlike with respect to $G(0) = 1$. Also $G'(0) > 0$ and $G(z)$ has positive real part in $\mathbb{D}$. Hence, $G(z)$ falls under the category of Ma–Minda functions. So, the classes $\mathcal{S}^*(G)$ and $\mathcal{C}(G)$ naturally become the subclasses of $\mathcal{S}^*$ and $\mathcal{C}$. Let us set

$$\mathcal{S}_{SG}^* = \mathcal{S}^*(G) \quad \text{and} \quad \mathcal{C}_{SG} = \mathcal{C}(G).$$

Analytically, a function $f \in \mathcal{S}_{SG}^*$ if and only if $zf'(z)/f(z)$ lies in the region Δ_{SG}. From this definition, we have the following representation formula:
A function f is in $\mathcal{S}_{SG}^*$ if and only if there exists an analytic function ϕ, satisfying $\phi(z) \prec G(z) = 2/(1 + e^{-z})$ such that

$$f(z) = z \exp\left(\int_0^z \frac{\phi(t) - 1}{t} dt\right). \tag{1}$$

Here are some examples of the functions which belong to the class $\mathcal{S}_{SG}^*$: Let

$$\phi_1(z) = 1 + \frac{z}{4}, \quad \phi_2(z) = \frac{4 + 2z}{4 + z}, \quad \phi_3(z) = \frac{7 + ze^z}{7} \quad \text{and} \quad \phi_4(z) = 1 + \frac{z \sin z}{3}.$$

Since $G(z)$ is univalent in $\mathbb{D}$, $\phi_i(0) = G(0)$ $(i = 1, 2, 3, 4)$ and $\phi_i(\mathbb{D}) \subset G(\mathbb{D})$, it is easy to deduce that $\phi_i \prec G$. Thus, the functions in the class $\mathcal{S}_{SG}^*$ corresponding to each of the $\phi_i's$ are obtained by using the representation formula given by (1), respectively, as follows:

$$f_1(z) = ze^{z/4}, \quad f_2(z) = z + \frac{z^2}{4}, \quad f_3(z) = z\exp\left(\frac{e^z - 1}{7}\right) \text{ and}$$

$$f_4(z) = z\exp\left(\frac{1 - \cos z}{3}\right).$$

In particular, if we take $\phi(z) = G(z) = 2/(1 + e^{-z})$, then the corresponding function

$$\tilde{f}(z) = z\exp\left(\int_0^z \frac{e^t - 1}{t(e^t + 1)}dt\right) = z + \frac{z^2}{2} + \frac{z^3}{8} + \frac{z^4}{144} - \frac{5z^5}{1152} + \dots, \quad (2)$$

plays the role of an extremal function for many extremal problems for the class $\mathcal{S}_{SG}^*$. In [8], Ma and Minda proved some subordination results which yield that if $f \in \mathcal{S}_{SG}^*$, then $f(z)/z \prec \tilde{f}(z)/z$ and therefore, the following result is obtained.

Theorem 1.1 *Let $f \in \mathcal{S}_{SG}^*$ and $\tilde{f}(z)$ be the extremal function given by* (2). *Then, the following holds whenever $|z| = r < 1$:*

(i) *Growth theorem:* $-\tilde{f}(-r) \leq |f(z)| \leq \tilde{f}(r)$. *In particular, $f(\mathbb{D})$ contains $\Delta :=$ $\{w : |w| < -\tilde{f}(-1) \approx 0.614535\}$.*

(ii) *Rotation theorem:* $|\arg(f(z)/z)| \leq \max_{|z|=r} \arg(\tilde{f}(z)/z)$.

(iii) *Distortion theorem:* $\tilde{f}'(-r) \leq |f'(z)| \leq \tilde{f}'(r)$. *Equality holds for some $z \neq 0$ if and only if f is a rotation of $\tilde{f}$.*

In [9], Miller and Mocanu studied the general theory of differential subordination. Using this theory, Tuneski [19] and Tuneski et al. [18] gave conditions for functions in $\mathcal{A}$ to be in $\mathcal{S}^*[A, B]$. In 2007, Ali et al. [1] gave sufficient conditions for β so that for $j = 0, 1, 2$, the following differential subordination implication holds: If $1 + \beta(zp'(z))/(p(z))^j \prec (1 + Dz)/(1 + Ez)$, then $p(z) \prec (1 + Az)/(1 + Bz)$, where $-1 \leq B < A \leq 1$ and $-1 \leq E < D \leq 1$. In 2013, Kumar et al. [6] obtained sufficient conditions on β for $1 + \beta(zp'(z))/(p(z))^j \prec (1 + Dz)/(1 + Ez)$, where $j = 0, 1, 2$ to imply that $p(z) \prec \sqrt{1 + z}$, where $-1 \leq E < D \leq 1$. Kumar and Ravichandran [7] obtained sharp bounds on β so that $p(z) \prec e^z$, whenever $1 + \beta zp'(z)/(p(z))^j \prec (1 + Az)/(1 + Bz)$ $(j = 0, 2), 1 + \beta zp'(z)/(p(z))^j \prec \sqrt{1 + z}$ $(j = 0, 2)$ and many more functions. Lately, Cho et al. [2] obtained sharp bounds on β so as to prove that $1 + \beta zp'(z)/(p(z))^j \prec 1 + z/(1 - \alpha z^2)$ implies $p(z) \prec e^z, \sqrt{1 + z}$ and several other functions. Motivated by these works, we find sharp bounds on β so that $1 + \beta(zp'(z))/(p(z))^j \prec 2/(1 + e^{-z})$ implies $p(z) \prec \phi_0(z)$ for $\phi_0(z) = (1 + Az)/(1 + Bz)$ or $\sqrt{1 + z}$. Also, sufficient conditions on β are obtained in order to prove the implication formed by interchanging the functions $2/(1 + e^{-z})$ and $\phi_0(z)$. Further, these results are also considered for a complex β. In addition, we establish many inclusion relations and find radius as well as coefficient estimates. Also, we establish a result which ascertains the largest disk that can be inscribed inside Δ_{SG} as well as the smallest disk that contains Δ_{SG}.

2 About $\mathcal{S}_{SG}^*$

Before proving the main results, we shall proceed to find the bounds of the real part of $2/(1 + e^{-z})$.

Lemma 2.1 *The function* $G(z) = 2/(1 + e^{-z})$ *satisfies*

$$\min_{|z|=r} \operatorname{Re} G(z) = G(-r) \quad and \quad \max_{|z|=r} \operatorname{Re} G(z) = G(r),$$

whenever $0 < r < 1$.

Proof Let $G(z) = 2/(1 + e^{-z})$. Then, a boundary point of $G(\mathbb{D}_{r_0})$, where $\mathbb{D}_{r_0} = \{z \in \mathbb{C} : |z| < r_0\}$, can be written in the form $G(r_0 e^{i\theta}) = 2/(1 + e^{-r_0 e^{i\theta}})$. The outward normal at the point $G(\zeta)$ is given by $\zeta G'(\zeta)$ where $|\zeta| = r_0$. Thus, for $\zeta = r_0 e^{i\theta}$, we have

$$\zeta G'(\zeta) = \frac{2r_0 e^{i\theta} e^{-r_0 e^{i\theta}}}{(1 + e^{-r_0 e^{i\theta}})^2}.$$

Since we need to find the bounds of the real part, it is sufficient to find the points at which, the imaginary part of the normal, is a constant. The imaginary part of $\zeta G'(\zeta)$ is given by

$$h(\theta) = \delta(2e^{-r_0 \cos\theta} r_0 \sin(\theta - r_0 \sin\theta) + 4e^{-2r_0 \cos\theta} r_0 \sin\theta$$
$$+ 2e^{-3r_0 \cos\theta} r_0 \sin(\theta + r_0 \sin\theta)),$$

where

$$\delta = \frac{1}{|1 + e^{-r_0 e^{i\theta}}|^4}.$$

A simple computation yields that $h(\theta) = 0$ for $\theta = 0$ and π. It is easy to check that the maximum value is obtained at $\theta = 0$ and the minimum value is obtained at $\theta = \pi$. Since r_0 is arbitrary, it follows that

$$\min_{|z|=r} \operatorname{Re} G(z) = \frac{2}{1 + e^r} \quad and \quad \max_{|z|=r} \operatorname{Re} G(z) = \frac{2}{1 + e^{-r}}.$$

$\square$

In the following lemma, we find the radius of the largest disk that can be inscribed in the domain Δ_{SG} with center $(a, 0)$, where a lies between the bounds of the real part of $2/(1 + e^{-z})$.

Lemma 2.2 *Let* $2/(1 + e) < a < 2e/(1 + e)$. *If*

$$r_a = \frac{e - 1}{e + 1} - |a - 1|,$$

then

$${w \in \mathbb{C} : |w - a| < r_a} \subset \Delta_{SG}. \tag{3}$$

Proof Let $\phi(z) = 2/(1 + e^{-z})$. Then, a boundary point of the domain $\phi(\mathbb{D})$ can be represented as

$$\phi(e^{i\theta}) = \frac{2(1 + e^{-\cos\theta}\cos(\sin\theta))}{1 + e^{-2\cos\theta} + 2e^{-\cos\theta}\cos(\sin\theta)} + i\frac{2e^{-\cos\theta}\sin(\sin\theta)}{1 + e^{-2\cos\theta} + 2e^{-\cos\theta}\cos(\sin\theta)},$$

where $-\pi \le \theta \le \pi$. Now, consider

$$h(\theta) = \frac{4 - 4a((1 + e^{-\cos\theta}\cos(\sin\theta)))}{1 + e^{-2\cos\theta} + 2e^{-\cos\theta}\cos(\sin\theta)} + a^2, \tag{4}$$

which is the square of the distance of $\phi(e^{i\theta})$ from $(a, 0)$. Since $h(\theta) = h(-\theta)$, it is sufficient to consider the interval $0 \le \theta \le \pi$. A computation indicates that $h(\theta)$ is a decreasing function, whenever $2/(1 + e) < a \le e/(e + 1)$. Therefore,

$$r_a = \min_{0 \le \theta \le \pi} \sqrt{h(\theta)} = \sqrt{h(\pi)} = a - \frac{2}{1 + e}.$$

If $e/(e + 1) < a \le (e + 2)/(e + 1)$, then the graph of $h(\theta)$ reveals that it is increasing for $\theta \in [0, \theta_a]$ and decreasing for $\theta \in [\theta_a, \pi]$ where θ_a is a root of $h'(\theta)$, whose value depends on the value of a. Hence, the minimum of $h(\theta)$ in this case is attained either at 0 or π. Also,

$$h(\pi) - h(0) = \frac{4(a - 1)(e - 1)}{e + 1}.$$

Hence,

$$\min_{0 \le \theta \le \pi} h(\theta) = \begin{cases} h(\pi), & a < 1 \\ h(0), & a > 1. \end{cases}$$

In the end, let us assume $(e + 2)/(e + 1) < a < 2e/(e + 1)$. For this range of a, we find that $h(\theta)$ is an increasing function and therefore,

$$r_a = \min_{0 \le \theta \le \pi} \sqrt{h(\theta)} = \sqrt{h(0)} = \frac{2e}{1 + e} - a.$$

Combining the above three cases based upon the decreasing and increasing nature of the function $h(\theta)$, we have the following two cases:

(i) For $2/(1 + e) < a \le 1$, the minimum of $h(\theta)$ is attained at π. Therefore,

$$\min_{0 \le \theta \le \pi} h(\theta) = h(\pi)$$

and $r_a = a - 2/(1 + e)$.

(ii) For $1 \le a < 2e/(1 + e)$, the minimum of $h(\theta)$ is attained at 0. Therefore,

$$\min_{0 \le \theta \le \pi} h(\theta) = h(0)$$

and $r_a = 2e/(1 + e) - a$.

Upon fusing the above two cases, we have $r_a = (e - 1)/(e + 1) - |a - 1|$, whenever $2/(1 + e) < a < 2e/(e + 1)$. □

Remark 2.1 On the similar lines of the proof of Lemma 2.2, we conclude that

$$\Delta_{SG} \subset \{w \in \mathbb{C} : |w - a| < R_a\}$$

where R_a is given by

$$R_a = \begin{cases} \dfrac{2e}{e + 1} - a, & \dfrac{2}{e + 1} < a \le \dfrac{e}{e + 1} \\ h(\theta_a), & \dfrac{e}{e + 1} < a \le \dfrac{e + 2}{e + 1} \\ a - \dfrac{2}{1 + e}, & \dfrac{e + 2}{e + 1} < a < \dfrac{2e}{e + 1}, \end{cases}$$

$h(\theta)$ is given by (4) and θ_a is a root of $h'(\theta)$, whose value depends on a.

3 Inclusion Results

In this section, inclusion properties of the class $\mathcal{S}_{SG}^*$ associated with the other classes, namely $\mathcal{S}^*(\alpha), \mathcal{SS}^*(\beta), \mathcal{RS}^*(\alpha), \mathcal{M}(\beta), \mathcal{ST}(k, \alpha), k - \mathcal{ST}$ and $\mathcal{S}^*[A, B]$, are established (Fig. 1).

Theorem 3.1 *The class $\mathcal{S}_{SG}^*$ satisfies the following inclusion relations:*

(i) $\mathcal{S}_{SG}^* \subset \mathcal{S}^*(\alpha)$, whenever $0 \le \alpha \le 2/(1 + e)$.
(ii) $\mathcal{S}_{SG}^* \subset \mathcal{RS}^*(1/\beta) \subset \mathcal{M}(\beta)$, whenever $\beta \ge 2e/(1 + e)$.
(iii) *Let $s_0 \approx 1.94549$ be the smallest root of the equation $\cos t + e^{\cos t} \cos(\sin t - t) = 0$ and $h(z) = \arg(2/(1 + e^{-z}))$. Then, $\mathcal{S}_{SG}^* \subset \mathcal{SS}^*(\beta)$, whenever $\beta \ge 2h(e^{is_0})/\pi \approx 0.353914$.*
(iv) *If $k > 1$ and $0 \le \alpha < 1$, then $\mathcal{ST}(k, \alpha) \subset \mathcal{S}_{SG}^*$, whenever $k \ge (2e - \alpha(1 + e))/(e - 1)$. In particular, $k - \mathcal{ST} \subset \mathcal{S}_{SG}^*$, whenever $k \ge 2e/(e - 1)$.*
(v) *If $0 \le \alpha < 1$, then $\mathcal{S}_{SG}^* \subset \mathcal{ST}(1, \alpha)$, whenever $\alpha \le (3 - e)/(1 + e)$.*

Proof (i) and (ii) follow as under:

The figure contains the following curve definitions:

$$\gamma : \left|\log \frac{w}{2-w}\right| = 1$$

$$\gamma_1 : \operatorname{Re} w = \frac{2e}{e-1}|w-1|$$

$$\gamma_2 : |w-1| = \frac{e-1}{e+1}$$

$$\gamma_3 : |\arg w| = \frac{89}{500}\pi$$

$$\gamma_4 : \operatorname{Re} w - |w-1| = \frac{3-e}{1+e}$$

$$\gamma_5 : \operatorname{Re} w = \frac{2}{1+e}$$

$$\gamma_6 : \left|w - \frac{e}{1+e}\right| = \frac{e}{1+e}$$

$$A = \frac{2}{1+e}$$
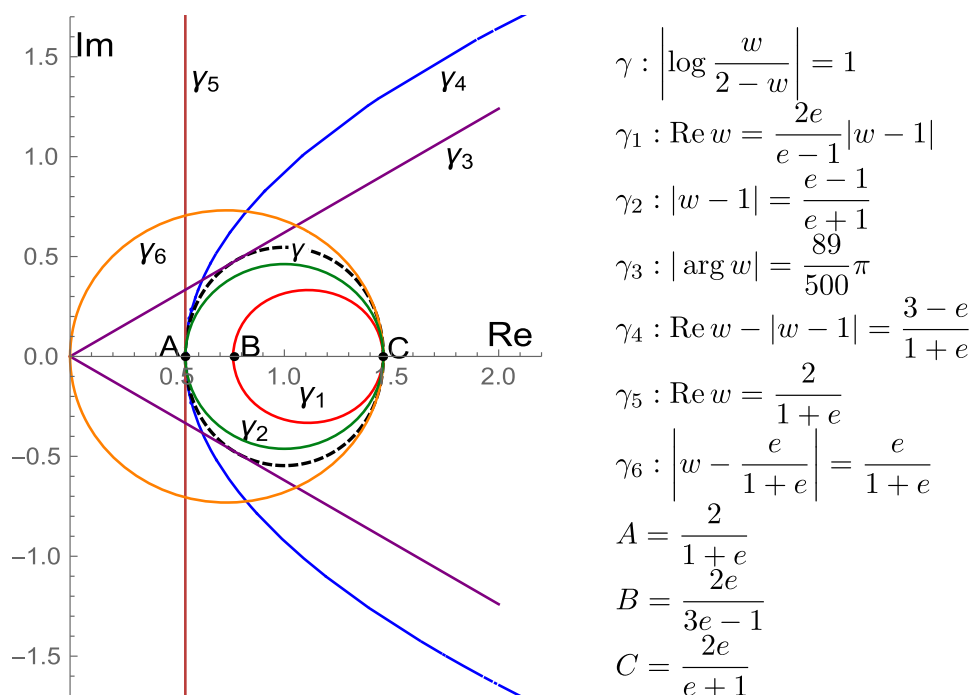
$$B = \frac{2e}{3e-1}$$

$$C = \frac{2e}{e+1}$$

Fig. 1 Boundary curves of best dominants and subordinants of modified Sigmoid function

Let $f \in \mathcal{S}_{SG}^*$, then $zf'(z)/f(z) \prec 2/(1+e^{-z})$. By Lemma 2.1, it is easy to deduce that

$$\min_{|z|=1} \operatorname{Re} \frac{2}{1+e^{-z}} < \operatorname{Re} \frac{zf'(z)}{f(z)} < \max_{|z|=1} \operatorname{Re} \frac{2}{1+e^{-z}},$$

which implies

$$\frac{2}{1+e} < \operatorname{Re} \frac{zf'(z)}{f(z)} < \frac{2e}{1+e}.$$

Thus, $f \in \mathcal{S}^*(2/(1+e)) \cap \mathcal{M}(2e/(1+e))$. Now, we consider

$$\operatorname{Re} \frac{f(z)}{zf'(z)} > \min_{|z|=1} \operatorname{Re} \frac{1+e^{-z}}{2} = \frac{1}{2}(1 + \min_{|z|=1} \operatorname{Re} e^{-z}) = \frac{1+e}{2e}.$$

From the above equation, it follows that $f \in \mathcal{RS}^*(\beta)$, whenever $\beta \leq (1+e)/2e$. Equivalently, $f \in \mathcal{RS}^*(1/\beta)$, whenever $\beta \geq 2e/(1+e)$. We know that $f \in \mathcal{RS}^*(1/\beta)$ if and only if

$$\left|\frac{zf'(z)}{f(z)} - \frac{\beta}{2}\right| < \frac{\beta}{2}, \tag{5}$$

which implies that $\operatorname{Re} zf'(z)/f(z) < \beta$. Using this fact, we have

$$\mathcal{S}_{SG}^* \subset \mathcal{RS}^*(1/\beta) \subset \mathcal{M}(\beta), \text{ whenever } \beta \geq 2e/(1+e).$$

Note that the class $\mathcal{RS}^*(\beta)$ is equivalent to the class $\mathcal{S}_M^*$ considered by Sokół [16], for the case when $M = 1/2\beta$. Thus, $f \in \mathcal{RS}^*(1/\beta)$ is equivalent to saying that Δ_{SG} is contained in the disk given in equation (5), whenever $\beta \geq 2e/(1+e)$.

(iii) If $f \in \mathcal{S}_{SG}^*$, then

$$\left| \arg \frac{zf'(z)}{f(z)} \right| < \max_{|z|=1} \arg \frac{2}{1+e^{-z}} = \max_{0 \le \theta < 2\pi} \arctan \left(\frac{\sin(\sin\theta)}{e^{\cos\theta} + \cos(\sin\theta)} \right)$$
$$= \max_{0 \le \theta < 2\pi} h(e^{i\theta})$$

As we put $h'(e^{i\theta}) = 0$, it reduces to $\cos\theta + e^{\cos\theta} \cos(\sin\theta - \theta) = 0$. Now, suppose $s_0 \approx 1.94549$ be a root of this equation. Then, $h''(e^{is_0}) < 0$ and hence $\max_{0 \le \theta < 2\pi} h(e^{i\theta}) = h(e^{is_0}) \approx 0.555926$. Thus, $f \in \mathcal{SS}^*(2h(e^{is_0})/\pi)$.

(iv) Consider the domain $\Omega_{k,\alpha} = \{w \in \mathbb{C} : Re\, w > k|w - 1| + \alpha\}$ whose boundary $\partial\Omega_{k,\alpha}$ represents an ellipse for $k > 1$ and is given by:

$$\frac{(x-\lambda)^2}{a^2} + \frac{(y-\delta)^2}{b^2} = 1,$$

where

$$\lambda = \frac{k^2 - \alpha}{k^2 - 1}, \; \delta = 0, \; a = \left| \frac{k(\alpha-1)}{k^2-1} \right| \text{ and } b = \left| \frac{(\alpha-1)}{\sqrt{k^2-1}} \right|.$$

For the ellipse $\Omega_{k,\alpha}$ to lie inside Δ_{SG}, $\lambda + a$ should not exceed $2e/(1+e)$ which yields the inequality $k \ge (2e - \alpha(e+1))/(e-1)$. Taking $\alpha = 0$, it follows that $k - \mathcal{ST} \subset \mathcal{S}_{SG}^*$, whenever $k \ge 2e/(e-1)$.

(v) Taking $k = 1$ in part (iv), we observe that the boundary of the domain $\Omega_{1,\alpha} = \{w \in \mathbb{C} : Re\, w > |w - 1| + \alpha\}$ represents a parabola. Now $\Delta_{SG} \subset \Omega_{1,\alpha}$, provided $Re\, w - |w - 1| > \alpha$, where $w = 2/(1 + e^{-z})$. Upon taking $z = e^{i\theta}$, we have

$$\frac{2(1 + e^{-\cos\theta} \cos(\sin\theta)) - \sqrt{1 + e^{-4\cos\theta} - 2e^{-2\cos\theta} + 4e^{-2\cos\theta} \sin^2(\sin\theta)}}{1 + e^{-2\cos\theta} + 2e^{-\cos\theta} \cos(\sin\theta)} > \alpha.$$

A calculation shows that the expression on the left-hand side attains its minimum at $\theta = \pi$ and is equal to $(3 - e)/(1 + e)$. Thus, $\mathcal{S}_{SG}^* \subset \mathcal{ST}(1, \alpha)$, whenever $\alpha \le (3 - e)/(1 + e)$. □

To derive the next result, we need to recall the following subclass of $\mathcal{S}^*$ and a result related to this class:

For $-1 \le B < A \le 1$, let

$$\mathcal{P}_n[A, B] := \left\{ p(z) = 1 + p_n z^n + p_{n+1} z^{n+1} + \ldots : p(z) \prec \frac{1 + Az}{1 + Bz} \right\}.$$

Taking $A = 1 - 2\alpha$ and $B = -1$, the above class reduces to $\mathcal{P}_n(\alpha)$ which can be further reduced to the Carathéodory class $\mathcal{P}$ by taking $\alpha = 0$ and $n = 1$.

Lemma 3.1 [11] *If $p \in \mathcal{P}_n[A, B]$, then for $|z| = r$,*

$$\left| p(z) - \frac{1 - ABr^{2n}}{1 - B^2 r^{2n}} \right| \leq \frac{(A - B)r^n}{1 - B^2 r^{2n}}.$$

In particular, if $p \in \mathcal{P}_n(\alpha)$, then

$$\left| p(z) - \frac{1 + (1 - 2\alpha)r^{2n}}{1 - r^{2n}} \right| \leq \frac{2(1 - \alpha)r^n}{1 - r^{2n}}.$$

Theorem 3.2 *Let $-1 < B < A \leq 1$, then $\mathcal{S}^*[A, B] \subset \mathcal{S}^*_{SG}$ if either of the following conditions hold:*

(i) $2(1 - B) \leq (1 - A)(1 + e)$ and $2(1 - B^2) < (1 - AB)(1 + e) \leq (1 - B^2)(1 + e)$.

(ii) $(1 + A)(1 + e) \leq 2e(1 + B)$ and $(1 - B^2)(1 + e) \leq (1 - AB)(1 + e) < 2e(1 - B^2)$.

Proof Let $f \in \mathcal{S}^*[A, B]$, then $zf'(z)/f(z) \in \mathcal{P}[A, B]$. Using Lemma 3.1, we have

$$\left| \frac{zf'(z)}{f(z)} - \frac{1 - AB}{1 - B^2} \right| < \frac{A - B}{1 - B^2},$$

which represents a disk. To show that this disk is contained in Δ_{SG}, it is sufficient to show that this disk is contained in the disk given in Equation (3). Let $a = (1 - AB)/(1 - B^2)$, then using Lemma 2.2, we have

$$r_a = \frac{e - 1}{e + 1} - \left| \frac{1 - AB}{1 - B^2} - 1 \right|. \tag{6}$$

Now, it suffices to show that $(A - B)/(1 - B^2) \leq r_a$. If part (i) holds, then by multiplying the first inequality by $(1 + B)/(1 + e)(1 - B^2)$, we obtain the required result for $2/(1 + e) < a \leq 1$. Similarly, if part (ii) holds, the result follows for the case when $1 \leq a < 2e/(1 + e)$. $\qquad\square$

4 Coefficient Bounds

Theorem 4.1 *If $f(z) = z + a_2 z^2 + a_3 z^3 + \ldots \in \mathcal{S}^*_{SG}$, then (i) $|a_2| \leq 1/2$, (ii) $|a_3| \leq 1/4$, (iii) $|a_4| \leq 1/6$ and (iv) $|a_5| \leq 1/8$. These bounds are sharp.*

Proof Let $f \in \mathcal{S}^*_{SG}$, then there exists a Schwartz function $\omega(z) = \sum_{k=1}^{\infty} w_k z^k$ such that

$$\frac{zf'(z)}{f(z)} = \frac{2}{1 + e^{-\omega(z)}}. \tag{7}$$

Suppose $\omega(z)$ is taken as $\omega(z) = (p(z) - 1)/(p(z) + 1)$, where $p(z) = 1 + c_1 z + c_2 z^2 + \ldots \in \mathcal{P}$. Then, by substituting $\omega(z)$, $p(z)$ and $f(z)$ in (7) and comparing the coefficients, we obtain a_i's in terms of c_i's as follows:

$$a_2 = \frac{1}{4}c_1, \quad a_3 = \frac{1}{8}\left(c_2 - \frac{c_1^2}{4}\right), \quad a_4 = \frac{1}{48}\left(\frac{7}{24}c_1^3 - \frac{5}{2}c_1c_2 + 4c_3\right)$$

and

$$a_5 = -\frac{1}{16}\left(\frac{17}{1152}c_1^4 - \frac{7}{24}c_1^2c_2 + \frac{3}{8}c_2^2 + \frac{2}{3}c_1c_3 - c_4\right).$$

(i) For a_2, we use the well-known coefficient estimate $|c_n| \leq 2$ $(n \geq 1)$ for the class of Carathéodory functions and it follows that $|a_2| \leq 1/2$.

(ii) For a_3, we use the inequality $|c_2 - \mu c_1^2| \leq 2\max\{1, |2\mu - 1|\}$ given by Ma–Minda [8], which yields $|a_3| \leq 1/4$.

(iii) For a_4, first we rewrite (7) as follows:

$$zf'(z) = (2f(z) - zf'(z))e^{\omega(z)}. \tag{8}$$

By substituting $f(z) = z + \sum_{k=2}^{\infty} a_k z^k$ and $\omega(z) = \sum_{k=1}^{\infty} w_k z^k$ in (8) and comparing the coefficient of z^4, we get

$$6a_4 = w_3 + \frac{3}{4}w_1 w_2 + \frac{1}{24}w_1^3.$$

Using [10, Lemma 2, p. 128], it follows that $|6a_4| \leq 1$ and hence the result.

(iv) For a_5, the result follows by applying [13, Lemma 2.1] with $\gamma = 17/1152$, $a = 3/8$, $\alpha = 1/3$ and $\beta = 7/36$.

The extremal functions for the initial coefficients $a_n (n = 2, 3, 4, 5)$ are of the form:

$$f_n(z) = z \exp \int_0^z \frac{e^{t^{n-1}} - 1}{t(e^{t^{n-1}} + 1)} dt,$$

obtained by taking $\omega(z) = z^{n-1}$ in (7). $\qquad \square$

Example 4.1 (i) Let $f(z) = z + a_2 z^2$. Then, $f \in \mathcal{S}_{SG}^*$ if and only if $|a_2| \leq \sqrt{(e-1)/2e}$.

(ii) Let $f(z) = z/(1-bz)^2$. Then, $f \in \mathcal{S}_{SG}^*$ if and only if $|b| \leq \sqrt{(e-1)/(1+3e)}$.

Proof (i) It is known that $f \in \mathcal{S}_{SG}^*$ if and only if $zf'(z)/f(z)$ lies in the domain Δ_{SG}. Since $\mathcal{S}_{SG}^* \subset \mathcal{S}^*$, it follows that if $f \in \mathcal{S}_{SG}^*$, then $|a_2| \leq 1/2$. We observe that $w(z) = zf'(z)/f(z) = (1 + 2a_2 z)/(1 + a_2 z)$ maps $\mathbb{D}$ onto the disk

$$\left| w - \frac{1 - 2|a_2|^2}{1 - |a_2|^2} \right| < \frac{|a_2|}{1 - |a_2|^2}. \tag{9}$$

Thus, $f \in \mathcal{S}_{SG}^*$ if and only if this disk is contained in Δ_{SG}. Now, it is sufficient to prove that the disk given by Equation (9) is contained in the disk (3), on the

left. Since $(1 - 2|a_2|^2)/(1 - |a_2|^2) \leq 1$, then using Lemma 2.2, the disk mapped by $w(z) = zf'(z)/f(z)$ is contained in Δ_{SG} if and only if

$$\frac{2}{1+e} \leq \frac{1 - 2|a_2|^2}{1 - |a_2|^2} \quad \text{and} \quad \frac{|a_2|}{1 - |a_2|^2} \leq \frac{1 - 2|a_2|^2}{1 - |a_2|^2} - \frac{2}{1+e}.$$

The above two inequalities yield

$$|a_2| \leq \sqrt{\frac{e-1}{2e}} \quad \text{and} \quad |a_2| \leq \frac{e-1}{2e}.$$

Hence, $f \in \mathcal{S}_{SG}^*$ if and only if

$$|a_2| \leq \sqrt{\frac{e-1}{2e}}.$$

(ii) We know that $f(z) = z/(1 - bz)^2 = z + 2bz^2 + 3b^2z^3 + \ldots \in \mathcal{S}_{SG}^*$. As $\mathcal{S}_{SG}^* \subset \mathcal{S}^*$, we have $|b| \leq 1$. Now, we observe that $w(z) = zf'(z)/f(z) = (1 + bz)/(1 - bz)$ maps $\mathbb{D}$ onto the disk

$$\left| w - \frac{1 + |b|^2}{1 - |b|^2} \right| \leq \frac{2|b|}{1 - |b|^2}.$$

Since $(1 + |b|^2)/(1 - |b|^2) \geq 1$, then by Lemma 2.2, it follows that Δ_{SG} contains the above disk if and only if

$$\frac{1 + |b|^2}{1 - |b|^2} \leq \frac{2e}{1+e} \quad \text{and} \quad \frac{2|b|}{1 - |b|^2} \leq \frac{2e}{1+e} - \frac{1 + |b|^2}{1 - |b|^2}.$$

The above two inequalities yield

$$|b| \leq \sqrt{\frac{e-1}{1+3e}} \quad \text{and} \quad |b| \leq \frac{e-1}{1+3e}.$$

Hence, $f \in \mathcal{S}_{SG}^*$ if and only if

$$|b| \leq \sqrt{\frac{e-1}{1+3e}}.$$

5 Radius Problems

Theorem 5.1 *Let* $f \in \mathcal{S}_{SG}^*$, *then the following hold:*

(i) *If $2/(1 + e) \leq \alpha < 1$, then f is starlike of order α in the disk $\mathbb{D}_{r(\alpha)}$, where*

$$r(\alpha) = \log\left(\frac{2}{\alpha} - 1\right).$$

(ii) *If $1 < \beta \leq 2e/(1 + e)$, then f is starlike of reciprocal order $1/\beta$ in the disk $\mathbb{D}_{r(\beta)}$, where*

$$r(\beta) = \log\left(\frac{\beta}{2 - \beta}\right).$$

Further, $f \in \mathcal{M}(\beta)$ in this disk.

(iii) *f is strongly starlike of order $\delta(0 < \delta \leq 1)$ in the disk $\mathbb{D}_{r(\delta)}$, where*

$$r(\delta) = \sqrt{((\delta + 1)\pi/2)^2 + \log^2(\sin(\delta\pi/2))}.$$

Proof (i) Let $f \in \mathcal{S}_{SG}^*$, then

$$\frac{zf'(z)}{f(z)} \prec \frac{2}{1 + e^{-z}}.$$

Therefore, by Lemma 2.1, we have

$$\frac{2}{1 + e^r} \leq \operatorname{Re}\frac{zf'(z)}{f(z)} \leq \frac{2e^r}{1 + e^r} \qquad (|z| = r < 1),$$

which yields the following inequality:

$$\operatorname{Re}\frac{zf'(z)}{f(z)} > \alpha, \quad \text{whenever} \quad \frac{2}{1 + e^r} > \alpha.$$

This inequality holds, whenever $r < \log(2/\alpha - 1)$.

(ii) Similarly,

$$\operatorname{Re}\frac{f(z)}{zf'(z)} > \frac{1}{\beta}, \quad \text{whenever} \quad \frac{1 + e^r}{2e^r} > \frac{1}{\beta}.$$

This inequality holds, whenever $r < \log(\beta/(2 - \beta))$. From Theorem 3.1, we have $\mathcal{RS}^*(1/\beta) \subset \mathcal{M}(\beta)$. Thus, $f \in \mathcal{M}(\beta)$ in $\mathbb{D}_{r(\beta)}$.

(iii) Let $f \in \mathcal{S}_{SG}^*$, then $f \in \mathcal{SS}^*(\delta)$ in $|z| < r$, whenever

$$\left|\arg\frac{2}{1 + e^{-re^{i\theta}}}\right| < \frac{\delta\pi}{2}$$

or equivalently, $|\arg(1 + e^{-re^{i\theta}})| < \delta\pi/2$. For the function $\tilde{f}$ given in equation (2) and $z_0 = -\log\sin(\delta\pi/2) + i(\delta + 1)\pi/2$, we have $|z_0| = $

$$\sqrt{((\delta + 1)\pi/2)^2 + \log^2(\sin(\delta\pi/2))}\} \text{ and}$$

$$\left|\arg\frac{z_0\tilde{f}'(z_0)}{\tilde{f}(z_0)}\right| = \left|\arg\frac{2}{1+e^{-z}}\right|_{z=z_0}$$

$$= |\arg(1 + e^{-z_0})|$$
$$= |\arg(1 + e^{\log(\sin(\delta\pi/2)) - i(\delta+1)\pi/2})|$$
$$= |\arg(1 + \sin(\delta\pi/2)(\cos(\delta+1)\pi/2 - i\sin(\delta+1)\pi/2))|$$
$$= |\arg(\cos^2(\delta\pi/2) - i\sin(\delta\pi/2)\cos(\delta\pi/2))|$$
$$= |\arctan(-\tan(\delta\pi/2))|$$
$$= \delta\pi/2.$$

Hence the result. □

6 Differential Subordination

In this section, we find sharp bounds on $\beta \in \mathbb{R}$ so that the following differential subordination implications hold:

$$1 + \beta\frac{zp'(z)}{(p(z))^k} \prec \frac{2}{1 + e^{-z}} \quad \Rightarrow \quad p(z) \prec \phi_0(z) \quad (k = 0, 1, 2),$$

where ϕ_0 is taken as $(1 + Az)/(1 + Bz)$ or $\sqrt{1 + z}$.

The following results from the theory of differential subordination are required to prove our main results.

Lemma 6.1 [9, Corollary 3.4h, p. 132] *Let q be univalent in $\mathbb{D}$, and let θ and ψ be analytic in a domain $\mathcal{D}$ containing $q(\mathbb{D})$ with $\psi(w) \neq 0$, when $w \in q(\mathbb{D})$. Set $Q(z) := zq'(z)\psi(q(z))$ and $h(z) := \theta(q(z)) + Q(z)$. Suppose that either h is convex or $Q(z)$ is starlike. In addition, assume that $\text{Re}(zh'(z)/Q(z)) > 0 \ (z \in \mathbb{D})$. If p is analytic in $\mathbb{D}$ with $p(0) = q(0)$, $p(\mathbb{D}) \subset \mathcal{D}$ and*

$$\theta(p(z)) + zp'(z)\psi(p(z)) \prec \theta(q(z)) + zq'(z)\psi(q(z)), \tag{10}$$

then $p \prec q$ and q is the best dominant.

Lemma 6.2 [9, Corollary 3.4a, p. 120] *Let h be analytic in $\mathbb{D}$. Let ϕ be analytic in a domain $\mathcal{D}$ containing $h(\mathbb{D})$, and suppose $\text{Re}\,\phi[h(z)] > 0$ and either h is convex, or $H(z) = zh'(z)\phi[h(z)]$ is starlike. If p is analytic in $\mathbb{D}$ with $p(0) = h(0)$, $p(\mathbb{D}) \subset D$ and*

$$p(z) + zp'(z)\phi[p(z)] \prec h(z),$$

then

$$p(z) \prec h(z).$$

Lemma 6.3 [9, Theorem 3.1a, p. 70] *Let h be convex in $\mathbb{D}$, and let $p : \mathbb{D} \to \mathbb{C}$, with $\mathrm{Re}\, P(z) > 0$. If p is analytic in $\mathbb{D}$, then*

$$p(z) + P(z)p(z) \prec h(z) \Rightarrow p(z) \prec h(z).$$

Theorem 6.1 *Suppose p is analytic in $\mathbb{D}$ and $p(0) = 1$ such that it satisfies $1 + \beta z p'(z) \prec 2/(1 + e^{-z})$ and*

$$g(z) = \int_0^z \frac{e^t - 1}{t(e^t + 1)} dt, \tag{11}$$

then the following hold:

(i) $p(z) \prec (1 + Az)/(1 + Bz)$, whenever $\beta \geq \max\{(1 + |B|)g(1)/(A - B),\ \mathrm{Im}\, g(i)(1 + B^2)/(A - B)\}$, where $-1 < B < A \leq 1$.

(ii) $p(z) \prec \sqrt{1 + z}$, whenever $\beta \geq g(1)/(\sqrt{2} - 1)$.

These bounds are sharp.

Proof The differential equation

$$1 + \beta z q'_\beta(z) = \frac{2}{1 + e^{-z}} = h(z)$$

has a solution $q_\beta : \bar{\mathbb{D}} \to \mathbb{C}$ defined as

$$q_\beta(z) = 1 + \frac{1}{\beta}\left[\frac{z}{2} - \frac{z^3}{72} + \frac{z^5}{1200} - \frac{17z^7}{282240} \cdots\right].$$

Taking $\theta(w) = 1$ and $\psi(w) = \beta$ in Lemma 6.1, the function $Q : \mathbb{D} \to \mathbb{C}$ becomes

$$Q(z) = z q'_\beta(z) \psi(q_\beta(z)) = \beta z q'_\beta(z) = \frac{e^z - 1}{e^z + 1}.$$

A calculation shows that, for $z \in \mathbb{D}$,

$$\mathrm{Re}\, \frac{z Q'(z)}{Q(z)} = \mathrm{Re}\, \frac{2z e^z}{e^{2z} - 1} > 0$$

and hence Q is starlike in $\mathbb{D}$. Since $h(z) = 1 + Q(z)$, $\mathrm{Re}(z h'(z)/Q(z)) > 0$ on $\mathbb{D}$. Hence, by Lemma 6.1, $1 + \beta z p'(z) \prec 1 + \beta z q'_\beta(z)$ implies $p(z) \prec q_\beta(z)$. Now, we only need to show that $q_\beta(z) \prec \phi_0(z)$ in each of the parts. Since $q_\beta(z) \prec \phi_0(z)$,

$$\phi_0(-1) < q_\beta(-1) < q_\beta(1) < \phi_0(1). \tag{12}$$

and

$$\mathrm{Im}\, q_\beta(i) < \mathrm{Im}\, \phi_0(i). \tag{13}$$

Note that $q_\beta(z)$ is analytic and maps $\mathbb{D}$ onto a domain which is convex and symmetric with respect to real axis. Also by looking at graphs of the respective functions, it is easy to conclude that the conditions given in (12) and (13) are necessary as well as sufficient in case of $\phi_0(z) = (1+Az)/(1+Bz)$. However, in case of $\phi_0(z) = \sqrt{1+z}$, condition (12) alone is necessary as well as sufficient.

(i) Let $\phi_0(z) = (1 + Az)/(1 + Bz)$. Then, (12) and (13) give the following three inequalities:

$$q_\beta(-1) \geq \frac{1-A}{1-B}, \quad \text{whenever} \quad \beta \geq g(1)\frac{1-B}{A-B} = \beta_1$$

$$q_\beta(1) \leq \frac{1+A}{1+B}, \quad \text{whenever} \quad \beta \geq g(1)\frac{1+B}{A-B} = \beta_2$$

and

$$\operatorname{Im} q_\beta(i) \leq \operatorname{Im}\frac{1+Ai}{1+Bi}, \quad \text{whenever} \quad \beta \geq \operatorname{Im} g(i)\frac{1+B^2}{A-B} = \beta_3,$$

where $g(1) \approx 0.486889$ and $\operatorname{Im} g(i) \approx 0.514788$. We observe that

$$\max\{\beta_1, \beta_2\} = \beta_0 = \begin{cases} \beta_1, & \text{if } B < 0 \\ \beta_2, & \text{if } B > 0. \end{cases}$$

Therefore, $q_\beta(z) \prec (1 + Az)/(1 + Bz)$, whenever $\beta \geq \max\{\beta_0, \beta_3\}$.

(ii) Let $\phi_0(z) = \sqrt{1+z}$. From (12), we have the following two inequalities:

$$q_\beta(-1) \geq 0, \quad \text{whenever} \quad \beta \geq g(1) = \beta_1$$

and

$$q_\beta(1) \leq \sqrt{2}, \quad \text{whenever} \quad \beta \geq \frac{g(1)}{\sqrt{2}-1} = \beta_2,$$

where $g(1) \approx 0.486889$. Since $\max\{\beta_1, \beta_2\} = \beta_2$, then $q_\beta(z) \prec \sqrt{1+z}$, whenever $\beta \geq g(1)/(\sqrt{2}-1)$.

$\square$

Corollary 6.1 *Suppose a function $f \in \mathcal{A}$ satisfies the subordination*

$$1 + \beta\frac{zf'(z)}{f(z)}\left(1 - \frac{zf'(z)}{f(z)} + \frac{zf''(z)}{f'(z)}\right) \prec \frac{2}{1+e^{-z}}$$

and $g(z)$ be defined by (11). Then,

(i) $f \in S^*[A, B]$, *whenever* $\beta \geq \max\{(1 + |B|)g(1)/(A - B), \operatorname{Im} g(i)(1 + B^2)/(A - B)\}$.

(ii) $f \in S_L^*$, *whenever* $\beta \geq g(1)/(\sqrt{2}-1)$.

Theorem 6.2 *Suppose p is analytic in $\mathbb{D}$ and $p(0) = 1$ such that it satisfies $1 + \beta z p'(z)/p(z) \prec 2/(1 + e^{-z})$ and $g(z)$ be defined by (11), then the following holds:*

(i) $p(z) \prec (1 + Az)/(1 + Bz)$, whenever $\beta \geq \beta_{max}$, where $-1 < B < A < 1$ and

$$\beta_{max} = \max \left\{ \frac{-g(1)}{\log\left(\dfrac{1-A}{1-B}\right)}, \frac{g(1)}{\log\left(\dfrac{1+A}{1+B}\right)}, \frac{\operatorname{Im} g(i)}{\arcsin\left(\dfrac{A-B}{1+B^2}\right)} \right\}. \qquad (14)$$

(ii) $p(z) \prec \sqrt{1+z}$, whenever $\beta \geq g(1)/\log(\sqrt{2})$.

These bounds are sharp.

Proof The differential equation

$$1 + \beta \frac{z q'_\beta(z)}{q_\beta(z)} = \frac{2}{1 + e^{-z}} = h(z)$$

has a solution $q_\beta : \bar{\mathbb{D}} \to \mathbb{C}$ defined as

$$q_\beta(z) = \exp\left[\frac{1}{\beta} \left(\frac{z}{2} - \frac{z^3}{72} + \frac{z^5}{1200} - \frac{17z^7}{282240} \cdots \right) \right].$$

Taking $\theta(w) = 1$ and $\psi(w) = \beta/w$ in Lemma 6.1, the function $Q : \mathbb{D} \to \mathbb{C}$ becomes

$$Q(z) = z q'_\beta(z)\phi(q_\beta(z)) = \beta \frac{z q'_\beta(z)}{q_\beta(z)} = \frac{e^z - 1}{e^z + 1}.$$

On the similar lines of the proof of Theorem 6.1, the following parts are proved.

(i) Let $\phi_0(z) = (1 + Az)/(1 + Bz)$. Then, (12) and (13) give the following three inequalities:

$$q_\beta(-1) \geq \frac{1-A}{1-B}, \quad \text{whenever} \quad \beta \geq \frac{-g(1)}{\log((1-A)/(1-B))} = \beta_1$$

$$q_\beta(1) \leq \frac{1+A}{1+B}, \quad \text{whenever} \quad \beta \geq \frac{g(1)}{\log((1+A)/(1+B))} = \beta_2$$

and

$$\operatorname{Im} q_\beta(i) \leq \operatorname{Im} \frac{1+Ai}{1+Bi}, \quad \text{whenever} \quad \beta \geq \frac{\operatorname{Im} g(i)}{\arcsin\left(\dfrac{A-B}{1+B^2}\right)} = \beta_3.$$

Let $\beta_{max} = \max\{\beta_1, \beta_2, \beta_3\}$. Then, $q_\beta(z) \prec (1 + Az)/(1 + Bz)$, whenever $\beta \geq \beta_{max}$.

(ii) Let $\phi_0(z) = \sqrt{1+z}$. Then, (12) gives the following two inequalities:

$$q_\beta(-1) \geq 0 \quad \text{for every } \beta$$

and

$$q_\beta(1) \leq \sqrt{2}, \quad \text{whenever } \beta \geq g(1)/\log(\sqrt{2}).$$

Thus, $q_\beta(z) \prec \sqrt{1+z}$, whenever $\beta \geq g(1)/\log(\sqrt{2})$.

$\square$

Corollary 6.2 *Suppose a function $f \in \mathcal{A}$ satisfies the subordination*

$$1 + \beta \left(1 - \frac{zf'(z)}{f(z)} + \frac{zf''(z)}{f'(z)} \right) \prec \frac{2}{1 + e^{-z}}$$

and $g(z)$ be defined by (11). Then,

(i) $f \in S^*[A, B]$, *whenever $\beta \geq \beta_{\max}$, where $\beta_{\max}$ is given in (14).*
(ii) $f \in S_L^*$, *whenever $\beta \geq g(1)/\log(\sqrt{2})$.*

Theorem 6.3 *Suppose p is analytic in $\mathbb{D}$ and $p(0) = 1$ such that it satisfies $1 + \beta z p'(z)/p^2(z) \prec 2/(1 + e^{-z})$ and $g(z)$ be defined by (11). Then, the following holds:*

(i) $p(z) \prec (1 + Az)/(1 + Bz)$, *whenever $\beta \geq (1 + |A|)g(1)/(A - B)$, where $-1 < B < A < 1$.*
(ii) $p(z) \prec \sqrt{1 + z}$, *whenever $\beta \geq g(1)\sqrt{2}/(\sqrt{2} - 1)$.*

These bounds are sharp.

Proof The differential equation

$$1 + \beta \frac{zq_\beta'(z)}{q_\beta^2(z)} = \frac{2}{1 + e^{-z}} = h(z)$$

has a solution $q_\beta : \bar{\mathbb{D}} \to \mathbb{C}$ defined as

$$q_\beta(z) = \frac{1}{1 - \dfrac{1}{\beta} \left[\dfrac{z}{2} - \dfrac{z^3}{72} + \dfrac{z^5}{1200} - \dfrac{17z^7}{282240} \cdots \right]}.$$

Taking $\theta(w) = 1$ and $\psi(w) = \beta/w^2$ in Lemma 6.1, the function $Q : \mathbb{D} \to \mathbb{C}$ becomes

$$Q(z) = zq_\beta'(z)\phi(q_\beta(z)) = \beta \frac{zq_\beta'(z)}{q_\beta^2(z)} = \frac{e^z - 1}{e^z + 1}.$$

A calculation shows that, for $z \in \mathbb{D}$,

$$\operatorname{Re} \frac{zQ'(z)}{Q(z)} = \operatorname{Re} \frac{2ze^z}{e^{2z} - 1} > 0$$

and hence Q is starlike in $\mathbb{D}$. Since $h(z) = 1 + Q(z)$, $\mathrm{Re}(zh'(z)/Q(z)) > 0$ on $\mathbb{D}$. Hence, by Lemma 6.1, $1 + \beta z p'(z) \prec 1 + \beta z q'_\beta(z)$ implies $p(z) \prec q_\beta(z)$. Now, we only need to show that $q_\beta(z) \prec \phi_0(z)$ in each of the parts. Since $q_\beta(z) \prec \phi_0(z)$,

$$\phi_0(-1) < q_\beta(-1) < q_\beta(1) < \phi_0(1).$$

This condition is necessary as well as sufficient as it is indicated by the graphs of the respective functions.

(i) Let $\phi_0(z) = (1 + Az)/(1 + Bz)$. Then, (12) gives the following two inequalities:

$$q_\beta(-1) \geq \frac{1 - A}{1 - B}, \quad \text{whenever} \quad \beta \geq g(1)\frac{1 - A}{A - B} = \beta_1$$

and

$$q_\beta(1) \leq \frac{1 + A}{1 + B}, \quad \text{whenever} \quad \beta \geq g(1)\frac{1 + A}{A - B} = \beta_2,$$

where $g(1) \approx 0.486889$. We observe that

$$\max\{\beta_1, \beta_2\} = \begin{cases} \beta_1, & \text{if } A < 0 \\ \beta_2, & \text{if } A > 0 \end{cases}$$

Therefore, $q_\beta(z) \prec (1 + Az)/(1 + Bz)$, whenever $\beta \geq g(1)(1 + |A|)/(A - B)$.

(ii) Let $\phi_0(z) = \sqrt{1 + z}$. Then, (12) gives the following two inequalities:

$$q_\beta(-1) \geq 0 \quad \text{for} \quad \begin{cases} \beta < -g(1), & if \ \beta < 0 \\ \text{any} \ \beta, & if \ \beta > 0 \end{cases}$$

and

$$q_\beta(1) \leq \sqrt{2}, \quad \text{whenever} \quad \beta \geq \frac{g(1)\sqrt{2}}{\sqrt{2} - 1}.$$

Since both the conditions hold for the case when $\beta \geq g(1)\sqrt{2}/(\sqrt{2} - 1)$, $q_\beta(z) \prec \sqrt{1 + z}$ for such β.

$\square$

Corollary 6.3 *Suppose a function $f \in \mathcal{A}$ satisfies the subordination*

$$1 + \beta \left(\frac{zf'(z)}{f(z)}\right)^{-1} \left(1 - \frac{zf'(z)}{f(z)} + \frac{zf''(z)}{f'(z)}\right) \prec \frac{2}{1 + e^{-z}}$$

and $g(z)$ be defined by (11). Then,

(i) $f \in S^*[A, B]$, *whenever $\beta \geq (1 + |A|)g(1)/(A - B)$.*

(ii) $f \in S_L^*$, *whenever $\beta \geq g(1)\sqrt{2}/(\sqrt{2} - 1)$.*

Further, we extend these results for $\beta \in \mathbb{C}$. In order to prove the next result, we first prove the following lemma:

Lemma 6.4 *Let $r_0 \approx 0.546302$ be the positive root of the equation $r^2 + 2\cot(1)r - 1 = 0$. Then,*

$$\left| \log\left(\frac{1+z}{1-z} \right) \right| \geq 1 \text{ if and only if } |z| \geq r_0.$$

Proof Let $z = re^{i\theta}$ be a boundary point of the disk $|z| < r$, where $0 < r \leq 1$. Then,

$$\left| \log\left(\frac{1+re^{i\theta}}{1-re^{i\theta}} \right) \right| \geq 1$$

if and only if

$$\left| \log\left| \frac{1-r^2+i2r\sin\theta}{1+r^2-2r\cos\theta} \right| + i \arctan\left(\frac{2r\sin\theta}{1-r^2} \right) \right| \geq 1,$$

which holds if and only if

$$\log^2 \sqrt{ \frac{(1-r^2)^2 + 2r\sin\theta}{(1+r^2-2r\cos\theta)^2} } + \left(\arctan\left(\frac{2r\sin\theta}{1-r^2} \right) \right)^2 \geq 1$$

The expression on the left-hand side attains its minimum at $\theta = \pi/2$, and therefore, the above inequality holds if and only if

$$\left(\arctan\left(\frac{2r}{1-r^2} \right) \right)^2 \geq 1$$

which is true if and only if

$$r \geq (-\cot(1) + \sqrt{1 + \cot^2(1)}) \approx 0.546302.$$

$\square$

Theorem 6.4 *Let p be a function analytic in $\mathbb{D}$ such that $p(0) = 1$ and*

$$1 + \beta \frac{zp'(z)}{p^k(z)} \prec \frac{2}{1+e^{-z}} \quad \text{for } k = 0, 1 \text{ and } 2.$$

Let $r_0 \approx 0.546302$ be the positive root of the equation $r^2 + 2\cot(1)r - 1 = 0$. Then, the following hold:

(i) $p(z) \prec (1+Az)/(1+Bz)$, whenever $|\beta| \geq r_0(1+|B|)^{2-k}(1+|A|)^k/(A-B)$.
(ii) $p(z) \prec \sqrt{1+z}$, whenever $|\beta| \geq 2^{(k+3)/2}r_0$.

Proof (i) Let $q(z) = (1 + Az)/(1 + Bz)$. Then, the function $Q(z)$ given by

$$Q(z) = \beta \frac{zq'(z)}{q^k(z)} = \frac{\beta z(A - B)}{(1 + Bz)^{2-k}(1 + Az)^k}$$

is starlike in $\mathbb{D}$ (see [6]). Therefore, if the subordination

$$1 + \beta \frac{zp'(z)}{p^k(z)} \prec 1 + \beta \frac{zq'(z)}{q^k(z)}$$

holds, then $p(z) \prec q(z)$ using Lemma 6.1. To prove the desired result, it suffices to show that

$$\frac{2}{1 + e^{-z}} \prec 1 + \frac{\beta zq'(z)}{q^k(z)} = 1 + \frac{\beta z(A - B)}{(1 + Bz)^{2-k}(1 + Az)^k} = h(z). \quad (15)$$

Let $w = \Phi(z) = 2/(1 + e^{-z})$. Then, $\Phi^{-1}(w) = \log(w/(2 - w))$. The subordination $\Phi(z) \prec h(z)$ is equivalent to $z \prec \Phi^{-1}(h(z))$. Thus, we need only to show that $|\Phi^{-1}(h(e^{it}))| \geq 1$. Taking $z = e^{it}$ ($0 \leq t \leq 2\pi$), we have

$$|\Phi^{-1}(h(e^{it}))| = \left| \log \left(\frac{1 + \dfrac{\beta e^{it}(A - B)}{(1 + Be^{it})^{2-k}(1 + Ae^{it})^k}}{1 - \dfrac{\beta e^{it}(A - B)}{(1 + Be^{it})^{2-k}(1 + Ae^{it})^k}} \right) \right| \geq 1.$$

By Lemma 6.4, it follows that the above inequality holds whenever

$$\left| \frac{\beta e^{it}(A - B)}{(1 + Be^{it})^{2-k}(1 + Ae^{it})^k} \right| \geq r_0,$$

which is true if

$$|\beta| \geq \frac{r_0(1 + |B|)^{2-k}(1 + |A|)^k}{A - B}.$$

(ii) Let $q(z) = \sqrt{1 + z}$. Then, the function $Q(z)$ given by

$$Q(z) = \beta \frac{zq'(z)}{q^k(z)} = \frac{\beta z}{2(1 + z)^{(k+1)/2}}$$

is starlike in $\mathbb{D}$ [6]. Therefore, if the subordination

$$1 + \beta \frac{zp'(z)}{p^k(z)} \prec 1 + \beta \frac{zq'(z)}{q^k(z)}$$

holds, then $p(z) \prec q(z)$ by Lemma 6.1. To prove the desired result, it is enough to show that

$$\frac{2}{1 + e^{-z}} \prec 1 + \frac{\beta z q'(z)}{q^k(z)} = 1 + \frac{\beta z}{2(1 + z)^{(k+1)/2}} = h(z). \qquad (16)$$

Let $w = \Phi(z) = 2/(1 + e^{-z})$. Then, $\Phi^{-1}(w) = \log(w/(2 - w))$. The subordination $\Phi(z) \prec h(z)$ is equivalent to $z \prec \Phi^{-1}(h(z))$. Thus, it suffices to show that $|\Phi^{-1}(h(e^{it}))| \geq 1$. Taking $z = e^{it}$ $(0 \leq t \leq 2\pi)$, we have

$$|\Phi^{-1}(h(e^{it}))| = \left| \log \left(\frac{1 + \dfrac{\beta e^{it}}{2(1 + e^{it})^{(k+1)/2}}}{1 - \dfrac{\beta e^{it}}{2(1 + e^{it})^{(k+1)/2}}} \right) \right| \geq 1.$$

Using Lemma 6.4, it follows that the above inequality holds, whenever

$$\left| \frac{\beta e^{it}}{2(1 + e^{it})^{(k+1)/2}} \right| \geq r_0,$$

which is true, if

$$|\beta| \geq 2^{(k+3)/2} r_0.$$

$\square$

Corollary 6.4 *Let r_0 be the positive root of the equation $r^2 + 2\cot(1)r - 1 = 0$. If a function $f \in \mathcal{A}$ satisfies the subordination*

$$1 + \beta \frac{zf'(z)}{f(z)} \left(1 + \frac{zf''(z)}{f'(z)} - \frac{zf'(z)}{f(z)} \right) \prec \frac{2}{1 + e^{-z}},$$

then

(i) *$f \in S^*[A, B]$, whenever $|\beta| \geq r_0(1 + |B|)^2/(A - B)$. In particular, f is starlike for $|\beta| \geq 2r_0$.*
(ii) *$f \in S_L^*$, whenever $|\beta| \geq 2\sqrt{2}r_0$.*

Corollary 6.5 *Let r_0 be the positive root of the equation $r^2 + 2\cot(1)r - 1 = 0$. If a function $f \in \mathcal{A}$ satisfies the subordination*

$$1 + \beta \left(1 + \frac{zf''(z)}{f'(z)} - \frac{zf'(z)}{f(z)} \right) \prec \frac{2}{1 + e^{-z}},$$

then

(i) *$f \in S^*[A, B]$, whenever $|\beta| \geq r_0(1 + |B|)(1 + |A|)/(A - B)$. In particular, f is starlike for $|\beta| \geq 2r_0$.*
(ii) *$f \in S_L^*$, whenever $|\beta| \geq 4r_0$.*

Corollary 6.6 *Let r_0 be the positive root of the equation $r^2 + 2\cot(1)r - 1 = 0$. If a function $f \in \mathcal{A}$ satisfies the subordination*

$$1 + \beta \left(\frac{zf'(z)}{f(z)} \right)^{-1} \left(1 + \frac{zf''(z)}{f'(z)} - \frac{zf'(z)}{f(z)} \right) \prec \frac{2}{1 + e^{-z}},$$

then

(i) $f \in S^*[A, B]$, *whenever* $|\beta| \geq r_0(1 + |A|)^2/(A - B)$. *In particular, f is starlike for $|\beta| \geq 2r_0$.*
(ii) $f \in S_L^*$, *whenever* $|\beta| \geq 4\sqrt{2}r_0$.

In the following results, we find sharp bounds on $\beta \in \mathbb{R}$ so that the following differential subordination implications hold:

$$1 + \beta \frac{zp'(z)}{p^k(z)} \prec \phi_0(z) \quad \Rightarrow \quad p(z) \prec \frac{2}{1 + e^{-z}} \quad (k = 0, 1, 2)$$

where ϕ_0 is taken as $(1 + Az)/(1 + Bz)$ and $\sqrt{1 + z}$.

Theorem 6.5 *Let p be a function analytic on $\mathbb{D}$ with $p(0) = 1$. If any of the following conditions is true:*

(i) $1 + \beta zp'(z) \prec (1 + Az)/(1 + Bz)$, *where* $\beta \geq (A - B)\log(1 - |B|)(1 + e)/((1 - e)|B|)$ *and* $-1 < B < A \leq 1$ $(B \neq 0)$
(ii) $1 + \beta zp'(z) \prec \sqrt{1 + z}$, *where* $\beta \geq 2(1 - \log 2)(e + 1)/(e - 1)$,

then $p(z) \prec \dfrac{2}{1 + e^{-z}}$.

Proof (i) The differential equation

$$1 + \beta z q_\beta'(z) = \frac{1 + Az}{1 + Bz} = h(z)$$

has a solution $q_\beta : \bar{\mathbb{D}} \to \mathbb{C}$ defined as

$$q_\beta(z) = 1 + \frac{(A - B)\log(1 + Bz)}{B\beta}.$$

Taking $\theta(w) = 1$ and $\psi(w) = \beta$ in Lemma 6.1, the function $Q : \mathbb{D} \to \mathbb{C}$ becomes

$$Q(z) = zq_\beta'(z)\phi(q_\beta(z)) = \beta z q_\beta'(z) = \frac{(A - B)z}{(1 + Bz)}.$$

A calculation shows that for $z \in \mathbb{D}$

$$\operatorname{Re} \frac{zQ'(z)}{Q(z)} = \operatorname{Re} \frac{1}{1 + Bz} > 0$$

and hence Q is starlike in $\mathbb{D}$. Since $h(z) = 1 + Q(z)$, $\mathrm{Re}(zh'(z)/Q(z)) > 0$ on $\mathbb{D}$. Hence, by Lemma 6.1, $1 + \beta z p'(z) \prec 1 + \beta z q'_\beta(z)$ implies $p(z) \prec q_\beta(z)$. Now, we only need to show that $q_\beta(z) \prec 2/(1 + e^{-z}) = \phi(z)$. Since $q_\beta(z) \prec \phi(z)$,

$$\phi(-1) < q_\beta(-1) < q_\beta(1) < \phi(1).$$

Graphically, it can be easily concluded that this condition is necessary as well as sufficient and yields the following two inequalities:

$$q_\beta(-1) \geq \frac{2}{1+e}, \quad \text{whenever} \quad \beta \geq \frac{(1+e)(A-B)\log(1-B)}{(1-e)B} = \beta_1$$

and

$$q_\beta(1) \leq \frac{2e}{1+e}, \quad \text{whenever} \quad \beta \geq \frac{(e+1)(A-B)\log(1+B)}{(e-1)B} = \beta_2.$$

We observe that

$$\max\{\beta_1, \beta_2\} = \begin{cases} \beta_1, & \text{if } B > 0 \\ \beta_2, & \text{if } B < 0. \end{cases}$$

Therefore, $q_\beta(z) \prec 2/(1+e^{-z})$, whenever $\beta \geq (1+e)(A-B)\log(1-|B|)/(1-e)|B|$.

(ii) The differential equation

$$1 + \beta z q'_\beta(z) = \sqrt{1+z} = h(z)$$

has a solution $q_\beta : \bar{\mathbb{D}} \to \mathbb{C}$ defined as

$$q_\beta(z) = 1 + \frac{2}{\beta}\left(\sqrt{1+z} - \log(\sqrt{1+z} + 1) + \log 2 - 1\right).$$

Taking $\theta(w) = 1$ and $\psi(w) = \beta$ in Lemma 6.1, the function $Q : \mathbb{D} \to \mathbb{C}$ becomes

$$Q(z) = zq'_\beta(z)\phi(q_\beta(z)) = \beta z q'_\beta(z) = \sqrt{1+z} - 1.$$

A calculation shows that $Q(z)$ is starlike and $\mathrm{Re}(zh'(z)/Q(z)) > 0$, for $z \in \mathbb{D}$. Proceeding in the same manner as in part (i), we have the following two inequalities:

$$q_\beta(-1) \geq \frac{2}{1+e}, \quad \text{whenever } \beta \geq \frac{2(e+1)(1-\log 2)}{(e-1)} = \beta_1$$

and

$$q_\beta(1) \leq \frac{2e}{1+e}, \text{ whenever } \beta \geq \frac{e+1}{e-1}\left(2\sqrt{2} - 2\log(\sqrt{2}+1) + 2\log 2 - 2\right) = \beta_2.$$

We observe that

$$\max\{\beta_1, \beta_2\} = \beta_1$$

Thus, $q_\beta(z) \prec 2/(1+e^{-z})$, whenever $\beta \geq (e+1)(2-2\log 2)/(e-1)$.

$\square$

Corollary 6.7 *Let $f \in \mathcal{A}$ and*

$$\Phi_\beta(z) = 1 + \beta \frac{zf'(z)}{f(z)}\left(1 + \frac{zf''(z)}{f'(z)} - \frac{zf'(z)}{f(z)}\right).$$

Then, $f \in S_{SG}^*$, if any of the following conditions hold:

(i) *$\Phi_\beta(z) \prec (1+Az)/(1+Bz)$, where $\beta \geq (A-B)\log(1-|B|)(1+e)/((1-e)|B|)$ and $-1 < B < A \leq 1$ ($B \neq 0$).*

(ii) *$\Phi_\beta(z) \prec \sqrt{1+z}$, where $\beta \geq (e+1)(2-2\log 2)/(e-1)$.*

Theorem 6.6 *Let p be a function analytic on $\mathbb{D}$ with $p(0) = 1$. If any of the following conditions hold:*

(i) *$1 + \beta zp'(z)/p(z) \prec (1+Az)/(1+Bz)$ $(-1 < B < A \leq 1)$ and $\beta \geq \beta_{\max}$, where*

$$\beta_{\max} = \begin{cases} \dfrac{(A-B)\log(1-B)}{\log(2/(1+e))B} & \text{if } B < (1-e)/(1+e) \\[3mm] \dfrac{(A-B)\log(1+B)}{\log(2e/(e+1))B} & \text{if } B \geq (1-e)/(1+e) \end{cases}$$

(ii) *$1 + \beta zp'(z)/p(z) \prec \sqrt{1+z}$, where $\beta \geq (2\sqrt{2} - 2\log(\sqrt{2}+1) + 2\log 2 - 2)/\log(2e/(1+e))$,*

then $p(z) \prec \dfrac{2}{1+e^{-z}}$.

Proof (i) The differential equation

$$1 + \beta \frac{zq'_\beta(z)}{q_\beta(z)} = \frac{1+Az}{1+Bz} = h(z)$$

has a solution $q_\beta : \bar{\mathbb{D}} \to \mathbb{C}$ defined as

$$q_\beta(z) = \exp\left(\frac{(A-B)\log(1+Bz)}{B\beta}\right).$$

Taking $\theta(w) = 1$ and $\psi(w) = \beta/w$ in Lemma 6.1, the function $Q : \mathbb{D} \to \mathbb{C}$ becomes

$$Q(z) = zq_\beta'(z)\phi(q_\beta(z)) = \frac{\beta z q_\beta'(z)}{q_\beta(z)} = \frac{(A-B)z}{(1+Bz)}.$$

Proceeding in the same manner as in Theorem 6.5 (i), we have the following two conditions:

$$q_\beta(-1) \geq \frac{2}{1+e}, \quad \text{whenever} \quad \beta \geq \frac{(A-B)\log(1-B)}{\log(2/(1+e))B} = \beta_1$$

and

$$q_\beta(1) \leq \frac{2e}{1+e}, \quad \text{whenever} \quad \beta \geq \frac{(A-B)\log(1+B)}{\log(2e/(e+1))B} = \beta_2.$$

We observe that

$$\max\{\beta_1, \beta_2\} = \beta_{max} = \begin{cases} \beta_1, & \text{if } B < (1-e)/(1+e) \\ \beta_2, & \text{if } B \geq (1-e)/(1+e). \end{cases}$$

Thus, $q_\beta(z) \prec 2/(1+e^{-z})$, whenever $\beta \geq \beta_{max}$.

(ii) The differential equation

$$1 + \beta\frac{zq_\beta'(z)}{q_\beta(z)} = \sqrt{1+z} = h(z)$$

has a solution $q_\beta : \bar{\mathbb{D}} \to \mathbb{C}$ defined as

$$q_\beta(z) = \exp\left(\frac{2}{\beta}\left(\sqrt{1+z} - \log(\sqrt{1+z}+1) + \log 2 - 1\right)\right).$$

Taking $\theta(w) = 1$ and $\psi(w) = \beta/w$ in Lemma 6.1, the function $Q : \mathbb{D} \to \mathbb{C}$ becomes

$$Q(z) = zq_\beta'(z)\phi(q_\beta(z)) = \beta\frac{zq_\beta'(z)}{q_\beta(z)} = \sqrt{1+z} - 1.$$

Proceeding in the same manner as in Theorem 6.5 (ii), we have the following two conditions:

$$q_\beta(-1) \geq \frac{2}{1+e}, \quad \text{whenever} \quad \beta \geq \frac{2\log 2 - 2}{\log(2/(1+e))} = \beta_1$$

and

$$q_\beta(1) \leq \frac{2e}{1+e}, \quad \text{whenever} \quad \beta \geq \frac{2\sqrt{2} - 2\log(\sqrt{2}+1) + 2\log 2 - 2}{\log(2e/(1+e))} = \beta_2.$$

Clearly,

$$\max\{\beta_1, \beta_2\} = \beta_2.$$

Thus, $q_\beta(z) \prec 2/(1 + e^{-z})$, whenever $\beta \geq (2\sqrt{2} - 2\log(\sqrt{2} + 1) + 2\log 2 - 2)/\log(2e/(1 + e))$.

□

Corollary 6.8 *Let $f \in \mathcal{A}$ and*

$$\Phi_\beta(z) = 1 + \beta \left(1 - \frac{zf'(z)}{f(z)} + \frac{zf''(z)}{f'(z)}\right).$$

Then $f \in S_{SG}^*$, if any of the following conditions hold:

(i) $\Phi_\beta(z) \prec \dfrac{1 + Az}{1 + Bz}$ *and $\beta \geq \beta_{\max}$, where $-1 < B < A \leq 1$ and*

$$\beta_{\max} = \begin{cases} \dfrac{(A - B)\log(1 - B)}{\log(2/(1 + e))B}, & \text{if } B < (1 - e)/(1 + e) \\[4mm] \dfrac{(A - B)\log(1 + B)}{\log(2e/(e + 1))B}, & \text{if } B \geq (1 - e)/(1 + e). \end{cases}$$

(ii) $\Phi_\beta(z) \prec \sqrt{1 + z}$, *where $\beta \geq (2\sqrt{2} - 2\log(\sqrt{2} + 1) + 2\log 2 - 2)/\log(2e/(1 + e))$.*

Theorem 6.7 *Let p be a function analytic on $\mathbb{D}$ such that $p(0) = 1$. If any of the following conditions hold:*

(i) $1 + \beta zp'(z)/p^2(z) \prec (1 + Az)/(1 + Bz)$ *and $\beta \geq \beta_{\max}$, where $-1 < B < A \leq 1$ and*

$$\beta_{\max} = \max\left\{\frac{2(A - B)\log(1 - B)}{(1 - e)B}, \frac{2e(A - B)\log(1 + B)}{(e - 1)B}\right\}$$

(ii) $1 + \beta zp'(z)/p^2(z) \prec \sqrt{1 + z}$, *where $\beta \geq 4e\left(\sqrt{2} - \log(\sqrt{2} + 1) + \log 2 - 1\right)/(e - 1)$,*

then $p(z) \prec \dfrac{2}{1 + e^{-z}}$.

Proof (i) The differential equation

$$1 + \beta \frac{zq_\beta'(z)}{q_\beta^2(z)} = \frac{1 + Az}{1 + Bz} = h(z)$$

has a solution $q_\beta : \bar{\mathbb{D}} \to \mathbb{C}$ defined as

$$q_\beta(z) = \frac{1}{1 - \dfrac{(A - B)\log(1 + Bz)}{B\beta}}.$$

Taking $\theta(w) = 1$ and $\psi(w) = \beta/w^2$ in Lemma 6.1, the function $Q : \mathbb{D} \rightarrow \mathbb{C}$ becomes

$$Q(z) = zq'_\beta(z)\phi(q_\beta(z)) = \beta\frac{zq'_\beta(z)}{q_\beta^2(z)} = \frac{(A-B)z}{(1+Bz)}.$$

Proceeding in the same manner as in Theorem 6.5 (i), we have the following two conditions:

$$q_\beta(-1) \geq \frac{2}{1+e}, \quad \text{whenever} \quad \beta \geq \frac{2(A-B)\log(1-B)}{(1-e)B} = \beta_1$$

and

$$q_\beta(1) \leq \frac{2e}{1+e}, \quad \text{whenever} \quad \beta \geq \frac{2e(A-B)\log(1+B)}{(e-1)B} = \beta_2.$$

Let $B_0 \approx 0.796615$ be the root of the equation $\log(1-B) + e\log(1+B) = 0$. Then,

$$\max\{\beta_1, \beta_2\} = \beta_{\max} = \begin{cases} \beta_1, & \text{if } B < B_0 \\ \beta_2, & \text{if } B \geq B_0. \end{cases} \tag{17}$$

Thus, $q_\beta(z) \prec 2/(1+e^{-z})$, whenever $\beta \geq \beta_{\max}$.

(ii) The differential equation

$$1 + \beta\frac{zq'_\beta(z)}{q_\beta^2(z)} = \sqrt{1+z} = h(z).$$

has a solution $q_\beta : \bar{\mathbb{D}} \rightarrow \mathbb{C}$ defined as

$$q_\beta(z) = \frac{1}{1 - \dfrac{2}{\beta}\left(\sqrt{1+z} - \log(\sqrt{1+z}+1) + \log 2 - 1\right)}.$$

Taking $\theta(w) = 1$ and $\psi(w) = \beta/w^2$ in Lemma 6.1, the function $Q : \mathbb{D} \rightarrow \mathbb{C}$ becomes

$$Q(z) = zq'_\beta(z)\phi(q_\beta(z)) = \beta\frac{zq'_\beta(z)}{q_\beta^2(z)} = \sqrt{1+z} - 1.$$

Proceeding in the same manner as in Theorem 6.5 (ii), we have the following two conditions:

$$q_\beta(-1) \geq \frac{2}{1+e}, \quad \text{whenever} \quad \beta \geq \frac{4(\log 2 - 1)}{1-e} = \beta_1$$

and

$$q_\beta(1) \le \frac{2e}{1+e}, \quad \text{whenever} \quad \beta \ge \frac{4e\left(\sqrt{2} - \log(\sqrt{2}+1) + \log 2 - 1\right)}{e-1} = \beta_2.$$

Clearly,

$$\max\{\beta_1, \beta_2\} = \beta_2.$$

Thus, $q_\beta(z) \prec 2/(1+e^{-z})$, whenever $\beta \ge 4e\left(\sqrt{2} - \log(\sqrt{2}+1) + \log 2 - 1\right)/(e-1)$.

$\square$

Corollary 6.9 *Let $f \in \mathcal{A}$ and*

$$\Phi_\beta(z) = 1 + \beta \left(\frac{zf'(z)}{f(z)}\right)^{-1} \left(1 + \frac{zf''(z)}{f'(z)} - \frac{zf'(z)}{f(z)}\right).$$

Then, $f \in S_{SG}^*$, if any of the following conditions hold:

(i) $\Phi_\beta(z) \prec (1+Az)/(1+Bz)$ *and* $\beta \ge \beta_{\max}$, *where* $\beta_{\max}$ *is given by equation* (17) *and* $-1 < B < A \le 1$.
(ii) $\Phi_\beta(z) \prec \sqrt{1+z}$, *where* $\beta \ge 4e\left(\sqrt{2} - \log(\sqrt{2}+1) + \log 2 - 1\right)/(e-1)$.

Again, we extend the preceding three results for $\beta \in \mathbb{C}$.

Theorem 6.8 *Let p be a function analytic in $\mathbb{D}$ such that $p(0) = 1$. If any of the following conditions hold for $k = 0, 1, 2$:*

(i) $1 + \beta z p'(z)/p^k(z) \prec (1 + Az)/(1 + Bz)$, *where* $|\beta| \ge (A - B)e^{k-1}(1 + e)^{2-k}/(1 - |B|)2^{1-k}$ *and* $-1 < B < A \le 1$
(ii) $1 + \beta z p'(z)/p^k(z) \prec \sqrt{1+z}$, *where* $|\beta| \ge (\sqrt{2}+1)e^{k-1}(1+e)^{2-k}$,

then $p(z) \prec \dfrac{2}{1+e^{-z}}.$

Proof Let $q(z) = \dfrac{2}{1+e^{-z}}$. Then, the function $Q : \mathbb{D} \to \mathbb{C}$ is given by

$$Q(z) = \beta \frac{zq'(z)}{q^k(z)} = \frac{2^{1-k}\beta z e^{-z}}{(1+e^{-z})^{2-k}}.$$

It is easy to see that $Q(z)$ is starlike in $\mathbb{D}$. By Lemma 6.1, if the subordination

$$1 + \beta \frac{zp'(z)}{p^k(z)} \prec 1 + \beta \frac{zq'(z)}{q^k(z)}$$

holds, then $p(z) \prec q(z)$.

(i) To prove the required result, we need to prove that

$$\frac{1 + Az}{1 + Bz} \prec 1 + \frac{\beta z q'(z)}{q^k(z)} = 1 + \frac{2^{1-k} \beta z e^{-z}}{(1 + e^{-z})^{2-k}} = h(z). \tag{18}$$

Let $w = \Phi(z) = (1 + Az)/(1 + Bz)$. Then, $\Phi^{-1}(w) = (w - 1)/(A - Bw)$. The subordination $\Phi(z) \prec h(z)$ is equivalent to $z \prec \Phi^{-1}(h(z))$. Thus, it suffices to show $|\Phi^{-1}(h(e^{it}))| \geq 1$. Taking $z = e^{it}$ $(0 \leq t \leq 2\pi)$, we have

$$|\Phi^{-1}(h(e^{it}))| \geq \frac{2^{1-k}|\beta|}{(A - B)e^{\cos t}(1 + e^{-2\cos t} + 2e^{-\cos t}\cos(\sin t))^{\frac{2-k}{2}} + 2^{1-k}|B\beta|}$$
$$= a(t).$$

A simple computation gives that $\min_{0 \leq t < 2\pi} a(t)$ is attained at $t = 0$. Thus,

$$a(0) = \frac{2^{1-k}|\beta|}{(A - B)e(1 + e^{-1})^{2-k} + 2^{1-k}|B\beta|} \geq 1,$$

whenever

$$|\beta| \geq \frac{(A - B)e(1 + e^{-1})^{2-k}}{(1 - |B|)2^{1-k}}.$$

(ii) Here, we need to prove that $\sqrt{1 + z} \prec h(z)$. Let $w = \Phi(z) = \sqrt{1 + z}$. Then, $\Phi^{-1}(w) = w^2 - 1$. To prove the required result, it suffices to show that $|\Phi^{-1}(h(e^{it}))| \geq 1$. Taking $z = e^{it}$ $(0 \leq t \leq 2\pi)$, we have

$$|\Phi^{-1}(h(e^{it}))| = \left| \left(1 + \frac{2^{1-k}\beta e^{it} e^{-e^{it}}}{(1 + e^{-e^{it}})^{2-k}} \right)^2 - 1 \right| \geq 1,$$

whenever

$$\left| 1 + \frac{2^{1-k}\beta e^{it} e^{-e^{it}}}{(1 + e^{-e^{it}})^{2-k}} \right| \geq \sqrt{2}.$$

The above inequality is true, whenever

$$\frac{2^{1-k}|\beta|e^{-\cos t}}{(1 + e^{-2\cos t} + 2e^{-\cos t}\cos(\sin t))^{(2-k)/2}} \geq \sqrt{2} + 1.$$

The function on the left-hand side attains its minimum at $t = 0$ and is equal to $2^{1-k}|\beta|e^{-1}/(1 + e^{-1})^{2-k}$. Thus, $\Phi(z) \prec h(z)$, whenever $|\beta| \geq 2^{k-1}(\sqrt{2} + 1)e(1 + e^{-1})^{2-k}$.

□

Corollary 6.10 *Let* $f \in \mathcal{A}$ *and*

$$\Phi_\beta(z) = 1 + \beta \frac{zf'(z)}{f(z)} \left(1 + \frac{zf''(z)}{f'(z)} - \frac{zf'(z)}{f(z)} \right).$$

Then, $f \in \mathcal{S}_{SG}^*$, *if any of the following conditions hold:*

(i) $\Phi_\beta(z) \prec (1 + Az)/(1 + Bz)$, *where* $|\beta| \geq (A - B)(1 + e)^2/2e(1 - |B|)$ *and* $-1 < B < A \leq 1$.

(ii) $\Phi_\beta(z) \prec \sqrt{1 + z}$, *where* $|\beta| \geq (\sqrt{2} + 1)(1 + e)^2/2e$.

Corollary 6.11 *Let* $f \in \mathcal{A}$ *and*

$$\Phi_\beta(z) = 1 + \beta \left(1 + \frac{zf''(z)}{f'(z)} - \frac{zf'(z)}{f(z)} \right).$$

Then, $f \in \mathcal{S}_{SG}^*$, *if any of the following conditions hold:*

(i) $\Phi_\beta(z) \prec (1 + Az)/(1 + Bz)$, *where* $|\beta| \geq (A - B)(1 + e)/(1 - |B|)$ *and* $-1 < B < A \leq 1$.

(ii) $\Phi_\beta(z) \prec \sqrt{1 + z}$, *where* $|\beta| \geq (\sqrt{2} + 1)(1 + e)$.

Corollary 6.12 *Let* $f \in \mathcal{A}$ *and*

$$\Phi_\beta(z) = 1 + \beta \left(\frac{zf'(z)}{f(z)} \right)^{-1} \left(1 + \frac{zf''(z)}{f'(z)} - \frac{zf'(z)}{f(z)} \right).$$

Then, $f \in \mathcal{S}_{SG}^*$, *if any of the following conditions hold:*

(i) $\Phi_\beta(z) \prec (1 + Az)/(1 + Bz)$, *where* $|\beta| \geq 2(A - B)e/(1 - |B|)$ *and* $-1 < B < A \leq 1$.

(ii) $\Phi_\beta(z) \prec \sqrt{1 + z}$, *where* $|\beta| \geq 2(\sqrt{2} + 1)e$.

Now using Lemma 6.3, we obtain the following subordination results pertaining to the class $\mathcal{S}_{SG}^*$. In particular, when $h(z) = 2/(1 + e^{-z})$ and $P(z) = \beta$, we have:

Theorem 6.9 *Let* p *be a function analytic on* $\mathbb{D}$ *with* $p(0) = 1$ *such that it satisfies*

$$p(z) + \beta z p'(z) \prec \frac{2}{1 + e^{-z}}, \qquad \text{Re } \beta > 0.$$

Then $p(z) \prec \dfrac{2}{1 + e^{-z}}$.

By taking $p(z) = zf'(z)/f(z)$ in Theorem 6.9, we obtain the following result.

Corollary 6.13 *If a function* $f \in \mathcal{A}$ *satisfies the subordination*

$$\frac{zf'(z)}{f(z)} \left[1 + \beta \left(1 + \frac{zf''(z)}{f'(z)} - \frac{zf'(z)}{f(z)} \right) \right] \prec \frac{2}{1 + e^{-z}},$$

then $f \in \mathcal{S}_{SG}^*$, *whenever* Re $\beta > 0$.

By taking $h(z) = 2/(1 + e^{-z})$ and $P(z) = \beta/p(z)$ in Lemma 6.3, we obtain the following result:

Theorem 6.10 *Let p be a function analytic in $\mathbb{D}$ with $p(0) = 1$ satisfying*

$$p(z) + \beta \frac{zp'(z)}{p(z)} \prec \frac{2}{1 + e^{-z}}$$

and $g(t)$ be defined as

$$g(t) = \frac{-\sin(\sin t)}{e^{\cos t} + \cos(\sin t)}.$$

Then, $p(z) \prec \dfrac{2}{1 + e^{-z}}$ whenever $\operatorname{Re} \beta > g(-s_0)|\operatorname{Im} \beta|$, where s_0 is given in Theorem 3.1.

Proof Let $h(z) = 2/(1 + e^{-z})$. Then, $h(0) = 1$ and $h(\mathbb{D}) = \{w \in \mathbb{C} : |\log(w/(2 - w))| < 1\}$ is a convex set. Therefore, h is a convex function. By taking $\phi(w) = \beta/w$ in Lemma 6.2, the function $H(z)$ becomes

$$H(z) = zh'(z)\phi(h(z)) = \frac{\beta z}{(1 + e^z)}.$$

A calculation show that, for $z \in \mathbb{D}$,

$$\operatorname{Re} \frac{zH'(z)}{H(z)} = 1 - \operatorname{Re}\left(\frac{ze^z}{1 + e^z}\right) > 0$$

and hence H is starlike in $\mathbb{D}$. Also,

$$\operatorname{Re} \phi[h(z)] = \frac{1}{2} \operatorname{Re} \beta(1 + e^{-z}) > 0,$$

whenever

$$\operatorname{Re} \beta . \operatorname{Re}(1 + e^{-z}) - \operatorname{Im} \beta . \operatorname{Im}(1 + e^{-z}) > 0. \tag{19}$$

The above inequality holds, for $z = e^{it}$ $(0 \leq t \leq 2\pi)$, whenever

$$\frac{\operatorname{Re} \beta}{\operatorname{Im} \beta} > \frac{-\sin(\sin t)}{e^{\cos t} + \cos(\sin t)} = g(t) \quad \text{for the case when} \quad \operatorname{Im} \beta > 0$$

and

$$\frac{\operatorname{Re} \beta}{\operatorname{Im} \beta} < \frac{-\sin(\sin t)}{e^{\cos t} + \cos(\sin t)} = g(t) \quad \text{for the case when} \quad \operatorname{Im} \beta < 0.$$

The function $g(t)$ attains its maximum at $t = -s_0 \approx -1.94549$, where $g(-s_0) \approx 0.621289$ and minimum at $t = s_0 \approx 1.94549$, where $g(s_0) \approx -0.621289$. So it is sufficient to take $\operatorname{Re} \beta > g(-s_0)|\operatorname{Im} \beta|$. Thus, the result follows, by applying Lemma 6.2. $\qquad \square$

Taking $p(z) = zf'(z)/f(z)$ in Theorem 6.10, we obtain the following result.

Corollary 6.14 *If a function $f \in \mathcal{A}$ satisfies the subordination*

$$\frac{zf'(z)}{f(z)} + \beta \left(1 + \frac{zf''(z)}{f'(z)} - \frac{zf'(z)}{f(z)} \right) \prec \frac{2}{1 + e^{-z}},$$

then $f \in S_{SG}^*$, whenever $\operatorname{Re} \beta > g(-s_0)|\operatorname{Im} \beta|$, where $g(-s_0)$ is as defined in Theorem 6.10.

By taking $h(z) = 2/(1 + e^{-z})$ and $P(z) = \beta/(p(z))^2$ in Lemma 6.3, we obtain the following result:

Theorem 6.11 *Let p be a function analytic on $\mathbb{D}$ with $p(0) = 1$ satisfying*

$$p(z) + \beta \frac{zp'(z)}{p^2(z)} \prec \frac{2}{1 + e^{-z}}$$

and $g(t)$ be defined as

$$g(t) = \frac{-\left(e^{-2\cos t} \sin(2\sin t) + 2e^{-\cos t} \sin(\sin t) \right)}{1 + e^{-2\cos t} \cos(2\sin t) + 2e^{-\cos t} \cos(\sin t)}.$$

Then, $p(z) \prec \dfrac{2}{1 + e^{-z}}$ whenever $\operatorname{Re} \beta > g(-s_0)|\operatorname{Im} \beta|$, where s_0 is given in Theorem 3.1.

Proof Let $h(z) = 2/(1 + e^{-z})$. Then, $h(0) = 1$ and $h(\mathbb{D}) = \{w \in \mathbb{C} : |\log(w/(2 - w))| < 1\}$ is a convex set. Therefore, h is a convex function. Taking $\phi(w) = \beta/w^2$ in Lemma 6.2, the function $H(z)$ becomes

$$H(z) = zh'(z)\phi(h(z)) = \frac{\beta z}{2e^z}.$$

A calculation show that, for $z \in \mathbb{D}$,

$$\operatorname{Re} \frac{zH'(z)}{H(z)} = 1 - \operatorname{Re} z > 0$$

and hence H is starlike in $\mathbb{D}$. Also,

$$\operatorname{Re} \phi[h(z)] = \frac{1}{4} \operatorname{Re}(\beta(1 + e^{-z})^2) > 0,$$

whenever

$$\operatorname{Re} \beta \operatorname{Re}(1 + e^{-z})^2 - \operatorname{Im} \beta \operatorname{Im}(1 + e^{-z})^2 > 0. \tag{20}$$

The above inequality holds, for $z = e^{it}$ ($0 \le t \le 2\pi$), whenever

$$\frac{\operatorname{Re} \beta}{\operatorname{Im} \beta} > \frac{-\left(e^{-2\cos t} \sin(2\sin t) + 2e^{-\cos t} \sin(\sin t) \right)}{1 + e^{-2\cos t} \cos(2\sin t) + 2e^{-\cos t} \cos(\sin t)} = g(t)$$

for the case when $\text{Im } \beta > 0$ and

$$\frac{\text{Re } \beta}{\text{Im } \beta} < \frac{-\left(e^{-2\cos t}\sin(2\sin t) + 2e^{-\cos t}\sin(\sin t)\right)}{1 + e^{-2\cos t}\cos(2\sin t) + 2e^{-\cos t}\cos(\sin t)} = g(t)$$

for the case when $\text{Im } \beta < 0$.

The function $g(t)$ attains its maximum at $t = -s_0$, where $g(-s_0) \approx 2.02374$ and minimum at $t = s_0$, where $g(s_0) \approx -2.02374$. So it is sufficient to take $\text{Re } \beta > g(-s_0)|\text{Im } \beta|$. Thus, the result follows, by applying Lemma 6.2. $\qquad \square$

Corollary 6.15 *If a function $f \in \mathcal{A}$ satisfies the subordination*

$$\frac{zf'(z)}{f(z)} + \beta \left(\frac{zf'(z)}{f(z)}\right)^{-1}\left(1 + \frac{zf''(z)}{f'(z)} - \frac{zf'(z)}{f(z)}\right) \prec \frac{2}{1 + e^{-z}},$$

then $f \in S^*_{SG}$, whenever $\text{Re } \beta > g(-s_0)|\text{Im } \beta|$, where $g(-s_0)$ is defined in Theorem 6.11.

References

1. Ali, R.M., Ravichandran, V., Seenivasagan, N.: Sufficient conditions for Janowski starlikeness. Int. J. Math. Math. Sci. **2007**, Art. ID 62925 (2007)
2. Cho, N.E., Kumar, S., Kumar, V., Ravichandran, V.: Differential subordination and radius estimates for starlike functions associated with the Booth lemniscate. Turk. J. Math. **42**(3), 1380–1399 (2018)
3. Goodman, A.W.: On uniformly convex functions. Ann. Polon. Math. **56**(1), 87–92 (1991)
4. Janowski, W.: Extremal problems for a family of functions with positive real part and for some related families. Ann. Polon. Math. **23**, 159–177 (1970/1971)
5. Kanas, S., Wiśniowska, A.: Conic regions and k-uniform convexity. J. Comput. Appl. Math. **105**(1–2), 327–336 (1999)
6. Kumar, S.S., Kumar, V., Ravichandran, V., Cho, N.E.: Sufficient conditions for starlike functions associated with the lemniscate of Bernoulli. J. Inequal. Appl. **2013**, 176 (2013). 13 pp
7. Kumar, S., Ravichandran, V.: Subordinations for functions with positive real part. Complex Anal. Oper. Theory **12**(5), 1179–1191 (2018)
8. Ma, W.C., Minda, D.: A unified treatment of some special classes of univalent functions. In: Proceedings of the Conference on Complex Analysis (Tianjin, 1992), pp. 157–169. Conf. Proc. Lecture Notes Anal., I, Int. Press, Cambridge, MA
9. Miller, S.S., Mocanu, P.T.: Differential Subordinations. Monographs and Textbooks in Pure and Applied Mathematics, vol. 225. Marcel Dekker, New York (2000)
10. Prokhorov, D.V., Szynal, J.: Inverse coefficients for (α, β)-convex functions. Ann. Univ. Mariae Curie-Skłodowska Sect. A **35**(1981), 125–143 (1984)
11. Ravichandran, V., Rønning, F., Shanmugam, T.N.: Radius of convexity and radius of starlikeness for some classes of analytic functions. Complex Var. Theory Appl. **33**(1–4), 265–280 (1997)
12. Ravichandran, V., Kumar, S.S.: Argument estimate for starlike functions of reciprocal order. Southeast Asian Bull. Math. **35**(5), 837–843 (2011)
13. Ravichandran, V., Verma, S.: Bound for the fifth coefficient of certain starlike functions. C. R. Math. Acad. Sci. Paris **353**(6), 505–510 (2015)
14. Rønning, F.: Uniformly convex functions and a corresponding class of starlike functions. Proc. Am. Math. Soc. **118**(1), 189–196 (1993)
15. Shanmugam, T.N.: Convolution and differential subordination. Int. J. Math. Math. Sci. **12**(2), 333–340 (1989)
16. Sokół, J.: Radius problems in the class $\mathscr{SL}^*$. Appl. Math. Comput. **214**(2), 569–573 (2009)

17. Sokół, J., Stankiewicz, J.: Radius of convexity of some subclasses of strongly starlike functions. Zesz. Nauk. Politech. Rzeszowskiej Mat. No. **19**, 101–105 (1996)
18. Tuneski, N., Bulboacă, T., Jolevska-Tuneska, B.: Sharp results on linear combination of simple expressions of analytic functions. Hacet. J. Math. Stat. **45**(1), 121–128 (2016)
19. Tuneski, N.: On the quotient of the representations of convexity and starlikeness. Math. Nachr. **248**(249), 200–203 (2003)
20. Uralegaddi, B.A., Ganigi, M.D., Sarangi, S.M.: Univalent functions with positive coefficients. Tamkang J. Math. **25**(3), 225–230 (1994)

EasyChair Preprint
№ 1172

Changing the state of literacy in the Digital Age in India

Aanandita Gahlot and Shubhankar Gahlot

June 12, 2019

Changing the state of literacy in the Digital Age in India

Aanandita Gahlot

Undergraduate Student
USME, Delhi Technological University, India
aananditagahlot@gmail.com

Shubhankar Gahlot

Graduate Student
Illinois Institute of Technology, Chicago
sgahlot@hawk.iit.edu

Abstract

India as an emerging economy deals with troubles in literacy due to factors like shortage of quality academic institutions and unsuitable curriculum. Digital Technology is accredited as something which can bridge the gap between quality institutions and individuals and make learning more engaging.

Indian Government has made use of technology in the best possible way and launched Pradhan Mantri Gramin Digital Saksharta Abhiyan (PMGDISHA)* under its Digital India initiative. It has been initiated to make at least one individual from each household digitally literate so that they develop the skills which will be needed to link with the rapidly growing digital world. This scheme aims to target the rural population including the disparaged sections of society like minorities, Below Poverty Line (BPL), women and differently-abled people.

The use of technology in education has transmuted the whole system of education. This paper is aimed at exploring the changing state of literacy in India after introducing PMGDISHA.

* Prime Minister Rural Digital Literacy Mission

1. Introduction

India being the second most populous country is also the youngest country in the world with 65% of the population below the age of 35 [1]. This means that there are more than 800 million people, getting ready as a workforce who will not only change the course of India but also the world. The major challenge which India faces is to provide a quality education to this emerging workforce. This can only be achieved by providing them a resourceful education that is not only enough to skill them but also enables them to contribute to the development of the society.

The pyramid of population density in Fig. 1 indicates the pattern of age distribution in India. The curve for India is highly voluminous till the age of 25 and then it tapers smoothly. United States has almost constant age distribution while China's Population curve is contorted due to its one child policy. [1]
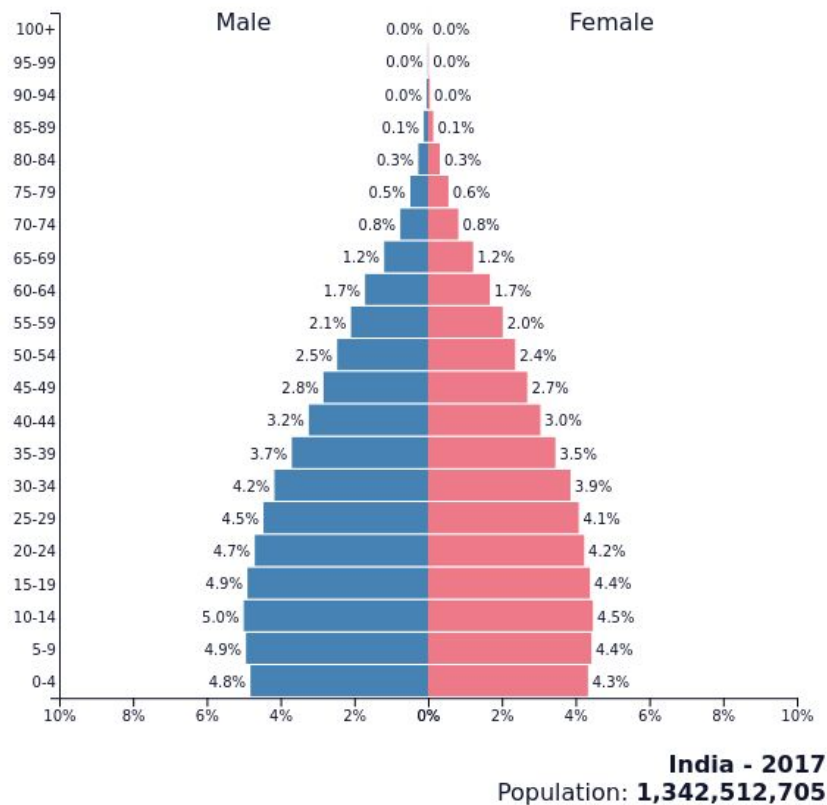
"Fig 1: Population density of India"

Fig. 1 evidently shows that India needs to strengthen its education system both at the policy as well as infrastructure level. The existing education infrastructure is insufficient for the growing demand of the emerging population and the only way to strengthen it is by leveraging digital technology and e-learning. According to 2015 world bank data, India has nearly 81% and 63% literate males and females respectively [4]. On one hand, the major drawback in the long-term education is the unsustainable economic condition of the family that keeps a child away from pursuing education while on the other it is the lack of proper education infrastructure in sub-urban and rural areas.

Furthermore, regions with restricted accessibility, for example north east India which are home to 39 million people have literacy level of 68.5%. The states of Assam and Arunachal Pradesh have literacy rate less than the national average. The land terrain, language barriers and other activities have prohibited easy access for people from these states into other states and vice-a-versa [3]. Other states also face the similar issues. But the advent of internet and other mobile technologies has opened new avenues for advancement. Mobile phone and internet penetration are rising rapidly with current mobile usage at 65-75% and internet usage at 40-50%. It is estimated that mobile phone penetration and internet penetration will reach 85-90% and 45-50% respectively by 2020 [2].
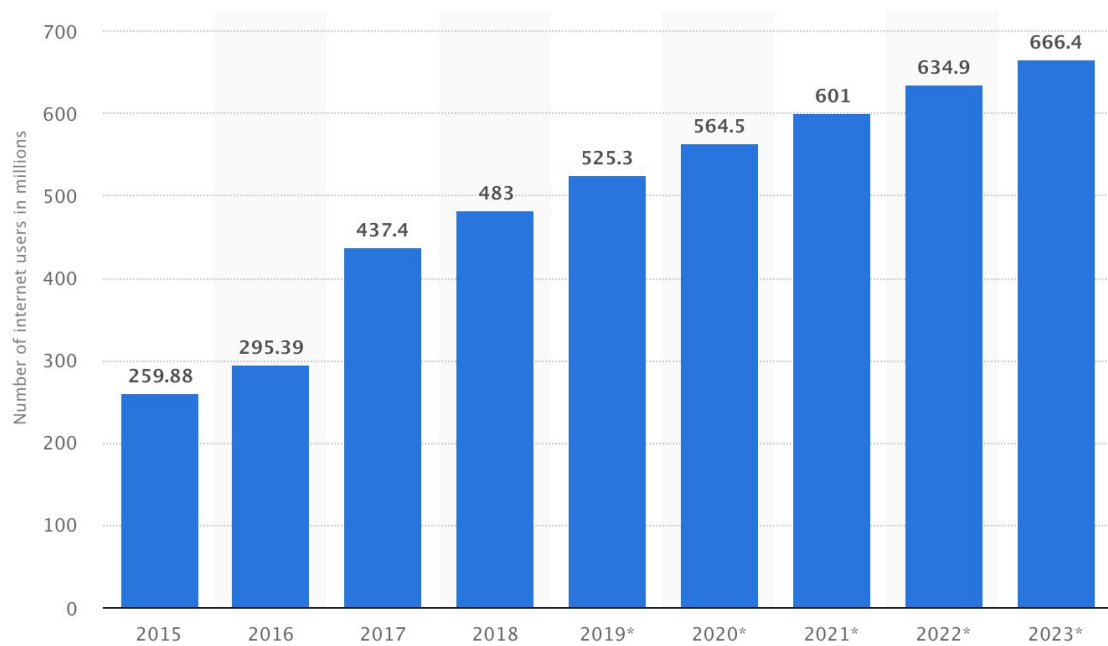
"Fig 2: Internet Users' growth in India [2]"

Fig. 3 clearly depicts that one out of every five people in India is illiterate. As more than 70% of the total population of India lives in rural areas, the status of literacy cannot improve without targeting them [4].
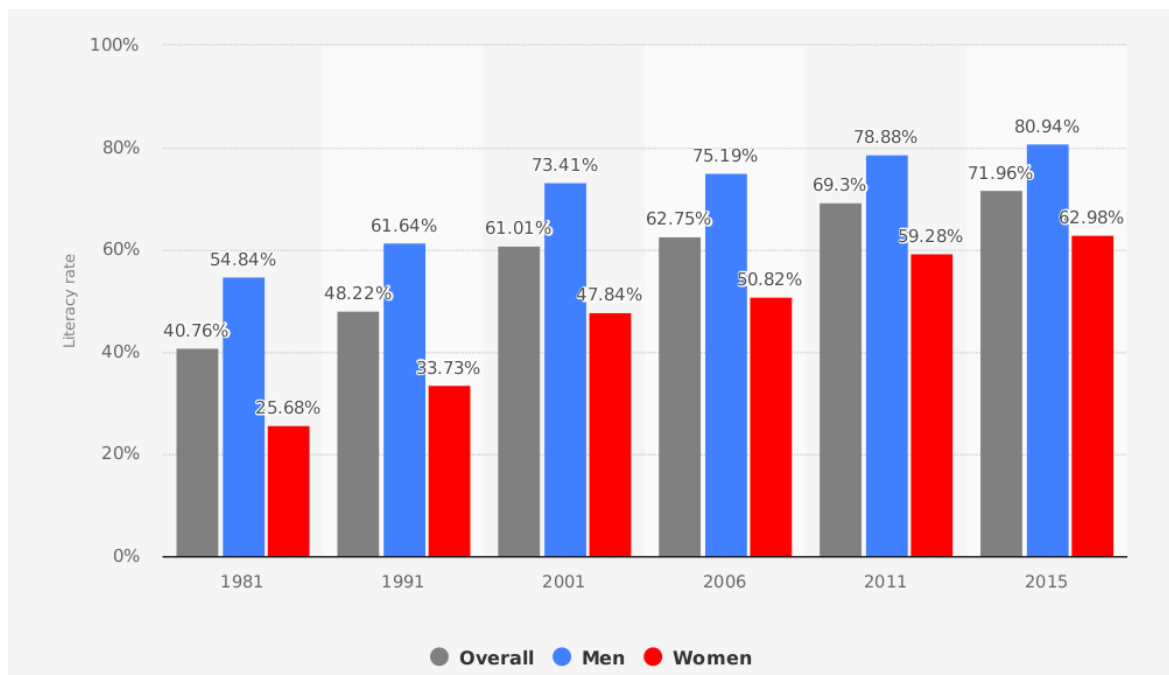
"Fig 3: Literacy in India from 1981-2015 [4]"

It is estimated that by 2020 more than 50% of the world's illiterate will reside in India. This made the government to take an initiative to introduce a digital literacy program to help people leverage the ever-growing mobile and internet penetration. It is a mechanism through which education in the rural India can be influenced the most. This paved the way for launching *Pradhan Mantri Gramin Digital Saksharta Abhiyan* (PMGDISHA) program under its Digital India initiative for spreading digital literacy to the remote areas and underprivileged people.

The implications of the scheme have been phenomenal. Digital literacy mission has accelerated the literacy growth in India especially in the rural parts of the country, which is very evident from the correlation between growth in digital literacy and number of private as well as public MOOCs (Massive Open Online Courses) registrations.

2. Education in Rural India

According to census 2011, India has a highly varied literacy rate. Kerala tops the list with 93.9% literacy rate and while Bihar has least literacy rate of 63.8%. Rural areas report a literacy rate of 68.9% and the urban areas register 85.0% literacy, resulting in an absolute difference of nearly 16 percentage points [5]. One of the main factors contributing to this relatively low literacy rate is shortage of school infrastructure to accommodate all the students. Also, the average pupil teacher ratio for all India is 42:1, implying a teacher shortage [13].

The condition becomes even worse if we take literacy in rural India into account as seen from the table below.

"Table 1: States with the Lowest Rural Literacy Rate [5]"

States	Literacy Rate in Rural (%)	Literacy rate in Urban (%)	Total Literacy (%)
Rajasthan	62.3	80.7	67.1
Jharkhand	62.4	83.3	67.6
Bihar	61.8	71.8	63.8
Andhra Pradesh	61.1	80.5	67.7
Arunachal Pradesh	61.6	82.9	67.0

The problems that India faces can be summarized as follows:
1. Large emerging youth population. [Ref Fig: 1]
2. Low literacy rate [Ref Fig: 3]
3. Huge rural population
4. Inadequate public infrastructure in rural areas.
5. Low literacy rate among women specifically, in rural areas. [Ref Table: 1]
6. Lack of proper educational infrastructure.

7. Lack of adequate number of qualified instructors. [7]

Policy intervention is needed in order to solve these problems so that it could impact a large number of people in a very small time span. This is where government launched the PMGDISHA program under Digital India initiative.

3. PMGDISHA (Pradhan Mantri Gramin Digital Saksharta Abhiyan/ Prime Minister Rural Digital Literacy Mission)

PMGDISHA is a scheme under NDLM (National Digital Literacy Mission) initiative of Digital India campaign which was launched in August 2014 by the government of India. Following the successful implementation of NDLM schemes, PMGDISHA was approved by the government in February 2017. The curriculum for the program was developed in 2014 in consultation with various agencies like UNESCO, National Association of Software and Services Companies (NASSCOM), Intel, Indira Gandhi National Open University (IGNOU), National Institute of Electronics & Information Technology (NIELIT), National Institute of Open Schooling (NIOS), Indian Institute of Mass Communication (IIMC), IT for Change, Open Knowledge Network India, and Digital Empowerment Foundation.

3.1 Objectives: The main objective of the program is to make six million people in rural areas, across States/UTs, by March 2019 digitally literate, reaching to around 40% of rural households by covering one member from every eligible household. The Scheme is aimed at empowering the citizens in rural areas by training them to operate computer or digital access devices (like tablets, smart phones etc.), send and receive emails, browse the Internet, access Government services, search for information, undertake digital payment, etc. and hence enable them to use the Information Technology and related applications especially Digital Payments to actively participate in the process of nation building. Thus, the Scheme aims to bridge the digital divide, specifically targeting the rural population including the marginalized sections of society like Scheduled Castes (SC) / Scheduled Tribes (ST), Below Poverty Line (BPL), women, differently-abled persons and minorities. The ultimate aim is to cover the gap between the rural and urban youth.

3.2 Implementation: The Scheme is implemented by using the affiliated Training Partners/Training Centers. Training Partners/Training Centers are assigned with a specified area of operation and target preferably within the same state. The Training Partners/Training Centers need to have basic facilities to conduct the training as per the accreditation norms prescribed by CSC-SPV (CSC e-Governance Services India Limited, a Special Purpose Vehicle incorporated under the Companies Act 1956).

These would include Common Service Centers (CSC), National Institute of Electronics & Information Technology (NIELIT) Centers or its accredited Centers, Adult Literacy Centers or schools implementing Information and Communication Technology (ICT@schools) scheme under the Ministry of Human Resources and Development (MHRD), Indira Gandhi National Open University (IGNOU) centers, NGOs involved in IT literacy, Rural Self-Employment Training Institutes, Industry partners, companies with CSR provisions, etc.

The eligible age of enrollment is 14-60 years. The duration of the course is 20 hours and it is delivered in all official languages of India. Candidates are evaluated by a national level certifying agency [14].

3.3 Training Fee: The candidate pays no training fee.

3.4 Registration Status: By the end of August 2018, 12,343,083 beneficiaries have been registered under the project and out of which 12,321,098 beneficiaries have completed training from all the States/UTs. [8]

"Table 2: Status of top 5 states as of Jan'18 [9]"

S.No.	State	Targets	Candidates Registered	Training Completed	Certified Candidates
1.	UTTAR PRADESH	11171000	2432262	2390272	1131112
2.	BIHAR	6630000	747778	736956	373082
3.	WEST BENGAL	4481000	280368	272757	124586
4.	MAHARASHTRA AND GOA	4433000	493103	482997	248473
5.	MADHYA PRADESH	3784000	704085	686995	332535

3.5 Examination Status: PMGDISHA examination is conducted across the country and stringent with biometric authentication of candidates by an Invigilator/Exam Superintendent. As of January 2018, a total of 5,329,989 candidates have been certified under the scheme [9]. The gender wise distribution among the certified candidates under PMGDISHA is almost equal, with 53% males and 47% females [8].
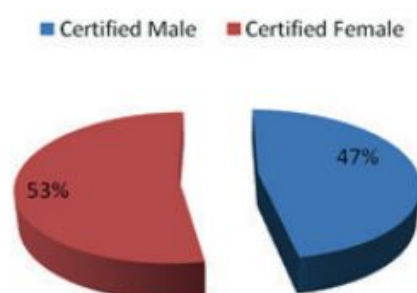

"Fig 4: Gender wise distribution of certified candidates [8]"

4. Impact on Massive Open Online Courses (MOOCs): Internet has disrupted all industries including the education industry by exponentially reducing infrastructure and operational costs. Therefore, online education has become a lucrative business and Massive Open Online Courses (MOOC) like Coursera, Udacity, Udemy, Edx, etc. are an outcome of this disruption. But in order to be part of this disruption one has to be digitally literate. That is where initiatives like PMGDISHA help make people digital ready.

As per 2016 statistics shared by Coursera there were 13 lakh online learners from India as compared to the total 180 lakh online learners on Coursera. There had been a 70% jump in the enrolment of courses by Indians. Edx, which is another MOOC platform, in 2017 has also announced 73% growth in the Indian market over the past year. In India Coursera is growing faster than the global average, with about 2 million Indian learners enrolled in various courses, ranging from a few weeks to two years. Even Indian government has built its own MOOC platform known as SWAYAM to leverage this digital wave [10][11][12].

By year 2030, the Indian government aims to increase the Gross Enrolment Ratio (GER) in universities to 30% from 23% in 2014-15. And this will practically not be possible by just setting up more traditional classrooms & universities.

Therefore, it's very well evident from the data that this digital literacy initiative is driving the MOOC industry in India and will keep doing so in the coming future. We will also see a greater number of people learning from these non-traditional sources as well.
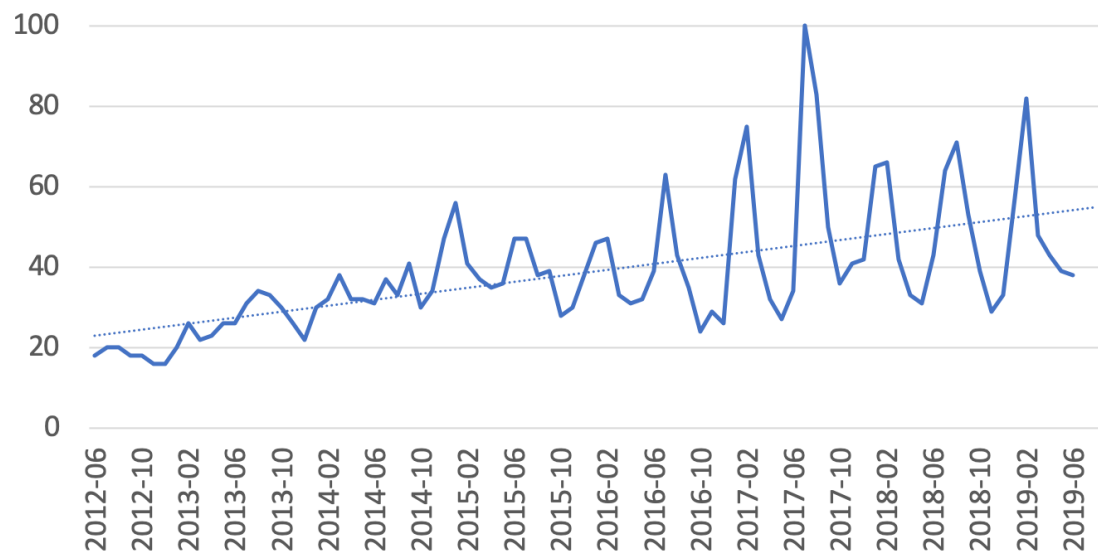
" Fig 5: Google Trends' results for Massive Open Online Course (topic) [15]"

In fig. 5, the numbers on the vertical axis represents the search interest relative to the highest point on the chart and horizontal axis represents the time period. A value of 100 is the peak popularity for the term which is attained in the second half of the year 2017.

Trend line shows a rapid increase in the number of google searches for the topic MOOC which can be attributed to increase in the internet penetration and growing digital literacy.

5. Conclusion

The best way to raise the standard of education and improve literacy in a country is to make its citizens digitally literate as early as possible so that they can utilise the available digital tools and technologies. This policy-based solution by government of India can become an inspiration for other countries to learn from and help them to raise their education standards. A small investment by the government of India in digital education of its citizens has proved to be a huge stepping stone in making its people self-reliant in educating themselves. Through this paper we have tried to explain how digital literacy can change the whole education scenario. The initiative has proved to be beneficial for all sections of the society. Due to its overwhelming success we expect other countries to follow suit and launch such initiatives to educate their citizens.

References:

[1] https://www.populationpyramid.net

[2] https://www.statista.com/statistics/255146/number-of-internet-users-in-india/

[3] http://ijmra.us/project%20doc/2018/IJRSS_NOVEMBER2018/IJMRA-14646.pdf

[4] https://www.moneycontrol.com/news/business/economy/data-story-this-international-literacy-day-lets-recap-indias-literacy-growth-2382359.html

[5] http://censusmp.nic.in/censusmp/All-PDF/6Literacy21.12.pdf

[6] https://www.mapsofindia.com/my-india/society/low-female-literacy-rate-and-its-impact-on-our-society

[7] Vikram Desai, Jagdish Murthy, Ravi Saksena, Ajay Gupta, Enhancement of primary education using EDUSAT: Rajiv Gandhi project for EDUSAT supported elementary education network (RGPEEE) overview, Acta Astronautica, Volume 65, Issues 9–10, November–December 2009, Pages 14401445, ISSN 00945765, 10.1016/j.actaastro.2009.03.086. (http://www.sciencedirect.com/science/article/pii/S0094576509002227)

[8] https://www.pmgdisha.in/wp-content/uploads/2018/10/PMGDISHA-booklet-August.pdf

[9] https://digitalindia.gov.in/writereaddata/files/PMGDISHA_Ministrial%20Conclave%20Revised.pdf

[10] "Coursera's second largest market–India", https://yourstory.com/2017/04/coursera-nikhil-sinha/

[11] "Online learners in India will grow by leaps & bounds", http://www.indiaeducation.net/online-education/articles/5-online-education-trends-to-watch-in-india.html

[12] https://www.indiainfoline.com/article/b-school-news/edx-marks-a-73-growth-in-india-in-one-year-117020100304_1.html

[13] https://data.gov.in/catalog/pupil-teacher-ratio-ptr

[14] https://graminshiksha.com/Projects/Pradhan-Mantri-Gramin-Digital-Shaksharta-Mission-Franchise-10-44

[15] https://trends.google.com/trends/explore?date=today%205-y&geo=IN&q=%2Fm%2F0gyvy46

Research Article

Open Access

Anuja Agrawal*, Raminder Kaur* and R.S. Walia

Development of vegetable oil-based conducting rigid PU foam

Abstract: In this study, carbon fibre powder has been used as reinforcement to enhance the electrical conductivity of bio-based rigid polyurethane foam. Effect of carbon fibre incorporation on the mechanical, thermal and flame retardant properties has also been investigated. Results concluded that the foams with 8% carbon fibre concentration showed up to 288% increase in compressive strength. Furthermore, up to 28% decrease in the peak of heat release rate (PHRR) was observed on the incorporation of carbon fibre powder. Additionally, the rate of smoke production was also found decreased for carbon fibre reinforced foams. Foams with 8% and 10% carbon fibre concentration show conductivity of 1.9×10^{-4} and 7.1×10^{-4} S/m, respectively. So, carbon fibre powder may be used as a potential filler to enhance the electrical conductivity of rigid foams without compromising the other properties.

Keywords: four probe measurement; heat release rate; mechanical strength; thermal conductivity; weight loss

1 Introduction

Electromagnetic interference (EMI) is the disturbance generated by some undesirable radiated signals emitted by electronic instruments which may affect the performance of other electronic devices. Nowadays, an expeditious rise in the use of wireless devices for communication, such as laptops, smartphones, routers, and others are polluting their surroundings in terms of electromagnetic pollution, which may be dangerous for the health of human beings as well as for information security. Therefore, an appropriate

EMI shield is required to protect the environment from electromagnetic waves used by many vital applications such as air traffic control, weather radar, satellite communications and others (1,2). These materials may also be used for evading radar detection by absorbing electromagnetic radiations. Metallic coating has been extensively used as EMI shielding materials, but they always suffer from some shortcomings of high density, poor resistance to corrosion and high cost of processing. As alternatives, polymeric foams incorporated with conductive fillers are explored to fabricate lightweight and tough shielding materials. These polymeric foams are a suitable material for such applications due to their various attractive properties such as better mechanical and electrical properties with lower density. A wide range of polymers, such as epoxies (3), poly (methyl methacrylate) (PMMA) (4,5), polyurethane (PU) (6), polystyrene (PS) (7) and polypropylene (PP) (8) have been utilized to develop EMI shielding foams. Kuang et al. (9) prepared poly lactic acid – MWCNT nanocomposite foam for EMI shielding applications and observed that conductivity of 3.4 S/m was obtained using the foam with 10 wt% of MWCNT and density 0.3 g/cm. Li et al. (10) fabricated epoxy-MWCNT nanocomposite foam and obtained a conductivity of 3.04×10^{-2} S/m by the addition of 5 wt% of MWCNT. Yan et al. (2) prepared polystyrene nanocomposite using reduced graphene oxide(rGO) and achieved electrical conductivity up to 43.5 S/m with 3.47 vol% loading of rGO. Hwang et al. (11) prepared polybutylene terephthalate (PBT)/carbon fibre composite and investigated the effect of carbon fibre on the EMI shielding performance. It was concluded that carbon fibre loading should be greater than 30 wt% to get better EMI shielding effectiveness. Zhang et al. (12) fabricated PMMA based foam with density 0.22-0.38 g/cm³ incorporated with Fe_3O_4 and MWCNT. It was observed that foams with 1.63% hybrid filler loading showed an electrical conductivity of 2×10^{-4} S/m. Li et al. (13) fabricated ultrathin carbon foams by the pyrolysis of polyimide/graphene composite foams. It was observed that up to 24 dB electromagnetic interference (EMI) shielding effectiveness exhibited by these graphene based foams with conductivity up to 2300 S/cm.

* Corresponding authors: Anuja Agrawal and Raminder Kaur,
Department of Applied Chemistry and Polymer Technology, Delhi Technological University, Delhi – 110042, India,
e-mail: agrawala918@gmail.com, rkaurdtu@gmail.com.
R.S. Walia, Department of Mechanical Engineering, Delhi Technological University, Delhi – 110042, India

Besides these materials, PU foam may be used as a promising material due to its low density and good mechanical properties. Commercially, PU foams are available in different forms such as flexible, rigid or elastomeric depending upon their structure. Rigid polyurethane foams (RPUFs) have been used in a wide variety of applications such as building and construction industry, transportation and others, for the insulation purpose. RPUF has also been used in radomes and high-speed aircrafts due to its ability to allow electric and magnetic waves to pass through it. Owing to its high dielectric constant and low weight it is being used in different fields of electronic industry such as potting and encapsulation of electronic components, microwave absorbers, and others. RPUF may also be used for electromagnetic wave absorption by incorporating some functional filler. Functional fillers contribute the plastic materials with a much wider range of properties including some unique properties not normally associated with plastics, such as high electrical conductivity or low flame retardancy. Li et al. (14) studied the effect of sandwich and gradient configuration on the EMI shielding performance and concluded that multilayered polyurethane grapheme composite may be used as a high-performance composite for microwave absorption and EMI shielding. Farhan et al. (15) prepared a different type of carbon foams using powdered PU and carbon precursors novolac and pitch. Silicon carbide (SiC) nano-wires were grown to enhance the absorption properties of this carbon foam. A maximum EMI shielding of 79.50 dB cm^3/g was achieved in the carbon foam containing 20% Si content with very low conductivity. Esfahani et al. (16) incorporated surface functionalized graphene sheets in thermoplastic PU and their EMI shielding effect has been investigated. Results showed that higher electrical conductivity and improved dielectric properties were achieved due to the stronger interfacial interaction between the filler and the TPU matrix. The TPU film with 5 vol% graphene and thickness of 1 mm exhibited commercially relevant EMI shielding effectiveness of 25 dB in the X-band frequency range. Commercially, PU has been prepared by the reaction of polyols with the polyisocyanate, both of them are petroleum-based raw materials. But, due to the depletion in petroleum resources and rising concern about the environment, bio-based raw materials are the requirement of the modern world (17-20). Ibrahim et al. (21) fabricated castor oil based PU films to be employed as a base material for electrolytes. It was observed that the conductivity of PU films increased from 1.18×10^{-9} S/m to 1.42×10^{-4} S/m on the incorporation of 30 wt% of LiI salt. Nevertheless, the

application of bio-based conductive RPUF has not been explored so far. So, in this study, we are exploring the electrical conductivity of bio-based RPUF incorporated with carbon fibre in varied proportion. The mechanical, thermal and flame retardant properties of these foams have also been investigated.

2 Materials and methods

2.1 Materials

Castor oil (99.9%, Hydroxyl value = 160 mg equivalent KOH/g) is purchased from Thomas Baker Chemicals (Pvt) Ltd and diphenylmethane diisocyanate (PMDI, 30-32 NCO %) is obtained from Krishna Enterprises. n-Pentane (99.5%) and Silicon oil, are purchased from CDH. Catalyst DABCO 33 LV is purchased from Sigma-Aldrich. Glycerol (99%) is supplied by Sisco Industries Pvt. Ltd. Carbon fibre is purchased from CFW Enterprises with tensile strength ≥3500 GPa, density 1.65-1.75 g/cm³. Carbon content ≥ 98%, electrical resistivity 1.5×10^{-33} Ω/cm and mesh size 50-1000. All the reagents were of analytical grade and used as supplied.

2.2 Methods

The RPUFs are obtained by the same method as reported in the literature (22-24), In brief, the procedure is as follows:

The modification of castor oil is carried out under the inert atmosphere of nitrogen using 2:1 ratio of castor oil to glycerol at the temperature 180-200°C for 4 h. The predetermined quantity of the carbon fibre powder is added to the modified polyol (Hydroxyl value = 350-450 mg equivalent KOH/g) taken in a beaker. Prior to addition, the fillers have been dehydrated in a vacuum oven at 60°C for 4 h. Then calculated amount of other ingredients such as catalyst, surfactant and blowing agent is added to the contents of the beaker and thoroughly mixed to form polyol-premix. A calculated amount of MDI is then added to the beaker. The resulted reaction mixture is poured into a metal mould (100 mm × 100 mm × 10 mm) coated with releasing agent i.e. silicone oil and a free rise foam is prepared.

To ensure complete curing, the moulds are left to stand for 72 h. After demoulding, the resulted RPUF is cut into desired dimensions and tested for its mechanical, thermal and anti-flammable properties. Figure 1 shows the reaction scheme for polyurethane foam synthesis and modification of castor oil. Table 1 presents the foaming

formulation of castor oil based RPUFs modified with different concentration of carbon fibre powder.

3 Characterization

Mechanical, thermal and morphological analysis of castor oil based RPUFs incorporated with different concentration of carbon fibre is performed to find out the performance

Table 1: Foaming formulation of castor oil-based RPUF.

Material	Amount (pbw)
Modified Polyol	100
DABCO 33 LV	3
n-Pentane (blowing agent)	10-15
Silicone oil (surfactant)	3
Carbon fibre	2-10
MDI	110

Pbw = parts by weight of Polyol

shown by these foams. Various characterization techniques used are described below.

3.1 FTIR and 1H NMR analysis

The chemical structure of transesterified castor oil was determined using FTIR spectroscopy on Nicolet 380 by preparing KBr pallets. The spectra were observed in the 450-4000 cm^{-1} range. 1H NMR of modified and virgin castor oil was also conducted (Bruker Avance II-400) at SAIF, Punjab University, Chandigarh, using dimethyl sulphoxide (DMSO) as a solvent. Characterization of prepared RPUFs was conducted using perkinElmer spectrophotometer version 10.5.3.

3.2 Mechanical testing

The mechanical properties of the castor oil based RPUF samples have been determined according to the standard procedures. Testing is conducted on three specimens

Reaction scheme of transesterification reaction
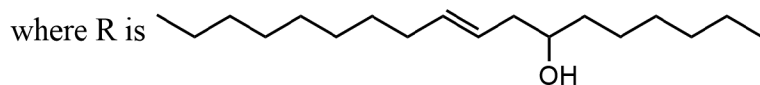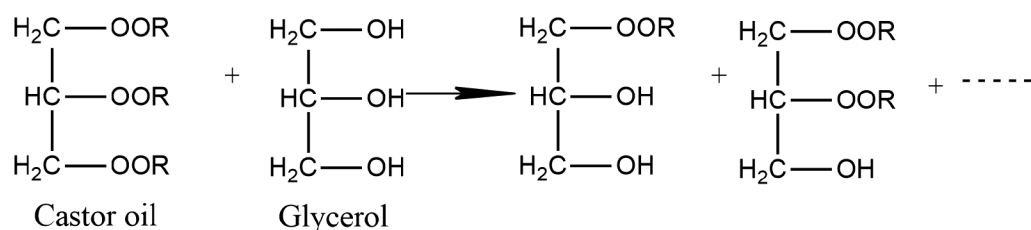
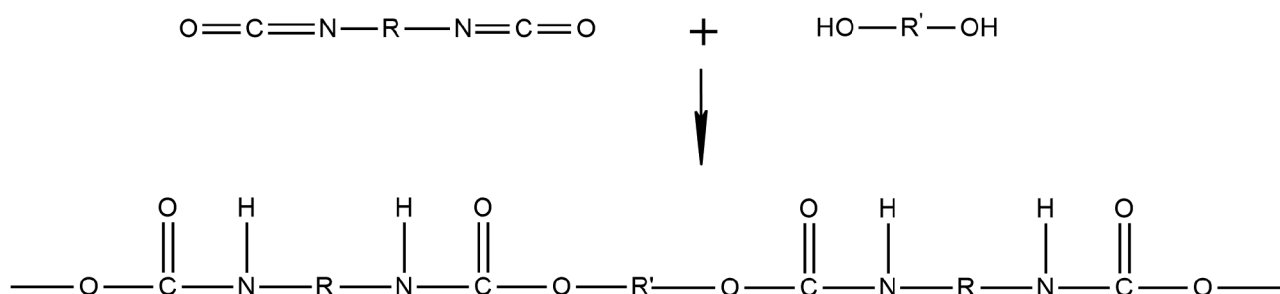**Reaction scheme of Polyurethane formation**

Figure 1: Reaction scheme of transesterification and polyurethane formation.

of each concentration and the average value has been reported. Compressive and flexural properties of the resulted foams are measured at room temperature using Instron (model No. 3369) universal testing machine (UTM). The compression tests are performed according to the ASTM D-695. Specimens of dimensions 25 mm × 25 mm × 25 mm are cut from the foam in the in-plain direction and tested for 10% compression. The compression strength has been measured along parallel foam rise direction. The flexural tests are performed according to the ASTM D-790. Specimens of dimensions 80 mm × 10 mm × 4 mm are cut from foam perpendicular to foam rise direction and loaded under three-point bending. The rate of crosshead movement is fixed at 2 mm/min for each sample.

3.3 Thermogravimetric analysis (TGA)

Thermogravimetric analysis (TGA) was performed utilizing a thermogravimetric analyzer (Perkin Elmer 4000) in a nitrogen atmosphere with a heating rate of 10°C/min. and the temperature ranging from 50 to 700°C.

3.4 Cone calorimeter testing

The fire performance of RPUF samples was analyzed with a Cone Calorimeter (Jupiter Electronics, Mumbai) according to ISO 5660-1 standard at an incident heat flux of 35 kW/m². The size of the samples was kept 100 mm × 100 mm × 20 mm. This instrument is capable of recording the time to ignition (TTI), total heat release (THR), heat release rate (HRR), smoke production rate (SPR) and total smoke production (TSP) etc.

3.5 Conductivity measurement

The conductivity of prepared rigid foam samples was measured by using four probe set-up (SES Instruments Pvt. Ltd., Roorkee).

4 Results and discussion

Carbon fibre in different proportion is added to PU foam to provide some desired functional properties. The foam architecture depends on the particle size and the dispersion of the filler in the reacting mixture. Moreover, an interaction between the filler and polymer matrix is the important parameter governing the mechanical properties of reinforced PU foam (25).

4.1 FTIR and 1H NMR analysis

Figure 2 shows the 1H NMR spectrum of modified and virgin castor oil. The sharp singlet at 1.23 ppm is attributed to the proton associated with hydroxyl group. The signal obtained as a multiplet at 1.50 ppm is attributed to the methylene protons of aliphatic chain. NMR spectrum of modified castor oil shows signals at 2.26 ppm and 3.29 ppm, which is assigned to the presence of proton α to carbonyl carbon of the ester bond. The multiplet signal at 4.25 ppm corresponds to the proton α to oxygen atom. The signal obtained at 5.20 ppm is associated with proton attached to alkene carbon. A signal at 0.87 ppm is assigned to terminal methyl proton. Similar results were obtained by Narwal et al. (26) Modified castor oil shows similar peaks except increase in intensity of peak at 1.23 ppm due to hydroxyl proton, which confirms the increase in hydroxyl value of castor oil by transesterification reaction. In addition, peaks get broadened in the NMR spectrum of modified castor oil, which is attributed to the broad range of different molecular weight compounds in modified polyol.

The FTIR spectra of polyol samples confirmed the presence of the C−H symmetric and asymmetric stretching vibrations of CH_2 groups at 2925.3 cm^{-1} and 2854.2 cm^{-1} respectively. The intense band at 1742.9 cm^{-1} was due to C=O stretching of ester groups and the absorption bands at 1480.3 and 1373.8 cm^{-1} were attributed to CH_2 bending and C−H bending vibration, respectively. As illustrated in Figure 3a, the broad and strong band corresponding to the OH group (3357.3 cm^{-1}) in the castor oil was also noted and intensity of this peak increases in the spectra of polyol, which confirms the increase in hydroxyl number by the transesterification reaction (26).

The FTIR spectrum of RPUFs shows all the characteristic peaks of urethane linkage, as seen in Figure 3b. Absorption maxima at 3331-3411 cm^{-1} is attributed to stretching vibrations of N−H groups present in urethane linkages, while peaks at 1510-1523 cm^{-1} attributed to the bending vibrations of these groups. Incorporation of carbon fibre shifted the band towards the lower wavenumber. Signals associated with the stretching vibrations of C=O bonds were shown at 1705-1738 cm^{-1}. Absorption bands characteristic to stretching vibrations of C−N bonds present in urethane linkages were also observed at 1206-1261 cm^{-1}.

The absorption maxima at 2854-2870 and 2925-2963 cm^{-1} are attributed to the symmetric and asymmetric stretching vibrations of C−H bonds present in aliphatic chains (21,27). Intensity of bands associated with stretching vibration of C=O groups and C−H bonds at 1705-1738 cm^{-1} and 2854-2963 cm^{-1}, respectively
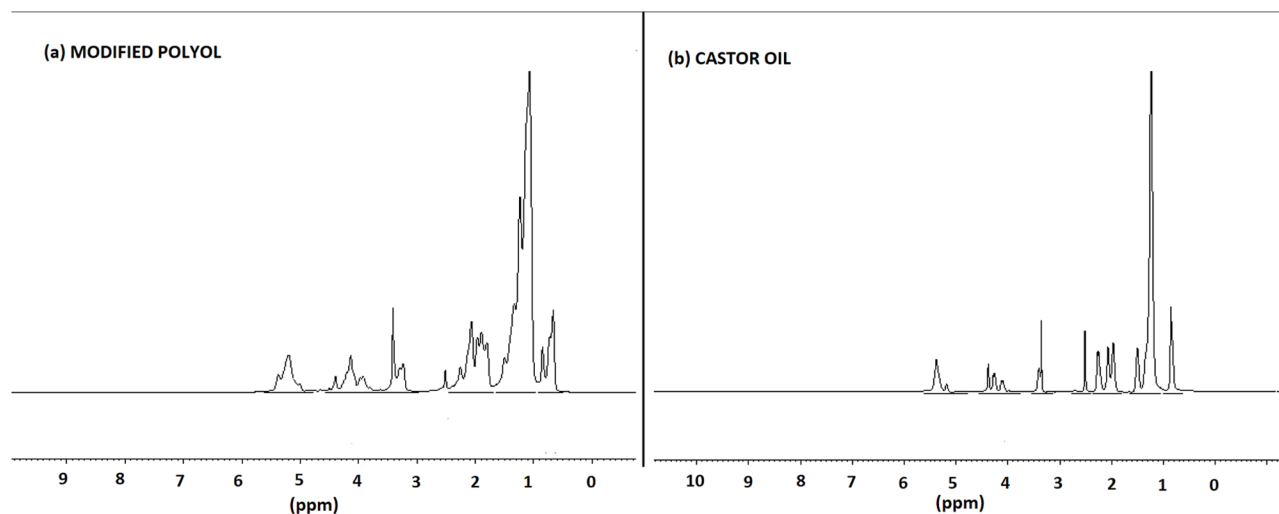
Figure 2: 1H NMR of (a) modified polyol and (b) castor oil.
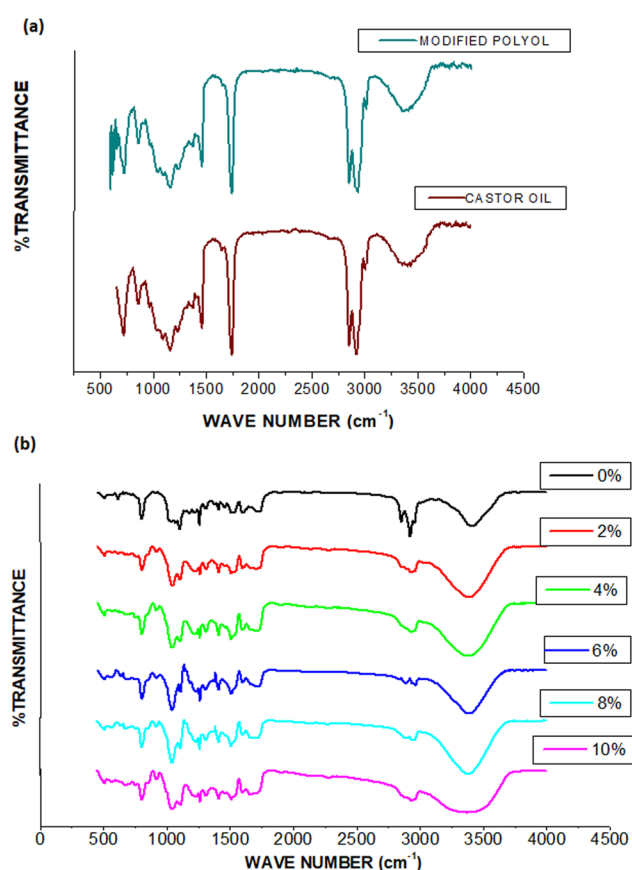

Figure 3: (a) FTIR of castor oil and modified polyol, (b) FTIR spectra of prepared RPUFs.

decreases in the foams incorporated with carbon fibre. It is attributed with the heterogeneity produced by the carbon fibre consequently decreasing the mechanical strength. Additionally, the absorption band around

2250 cm^{-1}, which is associated with −NCO groups, was not observed up to 8% concentration of filler. It indicates the reaction of all NCO groups with the hydroxyl groups of polyol to synthesize RPUF. While RPUF with 10% concentration of carbon fibre shows a small peak at 2277 cm^{-1} and broadening of bands of stretching vibrations of N−H groups, which indicates the incomplete reaction between polyol and isocyanate as well as deterioration in the structure of RPUF.

4.2 Mechanical properties

Mechanical properties of PU foam are influenced by several factors such as density of the foam, cell geometry as well as number and size of cells. In general, foams with higher density are expected to be more rigid which in turn exhibit higher mechanical strength. PU foam without fillers has a large number of cells with a comparatively larger cell size, but when carbon fibre is incorporated, it is evident from SEM images that foam cell size decreased.

Figure 4 shows the change in mechanical properties of rigid polyurethane foam on the addition of carbon fibre powder. Foam with 8% concentration of carbon fibre shows higher mechanical properties with compressive strength 6.88 MPa and flexural strength 2.97 MPa, which is almost 3 times in comparison to the unreinforced foams (Figure 4a). Figure 4c shows the variation in specific strength or reduced strength (strength/density) on increasing the concentration of carbon fibre powder. It is observed that the specific strength decreases initially but again on increasing the concentration of filler up to 8%, there is an increase in the specific compressive
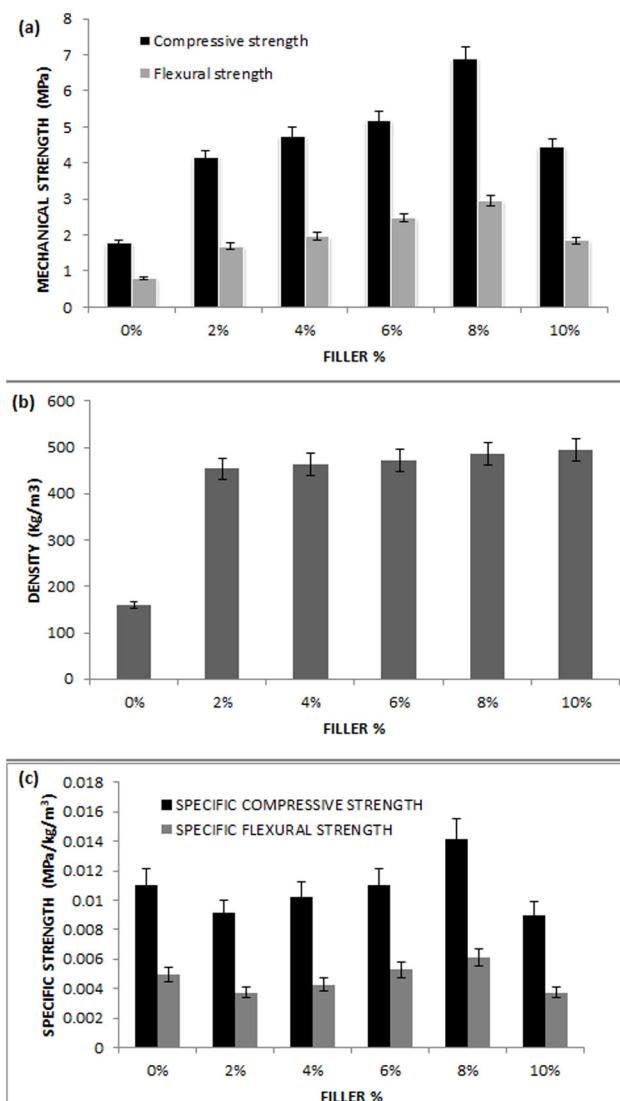
Figure 4: Plots of (a) mechanical strength vs. filler concentration, (b) density vs. filler concentration, (c) specific strength vs. filler concentration.

strength and specific flexural strength by 28% and 24% respectively as compared to the neat foam. This behaviour is attributed to the decrease in cell size and increase in cell number as more cell walls and struts per unit area of PU foams are present to support the foam structure under loading. This is also confirmed by SEM images of RPUFs as shown in Figure 5.

An initial slight decrease in the specific strength is attributed to the heterogeneity produced by the addition of filler, it is also confirmed by the FTIR of carbon fibre incorporated RPUFs. Furthermore, incorporation of fillers in the cell walls and struts strengthened the foam structure, consequently increasing the mechanical strength. It is evident from the literature that hydrogen bond formation

among urethane groups greatly contributes to the strength of RPUFs. But the filler introduced may interfere with the hydrogen bond formation, thus causing a negative effect on the properties of RPUFs. The overall performance of RPUFs depends on the competition between the positive effects of carbon fibre reinforcement and the negative effects on hydrogen bond formation (28).

A similar decrease in cell size has been reported for the addition of carbon nanotubes to the polyurethane foams (29).

4.3 Thermogravimetric analysis (TGA)

The TGA and Derivative Thermogravimetry (DTG) of carbon fibre powder incorporated RPUF are illustrated in Figures 6a and 6b. To evaluate the thermal stability of these foams TGA is conducted under the flow of nitrogen.

Generally, the thermal stability of RPUFs is described by the degradation onset temperature, i.e. the temperature of 5% weight loss ($T_{5\%}$). Results show a decrease in 5% weight loss temperature ($T_{d5\%}$) from 192°C to 148°C for the foam with 10% concentration of carbon fibre. This behaviour of RPUF is attributed to the increased thermal conductivity of foams, consequently increasing the heat to spread more rapidly only on the percolation path made by the carbon fibre and initializing some initial weight loss (30). Similar decrease in 5% weight loss temperature was observed by Ciecierska et al. on the addition of graphite in RPUF (29). Char residue also increases on increasing the filler concentration. All the samples show three weight loss stages, giving at 195°C, 330°C and 490°C. The beginning slow weight loss stage at 195°C is caused by the initial weight loss of some hard segments around the carbon fibres. Foam with 8% concentration of carbon fibres shows the fastest degradation, which is attributed to better dispersion of carbon fibre consequently providing the longest percolation path for heat transfer. On the other hand, although foam with 10% concentration of carbon fibre possesses a higher concentration of filler, poor dispersion provides comparatively shorter percolation path for heat transfer. The quick weight loss stage at 330°C is related to the degradation of hard segments resulting in the formation of isocyanate, alcohol, amine, olefin and CO_2. The third slow weight loss stage at 490°C is attributed to the degradation of soft segments and thermolysis of the organic residues. It was observed that the increase in the concentration of filler slows down the degradation up to 8% filler concentration, on increasing the concentration of carbon fibre beyond this limit increases the rate of degradation owing to the poor dispersion of the filler.
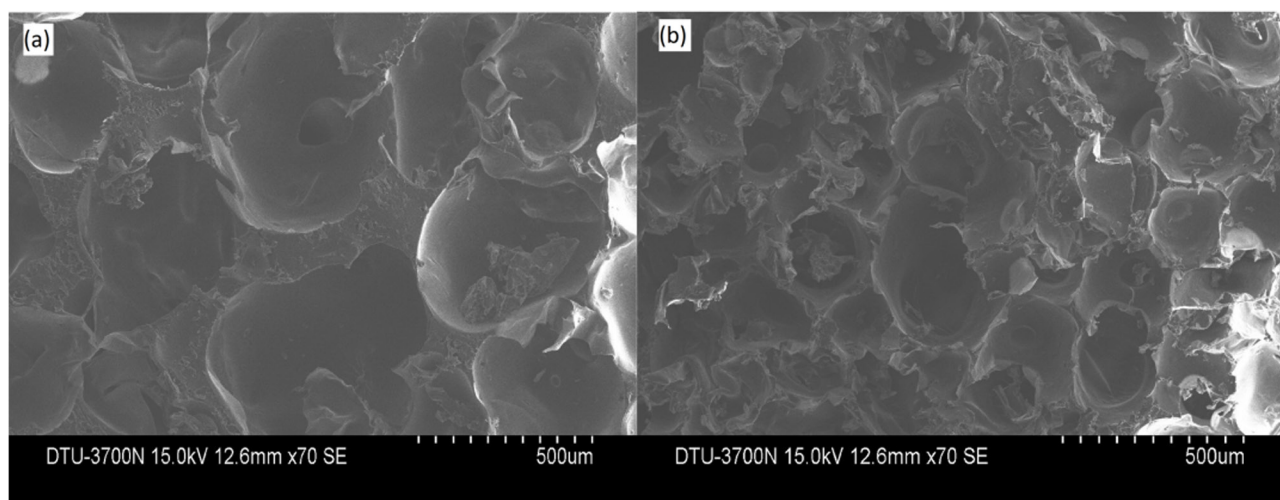
Figure 5: SEM micrographs of RPUF with (a) 0% and (b) 8% concentration of carbon fibre powder.

4.4 Cone calorimeter testing

Figures 6c-f show the cone calorimeter performance of RPUF containing a varied concentration of carbon fibre filler and the results are compiled in Table 2. It is evident that the TTIs (time to ignition) of carbon fibre filler incorporated RPUFs have shown a slight increase from 2 s to 5 s for the foams incorporated with 8% carbon fibre powder. Conventionally, the intensity of fire is correlated with the heat release rate (HRR) (31). Results showed that peak heat-release rate (PHRR) were decreased from 118 kW/m^2 to 85 kW/m^2 for the foam containing 8% carbon fibre powder (Figure 6c). PHRR signifies the surface pyrolysis of RPUF and evolution of a large quantity of flammable low molecular weight by-products such as primary or secondary amine, isocyanate, alcohol and olefin (32,33). Figure 6d shows that total heat release (THR) also decreases on the incorporation of carbon fibre filler. The char residue increased from 11.5% for neat RPUF to 44.4% for RPUF with 10% carbon fibre powder. Figure 6e shows the smoke production rate (SPR) and the first peak of SPR denotes that the rate of smoke production decreased from 0.008 to 0.004 m^2/s for 8% carbon fibre powder loading. The total smoke release (TSR) also decreases from 347 m^2/m^2 to 116 m^2/m^2 on the addition of 8% carbon fibre powder (Figure 6f). This behaviour of RPUF incorporated with carbon fibre powder is associated with the formation of the carbon layer on the surface and consequently reduction in combustion gases, which is analogous to the observations of Ciecierska et al. (29).

4.5 Conductivity measurement

Incorporation of carbon fibre in the RPUF generates conductivity in the foam. Figure 7 shows the change in conductivity of RPUF on the incorporation of carbon fibre.

It is clearly observed by the results that the incorporation of conducting carbon fibre increased the conductivity of RPUFs and the foams with 8% and 10% carbon fibre contents exhibits a conductivity of 1.9×10^{-4} and 7.1×10^{-4} S/m respectively. A similar range of electrical conductivity was obtained by Ibrahim et al. in castor oil-based polyurethane films incorporated with LiI salt (21). So, these foams may be used in the applications where conducting rigid foams are required.

5 Conclusion

RPUFs were prepared by incorporating carbon fibre powder to develop electromagnetic shields using bio-based raw materials. Mechanical, thermal and flame retardant properties of these foam shields have also been studied. FTIR and 1H NMR spectra of the prepared polyol confirm the transesterification of castor oil. Foams with 8% and 10% carbon fibre concentration show conductivity of 1.9×10^{-4} and 7.1×10^{-4} S/m respectively. Results concluded that RPUF with 8% carbon fibre concentration showed higher mechanical properties with 3-fold increase in compressive and flexural strength respectively. Specific compressive strength was also found to increase by 28% for the
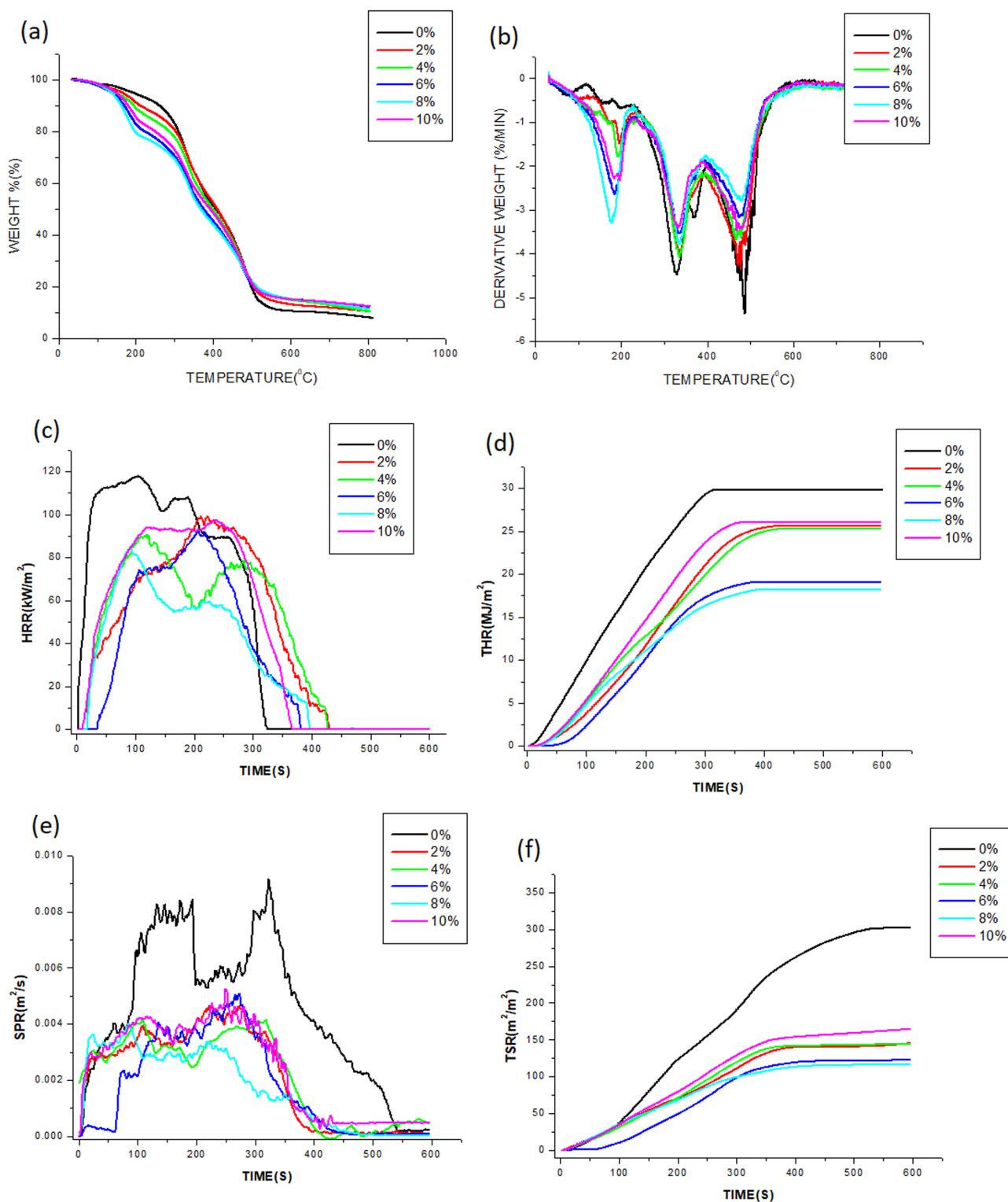
Figure 6: (a) TGA plots, (b) DTG plots, (c) HRR (Heat Release Rate), (d) THR (Total Heat Release), (e) SPR (Smoke Production Rate) and (f) TSR (Total Smoke Release) of RPUFs incorporated with carbon fibre.

foams with 8% concentration of carbon fibre powder. The peak of heat release (PHRR) was found to decrease from 118 kW/m² to 85 kW/m² on the incorporation of carbon fibre powder. Additionally, the rate of smoke production was also observed to decrease for composite RPUFs. As the incorporation of carbon fibre in RPUF provides a reasonable amount of conductivity without deteriorating the other properties of vegetable oil based

Table 2: Cone calorimeter data of RPUF incorporated with carbon fibre.

Concentration of filler	PHRR (kW/m²)	THR (MJ/m²)	TSR (m²/m²)	RESIDUE (%)	TTI (s)
0%	118	29.8	347	11.5	2
2% carbon fibre	99	25.7	144	31.6	3
4% carbon fibre	91	25.3	145	36.1	4
6% carbon fibre	92	19.0	123	40.5	5
8% carbon fibre	85	18.2	116	44.0	5
10% carbon fibre	97	26.0	165	44.4	4
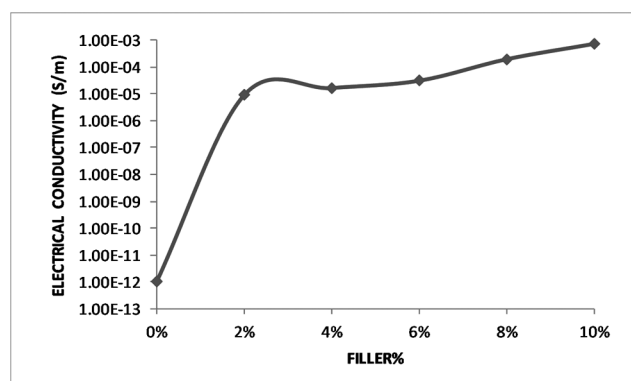
Figure 7: Plots of electrical conductivity(S/m) vs. filler %.

rigid PU foams, so carbon fibres are a potential additive to yield conducting PU foam.

References

1. Nasouri K., Shoushtari A.M., Mojtahedi M.R.M., Theoretical and experimental studies on EMI shielding mechanisms of multi-walled carbon nanotubes reinforced high performance composite nanofibers. J. Polym. Res., 2016, 23(4), 3-10.

2. Yan D.X., Pang H., Li B., Vajtai R., Xu L., Ren P.G., et al., Structured reduced graphene oxide/polymer composites for ultra-efficient electromagnetic interference shielding. Adv. Funct. Mater., 2015, 25(4), 559-566.

3. Huang Y., Li N., Ma Y., Du F., Li F., He X., et al., The influence of single-walled carbon nanotube structure on the electromagnetic interference shielding efficiency of its epoxy composites. Carbon, 2007, 45(8), 1614-1621.

4. Aram E., Ehsani M., Khonakdar H.A., Jafari S.H., Nouri N.R., Functionalization of graphene nanosheets and its dispersion in PMMA/PEO blend: Thermal, electrical, morphological and rheological analyses. Fibers Polym., 2016, 17(2), 174-180.

5. Tripathi S.N., Saini P., Gupta D., Choudhary V., Electrical and mechanical properties of PMMA/reduced graphene oxide nanocomposites prepared via in situ polymerization. J. Mater. Sci., 2013, 48(18), 6223-6232.

6. Stiebra L., Cabulis U., Knite M., Polyurethane foams obtained from residues of PET manufacturing and modified with carbon nanotubes. J. Phys. Conf. Ser., 2016, 709, 012002.

7. Yang Y., Gupta M.C., Dudley K.L., Lawrence R.W., Novel carbon nanotube - Polystyrene foam composites for electromagnetic interference shielding. Nano. Lett., 2005, 5(11), 2131-2134.

8. Ameli A., Jung P.U., Park C.B., Electrical properties and electromagnetic interference shielding effectiveness of polypropylene/carbon fiber composite foams. Carbon, 2013, 60, 379-391.

9. Kuang T., Chang L., Chen F., Sheng Y., Fu D., Peng X., Facile preparation of lightweight high-strength biodegradable polymer/multi-walled carbon nanotubes nanocomposite foams for electromagnetic interference shielding. Carbon, 2016, 105, 305-313.

10. Li J., Zhang G., Zhang H., Fan X., Zhou L., Shang Z., et al., Applied Surface Science Electrical conductivity and electromagnetic interference shielding of epoxy nanocomposite foams containing functionalized multi-wall carbon nanotubes. Appl. Surf. Sci., 2018, 428, 7-16.

11. Hwang S., Tensile, electrical conductivity and EMI shielding properties of solid and foamed PBT/carbon fiber composites. Compos. Part B-Eng., 2016, 98, 1-8. DOI:10.1016/j.compositesb.2016.05.028

12. Zhang H., Zhang G., Li J., Fan X., Jing Z., Li J., et al., Lightweight, multifunctional microcellular PMMA/Fe$_3$O$_4$ @ MWCNTs nanocomposite foams with efficient electromagnetic interference shielding. Compos. Part A-Appl. S., 2017, 100, 128-138.

13. Li Y., Shen B., Pei X., Zhang Y., Yi D., Zhai W., et al., Ultrathin carbon foams for effective electromagnetic interference shielding. Carbon, 2016, 100, 375-385.

14. Li Y., Shen B., Yi D., Zhang L., Zhai W., Wei X., et al., The influence of gradient and sandwich configurations on the electromagnetic interference shielding performance of multilayered thermoplastic polyurethane/graphene composite foams. Compos. Sci. Technol., 2017, 138, 209-216.

15. Farhan S., Wang R., Li K., Electromagnetic interference shielding effectiveness of carbon foam containing in situ grown silicon carbide nanowires. Ceram. Int., 2016, 42(9), 11330-11340.

16. Nasr Esfahani A., Katbab A.A., Taeb A., Simon L., Pope M.A., Correlation between mechanical dissipation and improved X-band electromagnetic shielding capabilities of amine functionalized graphene/thermoplastic polyurethane composites. Eur. Polym. J., 2017, 95, 520-538.

17. Stirna U., Cabulis U., Beverte I., Water-Blown Polyisocyanurate Foams from Vegetable oil polyols. J. Cell. Plast., 2008, 44, 139-160.

18. Malik M., Kaur R., Mechanical and Thermal Properties of Castor Oil-Based Polyurethane Adhesive: Effect of TiO_2 Filler. Adv. Polym. Technol., 2016, 1-7.

19. Malik M., Kaur R., Synthesis of NIPU by the carbonation of canola oil using highly efficient 5,10,15-tris(pentafluorophenyl) corrolato-manganese (III) complex as novel catalyst. Polym. Adv. Technol., 2018, 29(3), 1078-1085.

20. Malik M., Kaur R., Influence of aliphatic and aromatic isocyanates on the properties of poly(ether ester) polyol based PU adhesive system. Polym. Eng. Sci., 2018, 58(1), 112-117.

21. Ibrahim S., Ahmad A., Mohamed N.S., Synthesis and characterization of castor oil-based polyurethane for potential application as host in polymer electrolytes. B. Mater. Sci., 2015, 38(5), 1155-1161.

22. Kaur R., Kumar M., Function of silicon oil in the castor oil based rigid polyurethane foams. J. Polym. Eng., 2013, 33(9), 875-880.

23. Kumar M., Kaur R., Glass fiber reinforced rigid polyurethane foam: synthesis and characterization. e- Polymers, 2017, 17(6), 517-521.

24. Kaur R., Effect of Fillers on the Mechanical Properties of Castor Oil Bases Rigid Polyurethane Foams. Int. J. Res. Rev., 2018, 7(2), 296-302.

25. Agrawal A., Kaur R., Walia R.S., PU foam derived from renewable sources: Perspective on properties enhancement: An overview. Eur. Polym. J., 2017, 95, 255-274.

26. Narwal S.K., Saun N.K., Dogra P., Chauhan G., Gupta R., Production and Characterization of Biodiesel Using Nonedible Castor Oil by Immobilized Lipase from *Bacillus aerius*. Biomed. Res. Int., 2015, 281934, 1-6.

27. Hejna A., Kirpluks M., Kosmela P., Cabulis U., Haponiuk J., The influence of crude glycerol and castor oil-based polyol on the structure and performance of rigid polyurethane-polyisocyanurate foams. Ind. Crop. Prod., 2017, 95, 113-125.

28. Cao X., James Lee L., Widya T., Macosko C., Polyurethane/clay nanocomposites foams: Processing, structure and properties. Polymer, 2005, 46(3), 775-783.

29. Ciecierska E., Jurczyk-Kowalska M., Bazarnik P., Gloc M., Kulesza M., Kowalski M., et al., Flammability, mechanical properties and structure of rigid polyurethane foams with different types of carbon reinforcing materials. Compos. Struct., 2016, 140, 67-76.

30. Luyt A.S., Molefi J.A., Krump H., Thermal, mechanical and electrical properties of copper powder filled low-density and linear low-density polyethylene composites. Polym. Degrad. Stab., 2006, 91(7), 1629-1636.

31. Wang Y., Wang F., Dong Q., Xie M., Liu P., Ding Y., et al., Core-shell expandable graphite @ aluminum hydroxide as a flame-retardant for rigid polyurethane foams. Polym. Degrad. Stab., 2017, 146, 267-276.

32. Zhang M., Zhang J., Chen S., Zhou Y., Synthesis and fire properties of rigid polyurethane foams made from a polyol derived from melamine and cardanol. Polym. Degrad. Stab., 2014, 110, 27-34.

33. Yang R., Wang B., Han X., Ma B., Li J., Synthesis and characterization of flame retardant rigid polyurethane foam based on a reactive flame retardant containing phosphazene and cyclophosphonate. Polym. Degrad. Stab., 2017, 144, 62-69.

Electrochemical Hydrogen Gas Sensing Employing Palladium Oxide/Reduced Graphene Oxide (PdO-rGO) Nanocomposites

Kamal Arora[1], Saurabh Srivastava[1], Pratima Solanki[2], Nitin K. Puri[1*]

[1] Advanced Sensor Laboratory, Department of Applied Physics, Delhi Technological University, Bawana road, Delhi 110042, India
[2] Special Centre for Nanoscience, Jawaharlal Nehru University. New Mehrauli Road, New Delhi 110067, India
*corresponding author.

* Email address: nitinkumarpuri@dtu.ac.in, nitinpuri2002@yahoo.co.in

Abstract- This research work aims at proposing cheap, facile, sensitive and selective assembly of three electrode electrochemical hydrogen (H_2) gas sensor which operates on room temperature in ambient conditions. Palladium oxide-reduced graphene oxide (PdO-rGO) nanocomposite have been synthesized using insitu chemical sol-gel method and modified Hummer's method. The phase, structure, particle size and bonding information have been obtained using X-ray diffraction (XRD) analysis, Transmission electron microscopy (TEM), Fourier Transform Infrared (FTIR) spectroscopy and Ultraviolet-Visible (UV-Vis) absorption spectroscopy. Palladium oxide (PdO) nanoparticles of size ranging from 30 to35 nm have been successfully attached with uniform 2D network of reduced graphene oxide (rGO) sheets which offers large surface area for H_2 adsorption. The thin film of nanocomposite have been fabricated on conducting Indium tin oxide (ITO) glass substrates using electrophoretic deposition (EPD) process and is employed as working electrode (WE) in indigenously developed three electrode cell. Thin film surface morphology have been observed using Scanning Electron Microscopy (SEM) and it shows agglomerates of PdO nanoparticles with multiple randomly stacked rGO nanosheets uniformly spread across surface of the film. The amperometric response of the assembled electrochemical sensor has been recorded for the detection of 10 to 80 percent concentration of hydrogen gas using potentiostat/galvanostat autolab. The sensitivity of sensor is found out to be 0.462 $\mu A/\%$ H_2 concentration and sensing calibration curve shows uniform linear response. The stability and selectivity of the sensor has been enhanced using H_2 insensitive reference electrode (RE) and solid polymer electrolyte gas permeable membrane respectively which will aid new dimensions in designing robust H_2 sensor at room temperature.

Keywords: Amperometry, Hydrogen gas sensor, Metal oxide, Graphene, Nanocomposite

1. Introduction

Hydrogen (H_2) gas is reducing in nature and employed in aerospace, energy, medical, aerospace and petrochemical industries [1]. Its highly flammable and combustible characteristics lead to explosion on leakage and it causes hydrogen embrittlement on its penetration into metal and alloy systems. Additionally, hydrogen evolution results into corrosion of metals [2]. Thus, there is a significant need for highly sensitive, selective and stable hydrogen gas sensors which can detect even the order of parts per million of this gas i.e. lower explosive limit (LEL, 4% H_2 in air). These hydrogen sensors should operate in ambient, low temperature and even high temperature surroundings. The most effective sensors should also possess fast response towards the physically undetectable hydrogen gas accompanied with high sensitivity and selectivity [3].

Various types of sensors based on their mechanism have been used for hydrogen sensing application, but electrochemical and conductometric types of sensors have been researched more due to their peculiar merits. However, conductometric sensors require higher working temperature and low relative humidity (RH) for efficient working and it becomes difficult to detect gases in ambient condition, whereas electrochemical sensors can sense gases at room temperature with high degree of sensitivity and selectivity at cheaper cost [3-4]. Electrochemical sensors are divided into types i.e. potentiometric & amperometric. Although, former provides extensive dynamic range, but lacks accuracy towards its logarithmic response. On the other hand, latter provides highly linear and accurate sensing response [5]. In amperometric sensing, a constant potential is achieved across the circuit using variable resistor and relationship between current versus time is obtained [6].

Carbon based materials such as carbon nanotubes (CNT) and graphene received a lot of attention over others due to their remarkable physical, chemical and electrical properties. Graphene has been the source of major research work in developing new catalysts over other carbon allotropes due to its exceptional properties. Theoretical specific surface area of graphene is 2600 $m^2 g^{-1}$ which is double to that of CNT and much higher than other allotropes of carbon comprehensively. On comparison to carbon nanotubes, graphene especially pure chemically modified graphene (CMG) can be synthesized at large scale in much cheaper cost using graphite oxide as precursor without support of metallic catalysts. The inclusion of these catalysts leads to impurities in CNT, which affect its electrochemical properties. Graphene electronic structure contains free localized π electron which imparts it high electron mobility and conductivity as well as high catalytic activity. Graphene is highly stable in nature both physically and chemically, which provides it with longer lifetime in catalytic activities [7] [8]. Method adopted for synthesis of graphene determines the level of purity, however pure graphene is not electroactive towards hydrogen gas in nature, graphene extracted through chemical method leaves behind some chemical impurities and defects which gives them enhanced catalytic activity as compared to pure graphene, known as chemically

modified graphene (CMG) i.e. graphene oxide (GO) and reduced graphene oxide (rGO) [9]. Graphene oxide (GO) owing to large number of oxygenated functional groups and defects, is insulating in nature and shows poor electrochemical properties. To restore the conductivity of pristine graphene, its conversion to reduced graphene oxide (RGO) is essential for most of the electrochemical applications. High surface-to volume ratio and abundant surface defects provides rGO larger surface area for adsorption and other catalytic activity as compared to graphene oxide (GO) [10]. The electroactivity of rGO for hydrogen gas can further be enhanced by doping it with superior catalytic metals such as palladium (Pd) or platinum (Pt) or by forming their composites with other electroactive materials [11]. These doped or composite graphene materials can be used as working material in sensors and fuel cells [12].

Pd nanoparticles is most researched hydrogenation catalyst as it is a good initiator of hydrogen spillover over desired material [13-14], Pd-rGO nanocomposites has been used as sensing element in hydrogen conductometric sensor and it was found that Pd-rGO composite shows good sensitivity as compared to rGO [15-16]. Also, It has been found that Pd doped rGO and Pt doped rGO shows high hydrogen sensitivity and selectivity, but former reflects more sensitivity as compared to latter [17]. Nevertheless, pure Pd is costly material and over the time, it is poisoned due to the deposition of sulphur on being in contact with the atmosphere. Whereas, palladium oxide (PdO) is secured from the contamination as it has high operating temperature and protective sheath of oxide layer [18]. Thus, PdO nanoparticles can be substituted for pure Pd for hydrogen gas sensing. Pristine PdO nanoflakes and nanoparticles thin films have been used for conductometric hydrogen gas sensing application and it has been found that they showed high sensitivity and selectivity towards hydrogen gas [19-21]. Nanostructured PdO particles and their composites have been studied for carbon monoxide (CO) and other organic volatile gas sensing application [22-30]. In our preceding research work, PdO nanoparticles have been studied for amperometric hydrogen gas sensing at room temperature and they showed good sensitivity for H_2 gas among other similar sensors [31]. Nanocomposites of PdO with rGO will enhance the sensitivity of amperometric sensor towards hydrogen gas and moreover they have not been studied before to the best of our knowledge.

In the current work, PdO-rGO nanocomposite and rGO have been synthesized using simple and cost effective insitu chemical sol-gel method and improved modified Hummer's method respectively. PdO-rGO nanocomposite thin film has been fabricated on ITO glass substrate using electrophoretic deposition process. Consequently, PdO-rGO/ITO has been used as working electrode (WE) in indigenously developed three electrode cell for amperometric hydrogen gas sensing at room temperature.

2. Experimental

2.1 Electrochemical sensing setup

The setup consist of three electrodes (working electrode (WE), Counter electrode (CE) & Reference electrode (RE)) placed in a electrochemical cell attached to Potentiostat/galvanostat autolab instrument for amperometric (current (i) vs time (t)) measurement (fig. 1).
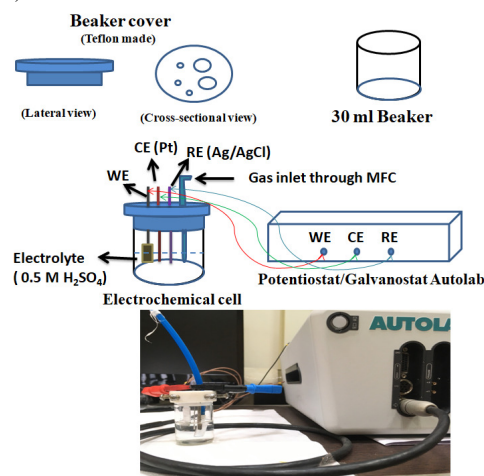

Fig. 1.Electrochemical sensing setup

The CE is made up of (4 cm x 1 mm) Platinum (Pt) cylindrical rod because of its lower oxygen reduction overpotential and less hydrogen solubility in comparison to palladium (Pd) [1]. Reference electrode (RE) is made up of Nafion coated (5 cm x 3mm) silver/silver chloride (Ag/AgCl) cylindrical rod, because Ag/AgCl remains stable and maintains zero potential shift throughout the reaction between the WE and CE and coating of Nafion polymer allow only hydrogen ion to diffuse to the RE while restricting diffusion of other ions [1]. Silver chloride (AgCl) is deposited onto silver (Ag) electrode by its chloridization in $FeCl_3$/0.1 M HCl solution for 24 hours. The traces of $FeCl_3$ are removed by rinsing electrode with DI water and immersing the electrode in saturated AgCl solution, which results in uniform gray black layer on the electrode. Consequently, Ag/AgCl electrode is coated with uniform Nafion coating by dipping it several times in 5% Nafion 117 polymer solution [32-33].

Working electrode consist of PdO-rGO nanocomposite thin film as a hydrogen sensing material placed inside electrochemical cell. The electrochemical cell has been fabricated using 30 ml glass beaker sealed with Teflon made beaker cover containing three electrode inlets, a gas inlet as depicted in fig. 1. The electrochemical cell is attached to potentiostat/galvanostat autolab using crocodile connectors and it is filled with 0.5 Molar concentration of sulphuric acid (0.5 M H_2SO_4). The use of proton conducting liquid electrolyte permits setup to be operated at room temperature in ambient conditions and mitigate the problem of relative humidity (RH) in sensor, whereas although solid polymer electrolyte are more stable and less corrosive, but they are strongly affected by humidity in the surrounding and have low conductivity at room temperature [34]. Also, the ionic liquid (IL) electrolytes which have the best traits of both liquid and solid polymer are not readily used in electrochemical gas sensors because they generate slower response time due to their low conductivity and high viscosity in ambient conditions [35]. The proposed electrochemical sensing

setup is attached to the Alicat scientific MC standard series gas mix mass flow controller (MFC) using Teflon pipes.

2.2 Fabrication of working electrode

The chemicals used in synthesis of Palladium oxide-reduced graphene oxide (PdO-rGO) nanocomposite are sulphuric acid (H_2SO_4), phosphoric acid (H_3PO_4), potassium permanganate ($KMnO_4$), graphite powder, distilled water (H_2O), hydrazine hydrate ($N_2H_4.H_2O$), palladium chloride ($PdCl_2$), ethanol (C_2H_5OH) and hydrochloric acid (HCl).All the chemicals used are procured from Fisher and Sigma Aldrich and belongs to AR grade purity (~99.9 %).

2.2.1 Synthesis of rGO

GO is synthesized using improved Hummer's method as suggested by Marcano et al., 26.7 mL of concentrated H_3PO_4 is added to 240 mL of concentrated H_2SO_4 in 9:1 ratio in a conical flask. 2 g graphite powder is added to the H_2SO_4/H_3PO_4 solution. 12 g of $KMnO_4$ is added to the resultant solution slowly as the reaction is highly exothermic. The addition of $KMnO_4$ is followed by stirring of solution at 50^0 C for 12 hours. The solution is mixed with 270 mL of ice along with slow addition of 2 mL H_2O_2. The resultant brown colored solution in the conical flask is filtered, washed with HCl and subsequently added with distilled water until pH value of 7 is obtained. The resultant solution is dried off at 70^0 C to obtain brown powder of GO [36].

Park et al. successfully produced high purity rGO using hydrazine hydrate ($N_2H_4.H_2O$) as reducing agent. 300 mg of GO is added to 300 mL of distilled water through continuous stirring in a 500 mL glass beaker. 100 μL of $N_2H_4.H_2O$ is dissolved into the beaker slowly and solution is left for 12 hours under continuous stirring. The final solution turns black colored which is filtered, washed with distilled water to remove traces of $N_2H_4.H_2O$ and is dried at 70^0 C to obtain black powder of rGO [37].

2.2.2 Synthesis of PdO-rGO nanocomposites

PdO-rGO nanocomposites have been synthesized using insitu chemical solution method. $PdCl_2$ is dissolved in 30 ml solution of rGO and ethanol (1μg/ml) such that their molar ratio remains (1:1) respectively. The solution is continuously stirred for 1 hour to mix uniformly. The resultant solution is kept untouched for 24 hours as a process of ageing. Thereafter, the solution is heated at 80^0 C for 24 hours to extract brown colored powder. The powder is washed and filtered with DI water several times. Subsequently, the filtered powder is annealed at 600^0 C to remove organic and chloride ions impurities which yields a black colored powder. The structure, morphology and nature of bonds of the black powder is determined through X-ray diffraction (XRD), Transmission electron microscopy (TEM), Scanning electron microscopy (SEM), Fourier Transform Infrared Spectroscopy and Ultraviolet-Visible (UV-Vis) absorption spectroscopy processes. The analysis of the data obtained from these processes shows the formation of PdO-rGO nanocomposites in the insitu as-synthesized black powder.

Subsequently, 1 μm thick uniform PdO-rGO nanocomposite thin film is deposited onto the conductive (5 mm x 10 mm) ITO coated glass substrate using electrophoretic deposition (EPD) process by applying a constant potential of 40 V for 2 minutes. These fabricated thin films of PdO-rGO are used as working electrode in electrochemical cell for hydrogen gas sensing.

3. Results and discussions

3.1 X-ray Diffraction analysis (XRD)

The graphs presented in fig. 2(a), (b) and (c) represent the XRD plot of GO, rGO and PdO-rGO nanocomposite respectively. Sharp peak at 11.01^0 in fig. 2(a) shows the formation of characteristics (002) plane of GO whereas a broad peak at 23.78^0 in fig. 2(b) confirms the formation of featured (002) plane of rGO. On comparison of intensity of peaks shown in fig. 2(c) with the published JCPDS data (CAS number: 750200 and 850624), it can be deducted that the intensity peaks (001)*, (100)*, (101)*, (110)*, (111)*, (003)*, (112)*, (103)*, (200)* and (202)* corresponds to tetragonal PdO (t-PdO), whereas small hump (002) at 25^0 belongs to rGO.
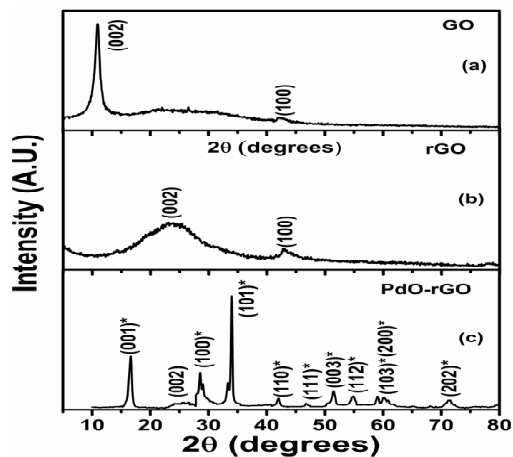

Fig. 2. XRD plot of (a) GO, (b) rGO, (c) PdO-rGO nanocomposite

Maximum sharp intensity peak at 34^0 and weaker broad peak at 25.45^0 belongs to (101) plane of t-PdO and (002) plane of rGO correspondingly. Hence, XRD analysis shows the formation of crystal structure which contains composite of both t-PdO and rGO collectively.

The average size of the t-PdO crystallites and number of rGO layers can be obtained using Scherrer and Bragg's formula. [Eq. 1 and 2] [38-39]. The d-value of GO for (002) plane is found to be 8.02 Å, whereas d-value of rGO for (002) plane is found to be 3.74 Å respectively. Tetragonal PdO crystallite size is calculated to be 23.72 nm and number of rGO layers is found to be equal to three.

$$t = \frac{0.9\lambda}{\beta cos\theta} \qquad (1)$$

$$2dsin\theta = n\lambda \qquad (2)$$

d is interplanar spacing, n is order of principal maxima, β is the FWHM (Full width half maxima), λ is wavelength, θ is the angle having maximum intensity and t represent crystallite size.

3.2 Fourier Transform Infrared (FTIR) spectroscopy

Fig. 3(a), (b) and (c) shows the FTIR plot of GO, rGO and PdO-rGO nanocomposite respectively. The graphs depicted in fig. 3(a) and (b) represent the FTIR spectra of GO and rGO respectively, the absorption bands generated at 1061.55 cm^{-1}, 1628.87 cm^{-1} and 1735.41 cm^{-1} correspond to -C-O- stretching, -C–O–H- deformation and C=O stretching of -COOH- group respectively [40]. The broad absorption band arising at wavenumber 3445.87 cm^{-1} denotes the existence of -O-H- functional groups. Nevertheless, on reduction of GO with hydrazine monohydrate, the oxygen functional groups present in GO FTIR spectra, reduced significantly in case of rGO, the new band at 1396.66 cm^{-1} arises due to the vibration of the graphene sheets skeletal (fig. 3(b)) [41].

In fig. 3(c), the bands arising at 601.61 cm^{-1} and 666.92 cm^{-1} correspond to formation of the -Pd-O- and -Pd-C- vibrational bonds respectively. Other absorption bands appearing in this plot are identical to that of rGO, (fig. 3(b)), but there is an apparent right shift and splitting in the bands, now appearing at 1589.96 cm^{-1}, 1635.80 cm^{-1} and 3465.26 cm^{-1}, due to formation of bonds between PdO and carboxylic as well as hydroxyl groups present in the rGO sheets.
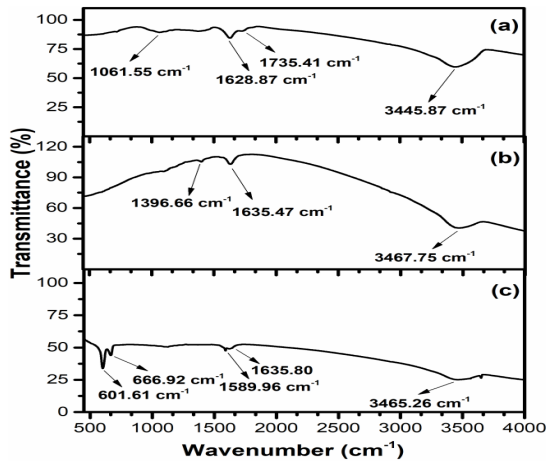

Fig. 3. FTIR spectroscopy plot of (a) GO, (b) rGO, (c) PdO-rGO nanocomposite

3.3 Ultraviolet Visible (UV-Vis) spectroscopy

UV-Vis spectra of GO, rGO and PdO-rGO nanocomposite are shown in fig. 4 through dotted, dashed and solid line respectively. The reduction of GO can be easily observed through this spectra as the absorption peak arising at 230 nm due to π-π^* transition of C-C bond shifted towards higher wavelength of 262 nm, indicating removal of oxygen containing functional groups present in GO structure which increased the

concentration of π electron and restored the sp^2 C-C conjugated structure [42].

There is an apparent red shift in absorption peak of rGO towards 280 nm from 262 nm in UV-Vis spectra of PdO-rGO nanocomposite. It can be attributed towards increase in the π electron concentrations and relaxation of the composite structure due to its doping with PdO nanoparticles [43]. Moreover, there is also an absorption peak present at 186 nm which affirms the formation of PdO in the PdO-rGO nanocomposite [18].
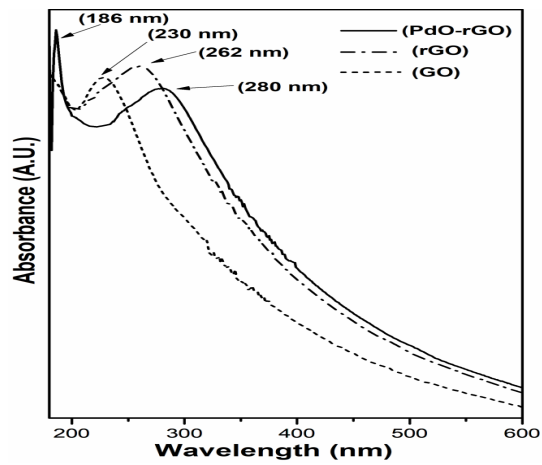

Fig. 4. UV-Vis Spectra of GO, rGO and PdO-rGO nanocomposite

The Tauc plot of the UV-Vis absorption spectra (Fig. 4) is represented by Fig. 5 which demonstrates the value of optical band gap of GO, rGO and PdO-rGO respectively.
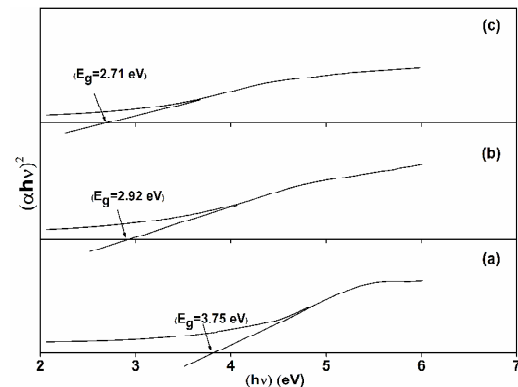

Fig. 5. Tauc plot of (a) GO, (b) rGO and (c) PdO-rGO

It can be observed in Fig, 5(a) that band gap of GO turns out to be 3.75 eV which gets minimized to 2.92 eV on its chemical reduction by hydrazine hydrate to form rGO (Fig. 5(b)), these computed values coincides with the already reported range of values [44-45]. On the other hand, formation of PdO-rGO nanocomposite further drops the band gap of material to 2.71 eV as visible in Fig. 5(c).

3.4 Transmission electron microscopy (TEM)

Fig. 6(a), (b) and (c) show the images of TEM, high resolution TEM (HRTEM) and selected area electron diffraction (SAED) for PdO-rGO nanocomposite. In fig. 6(a), nanoparticles of size of the order of 30 to 35 nm, with uniform shape and boundaries, can be seen embedded into the transparent 2D rGO sheet like structure. Fig. 6(b) shows the well-defined uniform parallel planes with spacing of 0.225 nm, which corresponds to the interplanar spacing of (101) plane of t-PdO crystal structure on comparison with published JCPDS data (CAS number 750200).

Rings formed by bright dots together with the presence of fused rings are visible in SAED pattern (Fig. 6(c)), which suggests the formation of polycrystalline (101), (112), (200) and (202) planes of t-PdO structure and amorphous rGO sheets.
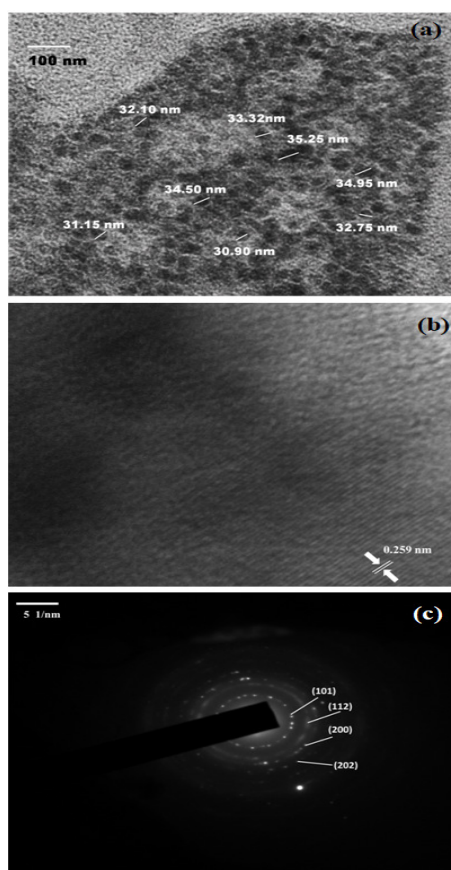

Fig. 6. (a) TEM image, (b) HRTEM image, (c) SAED image of PdO-rGO nanocomposite

Hence, TEM analysis agrees with the initial recommendation of XRD analysis about the formation t-PdO-rGO nanocomposite.

3.5 Scanning electron microscopy (SEM)

Fig. 7 illustrates the low resolution (1μm) and high resolution (500 nm) images of surface of thin film of PdO-rGO nanocomposite deposited on ITO glass substrate. Randomly blended and uniformly aggregated multiply stacked 2D nanosheets of rGO can be seen on the surface of the sample in form of dark grey area of the images. However, the bright clusters of spots in images represent the agglomerates of PdO nanoparticles within rGO nanosheets.

These wrinkled 2D nanosheets of rGO are folded at the edges and spread homogeneously along the surface of the sample offering large surface area to the clusters of PdO nanoparticles.
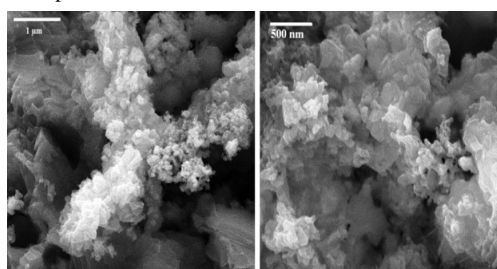

Fig. 7. Scanning electron microscopy (SEM) images of PdO-rGO nanocomposite thin film

Shape of nanoparticles along with the boundaries between particles and sheets are not visible, since the actual size of particles ranges from (30 to 35 nm), which are clearly visible in TEM image (fig. 6(a)).

3.6 Electrochemical H_2 amperometric sensing study

Various percentage concentration ratio of H_2/Argon gas is introduced into the electrochemical gas sensing setup (fig. 1.) by composing gas mixture through MFC under ambient condition at room temperature.

There are several factors which affect the sensing efficiency of electrochemical sensors; (a) Flow rate and (b) Selectivity. The flow rate determines the diffusion of gas into the electrolyte and since electrochemical reaction is diffusion limited process, thus, it is important to select suitable flow rate to achieve good sensing response from the sensor. The presence of other gases in surrounding could deter the selectivity of WE toward sensing of H_2 gas and hence would affect the efficiency of the electrochemical sensor [5]. Fig. 8 represents the plot between sensing response current (μA) and different flow rate (mL/min) in presence of 80% H_2 gas.

This plot has been fitted using non-linear curve fit with equation y=39.23*ln(1.31ln(x)) with R^2 value of 0.99128, where ln stands for natural logarithm, , y indicate the electrochemical sensing current in μA and x represent the flow rate of H_2 gas in ml/min. It can be seen that current raises steeply from flow rate of 10 mL/min to 60 mL/min and then increases steadily onwards upto 200 mL/min. Thus, flow rate of 60 mL/min has been selected as constant flow rate for obtaining amperometric sensing response of electrochemical sensor for various percentage concentration of H_2 gas.
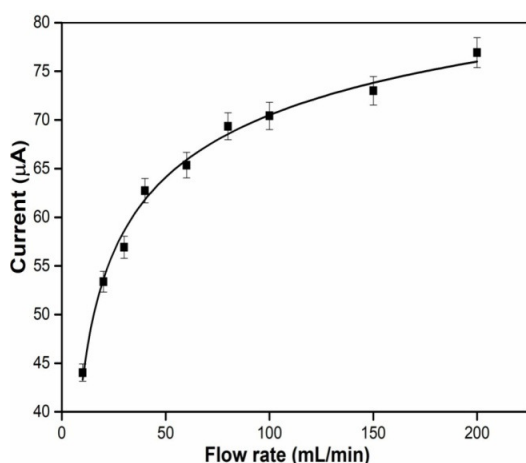
Fig. 8. Flow rate (ml/min) v/s current (µA) relation for 80% H_2 gas

Fig. 9. Response curve for different percentage concentration of H_2 gas

The electrochemical sensor is sealed with cylindrical Teflon cover and inlets with white Teflon tape to protect it from atmospheric gases. Although, Argon is an inert and non-reactive gas, but an 50 µm thick fluorinated ethylene propylene (FEP) selective gas permeable polymer membrane is placed in front of gas inlet to allow only H_2 gas out of H_2/Argon gas mixture to flow into the electrochemical cell to enhance its selectivity and efficiency.

The H_2 gas is allowed to flow into the electrochemical cell for 5 minutes and thereafter the flow is cutoff to measure the amperometric sensing response by maintaining a fixed potential of 1 V using potentiostat/galvanostat autolab.

Fig. 9 illustrates the amperometry of electrochemical sensor for various percentage (10-80) % of H_2 gas. Steep increase in current is observed on introduction of the gas which becomes constant after reaching a plateau and thereafter decays quickly as soon as gas is cutoff from flowing into the electrochemical cell.

The amperometric response of electrochemical sensor for different percentages of H_2 concentration is illustrated in fig. 9. It shows high sensitivity, stable and fast sensing response with quick recovery time. The time taken by the sensor to reach 90% of steady state current (t_{90}) ranges from 30 to 60 seconds for different percentage of H_2.

The calibration plot of sensor response is depicted in Fig. 10; it shows linear increase in current on raising the percentage concentration of H_2 gas from 10 to 80%. The sensitivity (S) of electrochemical sensor is found out to be (0.462 ± 0.023) µA/%(H_2) with R^2 variance of 0.98229 and fitted by linear regression equation $y=29.38 + 0.462x$, where x and y represent the percentage concentration (%) of H_2 gas and the response current (µA) of the electrochemical sensor respectively.

Thus, the sensitivity of amperometric sensor towards H_2 gas is enhanced on using PdO-rGO nanocomposite as WE in comparison to pristine PdO nanoparticles [31]. The Limit of detection (LOD) of the fabricated amperometric sensor is calculated to be equal to 0.13% H_2 [32].
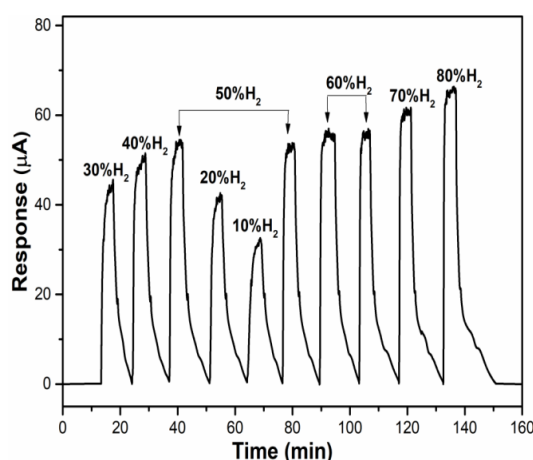
The catalytic behavior of palladium oxide (PdO) in presence of 0.5 M sulphuric acid (H_2SO_4) in a electrochemical reaction has been experimentally studied using cyclic voltammetry (CV) (fig. 11). The voltammerty study has been conducted using potential range from -0.2 mV to +1.3 mV with a scan rate of 100 mV s^{-1}. It is observed that the reoxidation of PdO occurs during anodic sweep and the maximum anodic oxidation current arises at 0.62 mV, whereas in the cathodic sweep,
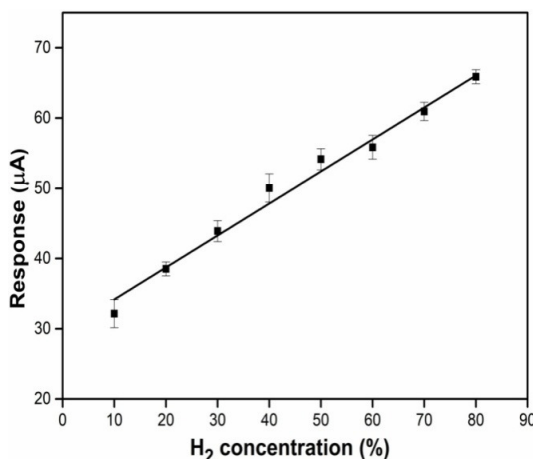

Fig. 10. Calibration plot of response current (µA) vs H_2 concentration (%)

the reduction of PdO takes place with maximum cathodic reduction current appears at 0.15 mV. This confirms the redox catalytic behavior of PdO and also agrees with the already published similar research work [46-47].

The cyclic voltammetry (CV) study of PdO-rGO thin film in 0.5 M Sulphuric acid (H_2SO_4) electrolyte has also been carried out before and after flowing hydrogen gas, with scan rate of 100 mV s^{-1}. Fig. 12 depicts the CV study of PdO-rGO nanocomposite thin film including both before and after flow of hydrogen gas for 5 minutes (Gas on time is same as used during amperometric H_2 sensing study).
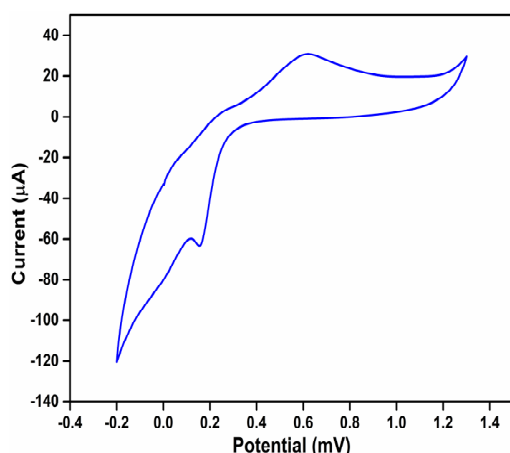
Fig. 11 Cyclic voltammetry study of PdO thin film

It can be seen that both CV curve coincides with each other perfectly (fig. 12). However, the maximum current value in both reduction as well as the oxidation peaks rises appreciably after the flow of hydrogen gas. The maximum oxidation current in cathodic cycle occurs at 0.65 mV, whereas the maximum reduction current during anodic cycle appears at 0.10 mV and after flow of hydrogen gas, the reduction potential shift towards 0.12 mV and oxidation potential moves towards 0.72 mV respectively.
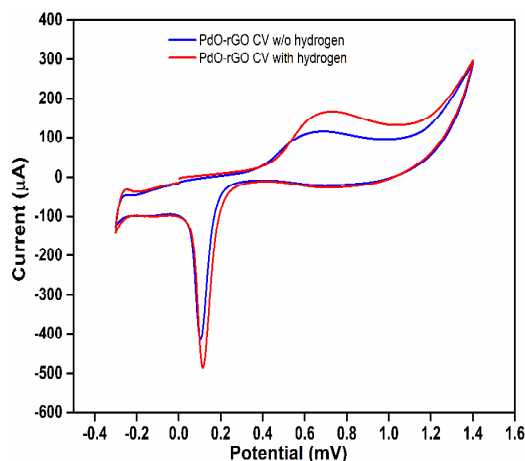

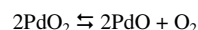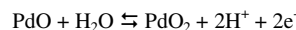Fig. 12 Cyclic voltammetry study of PdO-rGO nanocomposite thin film

This shift towards higher potential can be attributed to the high concentration of hydrogen ions within the electrolyte; the population of H^+ ions reaching the electrolyte-WE surface region rises to the point that it creates a barrier for other incoming H^+ ions to participate in the electrochemical reactions.

Hence, CV study affirms that PdO act as an electrocatalytic material towards H_2 gas and returns to its initial state after completion of electrochemical reaction. Wen et. al. showed the mechanism for probable redox reaction taking place on introducing PdO WE in H_2SO_4 electrolyte [47]. Also, after the flow of hydrogen gas in the electrochemical cell, the oxidation of H_2 takes place
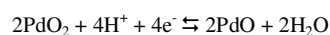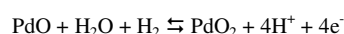
at the sensing electrode by which it ionizes itself and releases two electrons [1, 3, 5].

Thus, the possible redox mechanism explaining this electrochemical reaction may be as follows:

(Before Hydrogen gas flow)

$$PdO + H_2O \leftrightarrows PdO_2 + 2H^+ + 2e^-$$

$$2PdO_2 \leftrightarrows 2PdO + O_2$$

(After Hydrogen gas flow)

$$PdO + H_2O + H_2 \leftrightarrows PdO_2 + 4H^+ + 4e^-$$

$$2PdO_2 + 4H^+ + 4e^- \leftrightarrows 2PdO + 2H_2O$$

The selectivity of PdO-rGO nanocomposite based amperometric sensor towards various gases has been studied using similar parameters as in H_2 gas sensing and comparison of their sensing response is depicted in Fig. 13. 80 % concentration of Methane (CH_4), Carbon dioxide (CO_2) and Sulphur dioxide (SO_2) gas is introduced into electrochemical cell at flow rate of 60 ml/min and their sensing response is measured in terms of sensing current (μA) at room temperature. It is observed that PdO-rGO/ITO WE shows significant change in current for H_2 gas in comparison to other gases. Although, it shows sensitivity for CH_4 gas too, but it is comprehensively smaller in comparison to H_2. On the other hand, sensing response for CO_2 and SO_2 is negligibly minute, to be considered insensitive.

When SO_2 gas is introduced into the electrochemical cell containing PdO-rGO nanocomposite as WE and H_2SO_4 as electrolyte, the mechanism of its interaction can be divided into following steps, (a) Diffusion or Physical dissolution of SO_2 molecules to sulphite ions (SO_4^{2-})
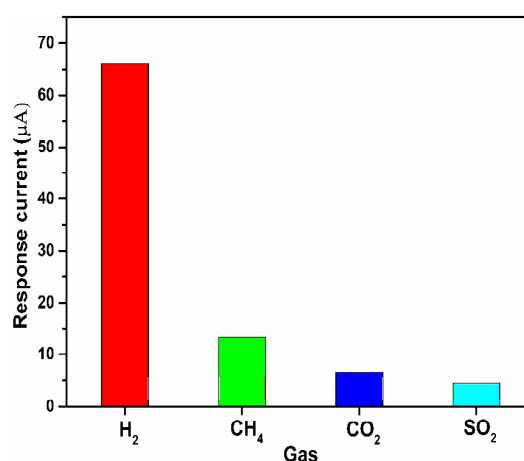
Fig. 13. Response of PdO-rGO nanocomposite based amperometric sensor to various gases

within the electrolyte, (b) transport of dissolved SO_4^{2-} ions to surface of WE, (c) Diffusion of SO_4^{2-} ions by WE, (d) electro-oxidation of SO_4^{2-} ions at PdO-rGO nanocomposite thin film surface, (e) simultaneous reduction of protons released during physical dissolution of SO_2 at CE to restore the ionic content of the system [6,

48-51]. The mechanism can also be understood using following electrochemical reactions:

$$SO_2 + 2H_2O \rightarrow SO_4^{2-} + 4H^+ + 2e^-$$

$$PdO + SO_4^{2-} + 2H^+ \leftrightarrow PdSO_4 + H_2O$$

$$\frac{1}{2}O_2 + 2H^+ + 2e^- \rightarrow H_2O$$
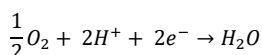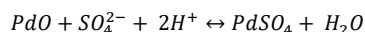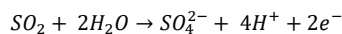
The mechanism of interaction of CO_2 gas inside the electrochemical cell containing H_2SO_4 as electrolyte can be explained by following steps and electrochemical equations, (a) ionization of H_2SO_4 to release H^+ ions (a) transport of dissolved H^+ ions and CO_2 molecules to surface of WE, (c) absorption of CO_2 molecules by WE, (d) electro-oxidation at PdO-rGO nanocomposite thin film surface, (e) simultaneous reduction of protons at CE to restore the ionic content of the system [52-54].

$$PdO + CO_2 + 2H^+ \leftrightarrow PdCO_3 + H_2O + 2e^-$$

$$\frac{1}{2}O_2 + 2H^+ + 2e^- \rightarrow H_2O$$
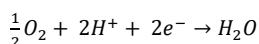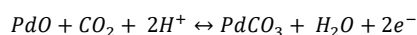
These results confirm that fabricated PdO-rGO nanocomposite based amperometric sensor is highly sensitive and selective towards H_2 gas and thus can be utilized for hydrogen gas sensing application in the environment.

The stability of PdO-rGO thin film WE used for the electrochemical sensing of H_2 has been determined using same set of parameters for 60 days (fig. 14). It has been found that there is no significant change in the response current of WE from day 1 to day 60. The current obtained on day 1 is found to be 65.89 µA which decrease to 63.42 µA on day 60. Thus, the results suggest that the fabricated WE is stable and aptly suited for electrochemical sensing of H_2 gas.
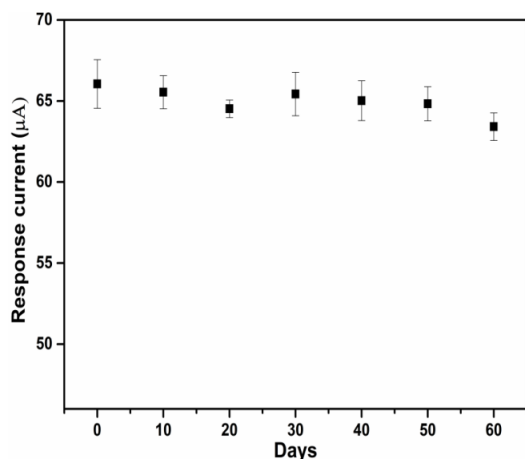

Fig. 14. Stability study of working electrode

Four sets of electrodes of PdO-rGO nanocomposite thin film have been fabricated by electrophoretic deposition
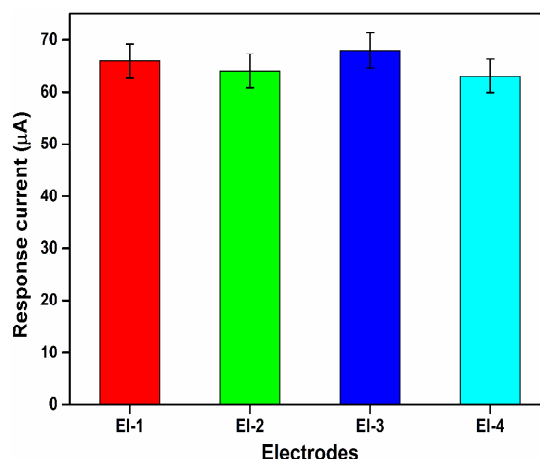

Fig. 15. Reproducibility study of working electrodes

method using same deposition parameters as mentioned in experimental details. These electrodes are then employed as WE for electrochemical sensing of H_2 in similar environmental conditions and the sensing currents are obtained respectively. It can be seen in fig. 15 that there is no considerable variations in the response current of the synthesized electrodes and relative standard deviation (RSD) of the reproducibility study is found to be 3.31% which indicates good reproducibility and precision.

Some of the similar amperometric sensors working on liquid electrolyte towards hydrogen sensing application along with their characteristics are reported in table 1.

Gas Analyte	Working Electrode	Liquid Electrolyte	Limit of Detection (%H_2)	Sensitivity (µA/% or (ppm)H_2)	References
H_2	Pt/Carbon	5M H_2SO_4	-	-	[55]
H_2	Gold	9M H_2SO_4	-	-	[56]
H_2	Pt-Ag/AgCl	1M H_2SO_4	<1%	0.0305	[57]
H_2-Air	Pt-Nafion	1 M H_2SO_4	<0.2%	0.008	[58]
H_2-Ar	PdO/ITO	0.5M H_2SO_4	<0.2%	0.222	[31]
H_2-Ar	**PdO-rGO/ITO**	**0.5 M H_2SO_4**	**<0.2%**	**0.462**	**Present work**

Table 1. Liquid electrolyte based amperometric hydrogen sensors

4. Conclusion

In the present research work, PdO-rGO nanocomposite is synthesized using in-situ chemical sol-gel method and modified Hummer's method. The structure, morphology, nature of bonds and its optical band gap are studied using XRD spectroscopy, FTIR transmission spectroscopy, UV-Vis absorption spectroscopy, TEM, HRTEM, and SAED images. TEM images confirm the formation of nanoparticles embedded on the 2D nanosheet, with particles size ranging from 30 to 35 nm. XRD analysis recommends the formation of t-PdO crystals structure in chemically synthesized PdO-rGO composite. HRTEM and SAED studies, also agree with the XRD regarding formation of t-PdO crystal structure along with amorphous rGO in form of PdO-rGO nanocomposite. The optical band gap of the

nanocomposite is found to be 2.71 eV as computed by UV-Vis absorption spectroscopy and its Tauc plot.

The thin films of PdO-rGO nanocomposite is fabricated on ITO glass substrate using electrophoretic deposition process. These thin films are used as WE in the proposed assembled electrochemical setup for H_2 sensing application. Different concentration (10 to 80%) of H_2 is introduced at 60 ml/min into electrochemical cell containing PdO-rGO nanocomposite thin film as WE and sensing response is measured using amperometry. The response curve shows good sensing response time ranging from 30-60 seconds and fast recovery time. The proposed electrochemical sensor shows high sensitivity of 0.462 $\mu A/\%(H_2)$ at room temperature in ambient atmospheric conditions. Moreover, the sensor is highly selective towards hydrogen gas compared to other environment pollutant gases. Thus, it can be employed for sensing low as well high concentration H_2 gas present in the surroundings. Further, different nano-hierarchal structures of PdO and its composites will be used to enhance sensitivity and selectivity of electrochemical H_2 sensor.

5. Acknowledgements

6. References

[1] G. Korotcenkov, S. D. Han, and J. R. Stetter, "Review of electrochemical hydrogen sensors," *Chemical reviews,* vol. 109, no. 3, pp. 1402-1433, 2009.

[2] J. Song, and W. Curtin, "A nanoscale mechanism of hydrogen embrittlement in metals," *Acta Materialia,* vol. 59, no. 4, pp. 1557-1569, 2011.

[3] T. Hübert, L. Boon-Brett, G. Black *et al.*, "Hydrogen sensors–a review," *Sensors and Actuators B: Chemical,* vol. 157, no. 2, pp. 329-352, 2011.

[4] W. J. Buttner, M. B. Post, R. Burgess *et al.*, "An overview of hydrogen safety sensors and requirements," *International Journal of Hydrogen Energy,* vol. 36, no. 3, pp. 2462-2470, 2011.

[5] X. Lu, S. Wu, L. Wang *et al.*, "Solid-state amperometric hydrogen sensor based on polymer electrolyte membrane fuel cell," *Sensors and Actuators B: Chemical,* vol. 107, no. 2, pp. 812-817, 2005.

[6] J. R. Stetter, and J. Li, "Amperometric gas sensors a review," *Chemical reviews,* vol. 108, no. 2, pp. 352-366, 2008.

[7] C. Huang, C. Li, and G. Shi, "Graphene based catalysts," *Energy & Environmental Science,* vol. 5, no. 10, pp. 8848-8868, 2012.

[8] M. J. Allen, V. C. Tung, and R. B. Kaner, "Honeycomb carbon: a review of graphene," *Chemical reviews,* vol. 110, no. 1, pp. 132-145, 2009.

[9] D. R. Dreyer, S. Park, C. W. Bielawski *et al.*, "The chemistry of graphene oxide," *Chemical Society Reviews,* vol. 39, no. 1, pp. 228-240, 2010.

[10] S. Stankovich, D. A. Dikin, R. D. Piner *et al.*, "Synthesis of graphene-based nanosheets via chemical reduction of exfoliated graphite oxide," *carbon,* vol. 45, no. 7, pp. 1558-1565, 2007.

[11] A. Esfandiar, S. Ghasemi, A. Irajizad *et al.*, "The decoration of TiO_2/reduced graphene oxide by Pd and Pt nanoparticles for hydrogen gas sensing," *International Journal of Hydrogen Energy,* vol. 37, no. 20, pp. 15423-15432, 2012.

[12] P. A. Russo, N. Donato, S. G. Leonardi *et al.*, "Room-Temperature Hydrogen Sensing with Heteronanostructures Based on Reduced Graphene Oxide and Tin Oxide," *Angewandte Chemie International Edition,* vol. 51, no. 44, pp. 11053-11057, 2012.

[13] V. V. e. Rozanov, and O. V. Krylov, "Hydrogen spillover in heterogeneous catalysis," *Russian chemical reviews,* vol. 66, no. 2, pp. 107-119, 1997.

[14] H. L. Tierney, A. E. Baber, J. R. Kitchin *et al.*, "Hydrogen dissociation and spillover on individual isolated palladium atoms," *Physical review letters,* vol. 103, no. 24, pp. 246102, 2009.

[15] P. A. Pandey, N. R. Wilson, and J. Covington, "Pd-doped reduced graphene oxide sensing films for H_2 detection," *Sensors and Actuators B: Chemical,* vol. 183, pp. 478-487, 2013.

[16] U. Lange, T. Hirsch, V. M. Mirsky *et al.*, "Hydrogen sensor based on a graphene–palladium nanocomposite," *Electrochimica Acta,* vol. 56, no. 10, pp. 3707-3712, 2011.

[17] R. Ghosh, S. Santra, S. K. Ray *et al.*, "Pt-functionalized reduced graphene oxide for excellent hydrogen sensing at room temperature," *Applied Physics Letters,* vol. 107, no. 15, pp. 153102, 2015.

[18] K. Arora, D. Sandil, G. Sharma *et al.*, "Effect of low pressure hydrogen environment on crystallographic properties of PdO nanoparticles," *International Journal of Hydrogen Energy,* vol. 41, no. 47, pp. 22155-22161, 2016.

[19] Y.-J. Chiang, K.-C. Li, Y.-C. Lin *et al.*, "A mechanistic study of hydrogen gas sensing by PdO nanoflake thin films at temperatures below 250° C," *Physical Chemistry Chemical Physics,* vol. 17, no. 5, pp. 3039-3049, 2015.

[20] Y. T. Lee, J. M. Lee, Y. J. Kim *et al.*, "Hydrogen gas sensing properties of PdO thin films with nano-sized cracks," *Nanotechnology,* vol. 21, no. 16, pp. 165503, 2010.

[21] S. Choudhury, C. Betty, K. Bhattacharyya *et al.*, "Nanostructured PdO thin film from Langmuir–Blodgett precursor for room-temperature H_2 gas sensing," *ACS applied materials & interfaces,* vol. 8, no. 26, pp. 16997-17003, 2016.

[22] C. Wang, P. Zhao, and S. Liu, "PdO/SnO_2 hollow nanospheres for carbon monoxide

detection," *physica status solidi (a),* vol. 212, no. 8, pp. 1789-1794, 2015.

[23] L. Wang, Z. Lou, R. Wang *et al.*, "Ring-like PdO–NiO with lamellar structure for gas sensor application," *Journal of Materials Chemistry,* vol. 22, no. 25, pp. 12453-12456, 2012.

[24] Y.-J. Chiang, and F.-M. Pan, "PdO nanoflake thin films for CO gas sensing at low temperatures," *The Journal of Physical Chemistry C,* vol. 117, no. 30, pp. 15593-15601, 2013.

[25] Z. Lou, J. Deng, L. Wang *et al.*, "Toluene and ethanol sensing performances of pristine and PdO-decorated flower-like ZnO structures," *Sensors and Actuators B: Chemical,* vol. 176, pp. 323-329, 2013.

[26] I. J. Kim, S. Do Han, I. Singh *et al.*, "Sensitivity enhancement for CO gas detection using a SnO_2–CeO_2–PdO_x system," *Sensors and Actuators B: Chemical,* vol. 107, no. 2, pp. 825-830, 2005.

[27] M. Tong, G. Dai, and D. Gao, "Gas-sensing properties of PdO-modified SnO_2–Fe_2O_3 double-layer thin-film sensor prepared by PECVD technique," *Vacuum,* vol. 59, no. 4, pp. 877-884, 2000.

[28] M. Yuasa, T. Masaki, T. Kida *et al.*, "Nano-sized PdO loaded SnO_2 nanoparticles by reverse micelle method for highly sensitive CO gas sensor," *Sensors and Actuators B: Chemical,* vol. 136, no. 1, pp. 99-104, 2009.

[29] G. Xie, P. Sun, X. Yan *et al.*, "Fabrication of methane gas sensor by layer-by-layer self-assembly of polyaniline/PdO ultra thin films on quartz crystal microbalance," *Sensors and Actuators B: Chemical,* vol. 145, no. 1, pp. 373-377, 2010.

[30] G. De, A. Licciulli, C. Massaro *et al.*, "Sol–gel derived pure and palladium activated tin oxide films for gas-sensing applications," *Sensors and Actuators B: Chemical,* vol. 55, no. 2, pp. 134-139, 1999.

[31] K. Arora, and N. K. Puri, "Electrophoretically deposited nanostructured PdO thin film for room temperature amperometric H_2 sensing," *Vacuum,* vol. 154, pp. 302-308, 2018.

[32] Y. Chao, S. Yao, W. J. Buttner *et al.*, "Amperometric sensor for selective and stable hydrogen measurement," *Sensors and Actuators B: Chemical,* vol. 106, no. 2, pp. 784-790, 2005.

[33] S. Yao, and M. Wang, "Electrochemical sensor for dissolved carbon dioxide measurement," *Journal of the electrochemical society,* vol. 149, no. 1, pp. H28-H32, 2002.

[34] R. S. Jayashree, M. Mitchell, D. Natarajan *et al.*, "Microfluidic hydrogen fuel cell with a liquid electrolyte," *Langmuir,* vol. 23, no. 13, pp. 6871-6874, 2007.

[35] M. C. Buzzeo, C. Hardacre, and R. G. Compton, "Use of room temperature ionic liquids in gas sensor design," *Analytical Chemistry,* vol. 76, no. 15, pp. 4583-4588, 2004.

[36] D. C. Marcano, D. V. Kosynkin, J. M. Berlin *et al.*, "Improved synthesis of graphene oxide," 2010.

[37] S. Park, J. An, J. R. Potts *et al.*, "Hydrazine-reduction of graphite-and graphene oxide," *carbon,* vol. 49, no. 9, pp. 3019-3023, 2011.

[38] B. D. Cullity, and J. W. Weymouth, "Elements of X-ray Diffraction," *American Journal of Physics,* vol. 25, no. 6, pp. 394-395, 1957.

[39] S. Srivastava, V. Kumar, M. A. Ali *et al.*, "Electrophoretically deposited reduced graphene oxide platform for food toxin detection," *Nanoscale,* vol. 5, no. 7, pp. 3043-3051, 2013.

[40] M. E. Uddin, R. K. Layek, N. H. Kim *et al.*, "Preparation and properties of reduced graphene oxide/polyacrylonitrile nanocomposites using polyvinyl phenol," *Composites Part B: Engineering,* vol. 80, pp. 238-245, 2015.

[41] D.-T. Phan, and G.-S. Chung, "P–n junction characteristics of graphene oxide and reduced graphene oxide on n-type Si (111)," *Journal of Physics and Chemistry of Solids,* vol. 74, no. 11, pp. 1509-1514, 2013.

[42] A. K. Das, M. Srivastav, R. K. Layek *et al.*, "Iodide-mediated room temperature reduction of graphene oxide: a rapid chemical route for the synthesis of a bifunctional electrocatalyst," *Journal of Materials Chemistry A,* vol. 2, no. 5, pp. 1332-1340, 2014.

[43] S. Gurunathan, J. W. Han, A. A. Dayem *et al.*, "Oxidative stress-mediated antibacterial activity of graphene oxide and reduced graphene oxide in Pseudomonas aeruginosa," *International journal of nanomedicine,* vol. 7, pp. 5901, 2012.

[44] M. Velasco-Soto, S. Pérez-García, J. Alvarez-Quintana *et al.*, "Selective band gap manipulation of graphene oxide by its reduction with mild reagents," *carbon,* vol. 93, pp. 967-973, 2015.

[45] Y. Shen, S. Yang, P. Zhou *et al.*, "Evolution of the band-gap and optical properties of graphene oxide with controllable reduction level," *carbon,* vol. 62, pp. 157-164, 2013.

[46] T. C. Wen, and C. C. Hu, "Cyclic Voltammetric Investigation of PdO-Coated Titanium Electrode in H_2SO_4," *Journal of The Electrochemical Society,* vol. 140, no. 4, pp. 988-995, 1993.

[47] C. C. Hu, and T. C. Wen, "Voltammetric Investigation of Hydrogen Sorption/Desorption at/within Oxide-Derived Pd Electrodes in NaOH and H_2SO_4," *Journal of The Electrochemical Society,* vol. 141, no. 11, pp. 2996-3001, 1994.

[48] C.-Y. Chiou, and T.-C. Chou, "Amperometric SO_2 gas sensors based on solid polymer electrolytes," *Sensors and Actuators B: Chemical,* vol. 87, no. 1, pp. 1-7, 2002.

[49] A. Hodgson, P. Jacquinot, and P. Hauser, "Electrochemical sensor for the detection of SO_2 in the low-ppb range," *Analytical Chemistry,* vol. 71, no. 14, pp. 2831-2837, 1999.

[50] E. Seo, and D. Sawyer, "Electrochemical oxidation of dissolved sulphur dioxide at platinum and gold electrodes," *Electrochimica Acta,* vol. 10, no. 3, pp. 239-252, 1965.

[51]   G. Belanger, "Determination of sulfur dioxide by anodic oxidation on lead dioxide electrodes," *Analytical Chemistry,* vol. 46, no. 11, pp. 1576-1577, 1974.

[52]   Z. Cao, W. J. Buttner, and J. R. Stetter, "The properties and applications of amperometric gas sensors," *Electroanalysis,* vol. 4, no. 3, pp. 253-266, 1992.

[53]   J. W. Fergus, "A review of electrolyte and electrode materials for high temperature electrochemical CO_2 and SO_2 gas sensors," *Sensors and Actuators B: Chemical,* vol. 134, no. 2, pp. 1034-1041, 2008.

[54]   J. Currie, A. Essalik, and J. Marusic, "Micromachined thin film solid state electrochemical CO_2, NO_2 and SO_2 gas sensors," *Sensors and Actuators B: Chemical,* vol. 59, no. 2-3, pp. 235-241, 1999.

[55]   V. Nikolova, I. Nikolov, P. Andreev *et al.*, "Tungsten carbide-based electrochemical sensors for hydrogen determination in gas mixtures," *Journal of applied electrochemistry,* vol. 30, no. 6, pp. 705-710, 2000.

[56]   K. Okamura, T. Ishiji, M. Iwaki *et al.*, "Electrochemical gas sensor using a novel gas permeable electrode modified by ion implantation," *Surface and Coatings Technology,* vol. 201, no. 19, pp. 8116-8119, 2007.

[57]   Y. C. Liu, B. J. Hwang, and Y. L. Chen, "Nafion Based Hydrogen Sensors: Pt/Nafion Electrodes Prepared by Takenata-Torikai Method and Modified with Polypyrrole," *Electroanalysis,* vol. 14, no. 7-8, pp. 556-558, 2002.

[58]   F. Opekar, "Detection of hydrogen in air with a detector containing a nafion membrane metallized on both sides," *Journal of electroanalytical chemistry and interfacial electrochemistry,* vol. 260, no. 2, pp. 451-455, 1989.

CrossMark
click for updates

Elicitation effect on the production of asiaticoside and asiatic acid in shoot, callus, and cell suspension culture of *Centella asiatica*

M. Laxmi Krishnan, Arpita Roy, Navneeta Bharadvaja[*]
Delhi Technological University, Shahbad Daulatpur, Delhi, India.

ARTICLE INFO	ABSTRACT
	Centella asiatica is an important medicinal plant which contains various phytocompounds. Asiatic acid and asiaticoside are two major compounds which are responsible for its various pharmaceutical activities. The present study analyzes the effect of elicitor, i.e., methyl jasmonate on the synthesis of asiaticoside and asiatic acid (ATA) in shoot, callus, and cell suspension cultures of *C. asiatica*. A high-performance liquid chromatography analysis showed that the elicitation with 100 µM concentration of methyl jasmonate enhanced asiaticoside content by 69-fold in callus culture, 39-fold in shoot cultures, and ATA by 1.9-fold in cell suspension culture. Thus, elicitation with methyl jasmonate is an effective method of increasing the rate of biosynthesis of asiaticoside and ATA in plant cell cultures of *C. asiatica*.

INTRODUCTION

     Centella asiatica is a perennial medicinal plant that belongs to Umbellifere (Apiaceae) family. It is found in tropical and subtropical regions, including India, Sri Lanka, Iran, New Guinea, Australia, Indonesia, and southern and central Africa (Hoang and Nguyen, 2010). This plant usually grows in shady, marshy, damp, and wet places, such as river banks, paddy fields, and higher elevations (Roy and Bharadvaja, 2017a). The flowers are white or light purple to pink in color, sessile arranged in simple umbels, and also bears small oval fruit (Gohil *et al.*, 2010). The form and shape of the plant can differ greatly by the environmental conditions. This plant is listed as threatened species by the International Union for Conservation of Nature and Natural Resources (Pandey *et al.*, 1993). Because of this, the wild population of *C. asiatica* was banned for commercial applications. Its scarcity is as a result of lack of proper cultivation practices and ruthless collection of herbs for medicinal purposes (Karthikeyan *et al.*, 2009). Tissue culture techniques play an important role in clonal multiplication of elite clones as well as conservation of *Centella* germplasm (Roy *et al.*, 2016). Plant tissue culture techniques provide an alternative approach to meet the current market demands of secondary metabolites from *Centella* (Prasad *et al.* 2012).

     Centella asiatica contains several valuable secondary compounds, including asiaticoside, madecassoside, centelloside, centellose, brahminoside, thankunizide, sceffoleoside, brahmoside, asiatic, centellic, brahmic, and madecassic acid. Among these, the important bioactive compounds are asiatic acid (ATA), asiaticoside, madecassoside, and madecassic acid (Roy and Bharadvaja, 2017b, Kundu *et al.*, 2016). Saponin ranges from 1% to 8% of total constituents, based on the plant's origin (Brinkhaus *et al.*, 2000). Asiaticoside is the most abundant triterpenoid saponin present in the leaves. It is used in the treatment of psoriasis, leprosy, and eczema due to its potent anti-inflammatory effects and cell proliferative activity (Bonfill *et al.*, 2011). ATA helps in controlling the cell division in breast cancer, colon cancer, human hepatoma, and cytotoxic activity on fibroblast cells (Kim *et al.*, 2009 , Roy and Bharadvaja, 2017c, Roy *et al.*, 2018). Moreover, ATA is known to revitalize the brain and nervous system and delays aging (Brinkhaus *et al.*, 2000).

     The benefit of plant cell culture is the possibility of manipulating synthesis of desirable compounds within the

---
[*]*Corresponding Author*
Navneeta Bharadvaja, Delhi Technological University, Shahbad Daulatpur, Delhi, India. E-mail: navneetab @ dce.ac.in

cells (James *et al.*, 2008). Elicitors have been found to increase triterpene saponin accumulation in plants and play an important role in signal transduction which regulates all the defense genes in plants (Mangas *et al.*, 2006). Metabolic synthesis in cultured cells can be enhanced by elicitor like methyl jasmonate (MeJA) (Suzuki *et al.*, 2005). Jasmonates are signaling molecules which leads enhanced production of many secondary metabolites, including triterpenoid saponins of the different plants (Memelink *et al.*, 2001). They induce transcriptional activation of genes involved in the formation of secondary metabolites (Yukimune *et al.*, 1996). The present study focuses on effects of MeJA on synthesis of asiaticoside and ATA in shoot culture, callus culture, and cell suspension cultures of *C. asiatica.*

MATERIALS AND METHODS

Establishment of shoot culture

In vitro grown culture of *C. asiatica*, accession number 347492, was collected from National Bureau of Plant Genetic Resources, New Delhi, India. The shoot cultures were grown in Murashige and Skoog (MS) media supplemented with 1 mg/l 6-benzylaminopurine (BAP) (Roy *et al.*, 2016). Nodes were inoculated vertically into culture tubes and incubated at 26°C ± 2°C under 16-hour photoperiod and light intensity of 3,000 lux with 55%–60% relative humidity. Readings and visual data were recorded.

Establishment of callus culture

Leaf explants of *C. asiatica* were excised from basal shoot culture and edges of the leaves and inoculated onto solid MS medium supplemented with 1 mg/l BAP and 1.5 mg/l naphthalene acetic acid (NAA). The culture was incubated at 26°C ± 2°C under 16-hour photoperiod and light intensity of 3,000 lux with 55%–60% relative humidity. Callus growth and visual data were recorded.

Establishment of cell suspension culture and growth curve analysis

To establish cell suspension culture, approximately 2 g of fresh callus was weighed and finely chopped into small pieces and transferred to 250 ml Erlenmeyer flask containing 50 ml of liquid MS medium supplemented with 3% (w/v) of sucrose, 1 mg/l BAP, and 1.5 mg/l NAA. It was kept in a rotary shaker at 100 rpm in dark conditions at 25°C for 45 days. For growth curve analysis, 5-ml sample was retrieved using sterilized pipette at 3-day interval until the 45th day. To measure wet cell weight, cells were filtered through nylon membrane, washed with distilled water, and weighed immediately. Dry cell weight was determined by drying the collected cells in nylon membrane at 50°C until a constant weight was attained.

Elicitation studies

To study the effect of MeJA on shoot multiplication, MS media was supplemented with 1 mg/l BAP along with different concentrations of MeJA, i.e., 50, 100, 150, 200, and 250 μM. Observations were recorded after 6 weeks of culture period. In callus culture, MS media was supplemented with 1 mg/l BAP and 1.5 mg/l NAA along with 100 μM MeJA. The cell suspension culture was supplemented with the same amount of BAP, NAA, and MeJA.

Quantitative estimation of asiaticoside and asiatic acid

Approximately, 0.5 g of air dried shoots grown in MS media with 1 mg/l BAP (control) and air dried callus grown in MS media with 1 mg/l BAP and 1.5 NAA (control) was taken. Samples were crushed to fine powder and dissolved in 5 ml of methanol:water (9:1) solution. Then, samples were sonicated for 10 minutes and after cooling, samples were filtered through polytetrafluoroethylene (PTFE) syringe filter (0.22 μM) and transferred to glass vials. Similar procedure was used for MeJA-elicited shoot and callus extracts.

For preparing cell suspension culture samples, control cultures were transferred into sterile tubes and centrifuged at 1,500 g for 15 minutes. Approximately, 0.5 g of cells was added in 5 ml of methanol:water (9:1 ratio). After sonication, samples were centrifuged at 1,500 g for 10 minutes, and supernatant was filtered through PTFE syringe filter (0.22 μM). Same procedures were followed for MeJA-treated suspension culture. Samples were stored at −20°C for further analysis. About 1 mg each of asiaticoside standard (Sigma Aldrich) and ATA standard (Sigma Aldrich) was dissolved in 1 ml of methanol:water (9:1) solution. For calibration, standards of asiaticoside and ATA were prepared at different concentrations, i.e., 1, 0.5, and 0.1 mg/ml. For HPLC analysis, C18 column was used, mobile phase was a mixture of methanol and water (70:30) for asiaticoside and (80:20) for ATA. Twenty microliters solution was injected into the column, with a flow rate of 0.5 ml/minute at 26°C. The absorbance was read at 214 nm wavelength.

Statistical analysis

In vitro experiments were performed in triplicates and HPLC analysis of samples was performed in duplicates. The data analysis was performed using one-way analysis of variance using Microsoft Excel 2007. Results were shown in mean ± standard error (M ± SE) with $p \leq 0.05$ and $F_{stat} > F_{critical\ value}$ considered as statistically significant.

RESULTS AND DISCUSSION

Shoot, callus, and cell suspension culture

Shoot cultures grown in different concentration of MeJA (50, 100, 150, 200, and 250 μM) resulted in decreased shoot proliferation compared to control (untreated) one (MS + 1 mg/l BAP) after 6 weeks of incubation (Table 1). The highest shoot multiplication was observed in control one with a shoot number of 31 ± 1 (Fig. 1a). Among the elicitor-treated cultures, shoot cultures supplemented with 1 mg/l BAP + 100 μM MeJA had the highest shoot number of 24 ± 1 (Fig. 1b).

Callus induction from leaf explants of *C. asiatica* in MS media supplemented with 1 mg/l BAP and 1.5 mg/l NAA was observed (Fig. 1c). After 6 weeks of incubation, callus was green colored and compact. However, after 10 weeks of incubation, it turned brown colored. Callus culture treated with 100 μM MeJA resulted in poor callus induction and turned yellow.

For establishment of cell suspension culture, MS liquid media supplemented with 1 mg/l BAP and 1.5 mg/l NAA was

Table 1. Effect of MeJA concentrations on growth of *Centella asiatica* (accession number 347492) supplemented with 1 mg/l 6-benzylaminopurine (BAP), and different concentrations of MeJA (50, 100, 150, 200, and 250 μM). Shoot number and shoot length were recorded after 6 weeks of culture period. Analysis was done in triplicate.

S. no.	Media composition	Shoot number (M ± SE)	Shoot length (cm) (M ± SE)
1	1 mg/l BAP + 50 μM MeJA	13.33 ± 1.52	2 ± 0.2
2	1 mg/l BAP + 100 μM MeJA	24 ± 1	3.4 ± 0.1
3	1 mg/l BAP + 150 μM MeJA	18.66 ± 0.57	2.46 ± 0.35
4	1 mg/l BAP + 200 μM MeJA	16.6 ± 1.52	2.33 ± 0.3
5	1 mg/l BAP + 250 μM MeJA	11 ± 1	1.6 ± 0.2
6	1 mg/l BAP (control)	31 ± 1	3.8 ± 0.25

Figure 1. Shoot culture of Centella asiatica grown in MS media supplemented with (a) 1 mg/l BAP (control) (b) 1 mg/l BAP with 100 μM MeJA (elicited) after 6 weeks of culture period (c) Callus culture treated with 1 mg/l BAP + 1.5 mg/l NAA + 100 μM MeJA after 6 weeks of culture period and (d) Cell suspension culture treated with 1 mg/l BAP + 1.5 mg/l NAA+100 μM MeJA after 6 weeks of culture period.

used. The results after 6 weeks of incubation is shown in Figure 1d. Growth curve was determined using dry weight (Fig. 2a) and wet weight analysis (Fig. 2b) for both control and MeJA-elicited cell suspension culture for 45 days.

In the present study, MeJA has an overall negative effect on shoot proliferation of *C. asiatica* this might be because MeJA disrupts the cortical microtubules of the plants which lead to growth inhibition, induction of leaf senescence, and promotion of ethylene production (Saniewski *et al.*, 1987). Previous studies reported that increase concentration of MeJA inhibits growth of the whole plant and cell culture (Kim *et al.*, 2004; Mangas *et al.*, 2006). Bonfill *et al.* (2006) reported that *Centella* plantlet treated with MeJA showed reduction in growth with over 50% in fresh weight (aerial parts) and also showed symptoms of leaves necrosis at the end of culture period. Although treatment with MeJA resulted to growth inhibition, it was able to increase the
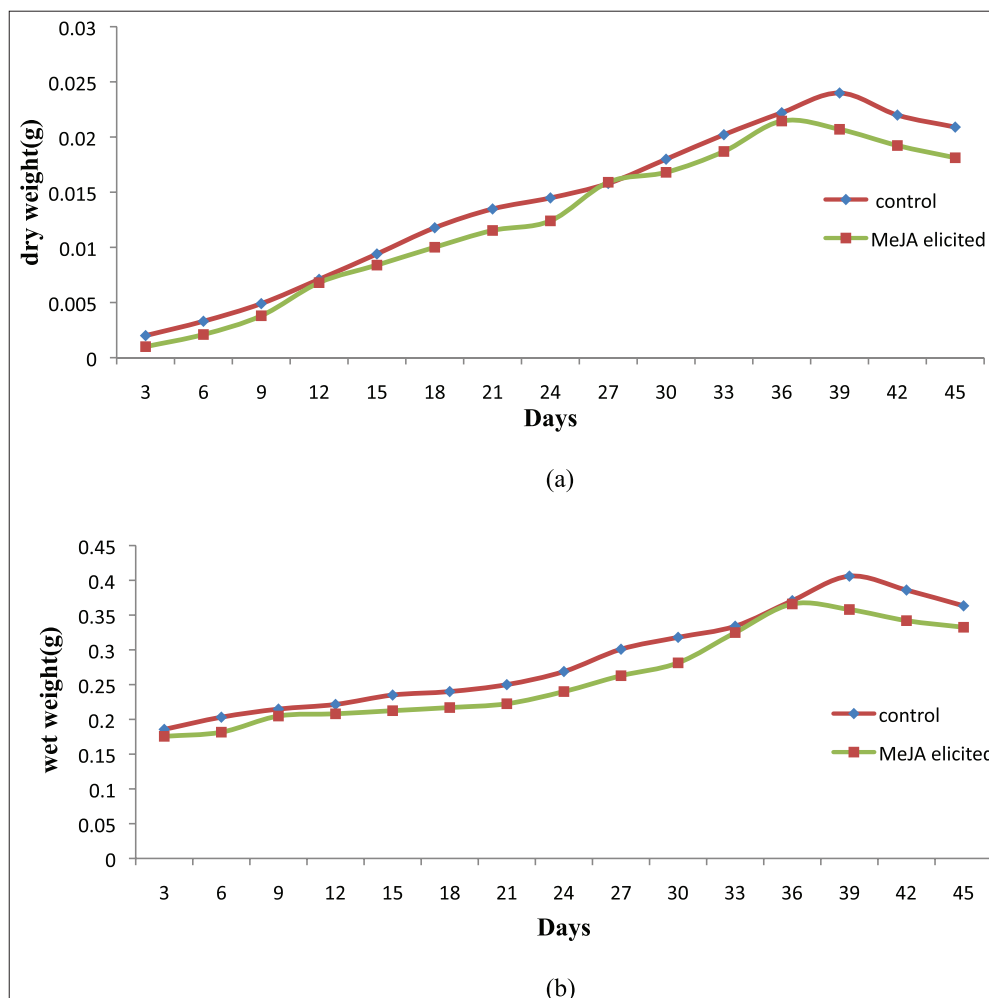
Figure 2. Growth curve of (a) dry weight and (b) wet weight for both control and MeJA-elicited cell suspension cultures treated with 1 mg/l BAP + 1.5 mg/l NAA + 100 μM MeJA up to 45 days. Suspension cultures (treated and untreated) were separated from cells using centrifugation, and wet weight and dry weight were determined and plotted against number of days.

secondary metabolites in *in vitro* cultures (Kim *et al.*, 2004) as same happened in our study.

In case of callus culture, change in color of callus may be due to the secretion of phenolic compounds in explant or explant tissues (Dan *et al.*, 2000). Previous studies reported that MS medium supplemented with 1 mg/l BAP and 1 mg/l NAA resulted in strong callus induction from petiole explants of *Centella* (Hoang and Nguyen, 2010). MeJA completely ceased the callus growth of *Taxus media var. Hatfieldii* (Furmanowa *et al.*, 1997) and callus cultures of *R. cordifolia* in a dose-dependent manner (Bulgakov *et al.*, 2002).

For cell suspension culture, a usual type of lag and stationary phase were not observed in the growth curve of both control and MeJA elicited cells. Exponential phase of the cells in the control culture lasted for 39 days and reached death phase by day 42, whereas exponential phase for MeJA elicited cells lasted for 36 days and reached death phase by day 40. Growth curve for MeJA-elicited and control cells were almost similar to each other but exponential phase of elicited cells was shorter than

control cells. The growth curve of control and MeJA-elicited cell suspension culture lacks a typical lag phase, and the stationary phase may be due to their shorter duration (Hoang and Nguyen, 2010). The control cells reached death phase by 42 days may be due to the nutrient depletion in the culture media (Bonfill *et al.*, 2011). Previous studies reported that viability of cells reduced by more than half of initial population of *C. asiatica* suspension cells at the end of the culture period when elicited with 100 μM MeJA (Bonfill *et al.*, 2011).

Quantitative estimation of asiaticoside and asiatic acid by HPLC

The approximate retention time for standard asiaticoside (ASD) was 8.9 minutes (Fig. 3a). It was observed that after treatment with 100 μM MeJA, there was a significant increase in asiaticoside content by 39-fold in shoot culture and about 69-fold in callus extracts (Table 2).

However, the asiaticoside content in cell suspension culture was reduced with MeJA addition. The asiaticoside content
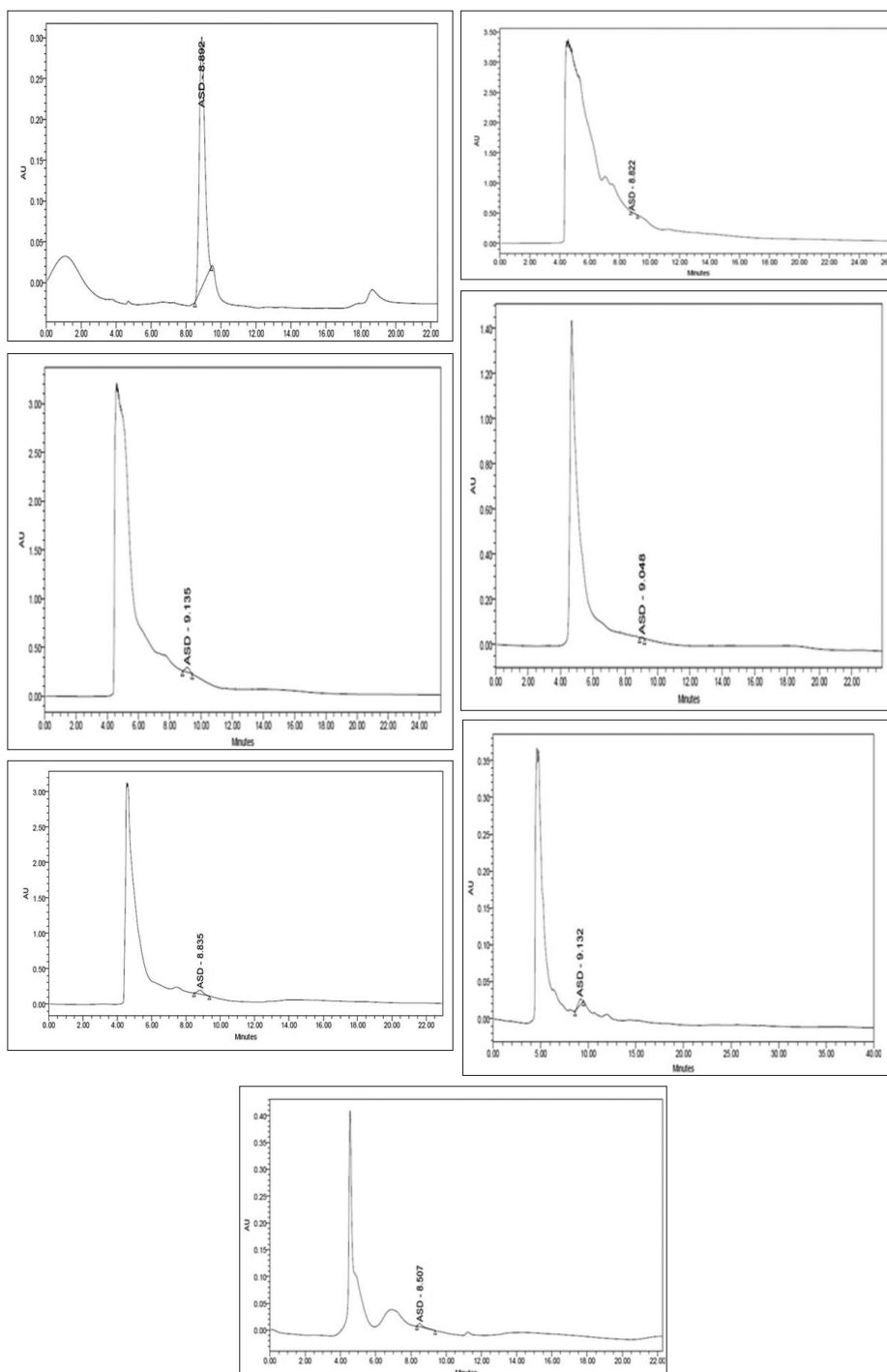
Figure 3. Chromatogram of (a) 1 mg/ml ASD standard (b) control shoot culture (MS +1 mg/l BAP) (c) elicitor treated shoot cultures (1 mg/l BAP + 100μM MeJA) (d) control callus cultures (1 mg/l BAP + 1.5 mg/l NAA) (e) elicitor elicited callus cultures (1 mg/l BAP + 1.5 mg/l NAA + 100 μM MeJA) (f) control cell suspension culture (1 mg/l BAP + 1.5 mg/l NAA) (g) elicited treated cell suspension culture (1 mg/l BAP + 1.5 mg/l NAA+100 μM MeJA).

in cell suspension culture was reduced after MeJA elicitation. Chromatogram of asiaticoside content before and after elicitation in shoot culture, callus culture and cell suspension culture are shown in Figure 3b–g. In *C. asiatica,* βAS (β-amyrin synthase), an important enzyme in the biosynthesis of triterpene saponins gets activated when elicited with MeJA, thereby boosting up the production of asiaticoside in shoot and callus culture (Kim *et al.*, 2005). Previous studies indicated that the highest expression of cycloartenol synthase) mRNA transcript in leaves of *C. asiatica* regulates phytosterol synthesis and gets decreased upon addition of MeJA to the medium (Kim *et al.*, 2005). This explains that MeJA inhibits the formation of phytosterol and promotes the asiaticoside

Table 2. Asiaticoside estimation in different cultures of *Centella asiatica* treated with 1 mg/l BAP + 100 μM MeJA in case of shoot culture and 1 mg/l BAP + 1.5 mg/l NAA + 100 μM MeJA in case of callus and cell suspension culture. In control cultures MeJA was not present.

| Plant cultures	Asiaticoside concentration in control (untreated) culture (mg/ml) (M ± SE)	Asiaticoside concentration in elicitated culture (treated) (mg/ml) (M ± SE)
Shoot culture	0.0036 ± 0.0001	0.1434 ± 0.004
Callus culture	0.0028 ± 0.0001	0.2004 ± 0.0023
Cell suspension culture	0.0323 ± 0.001	0.016 ± 0.0001
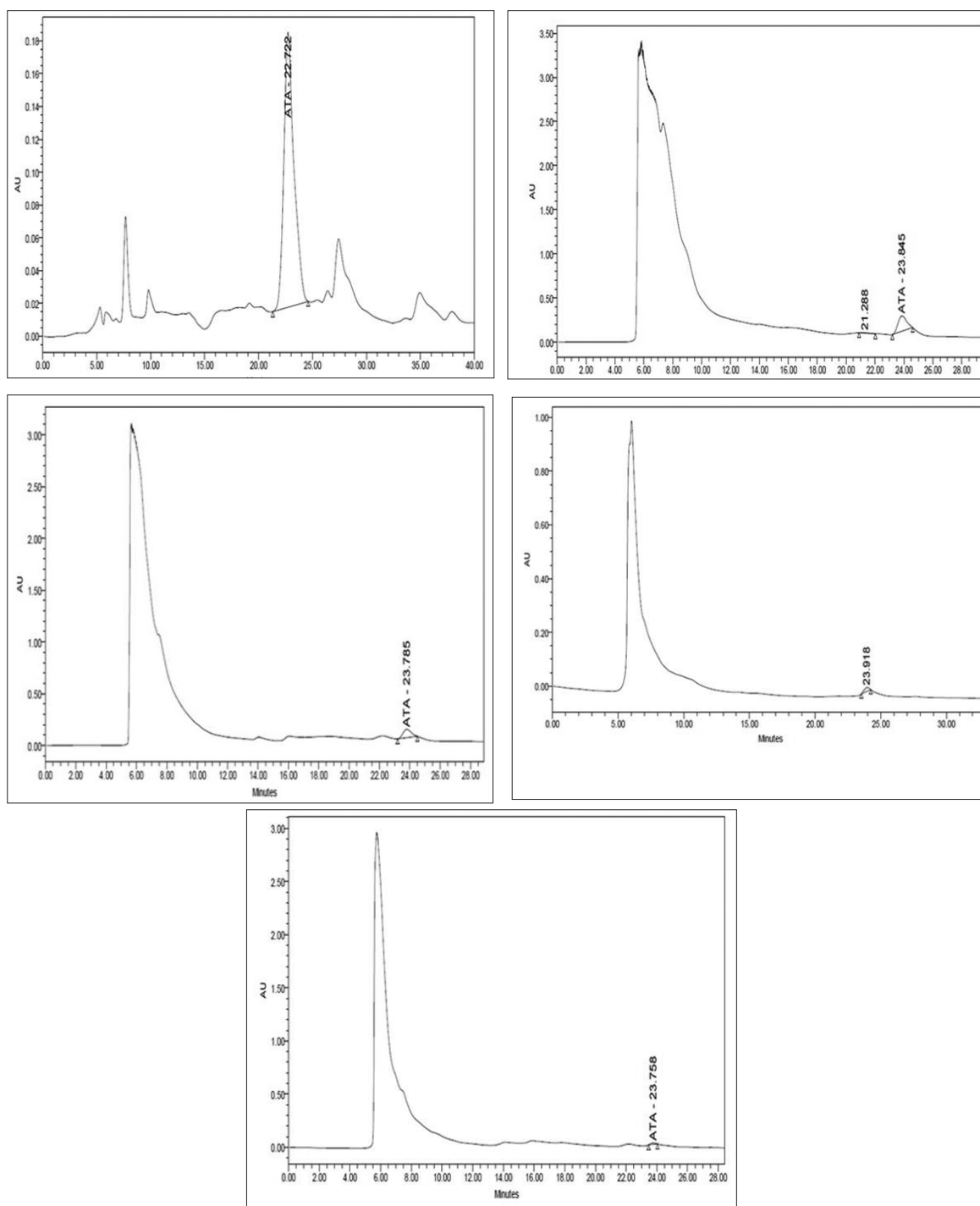
Figure 4. Chromatogram of (a) 1 mg/ml ATA standard (b) control shoot culture (MS + 1 mg/l BAP) (c) elicitor treated shoot cultures (1 mg/l BAP + 100 μM MeJA) (d) control callus cultures (1 mg/l BAP + 1.5 mg/l NAA) (e) elicitor elicited callus cultures (1 mg/l BAP + 1.5 mg/l NAA + 100 μM MeJA) (f) control cell suspension culture (1 mg/l BAP + 1.5 mg/l NAA) (g) elicited treated cell suspension culture (1 mg/l BAP + 1.5 mg/l NAA + 100 μM MeJA).

Table 3. ATA estimation in different cultures of *Centella asiatica* treated with 1 mg/l BAP + 100 µM MeJA in case of shoot culture, and 1 mg/l BAP + 1.5 mg/l NAA + 100 µM MeJA in case of callus and cell suspension culture. In control cultures MeJA was not present. There was no evidence of presence of ATA in both the treated and untreated cell suspension culture.

Plant cultures	ATA concentration in control (untreated) culture (mg/ml) (M ± SE)	ATA concentration in elicitated culture (treated) (mg/ml) (M ± SE)
Shoot culture	0.634 ± 0.026[*]	0.2681 ±0.010[*]
Callus culture	0.0339 ± 0.001[*]	0.0656 ± 0.0026[*]
Cell suspension culture	0	0

[*] Statistically significant at $P \leq 0.05$ and $F_{stat} >$ Fcritical value

pathway in shoot and callus cultures. Previous studies had shown that 0.1 mM MeJA is sufficient to upregulate the levels of squalene synthase mRNA and βAS mRNA, and thus enhance the triterpene saponin content in *C. asiatica* (Mangas *et al.*, 2006). Asiaticoside was reduced in cell suspension culture after MeJA treatment, maybe because the effect of MeJA is dependent on factors like elicitor's specificity, concentration, duration of treatment, and growth phase of the culture. Previous studies reported that asiaticoside synthesis in *Centella* is highly tissue-specific or organ specific, occurring mainly in the leaves cultured with 100 µM MeJA elicitor (Kim *et al.*, 2004). In certain cases, the metabolic flux of specific metabolic pathways gets manipulated in response to elicitors and signal molecules of plant defense responses (James *et al.*, 2008). Previous studies reported that callus and cell suspension of *Centella* from Indian origin synthesized asiaticoside (Nath and Buragohain, 2005). So far, biotechnological attempts to over produce asiaticoside through cell or tissue culture have encountered limited success (Kim *et al.*, 2002).

The retention time for standard ATA was found to be approximately at 22.6 minutes (Fig. 4a). Treatment with 100 µM MeJA resulted to 1.9-fold increase in ATA in callus extract, whereas in shoot extract ATA was reduced after elicitation (Table 3). ATA was found absent in both control and elicited culture of cell suspension culture. Chromatogram of ATA content before and after elicitation in shoot and callus culture are shown in Figure 4b–e. ATA was not detected in cell suspension culture even after the treatment with MeJA, because plant secondary metabolites are synthesized by specialized cells at particular stage of its development and certain compounds are not synthesized if cells remain undifferentiated as in cell suspension culture (Kim *et al.*, 2002). Another important factor for regulation of secondary metabolic processes is the distribution between mRNA transcripts, enzymes, and biosynthetic products within and between cells (James *et al.*, 2008). The callus is undifferentiated tissue which has the ability to develop into any plant organ such as root, shoot, or leaf under correct hormone concentrations and this might be the reason for presence of all the triterpenoids in callus and not in cell suspension culture (James *et al.*, 2008). Previous studies showed that four triterpenoid, asiaticoside, ATA, madecassic acid, and madecassoside were found in the undifferentiated cultures cells, with higher concentrations in calli as compared to the cell suspensions of *C. asiatica* belonging to two different phenotypes from South Africa (James *et al.*, 2008). Another problem is the instability of cell cultures for continued production of secondary products as some cell lines loss their ability to synthesize desired compound after prolonged culture (James *et al.*, 2008). Comparative estimation of asiaticoside and ATA are shown in Tables 2 and 3 for shoot, callus, and cell suspension culture, respectively. The highest asiaticoside content was found in MeJA-elicited callus culture, whereas the highest ATA content was found in the control shoot culture.

CONCLUSION

The present study showed that elicitation of MS media with methyl jasmonate caused growth inhibition in shoot, callus, and cell suspension culture of *C. asiatica.* However, biosynthesis of asiaticoside in shoot and callus cultures was enhanced and ATA in case of callus culture. Therefore, this method offers great potential for the enhancement of valuable secondary metabolites, and at the same time, it ensures a sustainable conservation of endangered medicinal plant.

ACKNOWLEDGMENTS

CONFLICT OF INTEREST

The authors have declared that they have no conflict of interest.

REFERENCES

Bonfill M, Mangas S, Cusidó RM, Osuna L, Piñol MT, Palazón J. Identification of triterpenoid compounds of *Centella asiatica* by thin-layer chromatography and mass spectrometry. Biomed Chromatogr, 2006; 20:151–3.

Bonfill M, Mangas S, Moyano E, Cusido RM, Palazon J. Production of centellosides and phytosterols in cell suspension cultures of *Centella asiatica*. Plant Cell Tissue Organ Cult, 2011; 104:61–7.

Brinkhaus B, Lindner M, Schuppan D, Hahn EG. Chemical, pharmacological and clinical profile of the East Asian medical plant *Centella asiatica*. Phytomedicine, 2000; 7:427–48.

Bulgakov VP, Tchernoded GK, Mischenko NP, Khodakovskaya MV, Glazunov VP, Radchenko SV, Zvereva EV, Fedoreyev SA, Zhuravlev YN. Effect of salicylic acid, methyl jasmonate, ethephon and cantharidin on anthraquinone production by *Rubia cordifolia* callus cultures transformed with the rolB and rolC genes. J Biotechnol, 2002; 97:213–21.

Dan Y, Armstrong CL, Dong J, Feng X, Fry JE, Keithly GE, Martinell BJ, Roberts GA, Smith LA, Tan LJ, Duncan DR. *Lipoic acid- an unique plant transformation enhancer. In Vitro Cell Dev Biol Plant, 2000; 45:630–8.*

Furmanowa M, Glowniak K, Syklowska-Baranek K, Zgórka G, Józefczyk A. Effect of picloram and methyl jasmonate on growth and taxane accumulation in callus culture of *Taxus* media var. *Hatfieldii.* Plant Cell Tissue Organ Cult, *1997;* 49:75–9.

Gohil KJ, Patel JA, Gajjar AK. Pharmacological review on *Centella asiatica*: a potential herbal cure-all. Indian J Pharm Sci, 2010; 72:546–56.

Hoang N, Nguyen LT. Asiaticoside production from *Centella* (*Centella asiatica* L. Urban) cell Culture. Biotechnol Bioprocess Eng, 2010; 15:1065–70.

James JT, Meyer R, Dubery IA. Characterization of two phenotypes of *Centella asiatica* in Southern Africa through the consumption of four triterpenoids in callus, cell suspension and leaves. Plant Cell Tissue Organ Cult, 2008; 94:91–9.

Karthikeyan K, Chandran C, Kulathungan S. Rapid clonal multiplication through in vitro axillary shoot proliferation of *Centella asiatica*. Indian J Biotechnol, 2009; 8:232–5.

Kim OT, Kim MY, Hong MH, Ahn JC, Hwang B. Stimulation of asiaticoside accumulation in the whole plant cultures of *Centella asiatica* Linn. urban by elicitors. Plant Cell Rep, 2004; 23:339–44.

Kim OT, Min-Young Kim MY, Hwang SJ, Ahn JC, Hwang B. Cloning and molecular analysis of cDNA encoding cycloartenol synthase from *Centella asiatica* (L.) urban. Biotechnol Bioprocess Eng, 2005; 10:16–22.

Kim WJ, Kim J, Veriansyah B, Kim JD, Lee YW, Oh SG, Tjandrawinata R. Extraction of bioactive components from *Centella asiatica* using subcritical water. J Supercrit Fluids, 2009; 48:211–6.

Kim Y, Wyslouzil BE, Weathers PJ. Secondary metabolism of hairy root cultures in bioreactors. In Vitro Cell Dev Biol Plant, 2002; 38:1–10.

Kundu K, Roy A, Saxena G, Kumar L, Bharadvaja B. Effect of different carbon sources and elicitors on shoot multiplication in accessions of Centella asiatica. Med Aromat Plants, 2016; 5:251.

Mangas S, Bonfill M, Osuna L, Moyano E, Tortoriello J, Cusido RM, Piñol MT, Palazón J. The effect of methyl jasmonate on triterpene and sterol metabolisms of *Centella asiatica, Ruscus aculeatus* and *Galphimia glauca* cultured plants. Phytochemistry, 2006; 67:2041–9.

Memelink J, Verpoorte R, Kijne JW. ORC anization of jasmonate-responsive gene expression in alkaloid metabolism. Trends Plant Sci, 2001; 6:212–9.

Nath S, Buragohain AK. Establishment of callus and cell suspension cultures of *Centella asiatica*. Biol Plant, 2005; 49:411–3.

Pandey NK, Tewari KC, Tewari RN, Joshi GC, Pande VN, Pandey G. 1993. Medicinal plants of Kumaon Himalaya. In: Dhar U, ed. Strategies for conservation of Himalayas. India: Himavikas Publication 293–302.

Prasad A, Mathur A, Singh M, Gupta M, Uniyal G, Lal RK, Mathur AK. Growth and asiaticoside production in multiple shoot cultures of a medicinal herb, *Centella asiatica* (L.) Urban, under the influence of nutrient manipulations. J Nat Med, 2012; 66:383–7.

Roy A**,** Bharadvaja N. *Centella asiatica*: a pharmaceutically important medicinal plant. Curr Trends Biomed Eng Biosci, 2017a; 5:555661.

Roy A, Bharadvaja N. Effect of different culture medias on shoot multiplication and stigmasterol content in accessions of Centella asiatica. Int J Ayurvedic Herb Med, 2017b; 7:2643–50.

Roy A, Bharadvaja N. Medicinal plants in the management of cancer: a review. J Int J Complement Alt Med, 2017c; 9:009291.

Roy A*,* Kundu K, Saxena G, Kumar L, Bharadvaja N. Effect of different media and growth hormones on shoot multiplication of in vitro grown *Centella asiatica* accession. Adv Tech Biol Med, 2016; 4:172.

Roy A, Jauhari N, Bharadvaja N. Medicinal plants as a potential source of chemopreventive agents. Anticancer plants: natural products and biotechnological implements. Springer, Singapore, pp. 109–39, 2018.

Saniewski M, Nowacki J, Czapski J. The effect of methyl jasmonate on ethylene production and ethylene forming enzyme activity in tomatoes. J Plant Physiol, 1987; 129:199–203.

Suzuki H, Reddy MS, Naoumkina M, Aziz N, May GD, Huhman DV, Sumner LW, Blount JW, Mendes P, Dixon RA. Methyl jasmonate and yeast elicitor induce differential transcriptional and metabolic re-programming in cell suspension cultures of the model legume *Medicago truncatula*. Planta, 2005; 220:696–707.

Yukimune Y, Tabata H, Higashi Y, Hara Y. Methyl jasmonate-induced overproduction of paclitaxel and baccatin III in *Taxus* cell suspension cultures. Nat Biotechnol, 1996; 14:1129–32.

emerald insight

Benchmarking: An International Journal

Evaluation of supply chain coordination index in context to Industry 4.0 environment

Rajesh Kumar Singh, Pravin Kumar, Mahesh Chand,

Article information:

For Authors

If you would like to write for this, or any other Emerald publication, then please use our Emerald for Authors service information about how to choose which publication to write for and submission guidelines are available for all. Please visit www.emeraldinsight.com/authors for more information.

About Emerald www.emeraldinsight.com

Emerald is a global publisher linking research and practice to the benefit of society. The company manages a portfolio of more than 290 journals and over 2,350 books and book series volumes, as well as providing an extensive range of online products and additional customer resources and services.

Emerald is both COUNTER 4 and TRANSFER compliant. The organization is a partner of the Committee on Publication Ethics (COPE) and also works with Portico and the LOCKSS initiative for digital archive preservation.

Evaluation of supply chain coordination index in context to Industry 4.0 environment

Rajesh Kumar Singh
Management Development Institute Gurgaon, Gurugram, India
Pravin Kumar
*Department of Mechanical Engineering,
Delhi Technological University, Delhi, India, and*
Mahesh Chand
*Department of Mechanical Engineering,
YMCA University of Science & Technology, Faridabad, India*

Abstract

Purpose – Today, most of the manufacturing systems are changing very fast in terms of the adoption of new technologies. New technologies being implemented are Internet of Things, cyber physical systems, cloud computing, Big Data analytics and information and communication technologies. Most of the organizations in the value chain are implementing these technologies at the individual level rather than across the whole supply chain. It makes the supply chain less coordinated and causes suboptimal utilization of resources. For efficient and optimal use of modern technologies, supply chains should be highly coordinated. The purpose of this paper is to illustrate an approach for determining the index to quantify coordination in the supply chain.
Design/methodology/approach – From the literature review, total 32 factors have been identified. These factors are further clubbed into six clusters for evaluation of the coordination index. The graph theoretic approach has been used for evaluating the coordination index of a supply chain of an Indian organization.
Findings – This study has illustrated a comprehensive approach to quantify coordination of a supply chains for effective benchmarking of the supply chain performance in the Industry 4.0 era. Presently, it is observed that top management is giving more focus on organizational issues such as lean organization structure, organization culture and responsiveness factors for improving coordination in the supply chain rather than on Industry 4.0 technologies.
Originality/value – This framework can also be used for comparison, ranking and analysis of coordination issues in different supply chains in the era of Industry 4.0. Organizations can use this approach for benchmarking purpose also to improve different supply chain processes for meeting dynamic market requirements.
Keywords Benchmarking, Coordination, Supply chain management, Industry 4.0,
Intelligent manufacturing, Graph theoretic approach
Paper type Research paper

1. Introduction

In the present context of a globalized market, manufacturing organizations are designing their operations based on changing customer needs (Gunasekaran, 2005). Organizations are trying to fulfill the continuously changing market requirements in terms of reducing lead time, variety of products, flexible manufacturing systems, etc. (Stock and Seliger, 2016). Internet of Things (IOTs), 3D printing, data analytics, artificial intelligence and cloud computing (Almada-Lobo, 2016) are some of the modern technologies implemented by managers in different manufacturing processes to become competitive. Supply chain management (SCM) definition has been transformed in comparison to traditional SCM definition (Tjahjono *et al.*, 2017) due to the use of these new technologies. In 2011, Hanover Messe introduced the concept of "Industry 4.0." Industry 4.0 can be defined as the "smart manufacturing" or "integrated industry." According to

Hofmann and Rüsch (2017), Industry 4.0 has potential to change the whole business in terms of product designing, manufacturing and delivery. Industry 4.0 helps in creating efficient production systems. Wang *et al.* (2016) observed that production systems can make quick decisions and monitor physical processes in the era of Industry 4.0 through real-time transmissions with humans, machines and sensors. It may also be termed as "Intelligent manufacturing." According to Kaushik (1990), the purpose of intelligent manufacturing is to optimize the resources by using advanced information and manufacturing technologies. In intelligent manufacturing, processes related to design, production and product life cycle management are continuously upgraded. Adaptive decision-making models, advanced materials, intelligent devices, smart sensors and data analytics are used to manage the product life cycle (Li *et al.*, 2017). It further improves performance and service levels (Davis *et al.*, 2012). Therefore, Industry 4.0 comprises highly developed automation and digitization of processes. Major requirements for Industry 4.0 to be interoperable are accessibility, multilingualism, security, privacy, subsidiarity, the use of open standards, open source software and multilateral solutions (Hermann *et al.*, 2016). Industry 4.0 makes factories more intelligent, flexible and dynamic by equipping manufacturing with sensors, actors and autonomous systems.

According to Van Hoek and Chapman, (2007), supply chains have become highly unpredictable due to increased product variety and shortening product life cycle. Zhang *et al.* (2016) observed that in the supply chain, the elimination of non-value-added activities and coordination are essential for bringing agility. Coordination in the supply chain means integration of all processes to ensure sharing of information, managing relationship, technology transfer and application of latest technologies such as IOTs, Industry 4.0 and cloud computing for the efficient management of supply chain operations. To assess the effectiveness of coordination in the supply chain, quality of product, innovation and customer satisfaction are major factors. Main factors involved in achieving coordination among members of the supply chain are human and resource development; applications of modern technologies and IT tools; development of effective strategies; sharing of profits and risks.

Most researchers have focused on the importance of coordination in a traditional supply chain but very limited research is available for developing the index to evaluate the effectiveness of coordination in context to supply chain in the era of Industry 4.0. Mainly researchers have used popular models such as Balance Score card, SCOR model, etc., for performance evaluation. The authors are of the opinion that performance can be improved only after ensuring coordination in the supply chain in the Industry 4.0 environment. These models can be further improved by making them more inclusive in terms of modern supply chains in the Industry 4.0 era. Most of the supply chains are not only struggling to ensure coordination in the Industry 4.0 environment but are also unable to measure it effectively. Therefore, the objectives of this study are:

- to identify major factors for coordination in supply chains; and

- to develop a framework for evaluating coordination effectiveness in Industry 4.0-based supply chains.

The remaining part of the paper is organized as follows: Section 2 studies the literature review for coordination factors; Section 3 explains different steps of graph theoretic approach with a case illustration and Section 4 talks about conclusion.

2. Literature review
In the era of Industry 4.0, supply chains are more technology based. Major technologies being used in different functions of supply chains are IOTs, Big Data analytics, cloud computing, artificial intelligence, machine learning, etc. Automation of different processes across the supply chain is essential for survival in the new business environment. It is very important to

have coordination among the members of the value chain for the integration of different supply chain functions (Soroor *et al.,* 2009). Manufacturing flexibility is the most important factor for being competitive (Singh and Sharma, 2014). For improving manufacturing flexibility, the coordinated supply chain is very crucial. Supply chain members need to be coordinated by efficiently managing dependencies between each other (Arshinder *et al.,* 2009). In a coordinated supply chain, the emphasis has been given to supplier–buyer relationship (Jain *et al.,* 2009). According to Lee (2000), the supply chain integration is due to organizational relationship, logistics coordination and information sharing. According to Melnyk *et al.* (2009), the supply chain is changing from tactical to strategic nature. Future supply chain will be more complex and demanding. Hsu *et al.* (2009) analyzed that the practices of SCM mediate the relationship between operations capability and firm performance.

The factors of coordination in the supply chain are analyzed based on the literature review and are grouped further into six clusters. These are discussed in the following section.

2.1 C1: top management commitment
The important variable for successful supply chain strategies is the top management commitment (Sun *et al.,* 2009; Skipworth *et al.,* 2015). Top management commitment helps organizations to go for the major decisions like investment of time and money for resources development (Shin *et al.,* 2000). It also helps in long-term goal for investment (Arshinder *et al.,* 2006), adoption of new technology (Arshinder *et al.,* 2006), better-focused communication system and employee training and empowerment (Simatupang *et al.,* 2002). In changing the business environment, the role of top management commitment has been emphasized as effective SCM (Sandberg and Abrahamsson, 2010). Singh *et al.* (2004) also observed in context to Indian SMEs that the top management support is essential for implementing new initiatives.

2.2 C2: organizational factors
Under dynamic market conditions, organizations are trying to make themselves more proactive for changes. Singh *et al.* (2004) observed that in many organizations, the parts are delivered by suppliers several times a day to the assembly lines directly without maintaining any big inventory. Lead time for replenishment and for customers is continuously decreasing. Organizational factors such as lean organization structure (Grittell and Weiss, 2004), JIT and lean practices (Arshinder *et al.,* 2006), organization culture for supply chain implementation and integration within the organization departments (Grittell and Weiss, 2004) are important for better coordination of the supply chain.

2.3 C3: mutual understanding
To ensure effective revenue and risk sharing among partners of the supply chain, mutual understanding is essential (Singh, 2013). Chopra and Meindle (2003) observed that trust is a favorable attitude for supply chain members to have confidence on each other. Conflicts of interest may occur when the existing revenue sharing system promotes for individual interest in place of whole supply chain interest (Cachon and Lariviere, 2005). Bianchi and Saleh (2010) observed that in developing countries, trust and commitment are essential for enhancing the performance of the supply chain. Arshinder *et al.* (2007) observed that the members of the supply chain need to have common goals and objectives for global optimization.

2.4 C4: flow of information
Embedded production system technologies with intelligent manufacturing processes are combined through Industry 4.0. It has potential to transform traditional supply chains into advanced IT-enabled supply chain. Manufacturing systems need to be continuously

upgraded in the context of Industry 4.0 environment. Intelligent manufacturing may make organizations smart, flexible and capable to meet dynamic market requirements (Shen and Norrie, 1999). Wan *et al.* (2017) observed that Industry 4.0 technologies can make organization agile and responsive.

Pyke *et al.* (2000) emphasized on information and knowledge sharing in the supply chain. The availability of real-time sales data is important for effective inventory management (Michelino *et al.*, 2008). The inventory cost at every stage of the supply chain is reduced by managing inventory efficiently (Marek and Malyszek, 2008). Stanley *et al.*, (2009) observed that responsiveness gets improved through information sharing among the supply chain members. Sharing of different operational issues such as inventory, market demand and product performance in the market are related to information sharing.

2.5 C5: relationship and decision making
Long-term relationship and collaborative decision making among the members of the supply chain are essential for streamlining the supply chain functions in the era of Industry 4.0. It also increases the mutual trust between the supply chain members and flow of information (Mehrjerdi, 2009). The store-level retailer's replenishment problem was analyzed and the collaborative replenishment mechanism model was proposed by Lyu *et al.* (2010). In supply chains, the important factors for relationship and decision-making are logistic synchronization (Simatupang *et al.*, 2002), rationalization of suppliers (Jain *et al.*, 2009) and supply chain integration (Arshinder *et al.*, 2006).

2.6 C6: responsiveness
According to Kim *et al.*, (2006), the responsiveness of a supply chain means how quickly it is able to react to market requirements. Moller (2006) observed that collaborative efforts of supply chain partners improve supply chain responsiveness. Agility in operations is an important factor for a responsive supply chain (Li *et al.*, 2008). Flexibility in the production system (Koh *et al.*, 2007), delivery on time (Mehrjerdi, 2009), service reliability (Konijnendijk, 1994) and ability to adopt process change (Li *et al.*, 2008) are major ingredients of the responsive supply chain. Differences in the goals and objectives among supply chain members lead to the local optimization of the whole supply chain (Arshinder *et al.*, 2007). Michelino *et al.* (2008) observed that the availability of point of sales data is important for improving the responsiveness of the supply chain. Delivery in time, cost reduction and accurate forecasting of data are ensured by the responsive supply chain (Mehrjerdi, 2009). Coordination in the supply chain helps in cost reduction (Hult *et al.*, 2002), improved product quality (Handfield, 1994) and better process design (Tan, 2002). Product and process design impacts the responsiveness of the supply chain (Khan *et al.*, 2012).

Based on the literature review, total 32 sub-factors have been identified and further grouped into six clusters. These are summarized in Table I.

3. Research methodology
Based on the literature review, 32 factors impacting coordination in the supply chains are identified. For validating the inclusion of these factors, in addition to the literature review, the opinion of experts was also considered. Based on the focused group discussion, these factors were categorized into six categories. To quantify coordination in the supply chain, the graph theoretic approach is used. Detailed steps are described in the following section.

3.1 Graph theoretic (digraph) approach
Diagraph representation, the matrix representation and the permanent function representation are the parts of the graph theoretical approach. Different factors with their

S. No.	Factors of coordination in supply chain	References
1	Top management commitment (C1)	
	(a) Investment of time and money for recourses development	Shin et al. (2000), Kumar et al. (2014), Skipworth et al. (2015), Kumar and Singh (2017)
	(b) Focused communication system	Kim and Narsimhan (2002), Stank et al.(1999)
	(c) Long-term investment motive	Arshinder et al. (2006), Skipworth et al. (2015)
	(d) Commitment to promises	Singh et al. (2010)
	(e) Ready to adopt new technology	Arshinder et al. (2006), Stanley et al. (2009), Zhang et al. (2016), Kumar and Singh (2017)
	(f) Employees training and empowerment	Simatupang et al. (2002)
2	Organizational factors (C2)	
	(a) Lean organization structure	Grittell and Weiss (2004), Zhang et al. (2016)
	(b) JIT and lean practices	Arshinder et al. (2006), Grittell and Weiss (2004)
	(c) Organization behavior for supply chain implementation	Arshinder et al. (2006), Grittell and Weiss (2004), Kumar and Singh (2017)
	(d) Organization culture for supply chain Implementation	Arshinder et al. (2006), Grittell and Weiss (2004)
	(e) Role in the supply chain with respect to other members	Freathy and O'Connell (1998)
	(f) Integration of departments within the organization	Grittell and Weiss (2004), Kumar et al. (2013), Kumar and Singh (2017)
3	Mutual understanding (C3)	
	(a) Agreed vision and goals of the members of the supply chain	Arshinder et al. (2006), Simatupang et al. (2002)
	(b) Trust development in supply chain members	Arshinder et al. (2006), Sahay (2003), Bianchi and Saleh, (2010), Zhang et al. (2016)
	(c) Effective implementation of joint replenishment and forecasting decisions	Arshinder et al. (2006)
	(d) Supply chain risk/reward sharing	Cachon and Lariviere (2005), Lee (2000), Kumar and Singh (2017)
4	Flow of information (C4)	
	(a) Usage of information technology (IT) tools and techniques	Simatugang and Sridharan (2002), Leeand Lee (2010)
	(b) Information sharing/exchange	Arshinder et al. (2009), Kumar and Singh (2017), Ozer(2003), Stanley et al. (2009)
	(c) Inventory tracking at supply chain linkage	Mentzer et al. (2001)
	(d) Data sharing related to purchasing and supplies	Simatugang and Sridharan (2002)
	(e) Knowledge sharing	Pyke et al. (2000), Simatupang et al. (2002)
	(f) Design data sharing	Kumar et al. (2017)
5	Relationship and decision making (C5)	
	(a) Long-term relationship with suppliers	Jain et al. (2009), Olorunniwo and Hartfield (2001)
	(b) Long-term relationship with customers	Jain et al. (2009), Olorunniwo and Hartfield (2001), Agrawal et al. (2016a, b)
	(c) Collaborative decision making/planning with supply chain members	Tsay (1999), Cachon and Fisher (2000), Disney and Towill (2003), Lyu et al. (2010)
	(d) Logistics synchronization	Simatugang and Sridharan (2002), Simatupang et al. (2002)
	(e) Supply chain integration	Arshinder et al. (2006), Lee (2000), Villa (2002), Chan et al. (2004)
	(f) Rationalization of suppliers	Jain et al. (2009)
6	Responsiveness (C6)	
	(a) Flexibility in the production system	Koh et al. (2007), Arshinder et al. (2006), Kumar et al. (2017), Singh (2015)
	(b) Delivery on time	Lee and Lee (2010), Mehrjerdi, (2009)
	(c) Service reliability	Konjnendijk (1994), Kumar and Singh (2017)
	(d) Ability to adopt process change	Li et al. (2008)

Table I.
Factors for
coordination in the
supply chain

mutual relationships are visually represented in the digraph. Index is determined by the permanent function of the matrix. Grover *et al.* (2004) used this approach in the area of total quality management. Agrawal *et al.* (2016a, b) used this approach for outsourcing decisions in reverse logistics. This approach was used in an automotive organization to evaluate the agility index (Kumar *et al.*, 2017).

The level of coordination in terms of a single numerical index (per C^*) can be evaluated using the graph theoretic approach which is given as below:

$$\text{Coordination index} = \text{per } C^* = f \text{ (main factors and their sub} - \text{factors)}.$$

The coordination index for the supply chain of an organization is found using the methodology presented in this paper. By comparing the coordination index for different supply chains, we can find weak links for further improvement. It is a versatile methodology, which can be used to find the supply chain coordination index in the era of Industry 4.0. The effect of factors and their interdependencies are taken into consideration in this analysis. The proposed methodology involves various steps which are:

(1) different factors for coordination in the supply chain are identified;

(2) categorize these factors into six clusters;

(3) a digraph among the clusters is developed depending on their mutual interactions (as shown in Figure 1);

(4) determine the interaction of different factors;

(5) develop a variable permanent matrix (VPM) at the system level based on the digraph developed in Step 3; and

(6) find the variable permanent function (VPF) using Equation (9).

For the absolute measure of factors, a scale from 1 to 9 has been used (1 – exceptionally low, 2 – very low, 9 – exceptionally high.). For the relative measure of interdependencies of factors, a scale from 1 to 5 is used (1 – very weak, 5 – very strong).

Above mentioned steps are applied to calculate the coordination index for a supply chain of an organization in the following section.

3.1.1 Cluster digraph. In the supply chain, digraph for clusters is prepared to represent coordination dynamics in terms of nodes and edges. Clusters/factors are represented by
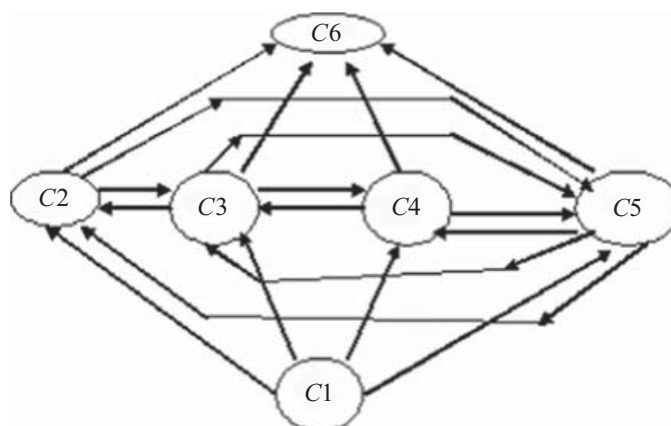

Figure 1.
Digraph for clusters of enablers for coordination in the supply chain

Note: $C1$ – top management commitment, $C2$ – organizational factors, $C3$ – mutual understanding, $C4$ – flow of information, $C5$ – relationship and decision making, $C6$ – responsiveness

nodes, whereas their mutual interactions are represented by edges. C_i indicates the absolute importance of factors and c_{ij} indicates the relative importance of jth factor on ith factor based on mutual interaction. A directed edge from node i to node j is represented by c_{ij} in the digraph. The proposed clusters of factors and their interactions are shown by the digraph. Top management commitment ($C1$), organizational factors ($C2$), mutual understanding ($C3$), flow of information ($C4$), relationship and decision making ($C5$) and responsiveness ($C6$) are identified as clusters and interactions amongst them are shown in the form of diagraph (Figure 1). A team of five experts was formed having more than 10 years of experience in the area of SCM. These had three experts from industry and two from academia.

3.1.2 Clusters matrix (Em). An expression for factor's effect is established by representing the digraph in the matrix form. In general case, if n factors are leading to nth order symmetric (0, 1) then matrix $A = [C_{ij}]$. The value of C_{ij} represents the interaction of ith factor with that of the jth factor:

$$C_{ij} = 1 \text{ if factor } i \text{ is linked to factor } j; = 0 \text{ otherwise.}$$

Generally, C_{ij}, the factor's effect is directional and if $C_{ii} = 0$ then factors are not interacting with itself. For coordination in the supply chain, six clusters of factors have been made (Figure 1) in this study. The digraph represented by factor's matrix as shown in Figure 1 is written as:

$$A = \begin{array}{c} \\ \\ \\ \\ \\ \\ \end{array} \begin{pmatrix} 0 & 1 & 1 & 1 & 1 & 1 \\ 0 & 0 & 1 & 1 & 1 & 1 \\ 0 & 1 & 0 & 1 & 1 & 1 \\ 0 & 1 & 1 & 0 & 1 & 1 \\ 0 & 1 & 1 & 1 & 0 & 1 \\ 0 & 0 & 0 & 0 & 0 & 0 \end{pmatrix}_{6 \times 6} \begin{array}{c} 1 \\ 2 \\ 3 \\ 4 \\ 5 \\ 6 \end{array} \qquad (1)$$

The interdependency of enablers is represented by the off-diagonal elements having value 0 or 1. In factor's matrix, if the effect of factors is not taken into consideration then the diagonal elements are 0. For this another matrix named factor's characteristic matrix is defined by B.

3.1.3 Clusters characteristic matrix. The characteristic matrix which is used in mathematics is also used to characterize factors affecting coordination in the supply chain. Enablers characteristic matrix is written as $B = [CI-A]$, where I is an identity matrix; C is a variable representing enabler and A is the same as in Equation (1):

$$I = \begin{array}{c} \\ \\ \\ \\ \\ \\ \end{array} \begin{pmatrix} 1 & 0 & 0 & 0 & 0 & 0 \\ 0 & 1 & 0 & 0 & 0 & 0 \\ 0 & 0 & 1 & 0 & 0 & 0 \\ 0 & 0 & 0 & 1 & 0 & 0 \\ 0 & 0 & 0 & 0 & 1 & 0 \\ 0 & 0 & 0 & 0 & 0 & 1 \end{pmatrix}_{6 \times 6} \begin{array}{c} 1 \\ 2 \\ 3 \\ 4 \\ 5 \\ 6 \end{array} \qquad (2)$$

$$
CI = \begin{array}{c} \\ \\ \\ \\ \\ \\ \\ \end{array}
\begin{pmatrix}
\overset{1}{C} & \overset{2}{0} & \overset{3}{0} & \overset{4}{0} & \overset{5}{0} & \overset{6}{0} \\
0 & C & 0 & 0 & 0 & 0 \\
0 & 0 & C & 0 & 0 & 0 \\
0 & 0 & 0 & C & 0 & 0 \\
0 & 0 & 0 & 0 & C & 0 \\
0 & 0 & 0 & 0 & 0 & C
\end{pmatrix}
\begin{array}{c} 1 \\ 2 \\ 3 \\ 4 \\ 5 \\ 6 \end{array}
\quad (3)
$$

$$
B = [CI - A] =
\begin{pmatrix}
\overset{1}{C} & \overset{2}{-1} & \overset{3}{-1} & \overset{4}{-1} & \overset{5}{-1} & \overset{6}{-1} \\
0 & C & -1 & -1 & -1 & -1 \\
0 & -1 & C & -1 & -1 & -1 \\
0 & -1 & -1 & C & -1 & -1 \\
0 & -1 & -1 & -1 & C & -1 \\
0 & 0 & 0 & 0 & 0 & C
\end{pmatrix}
\begin{array}{c} 1 \\ 2 \\ 3 \\ 4 \\ 5 \\ 6 \end{array}
\quad (4)
$$

The value of all diagonal elements in the above matrix is the same which means that all the factors have been assigned the same value. This is practically not true as all factors have different values (effects) based on various parameters affecting them. Depending on mutual relationship the values have been assigned to interdependencies. Variable characteristic matrix (VCM), i.e. R, is considered to see the effect of factors and their interdependencies.

3.1.4 Variable characteristic matrix. The VCM is used for various factors and their effects to characterize the coordination in the supply chain. For this, a digraph (Figure 1) is considered to define the factors' VCM. A matrix D is considered having off-diagonal elements C_{ij} which shows interactions between factors, i.e. instead of 1 (as in matrix 1). Another matrix E is considered with diagonal elements C_i, $i = 1, 2, \ldots, 6$, where C_i represents the effect of various factors, i.e. instead of C only (as in matrix 3).

The factors' VCM is written as R = [E−D] by considering matrices D and E:

$$
D =
\begin{pmatrix}
\overset{1}{0} & \overset{2}{C12} & \overset{3}{C13} & \overset{4}{C14} & \overset{5}{C15} & \overset{6}{C16} \\
0 & 0 & C23 & C24 & C25 & C26 \\
0 & C32 & 0 & C34 & C35 & C36 \\
0 & C42 & C43 & 0 & C45 & C46 \\
0 & C52 & C53 & C54 & 0 & C56 \\
0 & 0 & 0 & 0 & 0 & 0
\end{pmatrix}
\begin{array}{c} 1 \\ 2 \\ 3 \\ 4 \\ 5 \\ 6 \end{array}
\quad (5)
$$

$$
E = \begin{matrix} & 1 & 2 & 3 & 4 & 5 & 6 & \\ & \begin{pmatrix} C1 & 0 & 0 & 0 & 0 & 0 \\ 0 & C2 & 0 & 0 & 0 & 0 \\ 0 & 0 & C3 & 0 & 0 & 0 \\ 0 & 0 & 0 & C4 & 0 & 0 \\ 0 & 0 & 0 & 0 & C5 & 0 \\ 0 & 0 & 0 & 0 & 0 & C6 \end{pmatrix} & \begin{matrix} 1 \\ 2 \\ 3 \\ 4 \\ 5 \\ 6 \end{matrix} \\ & & 6\times6 \end{matrix}
\tag{6}
$$

$$
R = [E - D] = \begin{matrix} & 1 & 2 & 3 & 4 & 5 & 6 & \\ & \begin{pmatrix} C1 & -C12 & -C13 & -C14 & -C15 & -C16 \\ 0 & C2 & -C23 & -C24 & -C25 & -C26 \\ 0 & -C32 & C3 & -C34 & -C35 & -C36 \\ 0 & -C42 & -C43 & C4 & -C45 & -C46 \\ 0 & -C52 & -C53 & -C54 & C5 & -C56 \\ 0 & 0 & 0 & 0 & 0 & C6 \end{pmatrix} & \begin{matrix} 1 \\ 2 \\ 3 \\ 4 \\ 5 \\ 6 \end{matrix} \\ & & 6\times6 \end{matrix}
\tag{7}
$$

Some of the coefficients of the determinant for matrix Equation (7) possess positive and negative signs. Hence, complete information on factors' effect will not be obtained as some will be lost due to the addition and subtraction of the numerical values of diagonal and off-diagonal elements (i.e. C_i and C_{ij}). The complete information about factor's effect is not given by the determinant of matrix Equation (7). Hence, another matrix is introduced named VPM.

  3.1.5 Variable permanent matrix. Of all the factors if the value of the individual effect is maximum then the overall factors' effect is also maximum. In the VCM as the total quantitative information is not obtained, so the VPM in general is defined for the system considering interactions among all factors as:

$$
C^* = [E + D] = \begin{matrix} & 1 & 2 & 3 & 4 & 5 & 6 & \\ & \begin{pmatrix} C1 & C12 & C13 & C14 & C15 & C16 \\ 0 & C2 & C23 & C24 & C25 & C26 \\ 0 & C32 & C3 & C34 & C35 & C36 \\ 0 & C42 & C43 & C4 & C45 & C46 \\ 0 & C52 & C53 & C54 & C5 & C56 \\ 0 & 0 & 0 & 0 & 0 & C6 \end{pmatrix} & \begin{matrix} 1 \\ 2 \\ 3 \\ 4 \\ 5 \\ 6 \end{matrix} \\ & & 6\times6 \end{matrix}
\tag{8}
$$

E and D have the same meaning as described in matrix Equations (5) and (6), respectively. VPF which is also called permanent of C (per C) is the permanent of matrix Equation (8) which is multinomial. This is calculated by standard procedures same as that of the

determinant of factors' VCM but with all positive signs. In a general form, the permanent for matrix Equation (8) is written as:

$$
\begin{aligned}
\mathrm{VPM} = \mathrm{VPF} = \mathrm{per}\, C* = {}& \prod_{i=1} C_i + \sum_i \sum_j \sum_k \sum_l \sum_m \sum_n (C_{ij}C_{ji})C_k C_l C_m C_n \\
& + \sum_i \sum_j \sum_k \sum_l \sum_m \sum_n (C_{ij}C_{jk}C_{ki} + C_{ik}C_{kj}C_{ji})C_l C_m C_n \\
& + \left[\sum_i \sum_j \sum_k \sum_l \sum_m \sum_n (C_{ij}C_{ji})(C_{kl}C_{lk})C_m C_n. \right. \\
& + \sum_i \sum_j \sum_k \sum_l \sum_m \sum_n (C_{ij}C_{jk}C_{kl}C_{li} + C_{il}C_{lk}C_{kj}C_{ji})C_m C_n)] \\
& + \left[\sum_i \sum_j \sum_k \sum_l \sum_m \sum_n (C_{ij}C_{ji})(C_{kl}C_{lm}C_{mk} + C_{km}C_{ml}C_{lk})C_n. \right. \\
& + \sum_i \sum_j \sum_k \sum_l \sum_m \sum_n (C_{ij}C_{ji}C_{kl}C_{lm}C_{mi} + C_{im}C_{ml}C_{lk}C_{ki}C_{ji})C_n] \\
& + \sum_i \sum_j \sum_k \sum_l \sum_m \sum_n (C_{ij}C_{ji}C_{kl}C_{lm}C_{mi} + C_{im}C_{ml}C_{lk}C_{ki}C_{ji})C_n] \\
& + \sum_i \sum_j \sum_k \sum_l \sum_m \sum_n (C_{ij}C_{ji})(C_{kl}C_{lm}C_{mn}C_{nk} + C_{kn}C_{nm}C_{ml}C_{lk}) \\
& + \sum_i \sum_j \sum_k \sum_l \sum_m \sum_n (C_{ij}C_{jk}C_{ki})(C_{lm}C_{mn}C_{nl}) \\
& + \sum_i \sum_j \sum_k \sum_l \sum_m \sum_n (C_{ij}C_{ji})(C_{lk}C_{kl})(C_{mn}C_{nm}) \\
& \sum_i \sum_j \sum_k \sum_l \sum_m \sum_n (C_{ij}C_{ji}C_{kl}C_{lm}C_{mi} + C_{im}C_{ml}C_{lk}C_{ki}C_{ji})].
\end{aligned}
\tag{9}
$$

The above defined permanent function which is Equation (9) expresses the factors' effect due to the presence of all attributes and their interdependencies. A close look at multinomial, i.e. Equation (9), reveals the presence of factors' effect in a systematic manner. The terms in this expression are arranged in $n + 1$ grouping. Seven grouping are there as $n = 6$.

   3.1.6 Case illustration. The organization chosen for this case study is ABC Ltd (name changed), the member of automotive component manufacturers association of India. It was established in 1989. It is ISO9001 certified organization. It has an annual turnover of Rs 110m US$. It manufactures a variety of auto components and electric switches for two wheelers and four wheelers like combination switch, horns, etc. The supply chain of the organization consists of customers such as Hero Honda, Maruti Udyog Ltd, General Motors, TVS, Honda Motors Cycles and Scooter, etc., and different vendors, distributors and organization itself.

   The organization was facing problems from the last few years due to poor coordination among the members of the supply chain. Major problems faced by this organization are increasing inventory cost, lack of information flow, not able to deliver all products on time. So there was a need of study coordination issues of its supply chain. The authors made three visits to discuss supply chain coordination issues with management. The sample of study

includes supply chain managers, top management members, marketing and vendor development managers. To select the true representative sample of population, the professionals were selected from all levels of management. The sample was drawn from the managers, who were directly and indirectly involved in coordination with other members of the supply chain. For survey two well-structured, a multi-choice questionnaire was sent to professionals of the organization. Major clusters and sub-factors are shown in Figure 1. The first questionnaire was designed for collecting response on the importance of six main clusters ($C1$–$C6$). The second questionnaire was prepared for finding the influence of clusters on each other, i.e. C12 means the influence of top management commitment ($C1$) on organizational factors ($C2$); similarly, C23 means the influence of organizational factors ($C2$) on mutual understanding ($C3$).

From the questionnaire-based study, we will get the values of the following variables as used in Equation (8), i.e. VPM:

$$C1, \ C12, \ C13, \ C14, \ C15, \ C16, \ C2, \ C23, \ C24, \ C25, \ C26, \ C32, \ C3, \ C34,$$

$$C35, \ C36 \ C42, \ C43, \ C4, \ C45, \ C46, \ C52, \ C53, \ C54, \ C5, \ C56, \ C6.$$

We considered a team of five experts from the top- and mid-level management of this organization for taking the response on different dimensions of coordination. Values of the above variables coming from the response given by senior- and mid-level managers of the organization are given as follows:

$C1 = 4.5$,	$C12 = 3$,	$C13 = 3$,	$C14 = 4$,	$C15 = 3$,	$C16 = 4$
$C2 = 4.5$,	$C23 = 3$,	$C24 = 4$,	$C25 = 3$,	$C26 = 4$
$C32 = 3$,	$C3 = 4.5$,	$C34 = 2$,	$C35 = 3$,	$C36 = 4$
$C42 = 5$,	$C43 = 5$,	$C4 = 2.06$,	$C45 = 5$,	$C46 = 5$
$C52 = 3$,	$C53 = 3$,	$C54 = 3$,	$C5 = 3.02$,	$C56 = 3$
$C6 = 4.5$

Putting these values in Equation (9) for solution and find the value of per C^*. It is found as given below:

$$\text{Per } C^* = 70{,}236.$$

This is the index for coordination in the supply chain of the company ABC Pvt Ltd. It is observed that presently for improving coordination in the supply chain, top management ($C1$) is giving more focus on organizational factors ($C2$) such as lean organization structure, organization culture and responsiveness factors ($C6$). Flow of information ($C4$), relationship and decision making ($C5$) are weak areas. In the era of Industry 4.0, no organization can sustain without technology upgradation and smooth flow of information in the supply chain. Therefore, management needs to apply different technologies of Industry 4.0 such as artificial intelligence, cloud computing, Big Data analytics and machine learning for smooth integration of manufacturing systems. Top management needs to support for these initiatives by making investments and skilling the workforce for these emerging technologies. The organization also needs to develop the holistic strategy for operations, marketing, HR and business intelligence for successful coordination in the present Industry 4.0 environment.

Lu (2017) also analyzed similar kind of operational challenges in implementing Industry 4.0 technologies such as IoTs, cyber physical systems (CPS), ICT and enterprise

architecture. The study also observed that some countries have taken policy decisions to implement Industry 4.0 in an aggressive manner across all organizations. China has launched China Manufacturing 2025 (CM2025), which is on the track of Industry 4.0. We can compare this index for coordination of the supply chain with other organizations equipped with Industry 4.0 technologies for benchmarking purpose. The comparison will help the organization to compare different coordination groups, based on which weak link in the coordination of the supply chain could be analyzed and improved.

4. Conclusion

In the Industry 4.0 environment, supply chain coordination is essential for sustaining in the globalized market. To improve coordination in the supply chain, its evaluation and comparison with best in the industry are essential. This study has tried to suggest a framework for measuring the coordination index of a supply chain in the current business scenario. Total 32 factors for evaluating coordination in supply chains are identified. These are further grouped into six categories. The graph theoretic approach has been used in this study. For effective benchmarking, it is considered as a powerful tool to evaluate the degree of coordination in the supply chain. Factors and their interdependencies are visually represented by a digraph. The factors' matrix converts the digraph into mathematical form. The coordination index is determined by the mathematical model named factor's permanent function.

It is observed that presently for improving coordination in the supply chain, top management is giving more focus on organizational factors such as lean organization structure, organization culture and responsiveness factors. Flow of information, relationship and decision making are weak areas. Therefore, this organization needs to work on information flow and relationship building in the supply chain. Especially in the era of Industry 4.0, flow of information and upgradation of technological infrastructure are very important. Findings will motivate other organizations to adopt different Industry 4.0 technologies such as IoTs, AI, CPS and ICTs for improving coordination in supply chains.

Although the approach suggested in this study will be highly useful for benchmarking purpose, it has got some limitations. A major limitation is that the value of the coordination index may be influenced by the biased approach of experts in decision making. The proposed coordination framework of the study also needs to be validated on the basis of empirical studies before generalization. This study can be further extended for analyzing other issues of the supply chain such as flexibility, agility, overall performance, etc., and for comparing different sector's performance.

References

Agrawal, S., Singh, R.K. and Murtaza, Q. (2016a), "Outsourcing decisions in reverse logistics: sustainable balanced scorecard and graph theoretic approach", *Resources, Conservation and Recycling*, Vol. 108, pp. 41-53.

Agrawal, S., Singh, R.K. and Murtaza, Q. (2016b), "Disposition decisions in reverse logistics: graph theory and matrix approach", *Journal of Cleaner Production*, Vol. 137, pp. 93-104.

Almada-Lobo, F. (2016), "The Industry 4.0 revolution and the future of manufacturing execution systems (MES)", *Journal of Innovation Management*, Vol. 3 No. 4, pp. 16-21.

Arshinder, Kanda, A. and Deshmukh, S.G. (2006), "Supply chain coordination issues: an SAP-LAP framework", *Asia pacific Journal of Marketing and Logistics*, Vol. 19 No. 3, pp. 240-264.

Arshinder, Kanda, A. and Deshmukh, S.G. (2007), "Supply chain coordination issues: an SAP-LAP frame work", *Asia Pacific Journal of Marketing and Logistics*, Vol. 19 No. 3, pp. 240-264.

Arshinder, Kanda, A. and Deshmukh, S.G. (2009), "A framework for evaluation of coordination by contracts: a case of two-level supply chains", *Computers and Industrial Engineering an International Journal*, Vol. 56, pp. 1177-1191.

Bianchi, C. and Saleh, A. (2010), "On importer trust and commitment: a comparative study of two developing countries", *International Marketing Review*, Vol. 27 No. 1, pp. 55-86.

Cachon, G.P. and Fisher, M. (2000), "Supply chain inventory management and the value of shared information", *Management Science*, Vol. 46 No. 8, pp. 1032-1048.

Cachon, G.P. and Lariviere, M.A. (2005), "Supply chain coordination with revenue sharing contracts: strengths and limitations", *Management Science*, Vol. 51 No. 1, pp. 30-44.

Chopra, S. and Meindle, P. (2003), *Supply Chain Management: Strategic, Planning and Operation*, Pearson Education, Delhi.

Davis, J., Edgar, T., Porter, J., Bernaden, J. and Sarli, M. (2012), "Smart manufacturing, manufacturing intelligence and demand-dynamic performance", *Computers & Chemical Engineering*, Vol. 47, pp. 145-156.

Disney, S.M. and Towill, D.R. (2003), "Vendor-managed inventory and bullwhip reduction in a two-level supply chain", *International Journal of Operations & Production Management*, Vol. 23 No. 6, pp. 625-651.

Freathy, P. and O'Connell, F. (1998), "The role of the buying function in airport retailing", *International Journal of Retail & Distribution Management*, Vol. 26 No. 6, pp. 247-256.

Grittell, J.H. and Weiss, L. (2004), "Coordination networks within and across organizations: a multi-level framework", *Journal of Management Studies*, Vol. 41 No. 1, pp. 127-153.

Grover, S., Agarwal, V.P. and Khan, I.A. (2004), "A digraph approach to TQM evaluation of an industry", *International Journal of Production Research*, Vol. 42 No. 19, pp. 4031-4053.

Gunasekaran, A. (2005), "The build-to-order supply chain (BOSC): a competitive strategy for the 21st century", *Journal of Operations Management*, Vol. 23 No. 5, pp. 419-422.

Handfield, R. (1994), "US global sourcing: patterns of development", *International Journal of Operations and Production Management*, Vol. 14 No. 6, pp. 40-51.

Hermann, M., Pentek, T. and Otto, B. (2016), "Design principles for Industry 4.0 scenarios", *49th Hawaii International Conference on System Sciences, IEEE*, pp. 3928-3937.

Hofmann, E. and Rüsch, M. (2017), "Industry 4.0 and the current status as well as future prospects on logistics", *Computers in Industry*, Vol. 89, pp. 23-34.

Hsu, C.C., Tan, K.C., Kannan, V.R. and Leong, K.G. (2009), "Supply chain management practices as a mediator of the relationship between operations capability and firm performance", *International Journal of Production Research*, Vol. 47, pp. 835-855.

Hult, G.T.M., Ketchen, D. and Nichols, E. (2002), "An examination of cultural competitiveness and order fulfilment cycle time within supply chains", *Academy of Management Journal*, Vol. 45 No. 3, pp. 577-586.

Jain, V., Wadhwa, S. and Deshmukh, S.G. (2009), "Select supplier-related issues in modelling a dynamic supply chain: potential, challenges and direction for future research", *International Journal of Production Research*, Vol. 47 No. 11, pp. 3013-3039.

Kaushik, A. (1990), *Intelligent Manufacturing Systems*, Prentice Hall Press, Old Tappan, NJ.

Khan, O., Christopher, M. and Creazza, A. (2012), "Aligning product design with the supply chain: a case study", *Supply Chain Management: An International Journal*, Vol. 17 No. 3, pp. 323-336.

Kim, D., Cavusgil, S.T. and Calantone, R.J. (2006), "Information system innovations and supply chain management: channel relationships and firm performance", *Journal of Academy of Marketing Science"*, Vol. 34 No. 1, pp. 40-54.

Kim, S.W. and Narsimhan, R. (2002), "Information system utilization in supply chain integration efforts", *International Journal of Production Research*, Vol. 40 No. 18, pp. 4585-4609, available at: www.tandfonline.com/toc/tprs20/40/18; www.tandfonline.com/toc/tprs20/current

Koh, L.S.C., Mehmet, D., Erkan, B., Ekrem, T. and Selim, Z. (2007), "The impact of supply chain management practices on performance of SMEs", *Industrial Management & Data Systems*, Vol. 107 No. 1, pp. 103-124.

Konijnendijk, P.A. (1994), "Coordinating marketing and manufacturing in ETO companies", *International Journal of Production Economics*, Vol. 37 No. 1, pp. 19-26.

Kumar, P., Singh, R.K. and Kumar, R. (2017), "An integrated framework of interpretive structural modeling and graph theory matrix approach to fix the agility index of an automobile manufacturing organization", *International Journal of Systems Assurance Engineering and Management*, Vol. 8 No. 1, pp. 342-352.

Kumar, R. and Singh, R.K. (2017), "Coordination and responsiveness issues in SMEs supply chains: a review", *Benchmarking: An International Journal*, Vol. 24 No. 3, pp. 635-650.

Kumar, R., Singh, R.K. and Shankar, R. (2013), "Study on coordination issues for flexibility in supply chain of SMEs: a case study", *Global Journal of Flexible Systems Management*, Vol. 14 No. 2, pp. 81-92.

Kumar, R., Singh, R.K. and Shankar, R. (2014), "Strategy development by Indian SMEs for improving coordination in supply chain: an empirical study", *Competitiveness Review: An International Business Journal*, Vol. 24 No. 5, pp. 414-432.

Lee, H. and Lee, D. (2010), "Coordination contracts in the presence of positive inventory financing costs", *International Journal of Production Economics*, Vol. 124 No. 2, pp. 331-339.

Lee, H.L. (2000), "Creating value through supply chain integration", *Supply Chain Management Review*, Vol. 4 No. 4, pp. 30-36.

Li, B., Hou, B., Yu, W., Lu, X. and Yang, C. (2017), "Applications of artificial intelligence in intelligent manufacturing: a review", *Front Inform Tech El*, Vol. 18 No. 1, pp. 86-96.

Li, X., Chung, C., Goldsby, T.J. and Holsapple, C.W. (2008), "A unified model of supply chain agility: the work-design perspective", *The International Journal of Logistics Management*, Vol. 19 No. 3, pp. 408-435.

Lu, Y. (2017), "Industry 4.0: a survey on technologies, applications and open research issues", *Journal of Industrial Information Integration*, Vol. 6, pp. 1-10.

Lyu, J., Ding, J.H. and Chen, P.S. (2010), "Coordination replenishment mechanisms in supply chain: from the collaborative supplier and store-level retailer perspective", *International Journal of Production Economics*, Vol. 123 No. 1, pp. 221-234.

Marek, P. and Malyszek, E. (2008), "A local collaboration as the most successful co-ordination scenario in the supply chain", *Industrial Management and Data Systems*, Vol. 108 No. 1, pp. 22-42.

Mehrjerdi, Y.Z. (2009), "Excellent supply chain management", *Assembly Automation Journal*, Vol. 29 No. 1, pp. 52-60.

Melnyk, A.S., Lummus, R.R., Vokurka, J.R., Burns, J.L. and Sandor, J. (2009), "Mapping the future of supply chain management: a Delphi study", *International Journal of Production Research*, Vol. 47 No. 16, pp. 4629-4653.

Mentzer, J.T., De Witt, W., Keebler, J.S., Min, S., Nix, N.W., Smith, C.D. and Zacharia, Z.G. (2001), "Defining supply chain management", *Journal of Business Logistics*, Vol. 22 No. 2, pp. 1-25.

Michelino, F., Bianco, F. and Caputo, M. (2008), "Internet and supply chain management: adoption modalities for Italian firms", *Management Research News*, Vol. 31 No. 5, pp. 359-374.

Moller, K. (2006), "Role of competences in creating customer value: a value creation logic approach", *Industrial Marketing Management*, Vol. 35 No. 8, pp. 913-924.

Olorunniwo, F. and Hartfield, T. (2001), "Strategic partnering when the supply base is limited: a case study", *Industrial Management & Data Systems*, Vol. 101 No. 1, pp. 47-52.

Ozer, O. (2003), "Replenishment strategies for distribution system under advanced demand information", *Management Science*, Vol. 49 No. 3, pp. 255-272.

Pyke, D., Robb, D. and Farley, J. (2000), "Manufacturing and supply chain management in china: a survey of states, collective and privately owned enterprises", *European Management Journal*, Vol. 8 No. 6, pp. 577-589.

Sahay, B.S. (2003), "Supply chain collaboration: the key to value creation", *Work Study*, Vol. 52 No. 2, pp. 76-83.

Sandberg, E. and Abrahamsson, M. (2010), "The role of top management in supply chain management practices", *International Journal of Retail and Distribution Management*, Vol. 38 No. 1, pp. 57-69.

Shen, W.M. and Norrie, D.H. (1999), "Agent-based systems for intelligent manufacturing: a state-of-the-art survey", *Knowledge and Information Systems*, Vol. 1 No. 2, pp. 129-156.

Shin, H., Collier, D.A. and Wilson, D.D. (2000), "Supply management orientation and supplier/buyer performance", *Journal of Operations Management*, Vol. 18 No. 3, pp. 317-333.

Simatupang, T.M. and Sridharan, R. (2002), "The collaborative supply chain", *The International Journal of Logistics Management*, Vol. 13 No. 1, pp. 15-30.

Simatupang, T.M., Wright, A.C. and Sridharan, R. (2002), "The knowledge of coordination of supply chain integration", *Business Process Management Journal*, Vol. 8 No. 3, pp. 289-308.

Singh, R.K. (2013), "Prioritizing the factors for coordinated supply chain using analytic hierarchy process (AHP)", *Measuring Business Excellence*, Vol. 17 No. 1, pp. 80-98.

Singh, R.K. (2015), "Modelling of critical factors for responsiveness in supply chain", *Journal of Manufacturing and Technology Management*, Vol. 26 No. 6, pp. 868-888.

Singh, R.K. and Sharma, M.K. (2014), "Prioritizing the alternatives for flexibility in supply chains", *Production Planning and Control*, Vol. 25 No. 2, pp. 176-192.

Singh, R.K., Garg, S.K. and Deshmukh, S.G. (2004), "Competitiveness of small and medium enterprises: case of an Indian auto component manufacturing organization, IIMB", *Management Review*, Vol. 16 No. 4, pp. 94-102.

Singh, R.K., Garg, S.K. and Deshmukh, S.G. (2010), "Strategy development by Indian SSIs", *Industrial Management & Data Systems*, Vol. 110 No. 7, pp. 1073-1093.

Skipworth, H., Godsell, J., Wong, C.Y. and Julien, S.S. (2015), "Supply chain alignment for improved business performance: an empirical study", *Supply Chain Management: An International Journal*, Vol. 20 No. 5, pp. 511-533.

Soroor, J., Tarokh, J.M. and Shemshadi, A. (2009), "Theoretical and practical study of supply chain coordination", *Journal of Business and Industrial Marketing*, Vol. 24 No. 2, pp. 131-142.

Stank, T.P., Crum, M.R. and Arango, M. (1999), "Benefits of interim coordination in food industry supply chain", *Journal of Business Logistics*, Vol. 20 No. 2, pp. 21-41.

Stanley, E.F., Cynthia, W., Chad, A. and Gregory, M. (2009), "Supply chain information-sharing: benchmarking a proven path", *Benchmarking: An International Journal*, Vol. 16 No. 2, pp. 222-246.

Stock, T. and Seliger, G. (2016), "Opportunities of sustainable manufacturing in Industry 4.0", *Procedia CIRP*, Vol. 40, pp. 536-541.

Sun, S.Y., Hsu, M.H. and Hwang, W.J. (2009), "The impact of alignment between supply chain strategy and environmental uncertainty on SCM performance", *Supply Chain Management: An International Journal*, Vol. 14 No. 3, pp. 201-212.

Tan, K. (2002), "Supply chain management: practices, concerns, and performance issues", *Journal of Supply Chain Management*, Vol. 38 No. 1, pp. 42-53.

Tjahjono, B., Esplugues, C., Ares, E. and Pelaez, G. (2017), "What does Industry 4.0 mean to supply chain", *Procedia Manufacturing*, Vol. 13, pp. 1175-1182.

Tsay, A. (1999), "The quantity flexibility contract and supplier-customer incentives", *Management Science*, Vol. 45, pp. 1339-1358.

Van Hoek, R.I. and Chapman, P. (2007), "How to move supply chain beyond cleaning up after new product development", *Supply Chain Management: An International Journal*, Vol. 12 No. 4, pp. 239-244.

BIJ

Wan, J., Tang, S., Li, D., Wang, S., Liu, C. and Abbas, H. (2017), "A manufacturing Big Data solution for active preventive maintenance", *IEEE Transactions on Industrial Informatics*, Vol. 13 No. 4, pp. 2039-2047.

Wang, S., Wan, J., Zhang, D., Li, D. and Zhang, C. (2016), "Towards smart factory for Industry 4.0: a self-organized multi-agent system with Big Data based feedback and coordination", *Computer Networks*, Vol. 101, pp. 158-168.

Zhang, Y.K.T., Akhtar, P. and Mac Bryde, J. (2016), "Embracing supply chain agility: an investigation in the electronics industry", *Supply Chain Management: An International Journal*, Vol. 21 No. 1, pp. 140-156.

About the authors
Dr Rajesh Kumar Singh is Professor in Operations Management Area at Management Development Institute, Gurgaon, India. His areas of interest include small business management, quality management and supply chain management. He has about 160 research papers published in reputed international/national journals and conferences. He has published research papers in journals such as *Production Planning and Control, International Journal of Production Research, Resources, Conservation and Recycling, Journal of Cleaner Production, Annals of Operations Research, Industrial Management Data Systems, Measuring Business Excellence, Singapore Management Review, International Journal of Productivity and Performance Management, Benchmarking: An International Journal, Journal of Modelling in Management, Competitiveness Review: An International Business Journal, Global Journal of Flexible Systems and Management, International Journals of Productivity and Quality Management, International Journal of Services and Operations Management, International Journal of Automotive Industry and Management, International Journal of Logistic Systems Management* and *IIMB Management Review and Productivity Promotion*. He is also on editorial board of some reputed journals. Dr Rajesh Kumar Singh is the corresponding author and can be contacted at: rksdce@yahoo.com

Dr Pravin Kumar is Associate Professor in Mechanical Engineering Department, Delhi Technological University, Delhi, India. He received the PhD Degree in Supply Chain Management from IIT Delhi and MTech in Industrial Management from IT, BHU, Varanasi (Now IIT BHU Varanasi). He has published many research papers in international and national journals and conferences. His area of research is supply chain and logistics management. He has more than 14 years of teaching and research experience. He has authored the books on Engineering Economics and Industrial Engineering and Management by Wiley India and Pearson Learning, respectively.

Dr Mahesh Chand is working as Assistant Professor in Mechanical Engineering Department at the YMCA University of Science and Technology, Faridabad, India. He is working in the field of supply chain management, risk management, operation management, manufacturing technology and MCDM approaches. He has published about 30 research papers in reputed international journals which include *International Journal of Services and Operations Management, International Journal of Advanced Manufacturing Systems, International Journal Business Information System, International Journal of Productivity and Quality Management, International Journal of Logistics Systems and Management, Benchmarking: An International Journal*, etc.

GRAPHICAL ANALYSIS OF PERFORMANCE OF A VIBRATORY BOWL FEEDER FOR FEEDING BOTTLE CAPS

3 authors, including:

Manas Choudhary
Delhi Technological University

3 PUBLICATIONS   **0** CITATIONS

Some of the authors of this publication are also working on these related projects:

Project   Vibratory Bowl Feeder View project

GRAPHICAL ANALYSIS OF PERFORMANCE OF A VIBRATORY BOWL FEEDER FOR FEEDING BOTTLE CAPS

Manas Choudhary[1], Rishabh Narang[2], Pradeep Khanna[3]

[1]Student, Department of Mechanical Engineering, Delhi Technological University, New Delhi, India
[2]Student, Department of MPAE, Netaji Subhas Institute of Technology, New Delhi, India
[3]Associate Professor, Department of MPAE, Netaji Subhas Institute of Technology, New Delhi, India

Abstract

Automation in manufacturing industry has now become essential as it helps meeting the ever-increasing demands quantity, quality, consistency and precision.In automated production lines, synchronization of different processes is of utmost importance to achieve the predetermined cycle times. Automation not only has resulted in the cost reduction but it has also resulted in wastage reduction. Assembly lines are extensively used in mass production units where economy of scales is exploited to spread over the cost of production over a large batch size. These assembly lines actually streamline the movement of product from one assembly station to the other in predetermined sequence so as to meet the deadlines. Feeders form an integral part of automated assembly and production lines. The present study is aimed at graphically analysing the performance of a vibratory bowl feeder with varying sizes of laminated bottle caps used in the pharmaceutical industry and other consumer goods industries. In this study, the desired outcome was the feed rate, and the various input parameters were – part population, part size, and frequency of vibratory bowl feeder. Results obtained from the experiment were analysed and conclusions were drawn to explain the effects of various parameters and to predict the behaviour of the feeder.

Keywords: Automation, Feeder, Cycle time, Feed rate, Graphical Analysis.

--***--

1. INTRODUCTION

A feeder is a machine used to feed or load any kind of material, chemical or product to the assembly line, manufacturing stations or wherever necessary. [1]

The feeder selection is a key in success related to achieve desired feeding. Hence, different types of Feeders have been made to cater to different kinds of feeding requirement which are: [2]Centrifugal Feeder, Vibratory Feeder, Linear Feeder, Flex Feeder, Step Feeder and Elevator Feeder.

The feeder used during this experiment is Vibratory Bowl Feeder. It is an instrument that uses vibration to feed material. It uses both vibration and gravity to move materials. Gravity is used to determine the direction, either down, or down and to a side, and then vibration is used to move the materials. They are mainly used to transport a large number of smaller objects.

Vibratory bowl feeders are the commonly used feeding aides used to feed components in Industrial Assembly lines. They are self-contained systems, comprising of a specially designed bowl contains randomly placed components. This bowl is mounted on a vibrating drive unit facilitated by a variable-amplitude control box. The drive unit vibrates the bowl, forcing the parts to move up a circular, inclined spiral track. The track is designed to sort and orient the parts in consistent, repeatable positions. The track length, width, and depth are carefully chosen to suit the application and

component shape and size. Special track coatings are applied according to shape size and material of the parts which aids traction, damage to the product and lower acoustic levels. A variable frequency control box is used for controlling the vibration of the bowl feeder [3]. In the present investigations, a vibratory bowl feeder has been used owing to its ability to handle a variety of components and ease of operation. A number of research articles were referred to which have carried out research on different types of components on vibratory bowl feeder.

Jain et. al. [4] optimised the performance of vibratory bowl feeder by applying the Taguchi approach and found that part population had a negative effect on feed rate whereas, frequency had a positive effect on feed rate. Initially the effect of part size was negative but due to its interaction with frequency and part population, it became positive after a while.

In the investigation carried out by Jindal et. al. [5 &6] graphical and mathematical analysis of vibratory bowl feeder using clip shaped components revealed that the highest frequency with the highest part population gave the maximum feed rate for the smallest part size in graphical analysis.

According to Chauhan et. al. [7], a factorial approach to study the effects of various parameters on vibratory bowl feeder gives satisfactory results.

Bhagat et. al. [8&9], analysed graphically and mathematically, the behaviour of vibratory bowl feeder for feeding headed components and concluded that the developed model could estimate the magnitude and direction of the effects of variation in factors as well as predicts the effects of their mutual interactions.

2. EXPERIMENTAL SETUP

Figure 1 shows the experimental setup used for this investigation. The setup has a frequency regulation unit which allows stepless control of frequency of vibration of the bowl. The bowl is mounted on a vibrating drive unit. The setup consists of a vibratory bowl feeder with a bowl diameter of 300mm with tracks of 20 mm width running along the wall in a spiral. The components selected for the experiments were bottle caps of 3 different sizes viz. 16mm, 19mm and 22mm respectively. A number of trial runs were conducted for the purpose of identification of important input parameters and determination of their operating ranges. As shown in table-1.

Table 1: Input parameters and their operating limits

PARAMETERS	UNIT	LOWER LIMIT	UPPER LIMIT
FREQUENCY	Hz	45	50
PART SIZE	Mm	16	22
PART POPULATION	units.	45	135

Fig 1: The experimental set up

3. CONDUCTING THE EXPERIMENTS

Analysis was done by using OFAT (One factor at a time) based on 3 input parameters of which 2 factors were kept constant and the third was varied. Hence, all the 3 parameters were varied one by one and a total of 27 readings were obtained.

The experiments were conducted by using one factor at a time technique. Even though this technique does not take into accountthe interaction effects and hence it cannot precisely predict the outcome of an experiment. However, it is still better than random experimentation and successfully gives a brief idea of the performance of the unit, to some extent, and the study can be used as a preliminary to further conduct elaborated analysis on the unit.

Input parameters were varied at three levels the lowest, intermediate and the highest.3 runs were conducted for each of the 27 readings taken, in order to minimise the experimental errors as shown in table 2.

Table 2: Experimental Observations

PART SIZE	PART POPULATION	FREQUENCY	FEED RATE (PARTS/MIN)			MEAN FEED RATE
16	45	45	67	73	68	69
16	45	47.5	98	101	90	96
16	45	50	46	46	49	47
16	90	45	127	134	125	129
16	90	47.5	164	165	170	166
16	90	50	130	136	141	136
16	135	45	129	136	132	162
16	135	47.5	197	191	200	196
16	135	50	185	178	184	182
19	45	45	63	66	65	65
19	45	47.5	73	70	79	74
19	45	50	101	89	94	95

19	90	45	106	108	111	108
19	90	47.5	123	128	119	123
19	90	50	149	142	158	150
19	135	45	114	102	99	105
19	135	47.5	152	139	143	145
19	135	50	217	213	203	211
22	45	45	62	58	61	60
22	45	47.5	47	45	42	45
22	45	50	40	42	45	42
22	90	45	86	81	78	82
22	90	47.5	102	106	97	102
22	90	50	76	79	77	77
22	135	45	101	98	94	100
22	135	47.5	124	116	119	120
22	135	50	71	68	73	71

4. RESULTS AND DISCUSSION

The results obtained after conducting the experiments were plotted in the form of graphs as shown in figures 2,3,4. The interpretation of these graphical representations is given as below
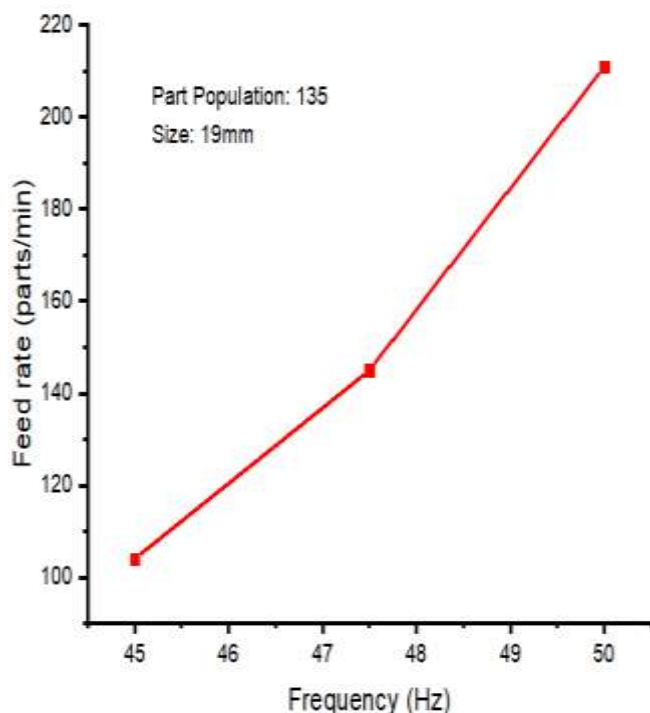
4.1 Effect of Frequency

Fig 2: Effect of Frequency on Feed rate

Fig.2 shows the effect of frequency on feed rate. As it is evident that the feed rate increased with increase in frequency,the increased agitation of the components might be responsible for pushing the components towards the delivery chute at a faster rate resulting in the increment in feed rate.

4.2 Effect of Part Size
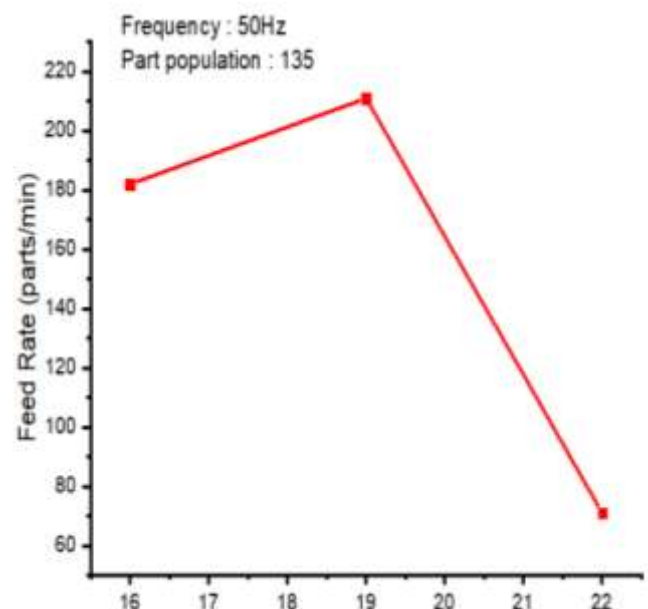
Fig 3: Effect of Part size on Feed Rate

Fig.3 shows the relation of feed rate per minute and part sizeThere is an increment in feed rate as part size is increased from 16mm to 19mm, as was predicted. with increase in size, another parameter, part mass changed. Increment in both these parameters resulted in more agitation, causing an increase in the pushing tendency of the components. Larger the part size higher the feed rate. This proportionality explains the trend satisfactorily.

However, on increasing part size from 19mm to 22mm there's a decrease in the feed rate, which seems to contradict the explanation offered previously. This can be explained by taking the fall-back factor into consideration. The width of the circular track inside the feeder bowl is 20mm. Even though 22mm parts are adequately stable on the 20mm wide

track in rest state, their stability decreases on being subject to agitation. A major fraction of the component population falls back into the bowl when the feeder is in active state. This explains the trend as observed in fig 3.

From the observed trend, we can infer that, the feed rate increases with increase in part size while the part size remains less than the width of the track, after which collapsibility factor comes in. Hence the optimum feed rate can only be obtained with the largest available part size that is smaller than the track width.

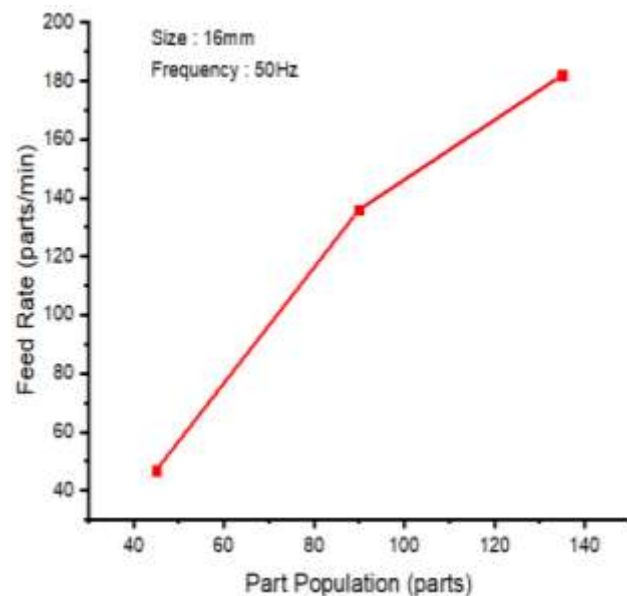## 4.3 Effect of Part Population

Fig 4: Effect of Part population on feed rate.

Fig.4 shows the relation of feed rate and part population. It is evident from the graph that feed rate increases almost linearly with increase in part population. This can be explained by the fact that with increase in part population, componentsinteract with each other more frequently compared to when same degree of agitation is generated for lower part population. More interaction means more parts pushing each other, resulting in increased feed rate.

5. CONCLUSION

The graphical analysis of the experimentation conducted show that maximum feed rate of 211 parts/min is obtained at part population of 135 units, frequency 50Hz and part size 19 mm.

ACKNOWLEDGEMENT

REFERENCES

[1] Slide no. – 2, https://www.slideshare.net/faugee/feeder-equipment, accessed on 29 June, 2018.

[2] http://www.hoosierfeedercompany.com/vibratory-rotary-feeder-insights/what-are-the-different-types-of-parts-feeder-systems , accessed on 29 June, 2018.

[3] https://www.rnaautomation.com/products/feeding-and-handling/vibratory-feeders/ , accessed on 29 June, 2018.

[4] Jain, A., Bansal, P., Khanna, P., "Application of Taguchi Technique to Optimize the Performance of a-Vibratory Bowl Feeder". Global Journal on Innovation, Opportunities and Challenges in AAI and Machine Learning, Vol. 1, pp. 13-18, Issue 1,2017.

[5] Jindal, U., Jain, S., Piyush, Khanna, P., "Graphical Analysis of a Vibratory Bowl Feeder for Clip shaped Components". IJISET - International Journal of Innovative Science, Engineering & Technology, Vol. 4 Issue 2, pp. 279-283, February 2017.

[6] Jain, S., Jindal, U., Piyush, Khanna, P., "Mathematical Analysis of Vibratory Bowl Feeder for Clip Shaped Components". Journal of Production Engineering, Vol.20, pp. 122-126, 2017.

[7] Chauhan, A., Nirman, G., "Mathematical Analysis of U-shaped Components in a Vibratory Bowl Feeder". International Journal of Electronics, Electrical and Computational Systems, Vol. 5, Issue 4, pp. 91-99, April, 2016.

[8] Bhagat, S., Pandey, T., Garg, V., Khanna, P., "Design, Fabrication and Analysis of Vibratory Feeder". IJRMET, Vol. 4, Issue 1, pp. 73-75, November 2013 - April 2014.

[9] Bhagat, S., Pandey, T., Garg, V., Khanna, P., "Mathematical Analysis of Vibratory Bowl Feeder". International Journal of Latest Trends in Engineering and Technology, Vol 4, Issue 1, pp. 315-324, 2014.

Kinetics of carbon and nitrogen assimilation by heterotrophic microorganisms during wastewater treatment

Sanak Ray · Miklas Scholz · A. K. Haritash

Abstract The present study highlights microbial assimilation of carbon (glucose) and nitrogen (NH_3–N) from wastewater using heterotrophic bioconversion process. Experiments were conducted to study the role of heterotrophic microbes towards removal of carbon and nitrogen at varying initial concentrations of carbon (COD, 533 to 1600 mg/l) and nitrogen (NH_3–N, 73 to 249 mg/l) keeping the initial biomass of microorganisms constant. Removal of COD and ammonia from wastewater represented a first-order rate reaction, upon analysis of kinetics, indicating that the rate of reaction is dependent on the initial concentration of nutrients available. Rate equations were developed using the Monod model, and the maximum specific consumption rate (k_4) and half saturation constant (K_s) values for NH_3–N and COD were found to be 2.59 mg/l/h and 64.13 mg/l/h and 38.46 mg/l and 2162.69 mg/l, respectively. Assimilation of NH_3–N followed the Freundlich isotherm model. The mass transfer coefficient for COD and NH_3–N were found to be 0.13 h^{-1} and 0.81 h^{-1} respectively. The NH_3–N is converted to N_2O during nitrification, and observed values of N_2O coincided with the empirically

predicted values indicating the activity of heterotrophic nitrifiers. The regeneration/doubling time of heterotrophic microbial biomass varied from 26 to 121 h. Statistical techniques, viz. analysis of variance, multi-linear regression analysis and principal component analysis, validated the results.

Keywords COD · Ammonia · Biological waste treatment · Freundlich isotherm · Multivariate analysis

Introduction

Urbanisation, industrialisation and agriculture lead to generation of huge volumes of wastewater, which initiates challenges related to collection, treatment and disposal particularly in developing countries. Wastewater generally contains organic and nitrogenous compounds, and ammonia is one of the important nitrogenous pollutants present in the water. Organic pollutants may come from the following sources: humans, pig slurry, cattle, fermented chicken manure, landfill leachate, wastewater released from fertiliser industries, biogas plants, sugar mills, distilleries, food processing and petrochemicals (Pant et al. 2010; Reddy 2010; Kinidi et al. 2018). The ammonia concentration in wastewater from livestock and slaughtering plants ranges between 400 and 500 mg/l, which may have negative impacts on the aquatic environment, including eutrophication and poor water quality through a decrease in DO levels and toxicity to aquatic biota (Horne 2002). Many countries are implementing environmental regulations for

S. Ray (✉) · A. K. Haritash
Department of Environmental Engineering, Delhi Technological University, Bawana Road, Shahbad Daulatpur, Delhi 110042, India
e-mail: sanakray@gmail.com

M. Scholz
Division of Water Resources Engineering, Department of Building and Environmental Technology, Faculty of Engineering, Lund University, P.O. Box 118, 22100 Lund, Sweden

Springer

ammonia in receiving water bodies to maintain the water quality.

Various biological treatment methods are carried out for removal of ammonia from wastewater. The most common method for its removal from wastewater is nitrification (Koren et al. 2000) or coupled nitrification-denitrification. Whereas physicochemical processes are cost and energy prohibitive and produce secondary pollutants, biological treatment processes are energy efficient and economically feasible and need no or less amount of chemical supplements for industrial and urban wastewater treatment (Al-Isawi et al. 2017). Various key processes, viz. assimilation, biodegradation, biosorption, bioaccumulation, precipitation and ion exchange, were observed during biological treatment (Wu et al. 2012; Mohanty et al. 2015). Transformation of NH_3–N to N_2O is frequently observed during biological wastewater treatment (Foley et al. 2010), and it is one of the prominent greenhouse gases, which heat up the environment.

The heterotrophic microorganisms are used for removal of NH_3–N for wastewater, where NH_3 is directly converted to total volatile suspended solids (TVSS). Heterotrophic biomass synthesis is carried out by facultative microorganisms, which require an oxidising environment for their growth and carbon as a source of energy (Ray et al. 2014), which results in a decrease in pH and CO_2 formation. Apart from it, heterotroph biomass synthesis also depends on parameters like pH, alkalinity, temperature, DO, COD and NH_3 during nutrient removal from wastewater (Ebeling et al. 2006). Nitrous oxide emissions are not observed during the process, because nitrogen is converted to biomass using NH_3 (Ebeling et al. 2006). Due to the high growth rate, heterotrophic biomass production is 40 times higher compared with the normal nitrification process (Mohanty et al. 2015). Moreover, the harvested biomass can be used as biofertiliser on the fields.

Another biological process like heterotrophic nitrification is carried out by heterotrophs, which convert NH_3 to NO_3^- under aerobic environments (Mohanty et al. 2015). Various intermediates like N_2O, NH_2OH and NO_2^- are produced during heterotrophic nitrification. Moreover, the higher the availability of carbon sources and DO concentrations, the higher will be the emission of N_2O. The same is again favoured, when the pH gets lower than neutral. The pH of around 6 to 8 is suitable for nitrifiers (Mohanty et al. 2015). Some specific heterotrophic nitrifiers are *Pseudomonas* spp., *Alcaligenes faecalis* and *Comamonas* spp. (Balagodatsky et al. 2006).

A nitrification study with suspended biomass was carried out using the one-dimensional Wanner-Gujer model (Masic and Eberl 2014). The removal of nutrients (ammonia and COD) from high-strength wastewater using heterotrophic microbes is a complex process. There have been a number of studies on the uptake of nutrients, but the efforts towards studying the kinetics involved and optimisation of the microbial uptake are very limited (Ray et al. 2014a; Ray et al. 2014; Mohanty et al. 2015). In order to get a better insight of this research problem, bench-scale experiments were performed for the removal of NH_3–N and COD from high-strength wastewater along with time. Further, the detailed kinetic study using varying combinations of carbon and nitrogen was undertaken. Attempts were made to identify the rate equation, regeneration time, adsorption isotherm, Monod model and diffusion model. At the same time, the data were statistically interpreted to validate the study.

Materials and methods

Experimental set-up

Using the aqueous media (chemical ingredients: sodium acetate (CH_3COONa), 7860 mg/l; potassium dihydrogen phosphate (KH_2PO_4), 200 mg/l; ammonium sulphate (($NH_4)_2SO_4$), 500 mg/l; magnesium sulphate heptahydrate ($MgSO_4.7H_2O$), 40 mg/l; and calcium nitrate ($Ca(NO_3)_2$), 40 mg/l), the heterotrophs were separated from paddy field soil and enriched usually to increase their activity. The dominant species found in the culture were *Pseudomonas aeruginosa*, *Proteiniphilum acetatigenes*, and *Alcaligenes faecalis* (Ray et al. 2014a). The study was undertaken in an aerobic environment as the identified species are facultative in nature. Ammonia nitrogen and chemical oxygen demand (COD) were selected to study the kinetics. Liquid NH_3 (converted into NH_4OH when dissolved in H_2O) and $C_6H_{12}O_6$ were utilized as NH_3–N and COD sources, respectively. The experiments used 100 ml of wastewater, having 90 ml of aqueous media (keeping out NH_3–N and COD), 9 ml mixed culture and 1 ml of NH_3–N in 250-ml borosil glass containers. The concentrations of variables viz NH_3-N (50–250 mg/l) as well as COD (533–5300 mg/l) were varied. In the study,

shaking incubators (Julabo SW-22, Julabo GmbH, Gerhard-juchheim-Strasse 1, 77960 Seelbach, Germany) were used to provide an aerobic environment to the samples present in the bottles at 35 °C. Initially 700 mg/l of microbial consortium was inoculated to each bottle during the start of the experiments, and the study was continued for three consecutive days.

Gaseous and water sample analyses

The gaseous as well as aqueous samples were taken at regular intervals of 12 h by means of syringes for N_2O estimation. In order to obtain the gaseous specimens, the bottles were wrapped with rubber crowns and kept stable for an hour. The N_2O analysis was done using gas chromatography (Shimadzu AA30) with an electron capture detector. The N_2O in solution was analysed as reported by using GC (Ray et al. 2014a). Water parameters including NO_3^-–N, NO_2^-–N, NH_3–N, DO, COD, pH and TVSS were analysed using prescribed protocols (APHA 2012).

Kinetic study

Various parameters, viz. rate determination, evaluation of rate equation, regeneration time, adsorption isotherm, diffusion and Monod model (Mohanty et al. 2015), were used to obtain the kinetics for the removal of NH_3–N and COD from wastewater. The evaluation was carried out using Microsoft Office Excel 2007.

Statistical analysis

The two way analysis of variance (ANOVA) using the null hypothesis technique was used to determine if any significant role is played between the variables like time, ammonia and COD, for which Microsoft Office Excel 2007 was used. Multivariate statistical techniques like multi-linear regression analysis (MLRA) and principal component analysis (PCA) were carried out using SPSSv20. The experimental data were fed to the PCA tool to evaluate the influence of different factors on the biological waste treatment process. The experimental data were collected in triplicates and the average was taken for interpretation. The experimental error was within ± 5%. The equation in this manuscript has been formatted using Microsoft Equation Editor 2003.

Results and discussion

Response of NH_3–N and COD concentrations

In this study, NH_4OH was used as a NH_3–N source, and its concentration ranged from 73 to 249 mg/l and maintained COD concentrations around 5310 (± 20.03 s) mg/l. During the wastewater treatment, removal of NH_3–N was 97%, 77%, 61%, 52% and 52% for initial NH_3–N concentrations of 73 mg/l, 121 mg/l, 181 mg/l, 233 mg/l, and 249 mg/l, respectively (Table 1). Simultaneously, removal of COD was 20%, 26%, 31%, 34% and 37% for initial COD concentrations of 5299 mg/l, 5330 mg/l, 5280 mg/l, 5318 mg/l and 5321 mg/l respectively. The heterotrophic biomass (TVSS) formed during NH_3–N, and COD removal was 114 mg, 167 mg, 180 mg, 196 mg and 208 mg, respectively, within a time period of 60 h. It indicated that the heterotrophic microbes can assimilate external carbon and nitrogen from the aqueous solution resulting in wastewater treatment. Heterotrophic biomass synthesis occurs in the presence of both NH_3–N and COD abiding to the given Eq. (1).

$$NH_4^+ + 1.18C_6H_{12}O_6 + HCO_3^-$$
$$+ 2.06O_2 \rightarrow C_5H_7O_2N + 6.06H_2O + 3.07CO_2 \quad (1)$$
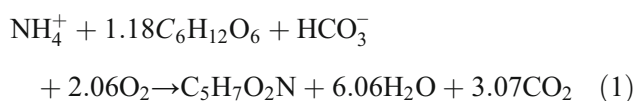
where, NH_4^+ is ammonium, $C_6H_{12}O_6$ is glucose, O_2 is oxygen, $C_5H_7O_2N$ is bacterial biomass, H_2O is water and CO_2 is carbon dioxide.

Ammonia is essentially consumed by heterotrophs for their growth and metabolism. In the treatment process NO_3^- concentration was observed to be increased, which may be an outcome of nitrification by heterotrophs (Ray et al. 2014a). Nitrous oxide and NO_2^- concentration rose in the initial hours, and after 24 h it showed a declining tendency. The nitrous oxide emission was observed during the treatment as an intermediate of the heterotrophic nitrification reaction associated with NO_2^- formation (Ni et al. 2011). Ammonia and COD concentrations decreased continuously during the treatment, thereby increasing the biomass concentration. The pH showed a decreasing trend (Fig. 1).

In the present study, it was noticed that the NH_3 consumption rate is directly related to the NH_3–N concentration. Table 2 shows the NH_3–N depletion rate kinetics along with other parameters for different NH_3–N concentration variations. Moreover, the consumption rate of COD is directly related to NH_3 concentrations. The significant consumption rate for NH_3

Table 1 Comparison of variables operated during the study

| Variables	Parameters								
	NH₃–N			COD			Biomass		
	Initial (mg/l)	Final (mg/l)	Removal (%)	Initial (mg/l)	Final (mg/l)	Removal (%)	Initial (mg)	Final (mg)	Formation (mg)
NH₃–N (mg/l)									
73	73	2	97	5299	4259	20	71	185	114
121	121	27	77	5330	3920	26	71	238	167
181	181	70	61	5280	3645	31	71	250	180
233	233	111	52	5318	3491	34	71	267	196
249	249	120	52	5321	3376	37	71	279	208
COD (mg/l)									
533	106	74	30	533	44	92	71	123	52
800	103	65	37	800	231	71	71	131	61
1060	97	55	43	1060	435	59	71	138	67
1330	96	30	69	1330	327	75	71	178	107
1600	121	35	71	1600	302	81	71	209	138

Operation time is 60 h

may be directly related to higher heterotrophic biomass synthesis rate (Table 2); i.e. increased biomass synthesis rate results in decrease in NH_3–N concentration in the solution.

To study the effect of varying COD concentrations, $C_6H_{12}O_6$ was used as a COD source, and its concentration was varied from 530 to 1600 mg/l, maintaining NH_3–N concentration at around 104 (± 9.9 s) mg/l. Removal of COD was observed to be 92%, 71%, 59%, 75% and 81% for initial COD concentrations of 533 mg/l, 800 mg/l, 1060 mg/l, 1330 mg/l and 1600 mg/

l, respectively (Table 1). Simultaneous removal of NH_3–N was 30%, 37%, 43%, 69% and 71% for initial NH_3–N concentrations of 106 mg/l, 103 mg/l, 97 mg/l, 96 mg/l and 121 mg/l, respectively. During the treatment period (60 h), heterotrophic biomass formed was 52 mg, 61 mg, 67 mg, 107 mg and 138 mg, respectively, indicating that the heterotrophic microbes assimilate external carbon and nitrogen from the aqueous solution resulting in biomass formation as shown in Eq. (1). The corresponding NO_3^-, NO_2^- and N_2O concentrations behaved similarly (Fig. 2). The NH_3–N

Fig. 1 Behaviour of variables like ammonia nitrogen (NH_3–N), nitrate nitrogen (NO_3^-–N), nitrous oxide nitrogen (N_2O–N), nitrite nitrogen (NO_2^-–N), chemical oxygen demand (COD), dissolved oxygen (DO), pH, biomass and time during incubation studies. Initial conditions for NH_3–N variation: NH_3–N, 249 mg/l; COD, 5.33 g/l; temperature, 35 °C; and pH, 7
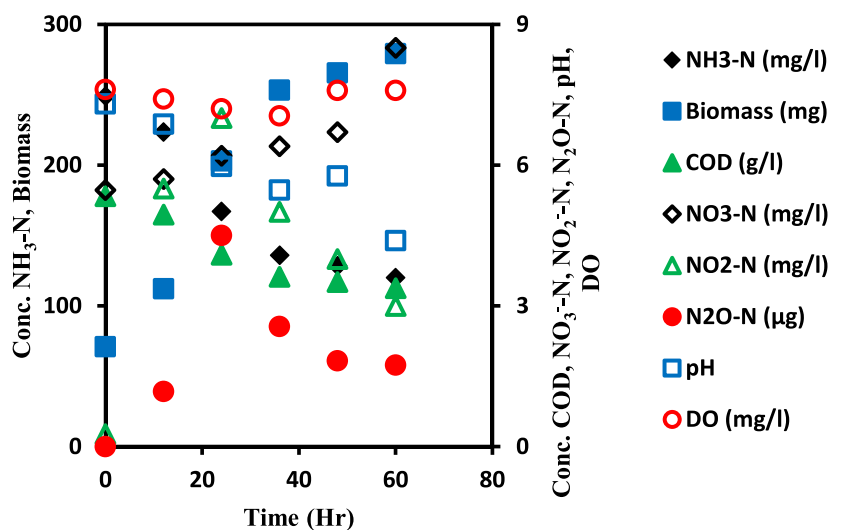
consumption rate was observed to be directly related to increasing COD concentration (shown in Eq. 1). Similarly, the COD consumption rate was directly related to the primary COD strength. Apart from it, the heterotrophic biomass synthesis is directly related to primary COD concentration in the wastewater (Table 2). Therefore, biological treatment process employs naturally occurring microbes to convert the organic substance into a thick biomass resulting in wastewater purification, and further it can be removed from the treated wastewater using sedimentation process. In this study, heterotrophic microbes use organic matter dissolved in the wastewater as their food, and two key processes are observed, viz. biological oxidation and biosynthesis. The biological treatment controls the wastewater treatment process efficiently and transforms the available substances in the wastewater into secure end products, resulting in safe disposal into water bodies without harming the environment.

Kinetic studies

Emission of N$_2$O

The N$_2$O emission was observed to increase initially, and then it decreased during the study in both aqueous as well as gaseous phases. A decrease in N$_2$O observed during the late phase indicated that the media became the sink for N$_2$O gas. If the formation of N$_2$O is of the first order, then, theoretically, the N$_2$O emission can be calculated using Eq. (2).

$$Y = Be^{-k_1 t} + Ce^{k_2 t} \tag{2}$$

where Y represents N$_2$O emission, t is time in hours, k_1 and k_2 are initial and final stage reaction rate constants, respectively, and B and C are fitting parameters.

Constants were calculated for all experimental conditions by applying the Excel solver technique (Ray et al. 2013). The k_1, k_2, B and C values were -0.70, 0.68, 0.51 and 0.52, respectively, for the corresponding incubation experiments.

Evaluation of rate equation

The reaction order for NH$_3$–N and COD was determined. In order to determine it, first- as well as second-order reactions were considered. The graph for the first-order reaction is drawn among ln$C$ (C (concentration)) versus time, which gives a straight line. Likewise, the graph for the second order is drawn among $1/C$ versus time giving a straight line. In both the cases, the slope of the straight line indicates the specific reaction rate, and by using the R^2 values as an indicator (Fig. 3), it was concluded that the reaction rate resulted in first order.

The kinetics of the microbial treatment process depend on the variables NH$_3$–N and COD. In all cases, the initial biomass is kept constant. Thus, the result out rate equation is

$$\text{Rate} = -dc/\text{dt} = k(\text{NH}_3-\text{ N})^{n_1}(\text{COD})^{n_2} \tag{3}$$

where c is the concentration of the components determining the biomass synthesis, t is time, n is the reaction order and k is a specific reaction constant in the rate equation.

Equation (3) in its logarithmic form can be written as

$$\text{Log(rate)} = \log k + n_1 \log(\text{NH}_3 - N) + n_2 \log(\text{COD}) \tag{4}$$

where n is the reaction order and k is the specific reaction constant for the unified rate equation.

The data obtained during the study are fitted in Eq. (4) for establishment of reaction order. During this arrangement, single variable was changed at a time maintaining the other variable constant. The value of n_1 and n_2 was obtained as 0.42 and 0.88 for NH$_3$–N and COD, while the corresponding R^2 values are shown in Table 2. Hence, the rate equation indicating the n_1 and n_2 values is as shown below.

$$\text{Rate} = -dc/\text{dt} = k(\text{NH}_3 - N)^{0.42}(\text{COD})^{0.88} \tag{5}$$

Regeneration time

Since the bacterial growth rate is directly proportional to the NH$_3$–N concentration, the specific growth rate constant of bacteria (μg) was calculated as the slope of the logarithmic plot of NH$_3$–N concentration against time for each data set. The regeneration time t_d was calculated using Eq. (6).

$$t_d = 0.693/\mu_g \tag{6}$$

where t_d is regeneration time and μg is the specific growth rate constant of bacteria.

The results are shown in Table 3. The regeneration time varied from 26 to 121 h for NH$_3$–N concentration.

Table 2 Determination of rates and dependence factors

Rate of NH₃–N variation							Dependence factor	
NH₃–N (mg/l)	N₂O–N (μg/h)	NO₃⁻–N (mg/l/h)	NO₂⁻–N (mg/l/h)	NH₃–N (mg/l/h)	COD (mg/l/h)	TVSS (mg/h)	R^2	n_1
73	0.08	0.05	0.20	1.17	17.73	1.89	0.96	0.42
121	0.10	0.07	0.22	1.49	22.60	2.73		
181	0.12	0.08	0.24	1.63	24.80	2.64		
233	0.15	0.11	0.26	2.10	31.79	3.38		
249	0.19	0.13	0.28	2.29	34.72	3.69		
Rate of COD variation							R^2	n_2
COD (mg/l)	N₂O–N (μg/h)	NO₃⁻–N (mg/l/h)	NO₂⁻–N (mg/l/h)	NH₃–N (mg/l/h)	COD (mg/l/h)	TVSS (mg/h)		
533	0.05	0.02	0.10	0.51	7.68	0.82	0.80	0.88
800	0.07	0.03	0.14	0.62	9.34	0.99		
1060	0.08	0.04	0.16	0.63	9.54	1.02		
1330	0.08	0.05	0.18	0.93	14.13	1.50		
1600	0.10	0.07	0.22	1.48	22.52	2.40		

NH₃–N, ammonia nitrogen; *N₂O–N*, nitrous oxide nitrogen; *NO₃⁻ N*, nitrate nitrogen; *NO₂⁻ –N*, nitrite nitrogen; *COD*, chemical oxygen demand; *TVSS*, total volatile suspended solids; *R^2*, coefficient of determination; *n*, order of reaction

Adsorption isotherm

In the biosynthesis process of heterotrophs, NH₃–N needs to be assimilated in the biomass so that the electron transport process is initiated. For the Freundlich adsorption isotherm, ln *X/M* was plotted against Ce, where *X* is the amount of NH₃–N sorbed; *M* is the mass of the corresponding biomass; Ce is the equilibrium NH₃–N concentration (mg/dm³); and *K* and *n* are the Freundlich constants. The slope (*n*) and intercept (ln *K*) values are calculated as 1.11 and − 5.14,

respectively. For the Langmuir adsorption isotherm, a plot was drawn between Ce*/(X/M)* versus Ce. From the slope and intercept, the *Q_0* and *b*, values were calculated to be 1.52 and 0.003, respectively, indicating that the sorption of NH₃–N follows the Freundlich sorption isotherm model.

Monod model

During the sole substrate limited process, the Monod equation (7) can be used to describe NH₃–N and COD

Fig. 2 Behaviour of variables like ammonia nitrogen (NH₃–N), nitrate nitrogen (NO₃⁻–N), nitrous oxide nitrogen (N₂O–N), nitrite nitrogen (NO₂⁻–N), chemical oxygen demand (COD), dissolve oxygen (DO), pH, biomass and time during incubation studies. Initial conditions for COD variation: N–NH₃, 106 mg/l; COD, 533 mg/l; temperature, 35 °C; and pH 7
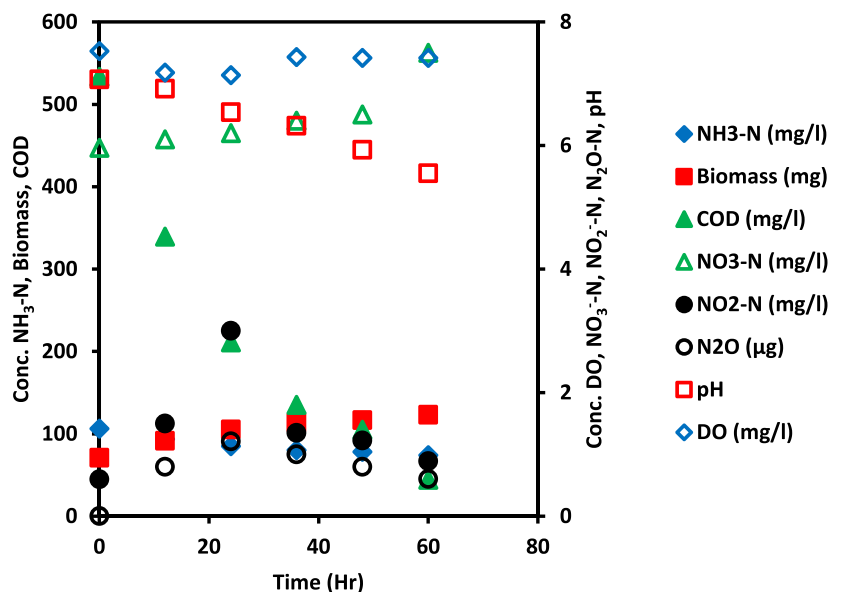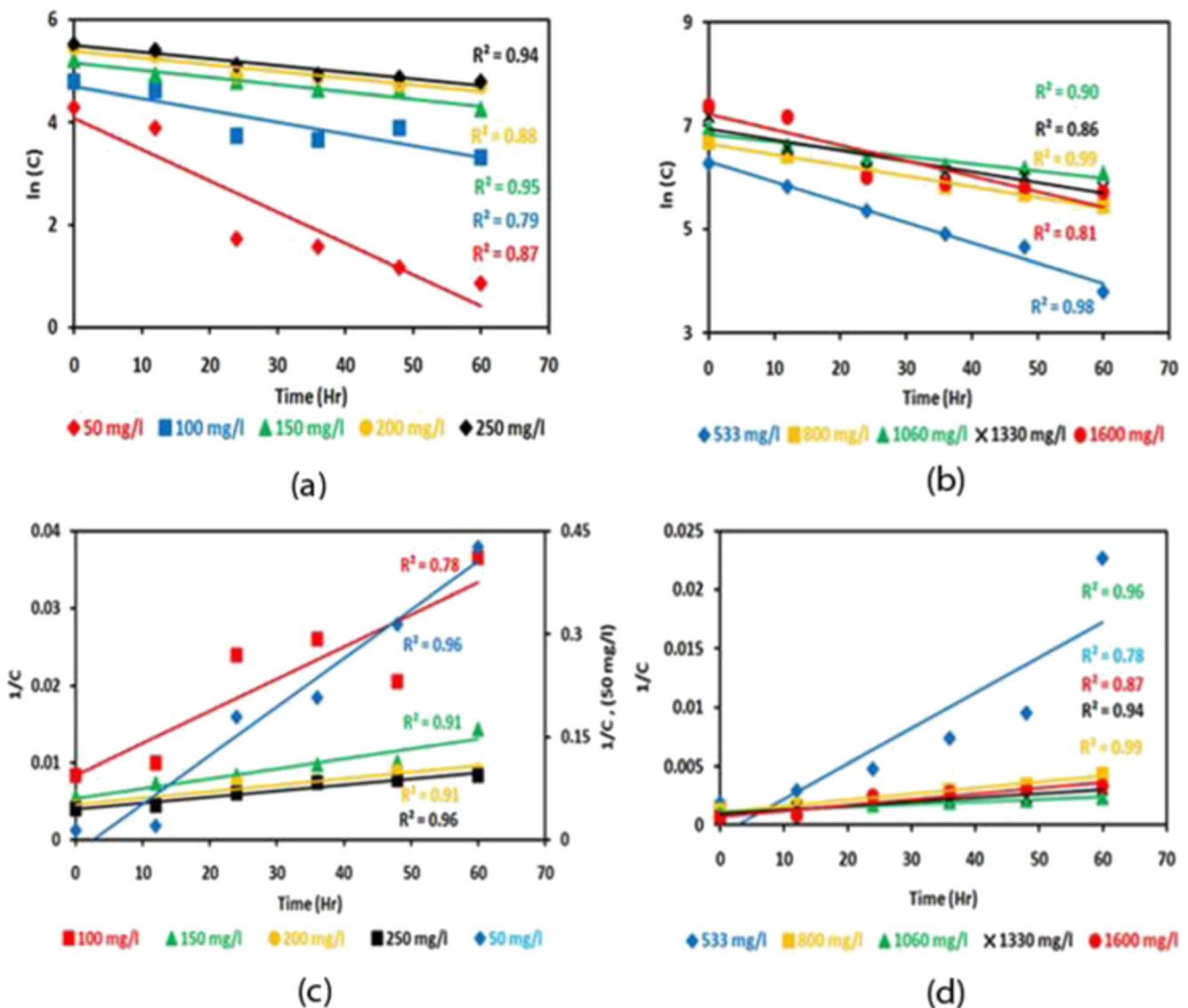
Fig. 3 Plot showing **a** ln(C) versus time for NH$_3$–N variations, **b** ln(C) versus time for COD variations, **c** 1/C versus time for NH$_3$–N variations and **d** 1/C versus time for COD variations

degradation along with microbial growth (Mohanty et al. 2015).

$$dC_s/\mathrm{dt} = k_4 C_x C_s/(K_s + C_s) \tag{7}$$

where dC_s/dt is the rate of substrate consumption (mg/l/h), K_s is the half saturation constant (mg/l), C_s is the substrate concentration (mg/l), C_x represents the TVSS (mg/l) and k_4 is the maximal specific consumption rate (mg/l/h).

Using the Lineweaver-Burk graphs, the slope and intercept of the straight line were obtained, from which the kinetic factors, viz. k_4 and K_s, were evaluated considering the C_x concentration as a constant. The TVSS concentration ranged from 0.71 to 2.79 g l^{-1} for all the experiments. By plotting the 1/rate of substrate (mg/l/h) and considering the substrate limitation, only 1/

concentration (mg/l), the values of the slope as well as intercept were obtained.

Table 3 Regeneration time

NH$_3$–N(mg/l)	μg (1/h)	t_d (h)
73	0.026	26.27
121	0.010	69.29
181	0.006	114.19
233	0.006	122.48
249	0.006	121.49

NH$_3$–N, ammonia nitrogen; t_d, regeneration time; μg, specific growth rate

Fig. 4 Plot establishing the
Monod model
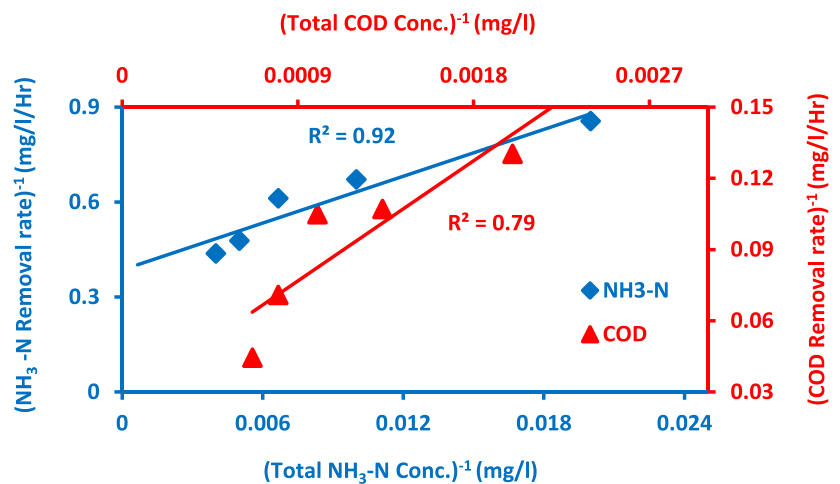
In this experiment, NH$_3$–N and COD were considered as two different substrate-limited variables. Hence, the kinetic factors, viz. K_s and k_4, were estimated (Fig. 4). The k_4 and K_s values for NH$_3$–N and COD were 2.59 and 64.13 and 38.46 and 2162.69, respectively. High R^2 values indicate that the data fits significantly. For both the substrates, the half saturation constant was observed to be high, which indicates the dependency of substrate consumption rate over initial concentration of substrate. Moreover, when the half saturation constant value is very less, it indicates that the microbial growth continues far towards completion, whereas a very high value of half saturation constant indicates formation of very small amount of TVSS.

Diffusion model

Consumption of substrate during microbial biosynthesis process with a biofilm might be interpreted using the diffusion model. Within the reactor, four different situations might arise, when the biomass synthesis process

is constrained by diffusion. These situations are shown below:

a. If the substrate concentration is low and the biofilm is thick, the substrate depletion rate takes place following pseudo-first-order kinetics, which is independent of the biofilm thickness.
b. When the substrate concentration and the biofilm thickness are high, then the substrate concentration on the biofilm is drawn near to the bulk. Therefore, the process kinetics might get controlled by diffusion and the rate equation is shown below (Converti et al. 1999).

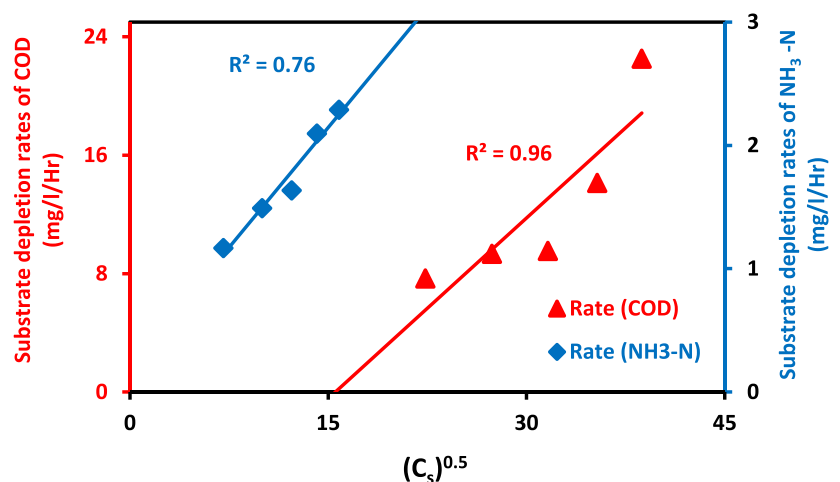$$dC_s/\mathrm{dt} = k_2(C_s)^{0.5} \qquad (8)$$

Fig. 5 Plot showing the rate of
substrate depletion as a function
of the square root of concentration

Table 4 Analysis of variance for various parameters

Variables for NH$_3$–N				
	F-value	p value	F-critical	Remarks
Depletion of NH$_3$–N				
Time (h)	49.75	1.33×10^{-10}	2.71	Significant
NH$_3$-N	133.04	4.14×10^{-14}	2.87	Significant
TVSS production				
Time (h)	55.30	5.03×10^{-11}	2.71	Significant
TVSS	5.56	0.003535	2.87	Significant
Variables for COD				
Depletion of NH$_3$–N				
Time (h)	15.38	2.92×10^{-6}	2.71	Significant
NH$_3$–N	9.27	0.000209	2.87	Significant
TVSS production				
Time (h)	15.38	2.92×10^{-6}	2.71	Significant
TVSS	12.09	3.7×10^{-5}	2.87	Significant

NH$_3$–N, ammonia nitrogen; *TVSS*, total volatile suspended solids; *COD*, chemical oxygen demand; level of significance 0.05

where, k_2 is the diffusion constant and Cs is initial substrate concentration.

c. When the substrate concentration is very low and the biofilm is porous, the process may result in pseudo-first-order reaction.
d. When the substrate concentration is high along with a porous biofilm, then the process may result in zero-order reaction and the rate equation is shown below.

$$dC_s/\mathrm{dt} = k_3 \tag{9}$$

where, k_3 is the constant for rate kinetics, dC_s/dt is the NH$_3$_N consumption rate, and t is the time.

The graphical representation among substrate consumption rate versus $(C_s)^{0.5}$ is given in Fig. 5. The R^2 values for NH$_3$–N and COD obtained were 0.96 and 0.76, suggesting the process might be controlled by diffusion. Thus, the diffusion coefficients for NH$_3$–N as well as COD consumption were obtained to be 0.13 as well as 0.81 h^{-1}.

Table 5 Model summary

Model summary	R	Standard error of coefficient	F change	Sig. F change
	0.79	39.03	30.12	9.95×10^{-12}
Variables	Coefficients	Standard error of coefficient	Beta	Significance
Constant	60.12	2.35	–	1.45×10^{-36}
Time	2.28	0.04	0.87	2.76×10^{-21}
COD	− 0.03	0.35	0.26	2.58×10^{-5}
NH$_3$–N	11.02	0.01	− 0.12	0.05

Dependent variable: TVSS

TVSS, total volatile suspended solids; *COD*, chemical oxygen demand; *NH$_3$–N*, ammonia nitrogen

Table 6 Principal component analysis

NH$_3$–N, ammonia nitrogen; *TVSS*, total volatile suspended solids; *COD*, chemical oxygen demand; *DO*, dissolved oxygen; *NO$_3^-$–N*, nitrate nitrogen; *NO$_2^-$–N*, nitrite nitrogen; *N$_2$O–N*, nitrous oxide nitrogen

Component matrix		
	Component	
	1	2
Time	0.91	
NH$_3$–N		0.53
TVSS	0.96	
COD		0.92
pH		
DO		
NO$_3^-$–N	0.86	
NO$_2^-$–N	0.88	
N$_2$O–N	0.97	
Eigenvalues	4.88	1.88
Cum variance	54.27	75.19

Statistical interpretation

Analysis of variance (ANOVA)

In this study, experiments were conducted for removal of nutrients (NH_3 and COD) from the wastewater along with time. Here NH_3–N and COD were considered as two parameters and their concentrations were varied. Analysis of variance using null hypothesis was undertaken as a statistical tool to check the existence of variation between both the variables (Table 4). In all the cases, significant ($p < 0.05$) variation has been observed between the variables, viz. time as well as nutrient concentration, thereby indicating the vital role played by them during the wastewater treatment. Initially during NH_3–N depletion both time and NH_3–N played a significant role, thereby determining the kinetics of NH_3–N depletion. Similarly for TVSS production, both time and TVSS concentration played a significant role. During COD variation, significant trends were observed for NH_3–N depletion and TVSS production.

Multi-linear regression analysis (MLRA)

MLRA as a statistical tool establishes the sole correlation among one dependent variable (i.e. TVSS) and multiple independent variables (i.e. NH_3–N, COD and time). It helps in predicting the dependent variable with the help of independent variables (with known values). The adequacy of this interpretation was checked by looking up on distinct statistical outputs, viz. R, standard error, beta, significance, F change and significance of F change (Table 5). Moreover, using Table 5, the results can be predicted using the regression equation due to high significance values.

Principal component analysis (PCA)

The PCA is a multi-variate statistical method, which was used to establish the interrelationships among distinct factors, viz. time, ammonia concentration, TVSS, COD, pH, DO, nitrate, nitrite and nitrous oxide. All the factors were explained using component 1 and component 2, which indicate that the variance of the observed factors had been accounted for both the components. The component matrix with factor loadings (> 0.5) and eigenvalues are shown in Table 6. The total number of factors generated from a typical factor analysis indicates the total number of possible sources of variation in the data. Component 1 explains 54.27% of the cumulative variance with a highest eigenvalue of 4.88 representing the most important source of variation in the data, and it is comprised of factors (loading value > 0.5) such as time, TVSS, nitrate, nitrite and nitrous oxide. The relationships between all the factors had positive correlations indicating that the increase of one factor would also lead to an increase of the other. The presence of NO_3^-–N, NO_2^-–N and N_2O–N in component 1 indicates the presence of nitrification mechanism during the wastewater treatment. Therefore, component 1 might be named as "nitrification". Similarly, component 2 explains a cumulative variance of 75.19% with a lowest eigenvalue of 1.88, which represents least data variation. It contains NH_3–N and COD. Here, both the factors perform an important portrayal for heterotrophic biosynthesis mechanism during the wastewater treatment. Therefore, component 2 can be interpreted as heterotrophic biosynthesis.

Conclusions

Based on the results obtained, it was observed that heterotrophic microorganisms can assimilate external carbon and nitrogen from wastewater resulting in its treatment. The removal of carbon in terms of COD was 58% to 92% within a period of 60 h, as against 52% to 97% in the case of NH_3–N. Production of N_2O during the biological uptake of NH_3–N is an indicator of nitrification by the nitrifiers. The mass transfer rates of 0.13 and 0.81 per hour and removal rate of 0.51 and 2.29 mg/l/h for NH_3–N and COD, respectively, and its kinetic study revealed that nutrient assimilation follows first-order rate kinetic signifying that the assimilation of nutrients would be more if their availability is increased. The doubling time of microbes varied from 26 to 121 h indicating that these microbes may be used in the heterotrophic biomass formation process. The ANOVA suggests the significance of time and nutrient concentration in the assimilation process. The PCA explained 75.19% of the total variance for the first (time, TVSS, NO_3^-, NO_2^-, N_2O) and second (NH_3–N and COD) components, which act as regulating parameters. The study concludes that computation of kinetics can help design and optimize the wastewater treatment process for effective nutrient removal by heterotrophic microbial biomass. This study is about the sustainable biodegradation process for wastewater treatment with a clear

mandate for translational research. The present study may be used to boost the bioaugmentation process, which otherwise helps in biodegradation of the toxic wastes, viz. nitrogen and organic carbon, into harmless and disposable products during the wastewater treatment and further beats the eutrophication of water bodies. Moreover, the microbial consortium for this study can be used for replacing the slow-growing microbes, which are used in sensitive field-scale technologies.

Compliance with ethical standards

Conflict of interest   The authors declare that they have no conflicts of interest.

References

Al-Isawi, R., Ray, S., & Scholz, M. (2017). Comparative study of domestic wastewater treatment by mature vertical-flow constructed wetlands and artificial ponds. *Ecological Engineering, 100*, 8–18.

APHA. (2012). *Standard methods for the examination of water and wastewater* (22nd ed.). Washington, DC: American Public Health Association.

Balagodatsky, S. A., Kesik, M., Papen, H., & Butterbach, B. K. (2006). Production of NO and N_2O by heterotrophic nitrifier Alcaligenes faecalis parafaecalis under varying conditions of oxygen saturation. *Geomicrobiology Journal, 23*(3–4), 165–176.

Converti, A., Borghi, A. D., Arni, S., & Molinari, F. (1999). Linearized kinetic models for the simulation of the mesophilic anaerobic digestion of pre-hydrolyzed woody wastes. *Chemical Engineering & Technology, 22*(5), 429–437.

Ebeling, J. M., Timmons, M. B., & Bisogni, J. J. (2006). Engineering analysis of the stoichiometry of photo autotrophic, autotrophic, and heterotrophic removal of ammonia-nitrogen in aquaculture systems. *Aquaculture, 257*(1–4), 346–358.

Foley, J., De Hass, D., Yuan, Z., & Lant, P. (2010). Nitrous oxide generation in full-scale biological nutrient removal wastewater treatment plants. *Water Research, 44*(3), 831–844.

Horne, A. J. (2002). Potential value of constructed wetlands for nitrate removal along some large and small rivers. *Internationale Vereinigung for Theoretische und Angcwandte Limnologie Verhandlungen (German), 27*, 4057–4062.

Kinidi, L., Tan, I. A. W., Wahab, N. B. A., Tamrin, K. F. B., Hipolito, C. N., & Salleh, S. F. (2018). Recent development in ammonia stripping process for industrial wastewater treatment. *International Journal of Chemical Engineering, 2018*, 1–14. https://doi.org/10.1155/2018/3181087.

Koren, D. W., Gould, W. D., & Bedard, P. (2000). Biological removal of ammonia and nitrate from simulated mine and mill effluents. *Hydrometallurgy, 56*(2), 127–144.

Masic, A., & Eberl, H. J. (2014). A modeling and simultaneous study of the role of suspended microbial populations in nitrification in a biofilm reactor. *Bulletin of Mathematical Biology, 76*(1), 27–58.

Mohanty, A., Ray, S., Yadav, A. K., & Chaudhury, G. R. (2015). Kinetics with optimization studies of nitrogen and organic elimination from wastewater via heterotrophic biomass conversion process. *Desalination and Water Treatment, 55*(6), 1542–1553.

Ni, B. J., Ruscalleda, M., Pellicer-Nacher, C., & Smets, B. F. (2011). Modeling nitrous oxide production during biological nitrogen removal via nitrification and denitrification, extensions to the general ASM models. *Environmental Science & Technology, 45*(18), 7768–7776.

Pant, D., Van Bogaert, G., Diels, L., & Vanbroekhoven, K. (2010). A review of the substrates used in microbial fuel cells (MFCs) for sustainable energy production. *Bioresource Technology, 101*(6), 1533–1543.

Ray, S., Mohanty, A., Ramulu, T. S., & Chaudhury, G. R. (2013). Emission of nitrous oxide and methane from alluvial soil through incubation. *Journal of Environmental Engineering and Landscape Management, 21*(3), 224–232.

Ray, S., Mohanty, A., Mohanty, S. S., Mishra, S., & Chaudhury, G. R. (2014). Optimization of biological elimination of ammonia and COD from waste water using response surface methodology. *Clean: Soil, Air, Water, 42*(12), 1744–1750.

Ray, S., Mohanty, A., Mohanty, S. S., Mishra, S., & Chaudhury, G. R. (2014a). Removal of nitrate and COD from wastewater using denitrification process: kinetic, optimization and statistical studies. *Clean Technologies and Environmental Policy, 16*(2), 291–301.

Reddy, K. R. (2010). Technical challenges to in-situ remediation of polluted sites. *Geotechnical and Geological Engineering, 28*(3), 211–221.

Wu, Y., Li, T., & Yang, L. (2012). Mechanisms of removing pollutants from aqueous solutions by microorganisms and their aggregates: a review. *Bioresource Technology, 107*, 10–18.

Leachate Characters and Impact at Bhalswa Landfill Site in Delhi, India

Lokesh Kumar, SK Singh

Department of Environmental Engineering, Delhi Technological University, Delhi, India

Abstract

A liquid which drained or leaches through the waste at a landfill site is known as leachate. Leachate from a landfill varies widely in composition depending on the age of the landfill and the type of waste that it contains. It can usually contain both dissolved and suspended material. This study concentrate on the composition of various parameters of leachate collected from a highly saturated sanitary landfill sites at Bhalswa, Delhi. it has been found that Bhalswa landfill leachate have highest concentration of different parameters such as total dissolve solid, total solid and electrical conductivity i.e., 9890 mg/l, 12580 mg/l and 14892 mho/cm respectively. These results will be helpful in future for determination of expected impact on ground water and biodiversity due to generation and percolation of leachate. This study will also be helpful to deal with the possible low cost treatment methods.

1. Introduction

The fast urbanization and economic growth in recent years leads to excessive municipal solid waste generation in the cities and creating a serious environmental problem in the world. It needs to be focused urgently for environmental protection. Almost all the countries collected their Municipal solid waste to be disposed to any landfill site[1-6] solid waste undergoes many physical chemical and biological changes on a landfill site, this process degrade the organic fraction of the waste along with the moisture content and suitable temperature. The percolating rain water leads to generation of a highly contaminated liquid called leachate, which contain large amount of organic matter like Ammonia nitrogen, heavy metal and chlorinated organic compound with inorganic salt. The composition and characteristic of landfill leachate varies with the age, precipitation waste type and composition and weather variation. That can be classified into three types based on the landfill leachate: old, intermediate and young. The classification and characteristic of landfill leachate is given in the table-1, (30). BOD and COD of young leachate is generally found high (4000-13000 mg/l) and (30000-60000 mg/l) respectively. BOD/ COD ratio ranging from 0.4 to 0.7, ammonium nitrogen varies 500 to 2,000 mg/l The pH found to be very low up to 4 with VFAs (10) As the landfill age increases and the fatty acid decomposition buy anaerobic bacteria it's about a period of 10 years it changes the characteristics of the leachate with a low COD ,less than 4000 mg per liter and pH range is 7.5 - 8.5 with low biodegradability(BOD5/COD <0.1) and high molecular weight compound[7-11]. For toxic analysis, different test organisms were used like Vibrio fischeri, Daphnia similes Artemia Salina and Brachydanio Rerio, which the standard for receiving water. In the early 1970 so many studies in Laboratories has been carried out for the effectiveness of various treatment method like biological physical and chemical processes on landfill leachate Biological treatment process is including anaerobic and aerobic processes are quite effective for leachate generated in the early stage with a high BOD/COD. However, for very low BOD/ COD ratio and higher concentration of toxic metals an aerobic process is not very effective [12-21]. Hence the physical and chemical processes are being used as a pre-treatment or the post treatment for this type of landfill leachate. After so many experiments and study is done by the researcher it concluded that the advanced oxidation process (AOPs) is the most suitable and easy chemical process by which the quality of landfill leachate can be improved. The advanced oxidation process can grade a variety of refractory compounds in landfill leachate [17]. The concept of the advanced oxidation process is based on the generation of highly reactive hydroxyle radical (.OH) as an oxidant. The different method like Ozone oxidation fenton oxidation and electrochemical oxidation system can generate or produce the radicals. Hydroxyl radical with an oxidation potential of 2.80 V (Table 1) can degrade recalcitrant organic such as aromatic, chlorinated and phenolic compound [18]. As soon as ozone or H_2O_2 initiate free radical a series of Oxidation reaction occurs in the

*Corresponding Author,

E-mail address:sksinghdce@gmail.com

solution and the radical rapidly react with the most of the target compounds, the rate of reaction depends upon the concentration of radical and pollutants, temperature, pH as well as the presence of scavengers such as bicarbonate ion [19]

Table 1: Landfill Leachate Classification Versus Age [8, 9]

	TYPE OF LEACHATE	YOUNG	INTERMEDIATE	OLD
1.	AGE (YEARS)	<5	5-10	>10
2.	PH	<6.5	6.5-7.5	>7.5
3.	COD (MG/L)	>10000	4000-10000	<4000
4.	BOD5/COD	0.5-1.0	0.1-0.5	<0.1
5.	ORGANIC COMPOUND	80% VFA	5% TO 30% VFA+ HUMIC AND FULVIC ACID	HUMIC AND FULVIC ACIDS
6.	AMMONIA NITROGEN (MG/L)	<400	N.A	>400
7.	TOC/COD	<0.3	0.3-0.5	>0.5
8.	HEAVY METAL (MG/L)	LOW TO MEDIUM	LOW	LOW
9.	BIODEGRADABILTY	IMPORTANT	MEDIUM	LOW

The chief probable ecological impact linked to landfill leachate is pollution of under groundwater and surface water. The hazard of groundwater the pollution is perhaps the most severe environmental impact from landfills because in the past most landfills were built without engineered liners and leachate gathering systems. More recently, regulations in many countries have required the installation of liners and leachate collection systems as well as a plan for leachate treatment reviewed the characteristics of leachate plumes down gradient of landfills. Delhi has 3 Landfill sites for the Municipal Solid Waste Disposal generated in all over Delhi on daily basis. The name of these landfill sites are – Bhalswa, Gazipur and Okhla. The largest Bhalswa landfill site was commissioned in the year 1993, Gazipur in 1984 and Okhla in 1994.

Table 2: Location and capacity

Name	Location	Area (hectares)	Starting year	Initial amount of MSW T/day	MSW received T/day	End of landfill life
Bhalswa	North Delhi	26.22	1993	1200	3200	2005
Gazipur	East Delhi	29.62	1984	800	2100	2008
Okhla	South Delhi	22.89	1994	400	1200	2005

These landfill sites are not designed as per the schedule 3 of MSWs rules which came into effect in year 2000. Even DPCC has not authorized to these landfill sites. The Bhalswa landfill site is used for disposal about 2150 MTD, which is the largest about all 3 landfill sites and overall MSW generated is about 8370 MTD. The solid waste including all commercial municipal, industrial and agricultural activities may contain different types of hazardous pollutants. Land filling is the preferred method for MSW disposal due to its favorable economics. Therefore it is required to have full proof designed landfill sites to prevent contamination of groundwater though Leachate, soil and air. The vicinity of this landfill site has reported the contamination of groundwater (Bharat Jhamnani and SK Singh-IJCEE1:32009) .The people residing in surrounding areas has reported to have different types of diseases and infections like Gastro intestinal diseases , Musculoskeletal pain , skin and eye irritation and

respiratory problems (Amita Bhaduri 08-2015 India Water Portal) This 40-45 acre landfill site was confirmed tired in 2006 but still the municipal corporation of Delhi continued to dumpe the solid waste in this site.

2. Geology of the Area

Fig. 1: Delhi Map

3. Characteristics of Leachate

The systematic study has revealed that the groundwater contamination at Bhalswa landfill is significantly high due to landfill leachate. The parameter for iron, copper, nickel, zinc and oxide are 20mg/Lt, <10mg/Lt, <3mg/Lt, <10mg/Lt and 4000mg/Lt respectively. The concentration Of BOD volatile solid and COD are much higher in the Bhalswa landfill sites in Delhi. These are approx. as follows:

1. BOD = 3300mg/Lt
2. Volatile Solids = 3100mg/Lt
3. COD = 5840 mg/Lt

The higher values of organic matter indicate that the groundwater has been highly contaminated due to landfill leachate and Bhalswa. It requires an efficient and economic method for the treatment. Here is a list of parameters tested for ground water at Bhalswa [4].
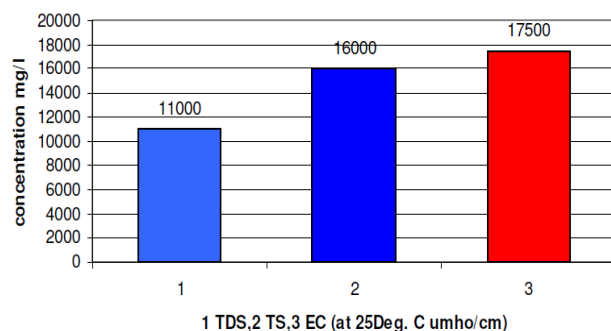

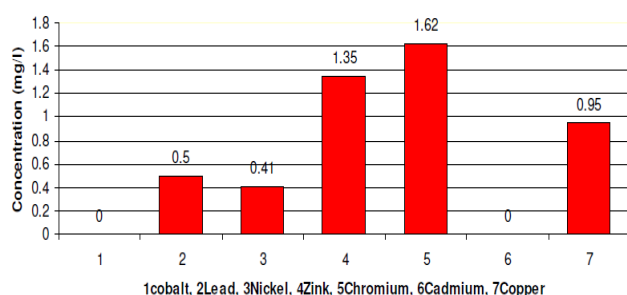**Fig.2:** Characterization of solids at Bhalaswa site

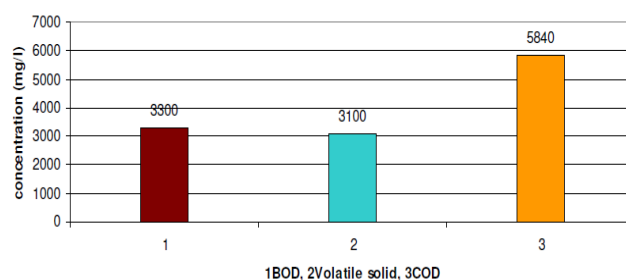**Fig.3:** Heavy Metals at Bhalswa
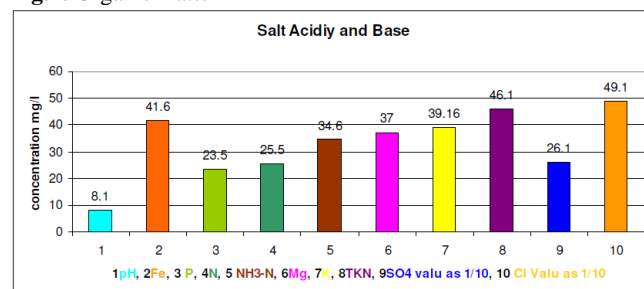

Fig.4: Organic matter

Fig.5: Salt Acidiy and Base

4. Methodology

Leachate Pollution Index (LPI) can be used in a number of conducts together with landfill ranking, allocation of resources for landfill remediation, trend analysis, standard enforcements, scientific research and public information. Leachate pollution potential of a landfill is known by assigning a single number grading from 5 to 100 on the basis of various leachate pollution parameters at a given time. The trend study developed based for the landfill can be used to decide the post closure monitoring periods. The overall pollution potential of landfill leachate is calculated by using Rand Corporation Delphi Technique for Leachate pollution index (Arif ahmad et. al. Elsevier 2018) LPI is an easy and means for assess the probable hazards of the leachate from the landfill sites located at Bhalswa landfill sites in Delhi. The concept and development of LPI has been accepted properly to another place by Kumar and Alappat [3]. The brief description of LPI is by eq. (1):

$$LPI = \sum_{i=1}^{n} W_i P_i \tag{1}$$

Where, W_i and P_i are the weight and sub-index values of the ith leachate pollutant variable, respectively and n is the total number of pollutant variables. If the numeral of total pollutant variables is equal to 18 then the total weight of the pollutant is equal to 1 and the LPI can be estimated using Eq. (1). In case, the number of pollutant variables less than 18 then for the estimating the LPI, Eq. (1) is divided by the total value of weights of the pollutant variables and so the LPI under this conditions is describe by eq 2:

$$LPI = \frac{\sum_{i=1}^{m} W_i P_i}{\sum_{i=1}^{m} W_i} \tag{2}$$

Where, m is less than n.

The leachate pollution changes in a particular landfill over a period of time and higher LPI number implies a poor environmental condition. It can be used to determine whether a landfill requires immediate attention in terms of introducing remedial actions.

5. Results and Discussion

LPI values were calculated for Bhalaswa landfills site of Delhi. The leachate sampling and analysis was carried out for landfill sites of Bhalswa. The Physical and chemical analysis of Bhalaswa landfill leachate were collected and analyzed in Jamia Millia Islamia Lab by Syed et al. [4]. The LPI values as estimated are tabulated in Tables

International Journal of Advance Research and Innovation

(1) for different landfill sites. The results of the samples illustrate that they were not found traces of cyanide, mercury and arsenic. So, in this study the weight age for these leachate pollutants have not been taken into thought while estimating the LPI values for this landfill site [5]. The concentrations of organic and inorganic compounds parameters were establish to be elevated in Bhalswa landfill leachate sample. Also, current (in Year 2018) BOD and COD of the Bhalswa landfill site were elevated and its range varies from 4100mg/l to 6540mg/l when test conducted in DTU lab,

Table 3: LPI Value at Bhalswa

Pollutant, ppm	LEACHATE	Wi	Pi	PiWi
pH	8.1	.055	5	0.276
TDS	11284	.050	8	5.020
BOD3	3300	.061	55	4.781
COD	5840	.062	80	5.727
Total kjehldahl nitrogen	46.1	.053	95	0.529
Ammonia Nitrogen	34.6	.051	100	0.510
Iron	41.6	.044	5	0.445
Copper	0.95	.050	5	0.249
Nickel	0.45	.052	5	0.313
Zinc	1.35	.056	5	0.338
Lead	0.56	.063	5	0.316
Chromium	1.84	.064	10	2.422
Chlorides	49.1	0.048	5.3	0.967
Final LPI= 30.88				

Source :-B.P Naveen et al [5]

Table 4: Source :- (Arif ahmad et. al. 2018)

Variation of leachate pollution index (LPI) in pre-monsoon and post-monsoon seasons adopted by (Kumar and Alappat, 2005) calculated as LPI = $\frac{\sum_{i=1}^{m} WiPi}{\sum_{i=1}^{m} Wi}$ Where m is the number of leachate pollutant parameters for which data are available, but in that case, m < 18 and $\sum_{i=1}^{m} Wi < 1$.

S.N.	Leachate constituent	Average value		Individual Pollution Rating (pi)		Weight (Wi)		Overall Pollution Rating (pi Wi)	
		Premonsoon	Postmonsoon	Premonsoon	Postmonsoon	Premonsoon	Postmonsoon	Premonsoon	Postmonsoon
1	pH	7.92	8.38	5	5	0.055	0.055	0.275	0.275
2	TDS	22395	19500	50	46	0.05	0.05	2.5	2.3
3	BOD3	10800	7975	60	58	0.061	0.061	3.66	3.538
4	COD	25400	22960	85	83	0.062	0.062	5.27	5.146
5	Fe	11.87	10.92	5	5	0.045	0.045	0.225	0.225
6	Cu	1.00	0.91	7	6	0.05	0.05	0.35	0.30
7	Ni	0.83	0.62	7	6	0.052	0.052	0.364	0.312
8	Zn	3.96	3.68	7	7	0.056	0.056	0.392	0.392
9	Pb	0.18	0.11	6	5	0.063	0.063	0.378	0.315
10	Cr	4.06	3.87	25	24	0.064	0.064	1.6	1.536
11	Cl	9150	7500	85	72	0.048	0.048	4.08	3.456
	Total					0.606	0.606	19.094	17.795
	Final LPI value by dividing Total Overall pollution rating by Total Wi							31.51	29.36

6. Conclusions

Due to the higher LPI value of Bhalswa landfill leachate sample, this site has been identified as the most contaminating site for solid waste dumping. It has already reached to its optimum capacity in 2006 but still it is being used by Municipal Corporation of Delhi which may leads very dangerous situation in terms of contamination and health to the surrounding biodiversity. High value of LPI in both the seasons shows that waste in the dumping site is not stabilized yet and it has more potential to deteriorate the quality of groundwater. The poorly managed dumping of municipal solid waste, in the speedy urbanizing Delhi region, at Bhalswa landfill site affected the groundwater quality of the shallow aquifers close to the site. To organize or reduce the crash of MSW leachate on groundwater resources around the landfill sites, construction of lined engineered dumping site and leachate collection ponds are the best way to protect the movement of the leachate into the shallow groundwater of the study area. A new site for dumping should be preferred as an substitute away from any residential settlement, river and agricultural field to minimize the environmental impact (Arif ahmad et. al. 2018).

REFERENCES

[1] BP Naveen, PV Sivapullaiah, TG Sitharam. Characteristics of a Municipal Solid Waste Landfill Leachate, Indian Geotechnical Conference on Geotechnics for Inclusive Development of India (GEOIND), (18- 20December) Kakinada, 2014, 1413-1419.

[2] BP Naveen, PV Sivapullaiah, TG Sitharam. Influence of Leachate Migration on Ground Water Quality, 5th Indian Young Geotechnical Engineer's Conference (5IYGEC-2015), Indian Geotechnical Society BarodaChapter, 14-15 March, 2015, 127-128.

[3] D Kumar, BJ Alappat. A technique to quantify landfill leachate pollution, Proc., 9th Int. Landfill Symp. 2003, 243-244.

[4] SA Syed, S Kumar, P Alam. Characterization of Leachate at Various Landfill Site of Delhi, India, 2nd International Conference on Science, Technology and Management, 2015,1078-1085.

[5] BP Naveen et.al. Assessment Of Leachate Pollution Index For Delhi Landfill Sites, India. OAIJSE, 2 (9), 2017, 98-101.

[6] S Esakku, A Selvam, KI Palanivelu, R Nagendran, J Kurian, Leachate Quality of MunicipalSolid Wste Dumpsites at Chennai, India, Asian Journal of Water, Environment and Pollution, 3(1), 2006, 69-76.

[7] MoEF, Municipal solid waste management and handling rules, Ministry of Environment and Forests, Govt. of India, 2000.

[8]OO Aluko, MKC Sridhar, PA Oluwande. Characterization of leachates from a municipal solid waste landfill site in Ibadan, Nigeria, J Environ Health Res., 2 (1), 2003, 32-37.

[9] P Vasanthi, S Kaliyappan, R Srinivasraghvan. Impact of poor solid waste management on ground water. Environmental Monitoring Assessment, 143, 2008, 227-238.

[10] LB Jorstad, J Jankowski, RI Acworth. Analysis of the distribution of inorganic constituents in alandfill leachate-contaminated aquifer Astrolabe park, Sydney, Australia, Environ Geology, 46, 2004, 263-272.

[11] K Joseph, S Esakku, R Nagendran, C Vishvanathan. A decision making tool for dumpsite rehabilitation in developing countries. In: proc Sardinia, Eleventh International waste management and landfill symposium, Italy, 2005.

[12] AK Karunarathna, BFA Basnayake. Sessional Variations in Leachate Characteristics from Municipal Solid Waste Dumpsites in India and Srilanka. International Conference on Sustainable Solid Waste Management, 2007, 341-347.

[13] YD Kim, DG Lee. Comparative study on leachate in closed landfill sites focusing on seasonal variations. J Mater Cycles Waste Manag., 11, 2009, 174-182.

[14] A Amokrane, C Comel, J Veron. Landfill leachates pretreatment by coagulationflocculation. Water Res., 31: 2775-2782. DOI: 10. 1016/S0043-1354, 1997, 00147-4.

[15] V Bigot, F Luck, H Paillard. A Wagner. Landfill leachate treatment: comparison of three oxidation processes using ozone. In: Proceedings of the International Ozone Association Regional Conference, European-African Group, , Zürich, Switzerland, 7, 1994, 219-228.

[16] CPHuang, C Dong, Z Tang. Advanced chemical oxidation: Its present role and potential future in hazardous waste treatment. Waste Management, 13, 1993, 361-377.

[17] A Lopez, M Pagano, A Volpe, AD Pinto. Fenton's pre-treatment of mature landfill leachate. Chemosphere, 54, 2004, 1005-1010.

[18] A Marco, S Esplugas, G Saum. How and why combine chemical and biological processes for wastewater treatment. Water Sci. Technol., 35, 1997, 321-327.

[19] TI Qureshi, HT Kim, YJ Kim. UV catalytic treatment of municipal solid-waste landfill leachate with hydrogen peroxide and ozone oxidation. J. Chem. Eng., 10, 2002, 444-449.

[20] FJ Rivas, F Beltran, O Gimeno, B Acedo, F Carvalho. Stabilized leachates: ozone activated carbon treatment and kinetics. Water Res., 37, 2003, 4823-4834.

[21] P Schulte, A Bayer, F Kuhn, T Luy, M Volkmer. 1995. H2O2/O3, H2O2/UV and H_2O_2/Fe_2+processes for the oxidation of hazardous wastes. Ozone Sci. Eng., 17, 1995, 119-134.

[22] AC Silva, M Dezotti, GL Sant'Anna. Treatment and detoxification of a sanitary landfill leachate. Chemosphere, 55, 2004, 207-214.

[23] M Steensen. Chemical oxidation for the treatment of leachate-process comparison and results from full-scale plants. Water Sci. Technol., 35, 1997, 249-256.

[24] O Wable, M Jousset, P Courant, JP Duguet. Oxidation of landfill leachates by ozone and hydrogen peroxide: A French example. In Proceedings of the International Symposium on Ozone-Oxidation Methods for Water and Wastewater Treatment, April 26-28, Wasser Berlin, Germany, 1993, 433-444.

[25] F Wang, DW Smith, MG El-Din. Application of advanced oxidation methods for landfill leachate treatment-a review. J. Environ. Eng. Sci., 2, 2003, 413-427.

[26] B Bae, E Jung, Y Kim, H Shin. Treatment of landfill leachate using activated sludge process and electron-beam radiation. Water Res., 33, 1999, 2669-2673.

[27] Cesaro et. al. J Bioremoved biodeg. 1000208 action of advance oxidation process for the pretreatment of waste water for its biological processing in order to highlight the enhancement of waste water biological treat ability supplied by different advance oxidation, JBRBD 8, 2014.

[28] N Narkis, RM Schneider. Evaluation of ozone included biodegradability of wastewater treatment plant effluent. Water research 14:929-939 worked on municipal waste water treatment plant effluents and aim on BOD5 process, 1980.

[29] ABC Alvers, C Diaper, SA Parson. Partial oxidation of hydrolysed and unhydrolysed textile Azo dyes by ozone and the effect on biodegradability process safety and environmental protection 79(2), 2001, 103-108.

[30] HSU Yc, HC Yang, JH Chen. The enhancement of the biodegradability of phenolic solution by using pre ozonation based on high ozone utilization. Chemosphere 56, 2004, 149-158.

[31] L Bijan, M Mohseni. Integrated zone and bio treatment of pulp mill effluent and change in biodegradability and molecular weight distribution of organic compounds. Water res. 39, 2005, 3763-3772.

[32] I Arslan-Alaton, AE Caglayan. Toxicity and biodegradability assessment of raw and ozonated procaive penicillin G formulation effluent. Ecotoxical Environ Saf 63, 2006, 131-140

[33] AD Coelho, C Sans, A Agnera, MJ Gomez, S Esplugas et al. Effect of Ozone pretreatment on diclofenac: intermediate biodegradability and toxicity assessment. Sci Total Environ 407, 2009, 3572-3578.

[34] CA Somensi at al. Use of ozone in a pilot scale plant for textile waste water pretreatment: Physicochemical efficiency, degradation by products identification and environmental toxicity of treated waste water. Journal of hazardous material 175, 2010, 235-240

[35] Y Sindhu at al., COD removal of different industrial waste water by Fenton oxidation process. IJESRT, 3(3), 2014.

Non-Quasi-Static Small-Signal Modeling of TGRC MOSFET in Parameter Perspective for RF/Microwave Applications

Ajay Kumar[1], Neha Gupta[2], M.M. Tripathi[1] and Rishu Chaujar[3*]

[1]*Electrical Engineering Department, Delhi Technological University, Delhi, India*
[2]*Applied Science and Humanity Department, AGITM, Indraprastha University, Delhi, India*
[3*]*Applied Physics Department, Delhi Technological University, Delhi, India*

Abstract— **This work reported an accurate modeling of the non-quasi-static small signal model of Transparent Gate Recessed Channel (TGRC) MOSFET in parameter perspective using ATLAS-3D device simulator. From the small signal equivalent circuit, simulated and modeled results are compared at THz frequency range in terms of *Y* (admittance) parameters, *Z* (impedance) parameters and *h* (hybrid) parameters. The input impedance enhances by 89.4% as when gate length (L_G) reduces from 40 nm to 20 nm while it improves by 68.6% when negative junction depth (NJD) reduces from 15 nm to 5 nm in the TGRC device. Moreover, it is also observed that, admittance and hybrid parameters are significantly improved with reduced device parameter and are found in good agreement between modeled and simulated results. All modeled results show that TGRC design improves the small signal behavior for sub-20 nm regime thus, providing the detailed insight to RF engineers for RF applications.**

Keywords— *Modeling; ITO; TGRC-MOSFET; Y, Z and h parameters.*

I.   INTRODUCTION

Transparent conducting oxide (TCO) is the most frequently used material today in the electronics and optoelectronics devices for the excellent performance of complement metal oxide semiconductor (CMOS) technology [1]. Polycrystalline or amorphous TCO thin film is generally used as a transparent electrode. It can also be used as semiconductor with higher concentration (more than 10^{20} cm^{-3}) and higher energy band gap (above 3 eV). Many TCO materials have been developed to obtained low resistivity and high conductivity such as ZnO:Ga, SnO$_2$:F, In$_2$O$_3$:Sn, SnO$_2$:Sb, and ZnO:Al wit binary compounds [2] but In$_2$O$_3$:Sn called Indium Tin Oxide (ITO), is the most popularly TCO because ITO has lowest deposition temperature, very high conductivity (1x10^5 S/cm), low resistivity (in the order of 10^{-5} Ω cm) and higher Hall mobility (53.5 cm^2 V^{-1}s^{-1}) [1]. Deposition of ITO on the gate is very easy during the fabrication process but for nano level electrode, a well-controlled etching is necessary to define. ITO has very low power consumption thus the circuit performance of a CMOS can be improved CMOS by ITO as a gate material [3].

Moreover, the shrinking of CMOS may enhance the RF figure of merits (FOMs) which has prepared it for system-
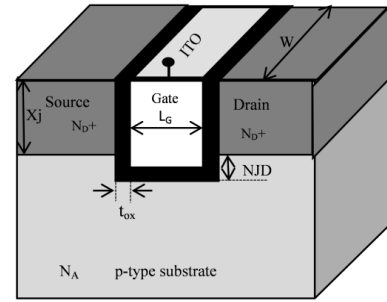

Fig. 1: 3D-Structure of TGRC MOSFET. Here, L_G = 20nm to 40 nm, t_{ox} = 2 nm, and width=200 nm. Source and drain regions are heavily doped with an n-type impurity of 5×10^{19} cm^{-3} and substrate doping with a p-type impurity is 1×10^{17} cm^{-3}. NJD=5 nm to 15 nm, V_{gs} = 0.7 V and V_{ds} = 0.5 V have been taken in to account.

on-chip applications and achieve very high (THz) cut-off frequencies, which makes it applicable to CMOS technology for RF and microwave applications [4, 5].

This paper presents an accurate modeling of non-quasi-static small signal model of TGRC device in which ITO, as a transparent gate material is amalgamated over the recessed channel (RC) MOSFET [6]. It is observed that the proposed device design (shown in Fig. 1) enhances the performance in terms of small signal parameters at THz frequency range [7] [8]. In previous work [9], all the small signal parameters have already been defined and all the simulated and modeled results have been compared with the conventional MOSFETs.

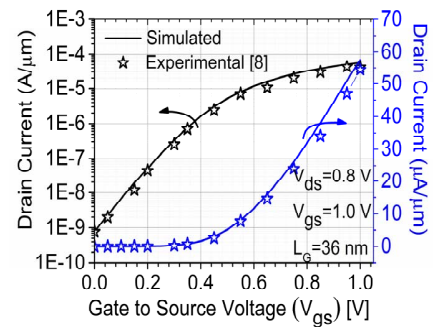## II.   SIMULATION METHODOLOGY, CALIBRATION

Fig. 2. Calibration of experimental and simulation data of 36 nm recessed channel MOSFET.

This work is based on TCAD simulations [10], and during the simulation, different models have been used such as, for mobility of carriers FLDMOB (Parallel Electric Field Dependence) under the impact of change in electric field. Another model, LKASRH (concentration-dependent Klaassen Shockley-Read-Hall Recombination) is used for carrier generation-recombination, and concentration-dependent lifetime of carriers has also been included [10]. Further, the calibration of models has been performed using simulated and experimental data [11]. The experimental data of fabricated grooved MOSFET (L_G=36 nm) is drawn out from [11] and plotted (as shown in Fig. 2) against simulated results for same device dimensions and it is observed from Fig. 2 that the modelled and simulated results are well calibrated, thus showing the validity of simulation models.

III. RESULTS AND DISCUSSION

All small signal parameters have been extracted by non-quasi-static (NQS) circuit of TGRC device and has been developed as shown in Fig. 3.
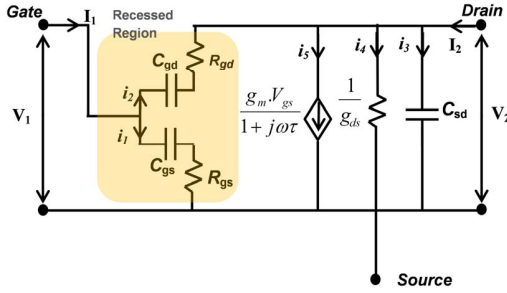

Fig. 3: RF MOSFET operated non-quasi-static (NQS) model.

A. Admittance (Y) parameters

Y-parameters are evaluated by solving the non-quasi-static small signal model shown in Fig. 3.

Total current at input port and out port is given by-

$$I_1 = i_1 + i_2 \tag{1}$$
$$I_2 = i_3 + i_4 + i_5 - i_1 \tag{2}$$

Applying nodal analysis at input node,

$$\frac{V_1}{X_1} + \frac{V_1 - V_2}{X_2} = 0 \tag{3}$$

$$\frac{V_2}{X_3} + \frac{V_2 - V_1}{X_2} + \frac{g_m V_{gs}}{1 + j\omega\tau} = 0 \tag{4}$$

Where $X_1 = \dfrac{1 + j\omega R_{gs} C_{gs}}{j\omega C_{gs}}$; $X_2 = \dfrac{1 + j\omega R_{ds} C_{ds}}{j\omega C_{ds}}$; $X_3 = \dfrac{1}{g_{ds} + j\omega C_{sd}}$

By solving equation (3) and (4), and using approximations

$$\omega^2 R_{gs}^2 C_{gs}^2 \ll 1, \; \omega^2 R_{gd}^2 C_{gd}^2 \ll 1 \text{ and } \omega^2 \tau^2 \ll 1$$

Input admittance (Short circuit) is calculated as-

$$Y_{11} \cong \omega^2 (R_{gs} C_{gs}^2 + R_{gd} C_{gd}^2) + j\omega(C_{gs} + C_{gd})$$

$$Y_{11} \cong \omega^2 (\alpha + \beta) + j\omega(C_{gs} + C_{gd}) \tag{5}$$

where, $\alpha = R_{gs} C_{gs}^2, \beta = R_{gd} C_{gd}^2$

Further, the output admittance (short circuit) is to be

$$Y_{22} \cong g_{ds} + \omega^2 \beta + j\omega(C_{gd} + C_{sd}) \tag{6}$$

Short circuit forward and reverse transfer admittance are as follows

$$Y_{12} \cong -\omega\beta - j\omega C_{gd} \tag{7}$$

$$Y_{21} \cong -\omega^2 \beta - j\omega C_{gd} + g_m(1+\tau) \tag{8}$$

Fig. 4(a) represents the influence of gate length variation on Y_{11} and Y_{22} w.r.t. frequency. It can be observed from Fig. 4(a) that, when the gate length shrinks from 40 nm to 20 nm then Y_{11} reduces while Y_{22} enhances as for better performance of device at RF region, Y_{11} should be low and Y_{22} should be high. From the results, it has also been observed that the modeled and simulated results are in good agreement. Further, other admittance parameters (Y_{12} and Y_{21}) have been evaluated for different gate lengths as shown in Fig. 4(b). It is observed that both the parameters are improved when device is modulated to 20 nm regime with a well match between modeled and simulated results. Similarly, when the NJD shrinks from 15 nm to 5 nm then Y_{11} reduces while Y_{22} enhances as shown in Fig. 5(a). Fig. 5(b) reflects that Y_{12} and Y_{21} are also improved when the device NJD reduces to 5 nm and modeled results well matched with simulated results.
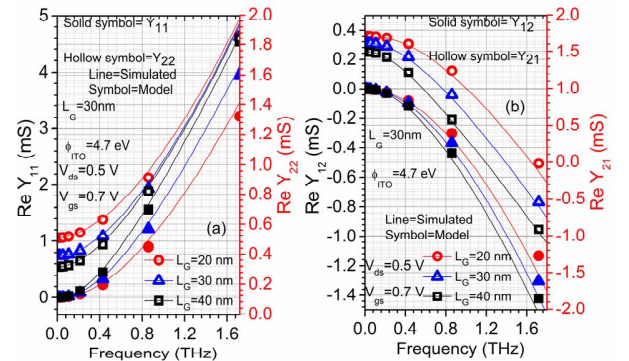

Fig. 4: (a) Y-parameters Re (Y_{11}, Y_{22}) and (b) Y-parameters Re (Y_{12}, Y_{21}) w.r.t. frequency at different gate length for TGRC-MOSFET.
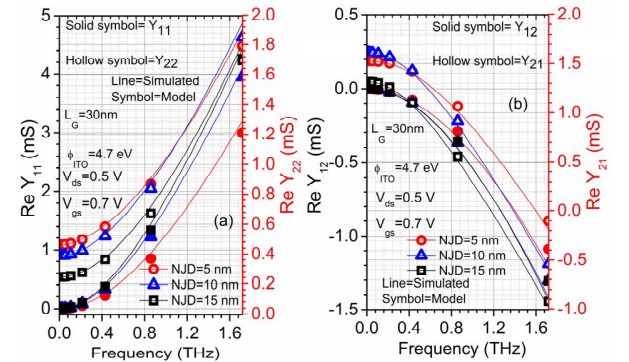

Fig. 5: (a) Y-parameters Re (Y_{11}, Y_{22}) and (b) Y-parameters Re (Y_{12}, Y_{21}) w.r.t. frequency at various NJDs for TGRC-MOSFET.

B. Impedance (Z) parameters

From the non-quasi-static small signal model (reflected in Fig.3), the *Z*-parameters can be investigated as follows:

Input and output impedance of (open circuit) has been calculated as-

$$Z_{11} \cong \frac{Y_{22}}{\Delta Y} \cong \frac{\begin{array}{c} g_{ds} + \omega^2 \beta + \\ j\omega(C_{gd} + C_{sd}) \end{array}}{\begin{array}{c} j\omega(C_{gs}g_{ds} + C_{gd}g_{ds} + C_{gd}g_m + \tau C_{gd}g_m) \\ + j\omega^3(\alpha C_{gd} + \beta C_{gs} + C_{sd}(\alpha + \beta)) + \alpha\beta\omega^4 \\ + \omega^2(\alpha g_{ds} + \beta g_{ds} - C_{gs}C_{sd} - C_{gd}C_{sd} + \beta g_m(1+\tau) + C_{gd}^2) \end{array}} \quad (9)$$

$$Z_{11} \cong \frac{g_{ds} + \omega^2\beta + j\omega(C_{gd} + C_{sd})}{\chi} \quad (10)$$

$$Z_{22} \cong \frac{Y_{11}}{\Delta Y} \cong \frac{\begin{array}{c} \omega^2(\alpha + \beta) \\ + j\omega(C_{gs} + C_{gd}) \end{array}}{\begin{array}{c} j\omega(C_{gs}g_{ds} + C_{gd}g_{ds} + C_{gd}g_m + \tau C_{gd}g_m) \\ + j\omega^3(\alpha C_{gd} + \beta C_{gs} + C_{sd}(\alpha + \beta)) + \alpha\beta\omega^4 \\ + \omega^2(\alpha g_{ds} + \beta g_{ds} - C_{gs}C_{sd} - C_{gd}C_{sd} + \beta g_m(1+\tau) + C_{gd}^2) \end{array}} \quad (11)$$

$$Z_{22} \cong \frac{\omega^2(\alpha + \beta) + j\omega(C_{gs} + C_{gd})}{\chi} \quad (12)$$

Input to output port and output to input port pen circuit transfer impedances will be as follows :

$$Z_{12} \cong \frac{-Y_{12}}{\Delta Y} \cong \frac{\omega\beta + j\omega C_{gd}}{\begin{array}{c} j\omega(C_{gs}g_{ds} + C_{gd}g_{ds} + C_{gd}g_m + \tau C_{gd}g_m) + \\ j\omega^3(\alpha C_{gd} + \beta C_{gs} + C_{sd}(\alpha + \beta)) + \alpha\beta\omega^4 \\ + \omega^2(\alpha g_{ds} + \beta g_{ds} - C_{gs}C_{sd} - C_{gd}C_{sd} + \beta g_m(1+\tau) + C_{gd}^2) \end{array}} \quad (13)$$

$$Z_{12} \cong \frac{\omega\beta + j\omega C_{gd}}{\chi} \quad (14)$$

$$Z_{21} \cong \frac{-Y_{21}}{\Delta Y} \cong \frac{\begin{array}{c} \omega^2\beta + j\omega C_{gd} \\ -g_m(1+\tau) \end{array}}{\begin{array}{c} j\omega(C_{gs}g_{ds} + C_{gd}g_{ds} + C_{gd}g_m + \tau C_{gd}g_m) + \\ j\omega^3(\alpha C_{gd} + \beta C_{gs} + C_{sd}(\alpha + \beta)) + \alpha\beta\omega^4 \\ + \omega^2(\alpha g_{ds} + \beta g_{ds} - C_{gs}C_{sd} - C_{gd}C_{sd} + \beta g_m(1+\tau) + C_{gd}^2) \end{array}} \quad (15)$$

$$Z_{21} \cong \frac{\omega^2\beta + j\omega C_{gd} - g_m(1+\tau)}{\chi} \quad (16)$$

where

$$\chi = j\omega(C_{gs}g_{ds} + C_{gd}g_{ds} + C_{gd}g_m + \tau C_{gd}g_m) + j\omega^3(\alpha C_{gd}$$
$$+ \beta C_{gs} + C_{sd}(\alpha + \beta)) + \alpha\beta\omega^4$$
$$+ \omega^2(\alpha g_{ds} + \beta g_{ds} - C_{gs}C_{sd} - C_{gd}C_{sd} + \beta g_m(1+\tau) + C_{gd}^2)$$
$$\alpha = R_{gs}C_{gs}^2$$
$$\beta = R_{gd}C_{gd}^2$$

τ = Time constant. Assume that
$$\omega^2 R_{gs}^2 C_{gs}^2 \ll 1, \ \omega^2 R_{gd}^2 C_{gd}^2 \ll 1 \text{ and } \omega^2\tau^2 \ll 1$$

Fig. 6(a) and Fig. 7(a) reflects the real values of *Z*-parameters Re (Z_{11}, Z_{22}) for various gate lengths and NJDs respectively. It is observed that Z_{11} and Z_{22} are higher at lower frequency and decrease w.r.t. frequency when the gate length and NJD reduces. Z_{12} and Z_{21} are known as transfer impedance and for better RF performance the value of these parameters should be high in the MOSFET. From Fig. 6(b) and Fig. 7(b) it is depicted that Z_{12} and Z_{21} both are high in TGRC for reduced gate length and NJD respectively due to ITO which increases the current driving capability, hence the gain of the device. The modelled and simulated results are well calibrated as reflected in Fig. 6 and Fig. 7.
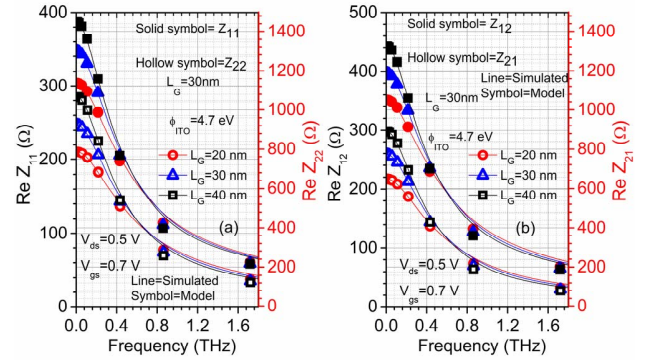
Fig. 6: (a) Z-parameters Re (Z_{11}, Z_{22}) and (b) Z-parameters Re (Z_{12}, Z_{21}) w.r.t. frequency at different gate length for TGRC-MOSFET.
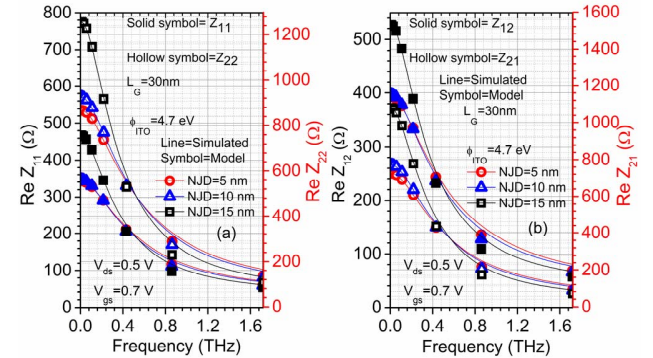
Fig. 7: (a) Z-parameters Re (Z_{11}, Z_{22}) and (b) Z-parameters Re (Z_{12}, Z_{21}) w.r.t. frequency at different NJDs for TGRC-MOSFET.

C. Hybrid (h) parameters

h-parameters can be easily calculated with the help of *Y*-parameters, as evaluated from equations (17) to (20) [12].

From equation (5), Short circuit input impedance can be obtained as follows.

$$h_{11} \cong \frac{1}{Y_{11}} \cong \frac{1}{\omega^2(\alpha + \beta) + j\omega(C_{gs} + C_{gd})} \quad (17)$$

Similarly, open circuit output admittance

$$j\omega(C_{gs}g_{ds} + C_{gd}g_{ds} + C_{gd}g_m + \tau C_{gd}g_m) +$$

$$j\omega^3(\alpha C_{gd} + \beta C_{gs} + C_{sd}(\alpha + \beta))$$

$$h_{22} \cong \frac{\Delta Y}{Y_{11}} \cong \frac{+ \alpha\beta\omega^4 + \omega^2(\alpha g_{ds} + \beta g_{ds} - C_{gs}C_{sd} - C_{gd}C_{sd} + \beta g_m(1+\tau) + C_{gd}^2)}{\omega^2(\alpha + \beta) + j\omega(C_{gs} + C_{gd})} \quad (18)$$

$$h_{22} \cong \frac{\Delta Y}{Y_{11}} \cong \frac{\chi}{\omega^2(\alpha + \beta) + j\omega(C_{gs} + C_{gd})}$$

Open circuit reverse voltage gain

$$h_{12} \cong \frac{-Y_{12}}{Y_{11}} \cong \frac{\omega\beta + j\omega C_{gd}}{\omega^2(\alpha + \beta) + j\omega(C_{gs} + C_{gd})} \quad (19)$$

Short circuit forward current gain,

$$h_{21} \cong \frac{Y_{21}}{Y_{11}} \cong \frac{-\omega^2\beta - j\omega C_{gd} + g_m(1+\tau)}{\omega^2(\alpha + \beta) + j\omega(C_{gs} + C_{gd})} \quad (20)$$

The real part of h_{11} and h_{22} are shown in Fig. 8(a) and Fig. 9(a) of TGRC MOSFET with varied gate length and negative junction depth respectively and modeled results have been compared with simulated results as well. It is evaluated that h_{11} reduces and h_{22} enhances with the reduction of gate length and NJD as shown in Fig. 8(a) and Fig. 9(a) respectively. Fig. 8(b) and Fig. 9(b) reflect the real of h_{12} and h_{21} respectively for different gate length and NJD w.r.t. frequency. h_{12} is less and h_{21} is high for higher dimensions.

Fig. 8: (a) h-parameter (h_{11}, h_{22}) and (b) h-parameter (h_{12}, h_{21}), w.r.t. frequency at different NJDs for TGRC-MOSFET.

Fig. 9: (a) h-parameter (h_{11}, h_{22}) and (b) h-parameter (h_{12}, h_{21}), w.r.t. frequency at different gate length for TGRC-MOSFET.

IV. CONCLUSION
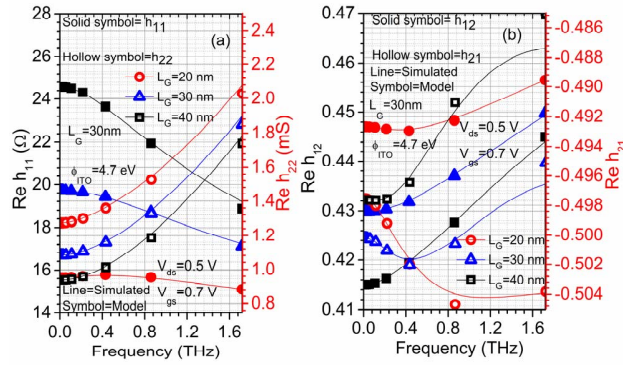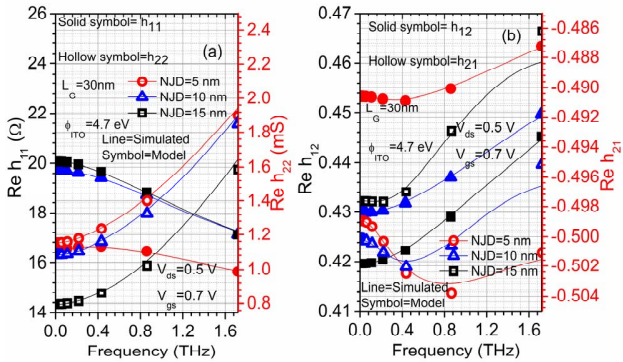
This work performs the parameter variation of TGRC MOSFET in non-quasi-static small signal modelling in terms of Y, Z, and h parameters. The modelled results and simulated results are simultaneously compared. It is evaluated that when the device is shrinking in terms of gate length and negative junction depth, small signal parameters are improved. Further, it is also observed that, when the device parameters are modulated from 40 to 20 nm gate length and from 15 to 5 nm negative junction depth, the transfer impedance also improves due to significant reduction in SCEs and improvement in ON current which enhances the gain and thus can be used in microwave and RF applications. From this analysis (in THz range), it is perceived that the results of small signal parameters for different device dimensions in the presented model are well matched with the simulated results and thus the proposed model is validated.

REFERENCES

[1] W.-M. Cho, G.-R. He, T.-H. Su, and Y.-J. Lin, "Transparent high-surface-work-function Al-doped CdO electrodes obtained by rf magnetron sputtering with oxygen flow," *Applied Surface Science,* vol. 258, pp. 4632-4635, 2012.

[2] H. Hartnagel, A. Dawar, A. Jain, and C. Jagadish, *Semiconducting transparent thin films*: Institute of Physics Bristol, 1995.

[3] S. Pammi, H.-J. Jung, and S.-G. Yoon, "Low-temperature nanocluster deposition (NCD) for improvement of the structural, electrical, and optical properties of ITO thin films," *Nanotechnology, IEEE Transactions on,* vol. 10, pp. 1059-1065, 2011.

[4] M. Saito, M. Ono, R. Fujimoto, H. Tanimoto, N. Ito, T. Yoshitomi*, et al.*, "0.15-μm RF CMOS technology compatible with logic CMOS for low-voltage operation," *Electron Devices, IEEE Transactions on,* vol. 45, pp. 737-742, 1998.

[5] W. Knap, S. Nadar, H. Videlier, S. Boubanga-Tombet, D. Coquillat, N. Dyakonova*, et al.*, "Field effect transistors for terahertz detection and emission," *Journal of Infrared, Millimeter, and Terahertz Waves,* vol. 32, pp. 618-628, 2011.

[6] R. Chaujar, R. Kaur, M. Saxena, M. Gupta, and R. Gupta, "TCAD assessment of Gate Electrode Workfunction Engineered Recessed Channel (GEWE-RC) MOSFET and its multi-layered gate architecture, Part II: Analog and large signal performance evaluation," *Superlattices and Microstructures,* vol. 46, pp. 645-655, 2009.

[7] A. Kumar, N. Gupta, and R. Chaujar, "TCAD RF performance investigation of Transparent Gate Recessed Channel MOSFET," *Microelectronics Journal,* vol. 49, pp. 36-42, 2016.

[8] P. Kopyt, B. Salski, J. Marczewski, P. Zagrajek, and J. Lusakowski, "Parasitic Effects Affecting Responsivity of Sub-THz Radiation Detector Built of a MOSFET," *Journal of Infrared, Millimeter, and Terahertz Waves,* vol. 36, pp. 1059-1075, 2015.

[9] A. Kumar, M. M. Tripathi, and R. Chaujar, "In2O5Sn based transparent gate recessed channel MOSFET: RF small-signal model for microwave applications," *AEU - International Journal of Electronics and Communications,* vol. 93, pp. 233-241, 2018/09/01/ 2018.

[10] I. SILVACO, "ATLAS User's Manual," *Santa Clara, CA, Ver,* vol. 5, 2011.

[11] J. Appenzeller, R. Martel, P. Avouris, J. Knoch, J. Scholvin, J. A. del Alamo*, et al.*, "Sub-40 nm SOI V-groove n-MOSFETs," *IEEE Electron Device Letters,* vol. 23, pp. 100-102, 2002.

[12] C. K. Alexander and M. N. Sadiku, *Fundamentos de circuitos eléctricos*: McGraw Hill Mexico, 2013.

Observational constraints on viscous Ricci dark energy model

C.P. Singh[1] · Amit Kumar[2]

Abstract In this paper, Ricci dark energy (RDE) model with bulk viscosity is studied to observe the cosmic accelerating expansion phenomena. It is thought that the negative pressure caused by bulk viscosity can play the role of a dark energy component. We assume that the total bulk viscosity coefficient is proportional to the velocity and acceleration of the expansion of the universe in the form, $\xi = \xi_0 + \xi_1 h + \xi_2 h'$ where ξ_0, ξ_1 and ξ_2 are the constants and $h = H/H_0$, the dimensionless Hubble's parameter. We give out the exact solutions of such model. We show that the model corresponds to early deceleration and then a smooth transition into an accelerated epoch. We analyze the model with statefinder and Om diagnostics and find that the model is different from standard ΛCDM model at present but approaches to ΛCDM as $t \to \infty$. We constrain the model using latest observational data namely Ia Supernovae data (SN Ia), observed Hubble parameter dataset (OHD) and baryon acoustic oscillations (BAO) measurement to evaluate the best estimated values of all bulk viscous parameters. It is claimed that the non-viscous RDE model suffers the age problem. However, we find that viscous RDE alleviates the age problem. The viscous Ricci dark energy model is compatible to explain the present accelerated expansion of the universe.

✉ C.P. Singh
  cpsphd@rediffmail.com

  A. Kumar
  amitkumar_bt2k15@dtu.ac.in

[1] Department of Applied Mathematics, Delhi Technological University, Bawana Road, Delhi 110 042, India

[2] Department of Applied Physics, Delhi Technological University, Bawana Road, Delhi 110 042, India

1 Introduction

The compelling evidence like recent type Ia Supernovae and many more cosmological observations (Riess et al. 1998; Perlmutter et al. 1998) have shown that baryonic matter only constitutes a negligent fraction of our Universe. The majority of the Universe is dominated by a mysterious component namely dark energy (DE). Dark energy, a form of energy with negative pressure, accounts for the present cosmic accelerated expansion of the Universe.

In the literature (Chiba et al. 2000; Armendariz-Picon et al. 2000), many models have been proposed to describe this late-time acceleration of the Universe. The two most accepted DE models are that of a cosmological constant and a slowly varying rolling scalar field (quintessence models). Though, the most successful cosmological model of the Universe is the cosmological constant cold dark matter (ΛCDM) model, which explains the current acceleration of the Universe (Weinberg 1989). Despite the cosmological constant model is preferred by the observations, this suffers from the fine tuning and the cosmological coincidence problems (Copeland et al. 2006).

Another possible way to explain this accelerated expansion is either modifying the matter sector or the gravitational sector including higher derivative terms that are relevant in the low curvature limit. The modification in the gravitational sector of Einstein-Hilbert action is very attractive way to resolve many problems of the cosmology. The most famous modification of general relativity is the $f(R)$ gravity in which the Ricci scalar R is replaced by a general function $f(R)$. The $f(R)$ gravity is consistent with the observations and successfully passes the solar system tests (Nojiri and Odintsov 2011; Bamba et al. 2008; Bamba 2012). The $f(G)$ gravity is another important modified theory of gravity in which R is replaced by a general function $f(G)$, where G is

the Gauss-Bonnet invariant (Nojiri and Odintsov 2005; De Felice and Tsujikawa 2009). There are other modified theories of gravity in the literature such as $f(T)$ gravity (T is the torsion), $f(R, G)$ gravity, etc. (Myrzakulo 2012; Bengochae and Ferraro 2009; Bamba 2010), which explain the present epoch of cosmic acceleration.

Bertolami et al. (2007) generalized $f(R)$ gravity by introducing an explicit coupling between arbitrary function of R and the matter Lagrangian density. Harko (2008) extended this new concept to the arbitrary coupling between matter and geometry. Harko et al. (2011) considered another extension of general relativity, where the gravitational Lagrangian is given by an arbitrary function of Ricci scalar R and of trace T of the stress-energy tensor, so called $f(R, T)$ gravity. The cosmic acceleration in $f(R, T)$ gravity results not only from geometrical effect but also from the matter contribution. This interesting feature of $f(R, T)$ gravity resolves several issues of cosmology. It can explain the late time accelerated expansion of the universe. Baffou et al. (2014) discussed the dynamics and the stability of $f(R, T)$ gravity for the de Sitter and power-law expansion of the universe taking the conservation of the energy-momentum tensor. Harko (2014) presented the thermodynamical interpretation of $f(R, T)$ gravity. Singh and Kumar (2014) have studied bulk viscosity in modified $f(R, T)$ gravity and analyzed the role of viscosity in the evolution of the universe.

Recently, the holographic dark energy (HDE) has been discussed extensively as a viable candidate for DE. This type of model was motivated by the holographic principle (t'Hooft 1993; Susskind 1995), which was further extended to the realm of string theory (Susskind 1995). By applying the principle to cosmology, Li (2004) proposed the energy density of HDE of the form $\rho_h = 3c^2 M_p^2 L^{-2}$, where c^2 is a dimensionless constant and M_p^2 is the reduced Planck Mass $M_p^{-2} = 8\pi G$.

Gao et al. (2009) proposed that the length scale L can also be given by the average radius of the Ricci scalar curvature. The authors have resolved the causality problem and shown that the result is phenomenologically viable. This model is called the Ricci dark energy (RDE) model pertaining to the connection with Ricci scalar. In this case, the energy density of RDE is given by

$$\rho_d = 3\alpha(\dot{H} + 2H^2) = (\alpha/2)R \tag{1}$$

where we have set $8\pi G = 1$ and α is a dimensionless parameter which will determine the evolution behavior of RDE.

Recent observations show that the phase transition plays a crucial role in describing the evolution of the universe. Also, it has been found that the non-viscous model does not show the phase transition because the deceleration parameter is constant. Thus, we must investigate the viscous model to ascertain if it shows the phase transition and argue that it

can be a possible candidate for dark energy. Some authors (Singh and Kumar 2018; Sasidharan and Mathew 2015) have studied the effect of bulk viscosity in HDE model. Based on thermodynamics (Eckart 1940; Landau and Lifshitz 1987; Israel and Stewart 1976), it is thought that viscosity can also play the role of DE in our universe. The simplest theory of this kind is constant bulk viscosity, regarded as equivalence to constant DE with cold dark matter. A widely investigated case is that bulk viscosity with the form as a linear function of the Hubble parameter, which is proved to be well consistent with the observed late-time acceleration.

In this paper we focus on RDE model with bulk viscosity largely motivated by the works of Cataldo et al. (2005), Feng and Li (2009) and Singh and Kumar (2018) who considered RDE in the presence of bulk viscosity. We extend the work of Singh and Kumar (2018) with a more general form of bulk viscosity coefficient, which can be dealt with analytically and perform well when comparing with observational data.

The paper is organized as follows: In the next section, we derive the explicit solution of the model and calculate analytically the corresponding cosmic quantities. In Sect. 3, we briefly review the statistical analysis employed for constraining model parameters by SNe Ia data, OHD dataset and BAO measurement. The figures and tables are listed as our results, in which the comparison with the ΛCDM model is also performed. Finally, Sect. 4 is conclusion which summarizes the results.

2 RDE model with bulk viscosity

We consider a homogeneous, isotropic and spatially flat Universe described by Friedmann-Robertson-Walker line element, which is given by

$$ds^2 = -dt^2 + a^2(t)\left[dr^2 + r^2(d\theta^2 + \sin^2\theta d\phi^2)\right], \tag{2}$$

where $a(t)$ defines the cosmic scale factor of the Universe.

The stress-energy-momentum tensor in the presence of bulk viscosity with a first-order deviation from the thermodynamic equilibrium has the form (Wilson et al. 2007)

$$T_{\mu\nu} = \rho U_\mu U_\nu + (p - 3\zeta H)h_{\mu\nu}, \tag{3}$$

where $\rho = \rho_m + \rho_d$ and $p = p_m + p_d$ are the total mass density and pressure, respectively of dark matter and Ricci dark energy, $U^\mu = (1, 0, 0, 0)$ the four velocity vector of the cosmic fluid in comoving coordinates, $h_{\mu\nu} = g_{\mu\nu} + U_\mu U_\nu$ the projection tensor, ζ the bulk viscous coefficient and $H = \frac{\dot{a}}{a}$ the Hubble parameter. A dot denotes differential with respect to cosmic time t. In such a background, the Einstein

field equations are given by

$$3H^2 = \rho \tag{4}$$

$$2\dot{H} + 3H^2 = -\tilde{p} \tag{5}$$

where $\tilde{p} = p_m + p_d - 3H\zeta$ is the effective pressure. If we assume the matter presented is cold thereby pressureless ($p_m = 0$), $\tilde{p}$ will have a simple form of $\tilde{p} = p_d - 3\zeta H$. The conservation equation for a complete dynamics system is given by

$$\dot{\rho} + 3(\rho + \tilde{p})H = 0. \tag{6}$$

Now by combining the above equations and considering that $p_d = \omega_d \rho_d$, where ω_d is the equation of state parameter of RDE, we find the following dimensionless equation

$$\frac{\dot{h}}{H_0} + \frac{3(1 + 2\alpha w_d)}{(2 + 3\alpha w_d)} h^2 - \frac{3\zeta}{(2 + 3\alpha w_d)H_0} h = 0, \tag{7}$$

where $h = \frac{H}{H_0}$ is the dimensionless Hubble parameter. Here H_0 is the present value of Hubble parameter. Using $\frac{d}{dt} = \frac{\dot{a}}{a}\frac{d}{d\ln a}$, the above equation can be written as

$$h' + \frac{3(1 + 2\alpha w_d)}{(2 + 3\alpha w_d)} h = \frac{3\zeta}{(2 + 3\alpha w_d)H_0}, \tag{8}$$

where prime denotes the derivative with respect to conformal time $\ln a$.

Now, we can principally solve the scale factor with respect to cosmic time t when the explicit form of ζ is specified. In this paper, we generalize the Ricci dark energy model (Singh and Kumar 2018) to that in more general form of bulk viscous coefficient. We consider a parameterized bulk viscosity of the form (Ren and Meng 2007)

$$\zeta = \zeta_0 + \zeta_1\left(\frac{\dot{a}}{a}\right) + \zeta_2\left(\frac{\ddot{a}}{\dot{a}}\right), \tag{9}$$

where ζ_0, ζ_1 and ζ_2 are constants. By transformation $\frac{\zeta}{H_0} = \xi$, $\frac{\zeta_0}{H_0} = \xi_0$, $\zeta_1 + \zeta_2 = \xi_1$ and $\zeta_2 = \xi_2$, we obtain the dimensionless form of viscosity,

$$\xi = \xi_0 + \xi_1 h + \xi_2 h' \tag{10}$$

Next, we define the effective equation of state for our viscous dark energy model by the ratio of effective pressure and total energy density, as $w_{eff} = w_d - \xi/h$. The behavior of w_{eff} will reveal the nature of our dark energy model: phantom behavior for ($w_{eff} < -1$) whereas a quintessence behavior for ($w_{eff} > -1$).

Further, using (10) into (8), we find the differential equation governing the dimensionless Hubble parameter

$$h' + \frac{3(1 - \xi_1 + 2\alpha w_d)}{(2 - 3\xi_2 + 3\alpha w_d)} h = \frac{3\xi_0}{(2 - 3\xi_2 + 3\alpha w_d)}. \tag{11}$$

On solving (11), we get

$$h(a) = \frac{3\xi_0}{3(1 - \xi_1 + 2\alpha w_d)} + \left(1 - \frac{3\xi_0}{3(1 - \xi_1 + 2\alpha w_d)}\right)$$
$$\times \left(\frac{a}{a_0}\right)^{-\frac{3(1 - \xi_1 + 2\alpha w_d)}{(2 - 3\xi_2 + 3\alpha w_d)}} \tag{12}$$

From (12), we get the solution of scale factor $a(t)$ as function of time,

$$\frac{a}{a_0} = \left[1 + \frac{(1 - \xi_1 + 2\alpha w_d)}{\xi_0}\left\{e^{\frac{3\xi_0 H_0(t-t_0)}{(2-3\xi_2+3\alpha w_d)}} - 1\right\}\right]^{\frac{(2-3\xi_2+3\alpha w_d)}{3(1-\xi_1+2\alpha w_d)}} \tag{13}$$

Hence, the Hubble parameter in terms of cosmic time t reads

$$H = H_0 e^{\frac{3\xi_0 H_0(t-t_0)}{(2-3\xi_2+3\alpha w_d)}}$$
$$\times \left[1 + \frac{(1 - \xi_1 + 2\alpha w_d)}{\xi_0}\left(e^{\frac{3\xi_0 H_0(t-t_0)}{2-3\xi_2+3\alpha w_d}} - 1\right)\right]^{-1} \tag{14}$$

Next, we find requisite conditions on the scale factor so that the universe shows the transition from the decelerated to an accelerated expansion (Sasidharan and Mathew 2015). The second derivative of a w.r.t $y = H_0(t - t_0)$ is given as

$$\frac{d^2 a}{dy^2} \propto \left[\frac{3(\xi_1 + \xi_0 - 1 - 2\alpha w_d)}{(3\alpha w_d - 3\xi_2 + 2)} + e^{\frac{3\xi_0 y}{3\alpha w_d - 3\xi_2 + 2}}\right] \tag{15}$$

The second derivative of a must be negative in the past to show decelerated expansion and it must go to positive values in the late time to result in a accelerated expansion which we observe today. The appropriate condition is given by the following inequalities.

$$\xi_0 > 0, \qquad 3\alpha w_d - 3\xi_2 + 2 > 0 \tag{16}$$

$$\xi_1 - 2\alpha w_d + \xi_0 - 1 < 0 \tag{17}$$

The thermodynamic study of a viscous cosmological model demonstrates that ξ should be positive at all times in accordance with the general law of thermodynamics. Using (12) into (10) we find a full form of ξ as a function of the dimensionless Hubble parameter and the bulk viscosity constants.

$$\xi = \xi_0 + \frac{3\xi_0\xi_2}{2 - 3\xi_2 + 3\alpha w_d} + h\left(\xi_1 - \frac{3\xi_2(1 - \xi_1 + 2\alpha w_d)}{2 - 3\xi_2 + 3\alpha w_d}\right) \tag{18}$$

Since the Hubble parameter is positive, the conditions for a positive ξ is given as follows

$$2 - 3\xi_2 + 3\alpha w_d > 0, \qquad 2 + 3\alpha w_d > 0 \tag{19}$$

$$\xi_0 > 0, \qquad 2\xi_1 - 3\xi_2 + 3\alpha\xi_1 w_d - 6\alpha\xi_2 w_d > 0 \tag{20}$$

We will use these inequalities along with the earlier conditions to fit our model to the observations.

It is also straightforward to show from (14) that the deceleration parameter, defined as $q = -a\ddot{a}/\dot{a}^2$, now takes the following form

$$q = -1 + \frac{3(1 - \xi_0 - \xi_1 + 2\alpha w_d)}{(2 - 3\xi_2 + 3\alpha w_d)} e^{-\frac{3\xi_0 H_0(t-t_0)}{(2-3\xi_2+3\alpha w_d)}} \quad (21)$$

Equation (21) can be written in terms of redshift as

$$q(z) = -1 + \frac{\frac{3(1-\xi_0-\xi_1+2\alpha w_d)(1-\xi_1+2\alpha w_d)}{\xi_0(2-3\xi_2+3\alpha w_d)}(1+z)^{\frac{3(1-\xi_1+2\alpha w_d)}{(2-3\xi_2+3\alpha w_d)}}}{\frac{(1-\xi_0-\xi_1+2\alpha w_d)}{\xi_0}(1+z)^{\frac{3(1-\xi_1+2\alpha w_d)}{(2-3\xi_2+3\alpha w_d)}} + 1} \quad (22)$$

From (22), we see that the value of $q(z)$ approaches to -1 in the future (negative redshifts). Note that for $z = 0$, one finds $q_0 = \frac{3(1-\xi_1+2\alpha w_d)}{(2-3\xi_2+3\alpha w_d)} - 1$. It is easy to check the transition redshift, (z_t), from early-time deceleration to late-time acceleration defined to be zero point of the deceleration parameter, is given by

$$1 + z_t = \left[\frac{(1-3\xi_1+3\xi_2+3\alpha w_d)(1-\xi_0-\xi_1+2\alpha w_d)}{(2-3\xi_2+3\alpha w_d)\xi_0} \right]^{\frac{(2-3\xi_2+3\alpha w_d)}{3(1-\xi_1+2\alpha w_d)}} \quad (23)$$

The age of our universe at redshift z is given by $t(z) = T(z)/H_0$, where

$$T(z) = \int_z^\infty \frac{dz'}{(1+z')(H(z)/H_0)} \quad (24)$$

For the ΛCDM model, in which the density parameter, $\Omega_{m0} \approx 0.27$, the age parameter is (Feng and Li 2009)

$$T(z) = \int_z^\infty \frac{dz'}{(1+z')[\Omega_{m0}(1+z)^3 + (1-\Omega_{m0})]^{1/2}} \quad (25)$$

2.1 Statefinder and Om diagnostics

In order to bring about the discrimination between the various contenders, Sahni et al. (2003) and Alam et al. (2003) proposed a new geometrical diagnostic named the statefinder pair $\{r, s\}$, where r is generated from the scale factor a and its derivatives with respect to the cosmic time t up to the third order and s is a simple combination of r and the deceleration parameter q. This statefinder pair is defined as follows.

$$r = \frac{\dddot{a}}{aH^3} \quad \text{and} \quad s = \frac{r-1}{3(q-1/2)} \quad (26)$$

Different models on the $r - s$ plane accordingly show different trajectories, e.g., the spatially flat ΛCDM scenario corresponds to a fixed point $\{1, 0\}$ and $SCDM$ scenario gives

a fixed point $\{1, 1\}$ in the statefinder diagnostic pair $\{r, s\}$ plane, with which the distance of other DE models from ΛCDM can therefore be established on the $r - s$ plane. For this model, the statefinder pair are given by

$$r = 1 + \frac{9(\xi_0-1+\xi_1-2\alpha w_d)(1-\frac{(1-\xi_1+2\alpha w_d)}{2-3\xi_2+3\alpha w_d})}{2-3\xi_2+3\alpha w_d} e^{\frac{3\xi_0 H_0(t_0-t)}{2-3\xi_2+3\alpha w_d}}$$
$$+ \frac{9(\xi_0-1+\xi_1-2\alpha w_d)^2}{(2-3\xi_2+3\alpha w_d)^2} e^{\frac{3\xi_0 H_0(t_0-t)}{(1-\frac{3}{2}\xi_2+\frac{3}{2}\alpha w_d)}} \quad (27)$$

and

$$s = \left[\frac{(1-3\xi_2+\alpha w_d+\xi_1)e^{\frac{3\xi_0 H_0(t-t_0)}{2-3\xi_2+3\alpha w_d}} + (\xi_0-1+\xi_1-2\alpha w_d)}{(1-\xi_1+2\alpha w_d-\xi_0) - (1-\frac{3}{2}\xi_2+\frac{3}{2}\alpha w_d)e^{\frac{3\xi_0 H_0(t-t_0)}{2-3\xi_2+3\alpha w_d}}} \right]$$
$$\times \left[\frac{(\xi_0-1+\xi_1-2\alpha w_d)}{(2-3\xi_2+3\alpha w_d)e^{\frac{3\xi_0 H_0(t-t_0)}{2-3\xi_2+3\alpha w_d}}} \right] \quad (28)$$

As a complementary to $\{r, s\}$, a new diagnostic called Om has been proposed by Sahni et al. (2008), which helps to distinguish the present matter density contrast Ω_{m0} in different models more effectively. The starting point for Om diagnostic is the Hubble parameter and it is defined as

$$Om(x) = \frac{h^2(x) - 1}{x^3 - 1}$$

where $x = z + 1$ and $h(x) = \frac{H(x)}{H_0}$. For the ΛCDM model Om diagnostic turns out to be a constant, since ΛCDM is independent of redshift z. This is the reason why we prefer Om diagnostic over statefinder parameters for the present study.

It can differentiate a dynamical dark energy model from ΛCDM, with and without reference to matter density. Constant behavior of $Om(z)$ with respect to z signifies that DE is a cosmological constant (ΛCDM). The positive slope of $Om(z)$ implies that dark energy is phantom ($w_{eff} < -1$) whereas the negative slope means that DE behaves like quintessence ($w_{eff} > -1$).

For this model, the value of $Om(z)$ can be obtained as

$$Om(z) = \frac{[\xi_0 + \{1-\xi_1+2\alpha w_d-\xi_0\}(1+z)^{\frac{3(1-\xi_1+2\alpha w_d)}{2-3\xi_2+3\alpha w_d}}]^2 - (1-\xi_1+2\alpha w_d)^2}{(1-\xi_1+2\alpha w_d)^2[(1+z)^3 - 1]}. \quad (29)$$

3 Data analysis

In this section, we test the viability of the model and constrain its free parameters ($\xi_0, \xi_1, \xi_2, \alpha, w_d$) using Type Ia Supernova (SNe Ia), Observational Hubble Parameter Data

(OHD) and Baryonic Acoustic Oscillation (BAO). We compute the best estimated values of free parameters and confidence interval by χ^2 function. We use the minimized chi-square test to obtain the best fit values of the free parameters while implementing Markov chain Monte Carlo (MCMC) analysis using Emcee (Foreman-Mackey et al. 2012). In this study we have taken the value of the Hubble constant, $H_0 = 67.8$ (Ade et al. 2016).

3.1 Type Ia Supernovae

It is believed that the SNe Ia observation can provide the most direct evidence of cosmic accelerating expansion. In this paper we use the cJLA data set of 31 check points (30 bins) covering the redshift range $z = [0.01, 1.3]$ (Betoule et al. 2014). We construct the statistical χ^2 function as

$$\chi^2_{SNeIa} = r^t C_b^{-1} r \tag{30}$$

where

$$r = \mu_b - M - 5\log_{10} d_L \tag{31}$$

in which μ_b is the observational distance modulus, M is a free normalization parameter and C_b is the covariance matrix of μ_b, see Table F.2 (Betoule et al. 2014). Also, the dimensionless luminosity distance is defined as

$$d_L = \frac{c(1+z)}{H_0} \int_0^z \frac{dz'}{H(z',\theta)} \tag{32}$$

where θ represents model parameters namely ξ_0, ξ_1, ξ_2, w_d and α and c is the speed of light. The χ^2 function, thus obtained is then minimized to obtain the best estimate of the parameters.

3.2 Observational Hubble parameter data

In order to study the expansion time line of the universe, the determination of Hubble parameter using observational data is the other important part of fitting parameters. In this paper we use the OHD dataset of 43 measurement points collected in Cao et al. (2018) in the redshift range $0 < z < 2.5$. The χ^2 for Observational Hubble Data is

$$\chi^2_{OHD} = \sum_{i=1}^{n} \frac{[H(z_i) - H_{obs}(z_i, \theta)]^2}{\sigma_i^2}, \tag{33}$$

where $H(z_i)$ and $H_{obs}(z_i)$ are the theoretical and observed values respectively and σ_i^2 the standard deviation of each $H_{obs}(z_i)$.

3.3 Baryonic acoustic oscillations

In this paper we use the sample of BAO distances measurements from $SDSS(R)$ (Padmanabhan et al. 2012), the $6dF$ Galaxy survey (Beutler et al. 2011), $BOSS\,CMASS$ (Anderson et al. 2014) and three parallel measurements from $WiggleZ$ survey (Blake et al. 2012).

The angular diameter, $d_A(z, \theta)$ is given by

$$d_A(z_*, \theta) = c \int_0^{z_*} \frac{dz'}{H(z', \theta)} \tag{34}$$

where z_* denotes the photons decoupling redshift and according to the Planck 2015 results (Ade et al. 2016) its value is $z_* = 1090$. Further, the dilation scale, $D_v(z, \theta)$ is given by $D_v(z, \theta) = (\frac{d_A^2(z,\theta)cz}{H(z,\theta)})^{\frac{1}{3}}$.

The corresponding χ^2 function is given by (Giostri et al. 2012)

$$\chi^2_{BAO} = A^T C^{-1} A \tag{35}$$

where A is a matrix given by

$$A = \begin{bmatrix} \frac{d_A(z_*, \theta)}{D_v(0.106, \theta)} - 30.84 \\ \frac{d_A(z_*, \theta)}{D_v(0.35, \theta)} - 10.33 \\ \frac{d_A(z_*, \theta)}{D_v(0.57, \theta)} - 6.72 \\ \frac{d_A(z_*, \theta)}{D_v(0.44, \theta)} - 8.41 \\ \frac{d_A(z_*, \theta)}{D_v(0.6, \theta)} - 6.66 \\ \frac{d_A(z_*, \theta)}{D_v(0.73, \theta)} - 5.43 \end{bmatrix}$$

and C^{-1} is the inverse of covariance matrix (Giostri et al. 2012). Here, we have adopted the correlation coefficients given in Hinshaw et al. (2013).

Let us discuss the constraints given by the above different sets of data. In our statistical analysis, we minimize the function χ^2_T

$$\chi^2_{total} = \chi^2_{SNeIa} + \chi^2_{OHD} + \chi^2_{BAO}, \tag{36}$$

where χ^2_{SNeIa}, χ^2_{OHD} and χ^2_{BAO} are given by expressions (30), (33) and (35) respectively. By minimizing the above quantity we can perform the best-fit values of the free parameters. The best-fit values of ξ_0, ξ_1, ξ_2, w_d and α are shown in Table 1. The contour plot is shown in Fig. 1 with 1σ (68.3%) and 2σ (95.4%) confidence level.

3.4 Results

In this section we perform best-fitting to the models mentioned in Sect. 2 and plot the evolution of the cosmological parameters, respectively. Using our best fitting data of parameters listed in Table 1 into (22) we plot q with z as shown in Fig. 2. It is observed that the deceleration parameter of
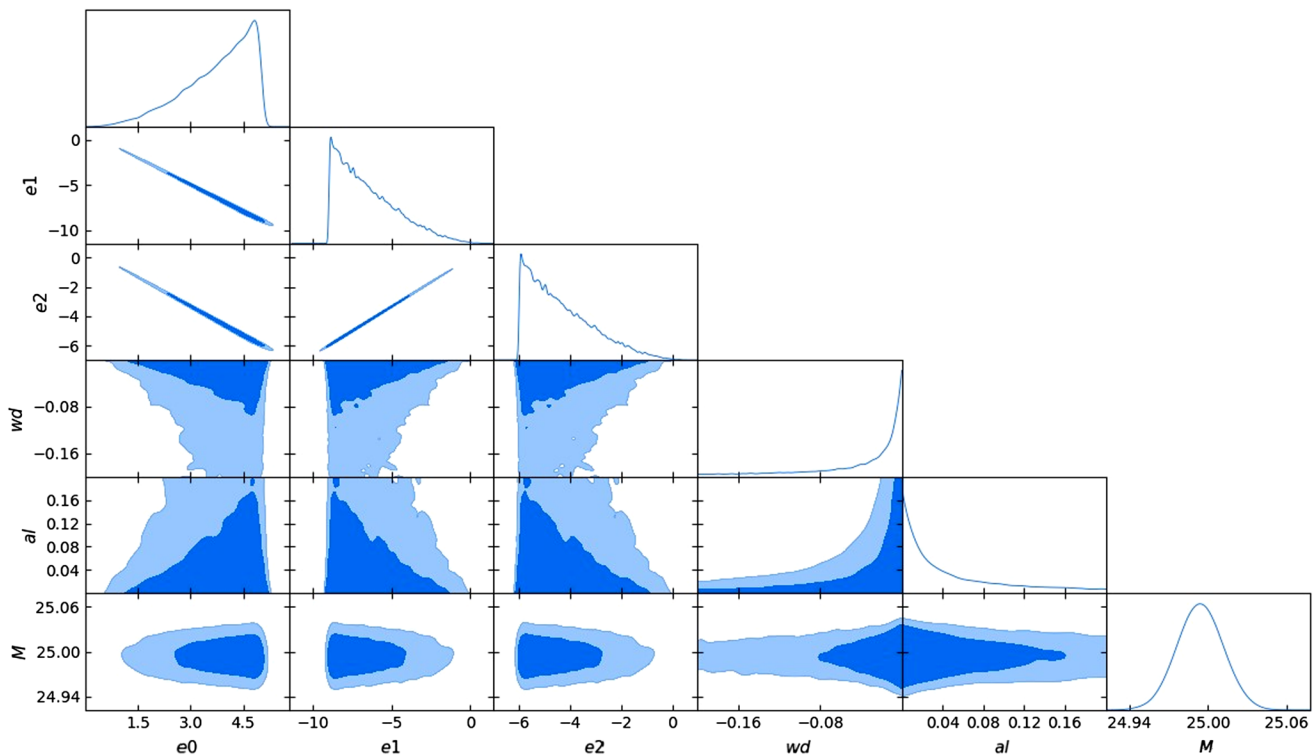
Fig. 1 The contour maps of ξ_0, ξ_1, ξ_2, w_d and α with 1σ (68.3%) and 2σ (95.4%) confidence level

Table 1 Fitting results for model parameters

Parameters	Best fit values	χ^2_{min}
ξ_0	4.021	
ξ_1	−6.972	
ξ_2	−4.656	87.98
w_d	−0.089	
α	0.01	
M	24.867	

Fig. 2 The plot of q with respect to z for best fitted values of parameters

this viscous model starts from negative redshift, $z = -1$ and takes the transition from negative to positive. By using the best-fit values of parameters, it follows that $q_0 = -0.257$.

Now, we study the evolution of bulk viscosity with the redshift. Using Table 1 into (18), the $\xi - z$ plot is shown in Fig. 3. It is observed that the bulk viscosity parameter is positive throughout the evolution and tends to a positive value i.e. $\xi = 0.5$ in late time. Therefore, we can say that our model is consistent with the second law of thermodynamics.

We plot the evolution of the effective equation of state, $w_{eff} = w_d - \frac{\xi}{h}$ with the redshift in Fig. 4. With our best fitting result, we can calculate the effective EoS of viscosity DE. We observe that $w_{eff} > -1$ for high redshifts or early time. However, our model does cross the phantom divide line in the very late time. Thus, we conclude that bulk viscosity effects can't avoid the big rip singularity in late time
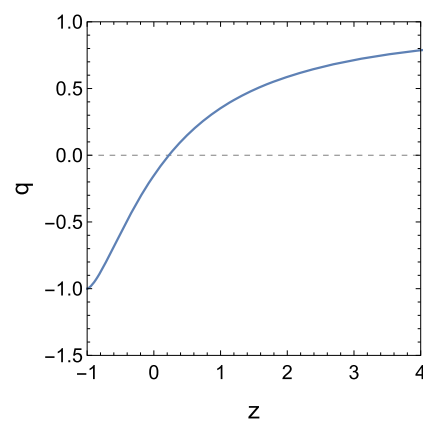
which has been a problem for the Holographic Ricci dark energy model.

Using Table 1 into (29), the trajectory of Om with redshift z is shown in Fig. 5. The trajectory reveals that the viscous Ricci dark energy model shows deviations from ΛCDM model which has horizontal line in the plot. Moreover, the negative slope of the trajectory indicates that our model has a quintessence behavior.

Using (27) and (28) with the best fitted parameters, the trajectory of $\{r, s\}$ in $r - s$ plane is shown in Fig. 6. It reveals that the (r, s) trajectory is lying in the region correspond-
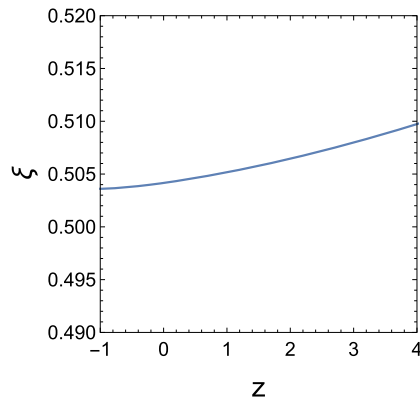
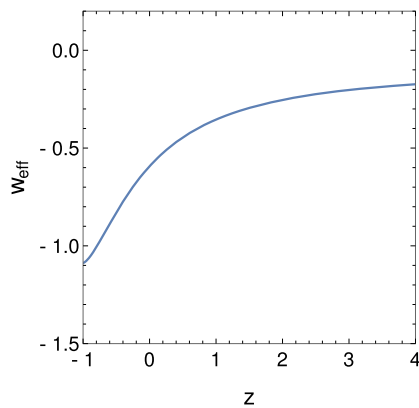**Fig. 3** The evolution of the viscous coefficient in $\xi - z$ plane for the best estimated parameters

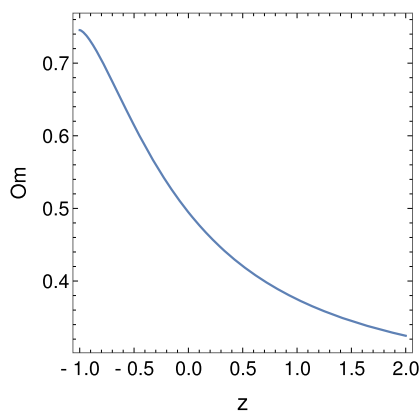**Fig. 4** The trajectory of w_{eff} with the redshift z for the best estimated parameters

Fig. 5 Om-z relation clearly shows the viscous dark energy model deviation from ΛCDM model for which Om is constant

Fig. 6 The trajectory of $\{r, s\}$ in $r - s$ plane for the best estimated parameters. The arrow shows the direction of the evolution of the trajectory
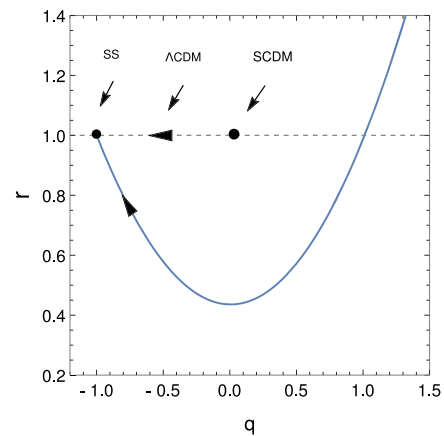
Fig. 7 The evolution of the viscous model in $r - q$ plane for the best estimated parameters. The arrow shows the direction of the evolution of the trajectory

ing to $r < 1$, $s > 0$, a feature similar to that of quintessence model.

The $r - q$ relation for the model is shown in Fig. 7. The SCDM model and steady state (SS) model correspond to fixed points $\{r, q\} = \{1, 0.5\}$ and $\{r, q\} = \{1, -1\}$, respectively. The horizontal li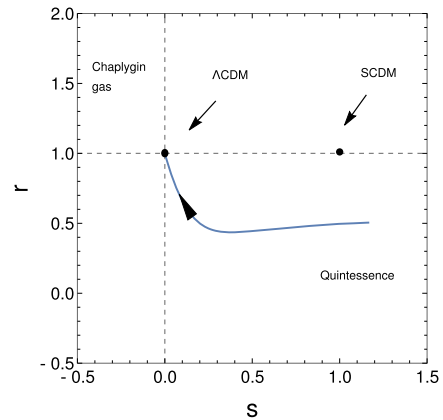ne at $r = 1$ corresponds to the time evolution of ΛCDM model. The changes of sign in q from positive to negative, signaling the transition from the decelerated to the accelerated phase. The viscous RDE model approaches to the standard model like ΛCDM and quintessence model ($Q - model$) (Sahni et al. 2003; Alam et al. 2003) in late time.

Using (24), we plot the age and its evolution with the different redshifts for best estimated parameters. It is to be noted that the present age of the universe for a flat CDM model dominated by matter ($\Omega_{m0} = 1$, $t_0 = 2/(3H_0)$) gives $t_0 \approx 8$–10 Gyr, which does not satisfy the stellar age bound: $t_0 > 11$–12 Gyr, namely the age of the universe should be longer than any objects living in the universe. However, for ΛCDM model, it easily satisfies the constraint $t_0 > 11$–12 Gyr. In RDE model without viscosity, the universe is also younger than some old objects at certain redshifts. Therefore, this model suffers the age problem. It seems that the problem is caused by the fact that matter is

Fig. 8 The time evolution of VRDE and ΛCDM model in the units of Gyr with redshift

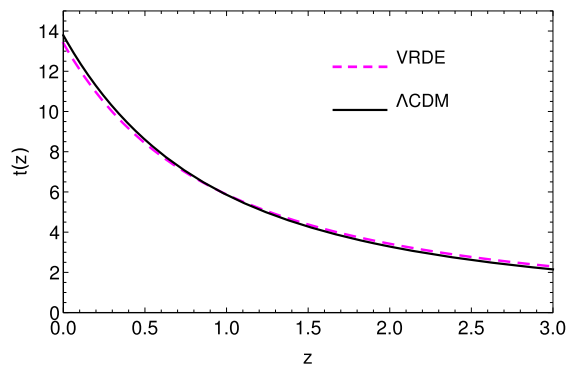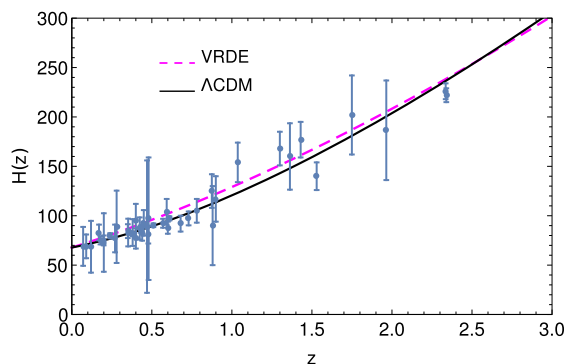**Fig. 9** The Hubble evolution of VRDE and ΛCDM model with error bar plots from Hubble data

diluted too fast. Feng and Li (2009) claimed that the age problem would resolve once the viscosity is taken into account in RDE model. In our model, Fig. 8 shows that the trajectory for the Viscous Ricci dark energy (VRDE) deviates very slightly from that of ΛCDM. It indicates that the viscosity could really alleviate the age problem. This is due to the change in the energy conservation equation by addition of viscosity which makes the matter diluted little bit slower, and then the age problem is alleviated.

Lastly, we compare our viscous RDE model with the ΛCDM model with the error bar plots of Hubble dataset as shown in Fig. 9. We conclude that the fitting achieved from our statistical analysis is compatible with the observational data.

4 Conclusion

In this paper we have presented viscous RDE model with a generalized form of bulk viscosity, $\xi = \xi_0 + \xi_1 h + \xi_2 h'$ to mimic dark energy behaviors and confront it with current observational data sets. We have considered only pressureless matter (cold matter) and effective pressure is provided by viscous term and dark energy. We have discussed the

evolution fate, like deceleration parameter, statefinder parameter and *om* diagnostic parameter for this viscous RDE model. We employ the SNe Ia data, OHD data and BAO dataset to generate the best-fit values of the parameters for the models and then accordingly draw the corresponding evolution diagrams, respectively. As comparison, we have also demonstrated that the resulting evolution of such models are precisely consistent with ΛCDM model in the region of the observational data.

In Sect. 2 we have derived the viscous field equations and obtained the explicit solution of the model and calculated analytically the corresponding cosmic quantities. We also have found the requisite conditions on the scale factor and viscous coefficients so that, our models shows the transition from decelerated to an accelerated expansion. Next, to differentiate our model from various dark energy models we have discussed statefinder and Om diagnostics.

In Sect. 3 we have discussed the observation analysis of our viscous model employed for constraining model parameters by SNe Type Ia data, OHD data and BAO data set. We have used cJLA data set of 31 check points (30 bins) covering the redshift range $z = [0.01, 1.3]$, OHD dataset of 43 measurement points collected in the redshift range $0 < z < 2.5$ and sample of BAO distances measurements from $SDSS(R)$ (Padmanabhan et al. 2012), the $6dF$ Galaxy survey (Beutler et al. 2011), $BOSS\,CMASS$ (Anderson et al. 2014) and three parallel measurements from $WiggleZ$ survey to generate the best fit values for the models. Then, accordingly the best fit values of model parameters is given in Table 1. The corresponding evolution diagrams have been plotted as our results.

The deceleration parameter is found to start with positive values in early time to them acquired negative values in the future. This change of sign shows the transition from the decelerated expansion to an accelerated one. Moreover, using the best fit values we have demonstrated that our model is consistent with the second law of thermodynamics as bulk viscous coefficient ξ is always positive during the evolution. The evolution of effective EoS reveals that out model has a quintessence behavior in early time and phantom at late time. The viscous model can't avoids the big-rip singularity. Further, we have investigated the nature of dark energy in more detail by studying statefinder and Om diagnostic tools and have concluded that our model has a quintessence behavior.

It has been found that Ricci dark energy model suffers the age problem since the age of the universe should be longer than any objects living in the universe. However, once the viscosity is considered, it changes the energy conservation equation and consequently it alleviates the age problem. Thus, on the basis of our analysis we can say that the cosmic acceleration may be powered by the viscosity which is consistent with the observational data and shows the transition

from decelerated phase to accelerated phase, and resolves the age problem.

References

Ade, P.A.R., et al.: Astron. Astrophys. **594**, 13 (2016)

Alam, U., et al.: Mon. Not. R. Astron. Soc. **344**, 1057 (2003)

Anderson, L., et al.: Mon. Not. R. Astron. Soc. **441**, 24 (2014)

Armendariz-Picon, C., Mukhanov, V.F., Steinhardt, P.J.: Phys. Rev. Lett. **85**, 4438 (2000)

Baffou, E.H., et al.: Astrophys. Space Sci. **355**, 2197 (2014)

Bamba, K.: Eur. Phys. J. C **67**, 295 (2010)

Bamba, K.: Astrophys. Space Sci. **342**, 155 (2012)

Bamba, K., Nojiri, S., Odintsov, S.D.: J. Cosmol. Astropart. Phys. **0810**, 045 (2008)

Bengochae, G.R., Ferraro, R.: Phys. Rev. D **79**, 124019 (2009)

Bertolami, O., Bochmer, C.G., Harko, T., Lobo, F.S.N.: Phys. Lett. B **619**, 5 (2007)

Betoule, M., et al.: Astron. Astrophys. **568**, 22 (2014)

Beutler, F., Blake, C., Colless, M., Jones, D.H., Staveley-Smith, L., Campbell, L., et al.: Mon. Not. R. Astron. Soc. **416**, 3017 (2011)

Blake, C., et al.: Mon. Not. R. Astron. Soc. **425**, 405 (2012)

Cao, S.-L., Teng, H.-Y., Wan, H.-Y., Yu, H.-R., Zhang, T.-J.: Eur. Phys. J. C **78**, 313 (2018)

Cataldo, M., et al.: Phys. Lett. B **619**, 5 (2005)

Chiba, T., Okabe, T., Yamaguchi, M.: Phys. Rev. D **62**, 4438 (2000)

Copeland, E.J., Sami, M., Tsujikawa, S.: Int. J. Mod. Phys. D **15**, 1753 (2006)

De Felice, A., Tsujikawa, S.: Phys. Rev. D **80**, 063516 (2009)

Eckart, C.: Phys. Rev. **58**, 919 (1940)

Feng, C.J., Li, X.M.: Phys. Lett. B **680**, 355 (2009)

Foreman-Mackey, D., Hogg, D., Lang, D., Goodman, J.: Publ. Astron. Soc. Pac. **125**, 306 (2012)

Gao, C., Wu, F., Chen, X.: Phys. Rev. D **79**, 043511 (2009)

Giostri, R., Santos, M.V.d., Waga, I., Reis, R.R.R., Calvao, M.O., Lago, B.L.: J. Cosmol. Astropart. Phys. **1203**, 027 (2012)

Harko, T.: Phys. Lett. B **669**, 376 (2008)

Harko, T.: Phys. Rev. D **90**, 044067 (2014)

Harko, T., Lobo, F.S.N., Nojiri, O.S.D.S.: Phys. Rev. D **84**, 024020 (2011)

Hinshaw, G., et al.: Astrophys. J. Suppl. Ser. **208**, 19 (2013)

Israel, W., Stewart, J.M.: Phys. Lett. A **58**, 213 (1976)

Landau, L.D., Lifshitz, E.M.: Phys. Lett. B **603**, 1 (1987)

Li, M.: Phys. Lett. B **603**, 1 (2004)

Myrzakulo, R.: Eur. Phys. J. C **72**, 2203 (2012)

Nojiri, S., Odintsov, S.D.: Phys. Lett. B **631**, 1 (2005)

Nojiri, S., Odintsov, S.D.: Phys. Rep. **505**, 59 (2011)

Padmanabhan, N., Xu, D.J., Eisenstein, X., Scalzo, R., Cuesta, A.J., Mehta, K.T., et al.: Mon. Not. R. Astron. Soc. **427**, 2132 (2012)

Perlmutter, S., et al.: Nature **391**, 51 (1998)

Ren, J., Meng, X.-H.: Int. J. Mod. Phys. D **16**(08), 1341 (2007)

Riess, A.G., et al.: Astron. J. **116**, 1009 (1998)

Sahni, V., Saini, T.D., Starobinsky, A.A.: JETP Lett. **77**(5), 201 (2003)

Sahni, V., Shafieloo, A., Starobinsky, A.A.: Phys. Rev. D **78**, 103502 (2008)

Sasidharan, A., Mathew, T.K.: Eur. Phys. J. C **75**, 348 (2015)

Singh, C.P., Kumar, P.: Eur. Phys. J. C **74**, 3070 (2014)

Singh, C.P., Kumar, A.: Eur. Phys. J. P **133**, 312 (2018)

Susskind, L.: J. Math. Phys. **36**, 6377 (1995)

t'Hooft, G.: Conf. Proc. C **930308**(603), 284 (1993)

Weinberg, S.: Rev. Mod. Phys. **61**, 1 (1989)

Wilson, J.R., Mathews, G.J., Fuller, G.M.: Phys. Rev. D **75**, 043525 (2007)

Optimal users based secure data transmission on the internet of healthcare things (IoHT) with lightweight block ciphers

S. Sheeba Rani[1] · Jafar A. Alzubi[2] · S. K. Lakshmanaprabu[3] · Deepak Gupta[4] · Ramachandran Manikandan[5]

Abstract

The ever-growing advancement in communication innovation of modern smart objects carries with it a new era of improvement for the Internet of Things (IoT) based networks. The health care system is the best approach to store the patient's health data online with high privacy. Ensuring the privacy and confidentiality of patient information in the cloud is of utmost importance; here, the enhanced security model of healthcare data gives rise to trust. For the secure communication, the healthcare data sensed by the IoT sensor network is encrypted by Lightweight SIMON block cipher. For improving the privacy of healthcare data among individuals, we implemented the share generation model. Then, share creation model, i.e., Chinese Remainder Theorem (CRT) is developed to generate the copy of every ciphertext based on the selected number of users and the data is shared among the optimal number of users. The selection of the users in IoHT is made by the metaheuristic algorithm called Hybrid Teaching and Learning Based Optimization (HTLBO). Then, we present healthcare service providers for giving the full scope of medical services to people enrolled in IoHT. The performance of Secure Data is approved through simulations in terms of energy cost, computation time, etc., of the proposed algorithms and the outcomes demonstrate that Secure Data can be efficient while applying for ensuring security chances in IoT-based healthcare systems.

Keywords Internet of things (IoT) · Multimedia · Security · Optimization · Sensor network · Share creation · Block ciphers

1 Introduction

The Internet of Things (IoT) is gathered of an extraordinary number of things (devices) that are linked through the Internet [28]. In everyday things, the framework can be equipped with

✉ Jafar A. Alzubi
    j.zubi@bau.edu.jo

Extended author information available on the last page of the article

distinguishing, measuring, network and processing capabilities; for such a way that this device can interact with different devices and it can give service to accomplish a specific objective through the internet [8]. In the attractive virtual and physical world, this system related to the communication between platforms as well as interrelated devices [30]. Thus, it is essential to building up an effective method to guarantee the security along with the integrity of the patient's diagnostic information transmitted as well as received from the IoT environment [22]. The sophisticated chips and sensors are surrounded in the physical things that envelop us, for each valuable transmitting data [29]. The way toward sharing such a substantial measure of information starts with the devices themselves which should safely communicate with the IoT stage [2]. In most countries, the healthcare data offer authentic information that should be confined via "Health Information and Portability Accountability Association (HIPAA)" [27].

E-health system lessens the healthcare cost, and besides, it will improve the quality of healthcare services and these components helped to optimize the healthcare field by utilizing innovative devices and solutions [9]. In the IoT network, the individual sensor device can be secured along with its integrity of healthcare providers [1]. This will make it hard to apply various conventional security answers for IoT, the broadly utilized public key scheme as well as IP-based security arrangement. Usually, it is easy to co-operate IoT devices than traditional computers because of inadequate IoT security plan [16]. Insecure systems secrecy of the information is kept up, and it is sure amid the procedure of trade the information, and it holds its creativity, and no change is hidden by the structure [17]. The function of a cipher is to encrypt a plain text into cipher text and yet again converts cipher text to plain text is the main aim of the security. The cryptographic algorithm is usually [4] classify as a hash function, a stream or a block cipher. In the cryptographic field, block ciphers are measured to be workhorses [8].

A need of sequential to parallel converter and parallel to the sequential converter is maintained a strategic distance from by picking lightweight figure (simeck, Simon, katan) family which is having versatility [10] in choosing variable information along with its key sizes [25]. In the secret cipher sharing, an entire cipher is examined into various offers at the processing layer [6]. The developed shares are sent through secure correspondence independently towards the cloud. For secure information, we apply the Slepian-Wolf coding-based sharing [14]. Each key is made-up to impacts each bit of cipher content. Dispersion proliferates impact of every piece in the block text over various bits in ciphertext block making cipher message over delicate to measurable assaults [12]. Once the encryption of input data is done, share creation model is developed.

The purpose of the share creation model is to generate the copy of every ciphertext and then it is stored in a cloud server. The number of copies generation is based on the optimal cloud server, next to that an innovative share creation model is used.

Moreover, an optimization strategy is used for selection of Number of the user in IoHT security process. It is considered as an optimization problem, and meta-heuristic algorithms are needed to solve it. An optimal cloud server is elected and secured by the implementation of a meta-heuristic algorithm called hybrid teaching and learning based optimization (HTLBO) algorithm. TLBO algorithm is chosen among the various optimization algorithms due to its nature of low computation complexity. It is a robust and effective evolutionary optimization algorithm. Parameter tuning is recognized as a crucial step when designing an optimization algorithm. The performance of the optimization algorithm is susceptible to parameter values. Therefore, finding a good parameter setting can be the difference between success and failure. To attain this, HTLBO algorithm is introduced.

This paper explains existing as well as the upcoming developments in the field of IoT based healthcare management, the significance of citizen commitment for the success of in-progress techniques to IoT-enabled healthcare services [21]. For secure communication, we employ a lightweight SIMON block cipher algorithm on sensed data, by the IoT sensor network. For improving the privacy of healthcare data among individuals, we implement a share generation model. The share generation is done by optimal user selection, and Chinese Remainder Theorem (CRT) technique shares the generated copy of every ciphertext. The outcomes demonstrate that the presented algorithm could optimize the number of users and enhance data privacy accuracy in the cloud. The paper's contributions are listed here.

- We employ a lightweight SIMON block cipher algorithm
- we implement a share generation model by optimal user selection
- We apply Chinese Remainder Theorem (CRT) technique to share the generated copy of every ciphertext
- We validate the performance of the presented method

The rest of the sections of the paper are organized as follows: Section 2 reviewed the recent literature about IoT security model and the overview of block ciphers in a security discussed in Section 3. In Section 4 current issues and challenges are analyzed. Our proposed security model for IoHT shows in Section 5; the implementation results are analyzed in Section 6; finally, conclude our proposed model with future scope.

2 Literature review

In 2018, SanazRahimiMoosavi et al. [18] presented the method is examined by both simulations as well as hardware/software prototype. The result showed that the energy-performance evaluation contrasted with accessible approaches. The proposed model reduces the communication latency between the smart gateways and end users by 16%. Investigation of our usage uncovered that the handover idleness caused by versatility is small and the handover procedure does not bring about any preparing or correspondence overhead on the sensors. The security system validates a user based on the OpenID standard by Mahmud Hossain et al. in 2018 [13]. In security the framework that guarantees client confirmation and ensured access to assets and administrations by IoT. When the confirmation is sufficient, the client has issued an approval ticket, called the Security Access Token (SAT). The SAT contains many benefits that concedes the client access to restorative IoT devices and their administrations as well as assets. The SAT is cryptographically secured to make preparations for phony. A therapeutic IoT device confirms the SAT preceding serving a demand, and in this way, guarantees ensured access.

A privacy-preserving data gathering method for IoT based human services framework named SecureData was analyzed by Hai Tao et al. [26]. We utilize the possibility of secret cipher sharing method to ensure patients' information protection, and it is actualized and upgraded in the FPGA equipment utilizing KATAN technique. In the distributed computing layer, apply a circulated database method that incorporates various cloud information servers to ensure patients' at the distributed computing layer. The outcome demonstrated that the protected information could be authoritative while regarding securing risks in IoT based social insurance.

An outline of Health care IoT is specified, accentuating its qualities to those of Big Data, and security, as well as protection design, is projected by VangalurAlagar et al. [1]. We have utilized the patient-driven data, for example, wellbeing status and therapeutic gadgets and it must be secured to regard safety and protection, while human services data ought to be aggregate in certainty by specialists for therapeutic services development and favorable treatment of patients.

The correlation between patient capacities for viable utilization of data and correspondence advances and the accomplishment of IoT-based human services proposed by Eva Martínez-Caro et al. [17]. For dominant usage of data and correspondence innovations, IoT-based human services were then approved by the subsequent hypothetical model. The approval depended on data gathered from a haphazardly chosen test of 256 clients of Internet-based social insurance administrations given by general society medicinal services arrangement of the Region of Murcia in Spain. The discoveries of this exploration illuminate future procedures for the execution of new ages of wellbeing and prosperity administrations dependent on IoT advances.

The patient information is stored as a cloud server in the hospital center because of which the security is essential by Mohamed Elhoseny et al. [11]. In this manner, the structure is required for the protected transmission and efficient storage of therapeutic images interleaved with patient data. For expanding the security dimension of encryption as well as decryption method, the ideal key will be chosen using hybrid swarm optimization, i.e., grasshopper and molecule swarm based approach in elliptic bend cryptography. In perspective of this technique, the therapeutic images are preserved in the IoT system.

In 2018 T. Avudaiappan et al. [3] proposed the double encryption strategy is used to scramble the therapeutic images. At first, the Blowfish Encryption is estimated, after that signcryption calculation is used to affirm the encryption. For enhancing the private and public keys, the Opposition based Flower Pollination (OFP) is introduced. The execution of the OFP is assessed utilizing some measures, for example, Peak Signal to Noise Ratio (PSNR), entropy, Mean Square Error (MSE), along with Correlation Coefficient (CC). Though various methods are available in the literature, there is still a chance for further improving the security level of communication. Also, there is a necessity to develop low complex security standards to satisfy real time requirements.

3 Overview of block ciphers for IoT security

Nowadays, various research works related to the execution of lightweight ciphers were analyzed by specialists. The performance is in both hardware and software which are intended for IoTapplications. Most of the block ciphers have a fixed block size and key size. Some lightweight block ciphers are explained in the below section [5]:

> **SIMON:** In this, the block cipher pursues a fair Feistel cipher with the n-bit word, and consequently the length is 2n. The block segment of the cipher is uniform between the Simon executions and its key age rationale is reliant on the usage of 2, 3 or 4 keys.
> **SPECK:** In this, the block is dependably in two words, the words might be 16, 24, 32, 48 or 64 bits in size. In other block ciphers, it is normal for usage to compute the round keys just once and store them, generally re-computing the keys for each block whether it is encoded or decoded.

KATAN: The KATAN block ciphers share the security level and 80-bit key size. The relation between KATAN is that at the key is scorched into the gadget and it cannot be misused. Therefore KATAN is very small block ciphers and more compact than SPECK, and it is used where the device is instated with one key.

TWINE: in TWINE, it incorporates a non-linear substitution layer for every round with 4-bits S-boxes; also with dispersion layer (4 bits). This function is repeated for different or multiple times based on the length of the key.

KLEIN: the significant factors for security in block ciphers are the critical length and block size. The 64-bit block size is fixed one and 64, 80 or 96-bits is variable key length. Based on different vital lengths, it will denote the ciphers by KLEIN-64/80/96.

LED: For a software implementation, LED is a practical device for performance profile, and it has 64 bits block cipher with ach four key sizes are represented as 64 bits, 80 bits, 96 bits, and 128 bits.

On the above-discussed ciphers, some of them are suitable for software implementation while others are used in hardware implementation. Further, the ciphered communication for IoHT network protects the system from randomly distributed hearer attack.

4 Security issue and challenges in IoHT

In this section, existing as well as the upcoming developments in the field of IoT based healthcare management, the security issues and challenges present in the IoT-enabled healthcare services are explained.

- Forgetting to IoT administrations, the interfaces utilized through web, mobile, and cloud are powerless against various attacks which may seriously influence the information privacy.
- The physical layer communication of IoHT should be secured to make it difficult to reach to unapproved recipients [17, 21].
- Privacy Violation on cloud-basedIoHT: Different attacks which may disregard personality and area privacy might be propelled on the cloud or defer tolerant network based IoHT [3].
- With the heterogeneous networks, structures, and conventions, the IoT pattern turns out to be more powerless against single points of failure than some other pattern.
- Within the comprehensive system, an efficient combination of security benchmarks at each layer would then be able to be characterized through IoHT structural requirements.

5 System model

Enhance the security model of Heath care medical information from a body sensor Network in IoT condition is proposed in this manuscript. To give the extra security, Lightweight SIMON block cipher based implementation is presented for the cipher information creation process. SIMON cipher family is chosen which is having adaptability in choosing variable information along with critical sizes. After this model imaginative Share creation model is used to produce the copy of cipher information in the cloud server. Besides, Selection of Number of the user in IoHT security process optimization is used. In

this way, security is a fundamental prerequisite of healthcare applications. The developed shares are sent via protected communication independently towards the cloud. The achievement of healthcare application depends mostly on patient security as well as privacy, for an ethical and legitimate reason.

This whole technique or proposed Health care information security partitioned in five stages which are (i) IoT Sensor Network Model, (ii) Cipher Generation Model, (iii) Share Generation (iv) Optimal Cloud Server Selection using HTLBO and (v) Health care Service Provider Model. From this, secure the information if a cloud server is arranged, mainly when a cloud server is under attacks by the insider or cloud provider.

- The primary reason for this Lightweight block cipher and share creation model clarified as pursues SIMON has convincing focal points for high-throughput ASIC applications.
- This appears to be clear, even in perspective of the difficulties inherent in contrasting implementations utilizing diverse innovations and libraries.
- Benefits of SIMON was improved for hardware, and it does not exploit this product situated optimization. Instead, it utilizes an essential timetable which was intended to be somewhat lighter than the round function.
- Our proposed CRT secret share creation Model uses, along with the Chinese remainder hypothesis, unique groupings of whole numbers that ensure the difficulty of recuperating the secret from many shares with not precisely specified cardinality.

5.1 Phase I: IoT sensor network model

IoT architecture is mainly made out of a lot of low processing detecting units called nodes, also a cloud-based layer that empowers the client to screen those nodes remotely and progressively. The work introduces an IoT approach for organizing a Wireless Sensor Network (WSN) connected to the natural observing of temperature and relative stickiness inside doctor's facilities or center labs.

The design of the IoT sensor network appears in Fig. 1. The proposed design is made out of three layers to be specific, node layer (sensor network) where the healthcare related data are sensed, local administration layer (computer) and cloud-based layer. The second layer gathers the detected information from the network and after that transfers the data to the cloud.

Fig. 1 IoT sensor network

5.2 Phase II: cipher information generation model

For secure transmission, the ciphertext is generated for the considered healthcare information. In the proposed study, SIMON block cipher is used to encrypt the input data.

5.2.1 SIMON block cipher

7The structure of SIMON [19] square cipher comprises parallelism of encryptions which includes round functions and key generation blocks. The essential capacity of block ciphers is to give security on stored information or information from the outsider utilizing symmetric encryption strategies. They perform an activity on fixed-size blocks of understandable content and resulting in about a block of cipher content for each. The most generally utilized block sizes in presently block ciphers are 64 bits and 128 bits. The structure of round configuration, as well as generation age, appears in Fig. 2.

Round configuration This work focuses on the 128/128 design of SIMON [19] security level correspondent to AES-128. In SIMON, round function utilizes the contributions of 128-piece of plaintext and 128- bit key to generate 128- bit cipher message in 68 rounds. 128- bit information has been partitioned into two equivalent parts alludes as an upper and lower block. The round capacity performs rationale and the output is XOR-ed with 64-bits and finally creates 64-bit round key ki. At the end of each round, the upper block is changed over to a lower block with newly generated qualities are composed once more into the upper block.

Key generation The key generation performs rationale tasks on most noteworthy of 64-bits, and the outcome is XOR-ed with the minimum critical 64-bits plus the 64-bit round consistent
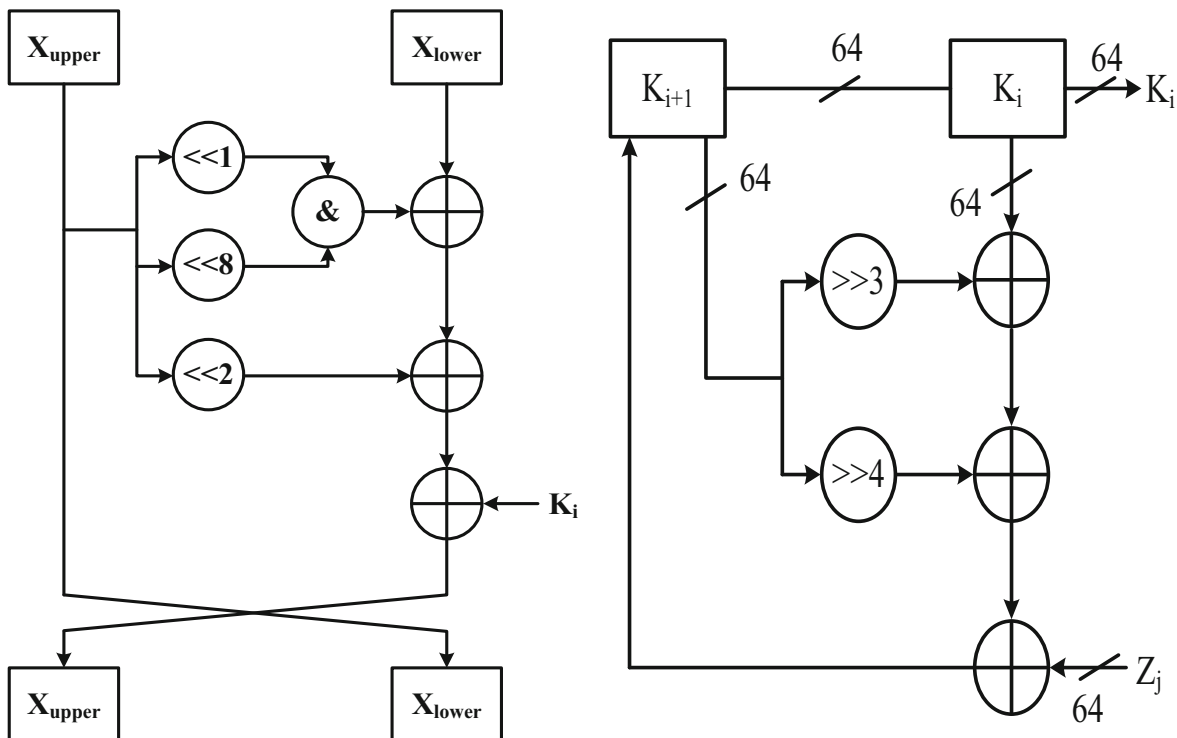

Fig. 2 Diagrammatic view of SIMON cipher **a** round configuration and **b** key generation

Zi. The steady is a structured time consistent value that is interestingly tuned for every design. The invention of the full key comprises two 64-bit shift operators (move right three and move right four) along with three 64-bit XOR administrators.

5.3 Phase III: Share generation model

After the conversion of input into ciphertext, share creation model is developed [23]. The purpose of the share creation model is to generate the copy of every ciphertext and then it is stored in a cloud server. The number of copies generation is based on the optimal cloud server, next to that an innovative share creation [23] model is used. Moreover, an optimization strategy is used for selection of Number of the user in IoHT security process. The process involved in share generation is depicted in Fig. 3.

5.3.1 Optimal cloud server selection model

An optimal cloud server is elected and secured by the implementation of a meta-heuristic algorithm, i.e., HTLBO. The TLBO method is working on the influence of a teacher on the output of learners in a class. The process of TLBO [15] is sectioned into three parts that are teaching phase, the learning phase, and studying phase.

The procedure involved in the HTLBO algorithm is explained as follows

Population Initialization: Generate a random population according to the population size (here, the number of users are considered) along with some design variables.
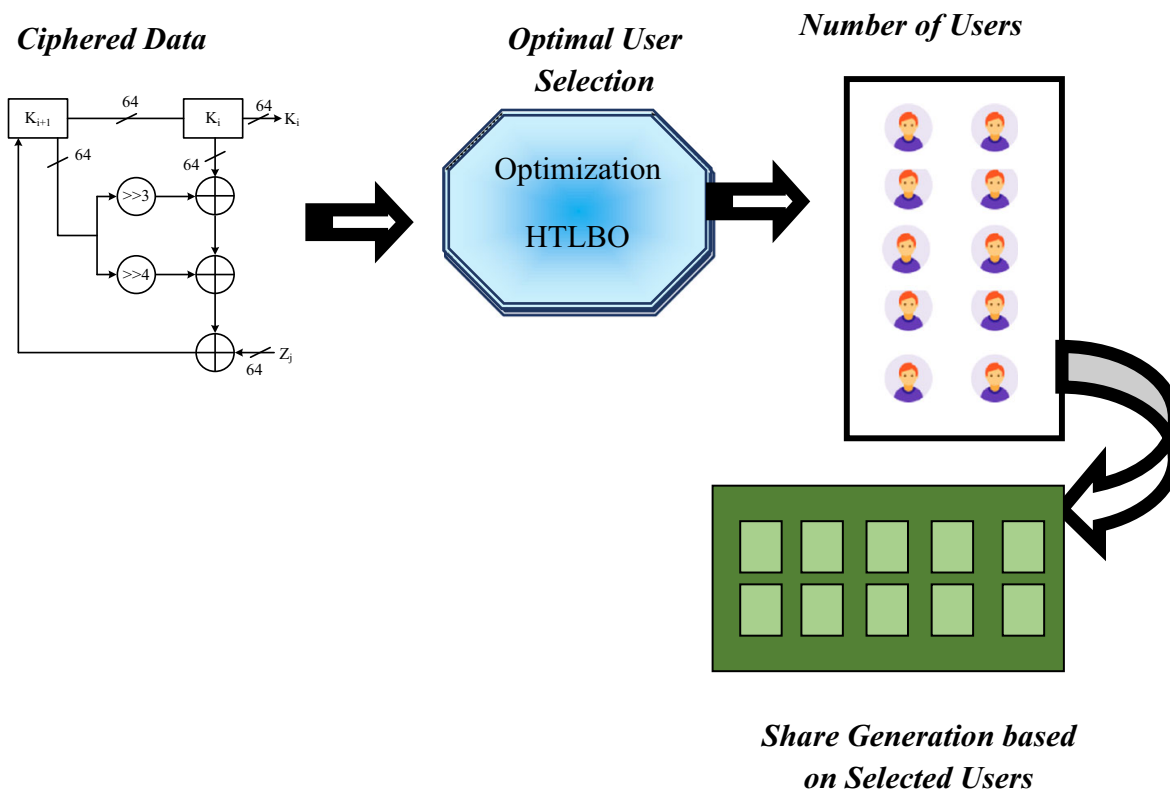

Fig. 3 Overview of share generation model

Fitness evaluation: It is defined as the objective function of secure data transmission on the cloud that is to find the optimal user of a sensor network by evaluating the energy value using Eq. (1).

$$Fitness = \min\_Energy \tag{1}$$

Updating process of HTLBO HTLBO involves three updating operations, namely: teaching phase and learning phase. In every phase, specific updating characteristics of metaheuristic algorithms have to be included. During the teaching phase in TLBO algorithm, the learners undergo training from the teachers. At some point, a teacher tries hard to improve the averge of the entire class, and the updation takes place by following the hunting nature of GWO. Also, the hunting behavior of Crow Search Algorithm (CSO) is used in the learning pahse of the algorithm [20].

(i) **Teaching phase:** In the teaching phase, learners are trained by the teacher. At this phase, a teacher struggles to enhance the mean of the whole class to his or her level. Here, the updation is done by the hunting behavior of the GWO [24]. It is discussed as below:

Hunting behavior of GWO: The mathematical simulation of hunting behavior of GWO, we assume that the alpha (best candidate solution for locating the prey) beta and Delta have better knowledge about the potential location of prey.

$$E^{\alpha} = |D_1.H_{\alpha} - H|, \ \ E^{\beta} = |D_1.H_{\beta} - H|, \ \ E^{\delta} = |D_1.H_{\delta} - H| \tag{2}$$

$$H_1 = H_{\alpha} - A_1.(E_{\alpha}), \quad H_2 = H_{\beta} - A_2.(E_{\beta}), \quad H_3 H_{\delta} - A_3.(E_{\delta}) \tag{3}$$

From the above equation, alpha (α), beta (β), and delta (δ) are the three best solutions attained from the entire search agents (including the omegas). Then, update their positions according to the position of the most excellent search agent.

(ii) **Learning phase:** A learner interacts randomly with a new learner for enhancing his or her knowledge. Mathematically the learning process of this phase is described with the help of hunting behavior of CSO algorithm [20] where the new position and memory of initial crow are updated using Eqs. (4 and 5).

The new position of crow $P^{i,\ iter}$ is attained by the following Eq. (4).

$$P^{i,iter+1} = \begin{cases} P^{i,iter} + r_i \times fl^{i,iter} \times \left(mem^{j,iter} - P^{i,iter}\right) & if \ r_j \geq AP^{j,iter} \\ rand \ P & otherwise \end{cases} \tag{4}$$

For the newly updated crow's position, its memory value is also updated using Eq. (5).

$$mem^{i,iter+1} = \begin{cases} P^{i,iter} & f\left(P^{j,iter+1}\right) > f\left(mem^{j,iter}\right) \\ mem^{i,iter} & otherwise \end{cases} \tag{5}$$

Variable description: r_i and r_j indicates a random number of crow i and j respectively, between [0 and 1], $fl^{i,\,iter}$ represents flight length of crow i, P symbolizes the position of crow, $P^{i,\,iter}$ and $mem^{j,\,iter}$ denotes the position and memory location of the ith and jth crow respectively and $AP^{j,\,iter}$ indicates the awareness probability of crow j at iteration.

Step 4: Termination process: The algorithm terminates its iterating procedure only if a maximum number of iterations are accomplished, also the solution which is holding the minimum energy value as optimal. That is, an optimal cloud server is selected with high secure communication.

Share generation using CRT: Using TLBO algorithm, an optimal cloud server is achieved and based on the available user, we can generate many shares, for that, an innovative share creation model is used, Chinese Remainder Theorem (CRT) [7]. CRT is issued to work out a set of simultaneous congruence equations, can be depicted as follows.

Let us assume co-prime positive integers as q_1, q_2, q_3, ...q_k and the non-negative integers as c_1, c_2, c_3, ...c_k, there exists exactly one solution, i.e., $s \in [q_1, q_2, q_3, ...q_k)$ for the simultaneous congruence evaluation, which is performed by the following equation.

$$
\begin{aligned}
s &\equiv c_1 \,(\mathrm{mod}\, q_1) \\
s &\equiv c_2 \,(\mathrm{mod}\, q_2) \\
&\;\;\vdots \\
s &\equiv c_k \,(\mathrm{mod}\, q_k)
\end{aligned}
\tag{6}
$$

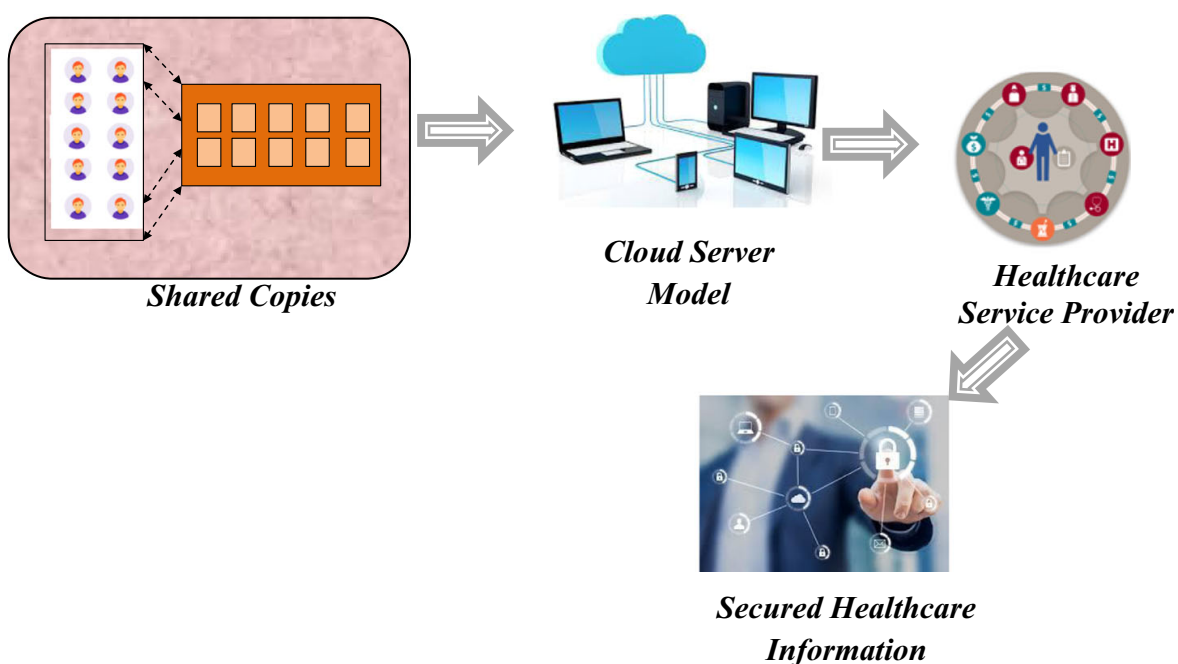The desired solution, i.e., a number of share creation can be performed by executing the following steps of CRT.

Fig. 4 The healthcare service provider model

Table 1 Our proposed Simon parameters for IoHT

Data size (health info)	Keywords	Key size	Number of rounds	Energy (PJ/bit)	Cipher secure level (%)
16	4	64	32	3.22	85.45
24	3	72	36	5.22	92.12
32	4	128	36	2.14	89.45
48	3,4	144,192	42	3.12	94.15
64	3,4	192,256	42,44	3.45	88.4
96	2,3	192,288	52,54	3.88	82.2
128	2,3,4	256,384,512	68,69,72	3.85	81.2

Stage 1: Designate $Q = \Pi_{i=1}^{k} q_i$ and assume $m_i = {Q}/{q_i}$, where the value of i ranges from $[1, k]$

Stage 2: Assume $n_i \equiv m_i^{-1} (\mathrm{mod}\, q_i)$ for $1 \leq i \leq k$

Stage 3: Let $s \equiv (c_1 m_1 n_1 + c_2 m_2 n_2 + c_3 m_3 n_3 + ... + c_k m_k n_k) \bmod Q$

Stage 4: in the fourth step, the unique solution of the algorithm is chosen as $s \equiv c_i (\mathrm{mod}\, q_i)$ for $1 \leq i \leq k$. An example is stated as s = 39 (mod 2 · 5 · 7) is the unique solution for the following congruence equations.

$$s \equiv 1\,(\mathrm{mod}\, 2), s \equiv 4\,(\mathrm{mod}\, 5), s \equiv 4\,(\mathrm{mod}\, 7) \tag{7}$$

Based on this CRT technique, several copies for healthcare data are generated and shared among the optimal users. Therefore, security is the primary requirement of healthcare applications. The shares are sent through secure communication separately towards the cloud.

5.4 Phase IV: The healthcare service provider model

In phase IV, we explain performance and security analysis of the proposed model for the most optimal cloud server with shared copies. For the efficient delivery of services to the users, the optimal network is monitored where the location of every user is proactively determined before the service is delivered. The health care service provider model is described in Fig. 4.
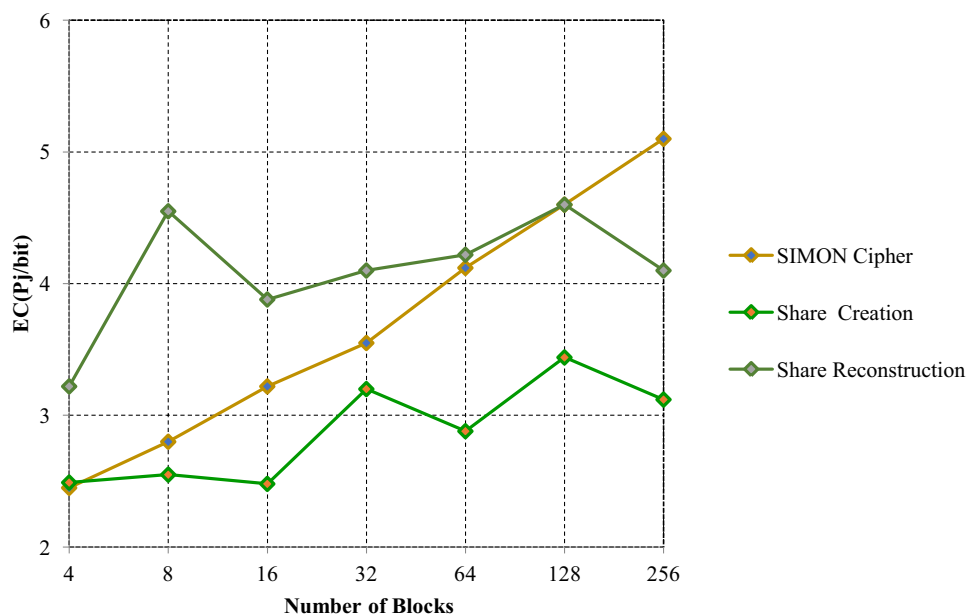
Fig. 5 Energy consumption analysis
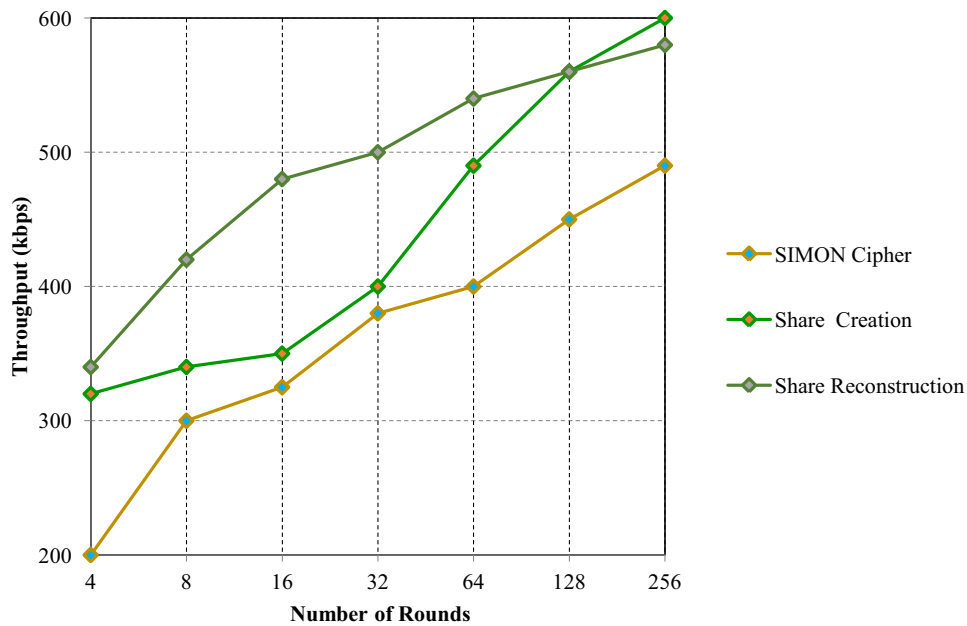
Fig. 6 Throughput analysis

This is done for improving the security of healthcare data between client and server. Also, it provides privacy from others, and it is established by SIMON [19] block cipher and CRT share generation. From this, secure the health care information if a cloud server is negotiated, mainly when a cloud server is under attacks by the insider or cloud provider.

6 Implementation results and analysis

Our proposed IoHT security model implemented in Net beans with JAVA programming language JDK 1.7.0 windows machine with the Intel (R) Core i5 processor, 1.6 GHz, 4 GB RAM. Moreover our proposed lightweight block cipher SIMON model compared with other cipher creation algorithm and optimization model, along with the Performance measure. The parameter setting is given as follows: Population size is 20, and the maximum number of fitness function evaluation is 4.0×10^4 for all functions. Here, Energy consumption, Throughput, Response time, Delay time, Encryption time, decryption time, Execution time and security level analysis are used as evaluation parameters.

Table 2 Analysis of share creation model

Number of shares	Response time (Sec)		Delay time (Sec)	
	Optimal- CRT	CRT	Optimal- CRT	CRT
2	2.52	1.45	2.88	3.08
3	2.88	1.22	3.22	3.41
6	3.22	0.99	3.89	3.55
8	3.55	2.22	4.12	3.44
9	3.88	2.41	3.55	3.14
11	4.02	2.37	4.24	3.42
12	4.08	3.22	4.51	4.01
15	4.12	3.22	4.71	4.04
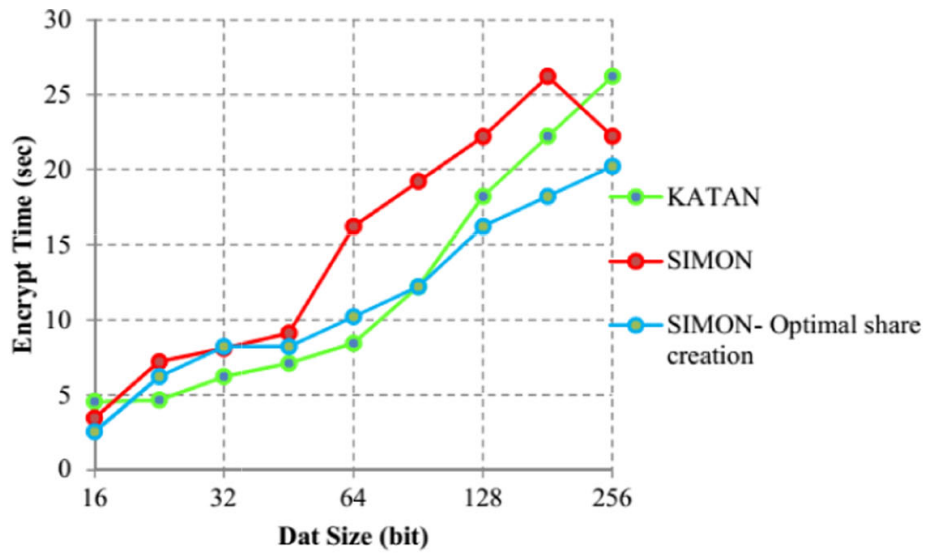
(a) Encryption Time
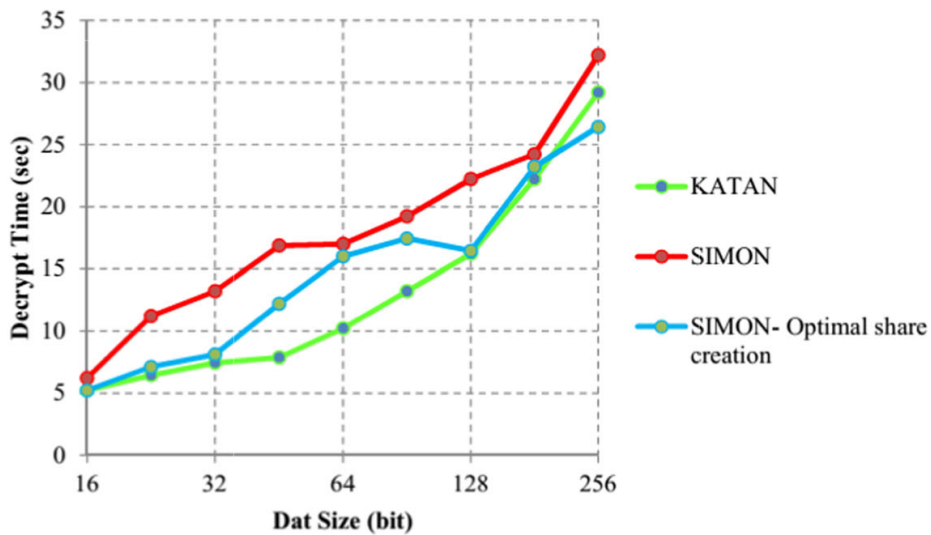
(b) Decryption Time
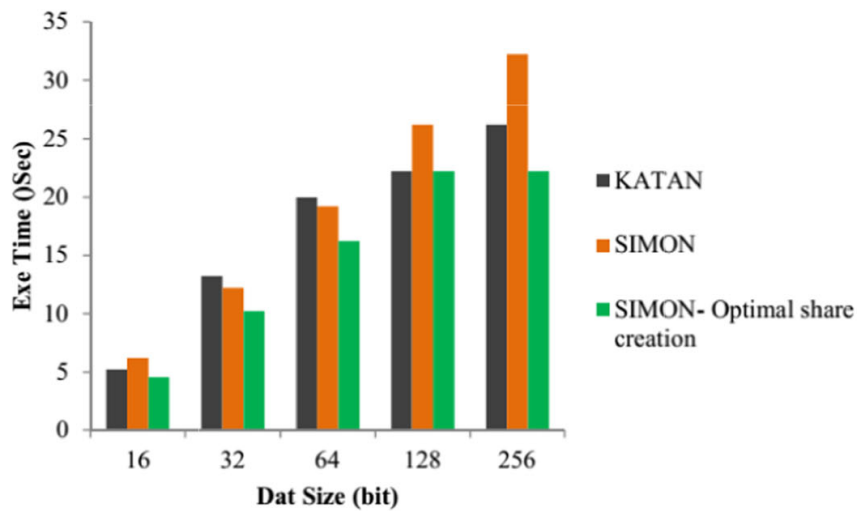
(c) Execution Time

Fig. 7 Time analysis for security model
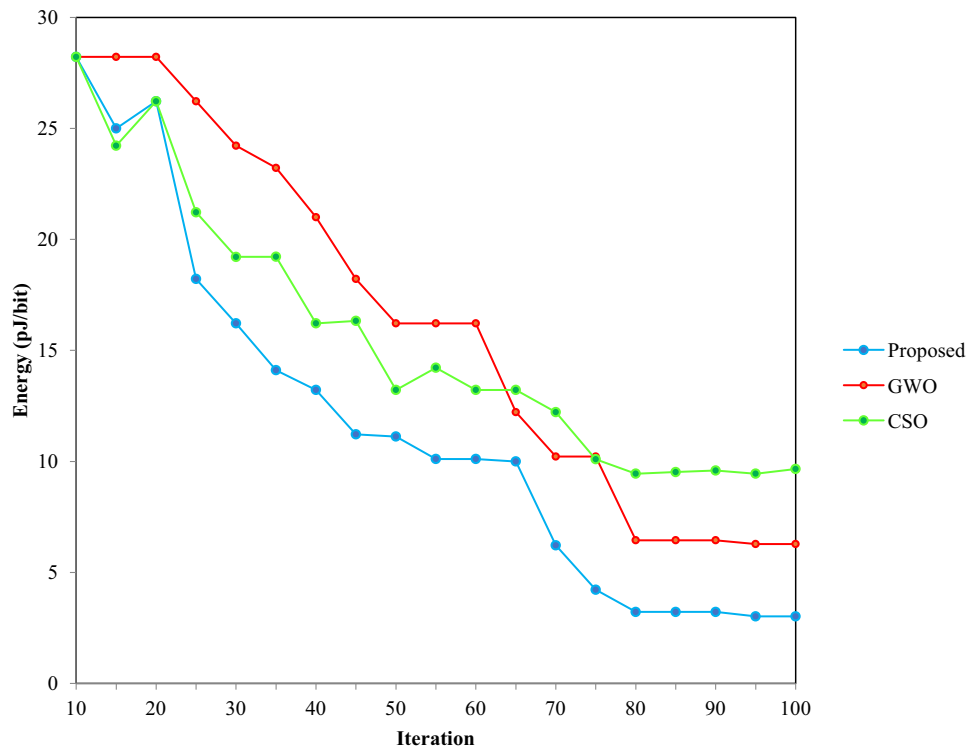
Fig. 8 Optimization objective function evaluation

6.1 Analysis

The HealthCare data securities the implementation model, the collected information's are converted to packets ready to transmit from an IoT device/sensor. Then the SIMON cipher model in hardware implementation, it maintains the security model in healthcare provider (owner/ doctor) to body sensor network information. The affirmation of a begin information initiates encryption tasks. In the first cycle of encryption tasks, the plaintext is stacked in hardware properties.

Table 1 shows the proposed Simon parameters for IoHT. Here, the parameters are analyzed based on healthcare data sizes. In this table we take some data sizes like 16, 24, 32, 48, 64,96 and 128, for example, if the data size is 16, the keywords reach 4, key size allotted as 64, the data performed in the Simon model for 32 rounds. The energy received as 3.22 PJ/bit, and the secure cipher level is 85.45%. If the data sizes are increased, key size and number of rounds are increased. Moreover, the secure cipher level reaches a maximum in the proposed Simon model.

Figure 5 shows the energy consumption for three techniques (SIMON cipher, share creation, and share reconstruction) based on certain blocks. In all the blocks the energy can be reached a maximum in SIMON cipher model (proposed); it increases gradually from 3.2 to 4.1 in increasing blocks compared to existing models. In Fig. 6 performs a throughput analysis based on several rounds. Similar to energy consumption, throughput also obtains the optimal result in the proposed model. For every round in data sizes the throughput value reduced; for instance, if the number of rounds is four the throughput value as 200 in Simon cipher, 315 in share creation, 320 in share recreation. This example shows the throughput analysis as a minimum (optimal) in the proposed technique compared to the other two for all other rounds.

Table 2 depicts the result of share creation models depends on users. Response time and the delay time is illustrated as per the number of shares. The proposed output parameter is
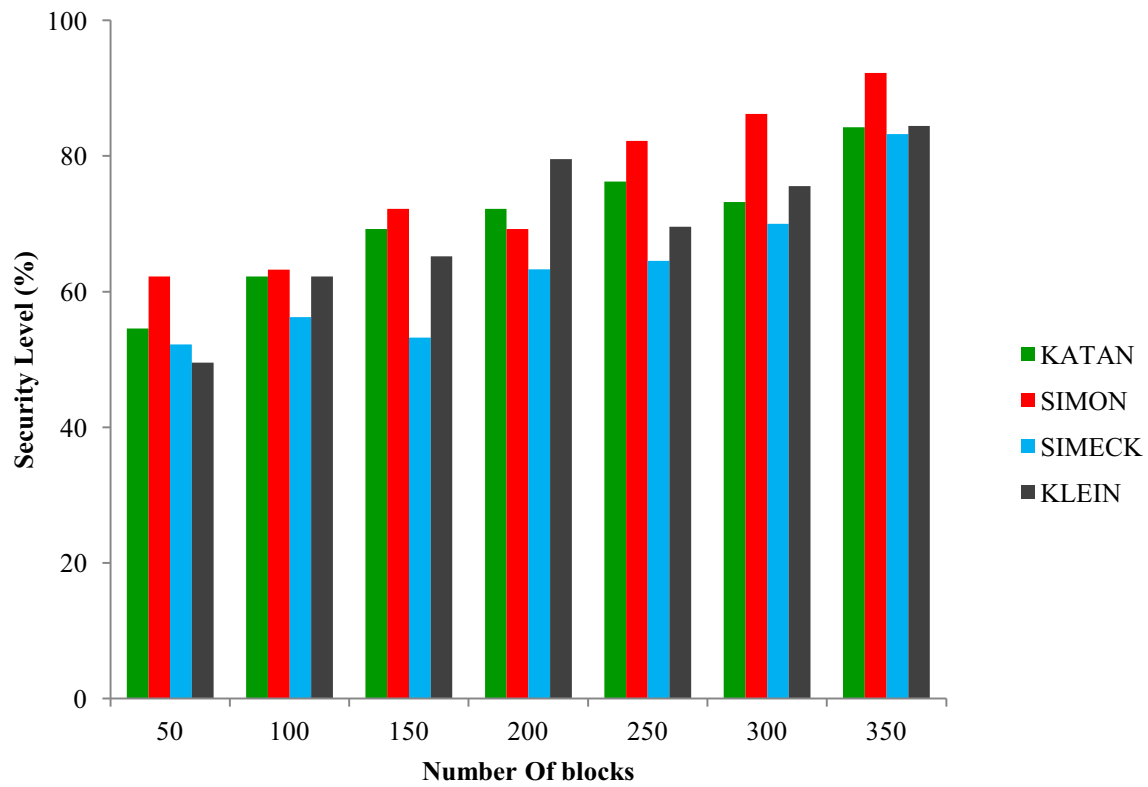
(a) Lightweight Cipher
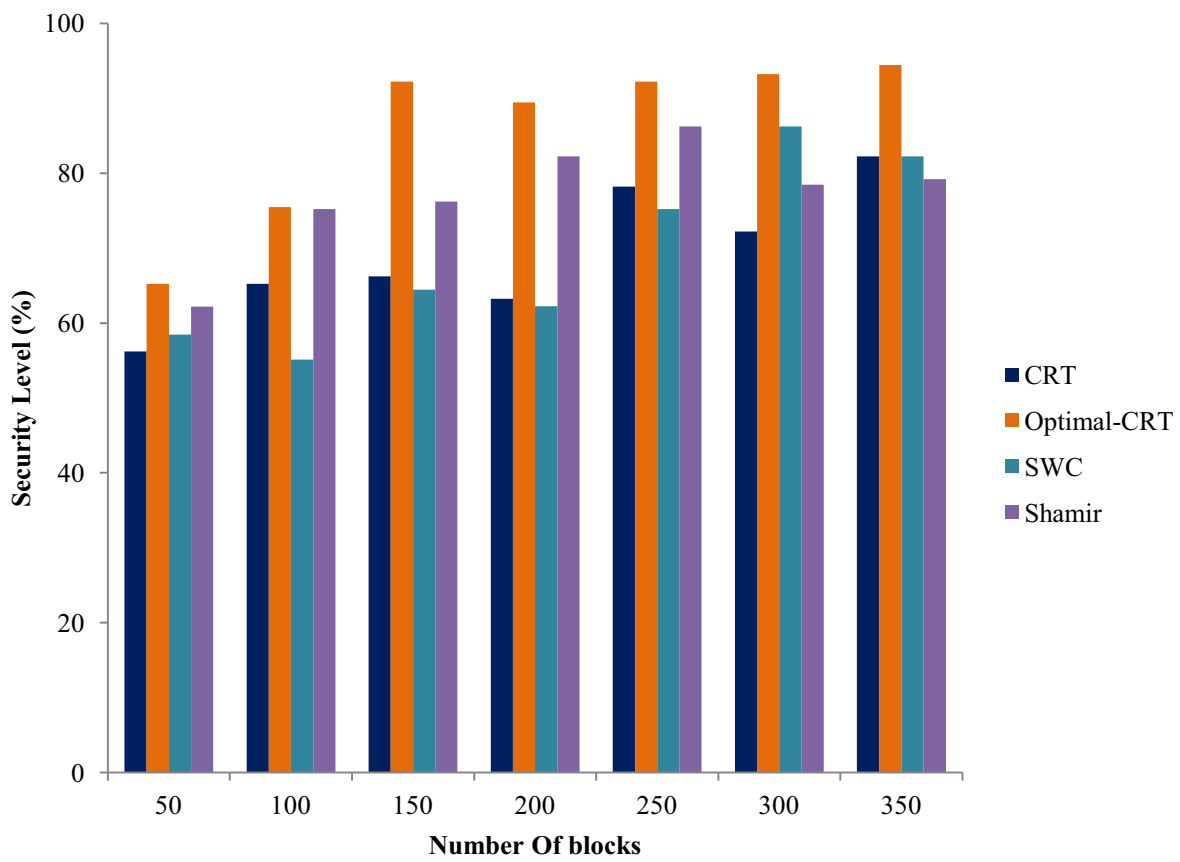
(b) Share Creation Model

Fig. 9 Security level analysis

compared to CRT. Here, we created the shares are 6; the response time is 2.52 s in optimal CRT, and 1.45 s in CRT. Delay time reaches 2.88 s in optimal CRT, and 3.08 s in CRT. The optimal CRT attains high response and less delay compared to CRT.

Figure 7 shows the time analysis for security models. In the security formation of IoHT data, we drawn the graphs for encrypt time, decrypt time and execution time based on data sizes. IoHT requires high security for each step, so we chose SIMON with optimal share creation (CRT) model. The performance of the security analysis is compared with KATAN and SIMON. Encrypted and decrypted time minimizes in the proposed model (SIMON-Optimal share creation) compared to KATAN and SIMON. In the proposed security model the execution time is reduced for every data sizes. The bar graph shows the result of the execution time for data sizes 16, 32, 64, 128, and 256.

Figure 8 shows the evaluation of the objective function. In our objective function, the fitness solution is the minimization of energy here, we compared with proposed and existing approaches. In our proposed hybrid model (HTLBO) minimized energy for every iteration. The iteration moves until we get an optimal solution here, 82nd iteration receives minimized solution as 4.6 PJ/ bit in proposed HTLBO.

Figure 9 shows the security level analysis for lightweight cipher and share creation model. In the lightweight cipher (Fig. 9a) analysis, the bar graph clearly shows the optimal level of security attains in SIMON model in the range of 61 to 91% next to SIMON model KATAN model shows achieves next level of security. In figure (b) shows the security level of share creation using CRT, Optimal CRT, SWC, and Shamir [7]. Here, optimal CRT depicts maximum security level as 65–95% for several blocks compared to other techniques.

7 Conclusion

In this research paper, we have analyzed the difficulties with data collection in IoT-based healthcare applications and presented a new healthcare data secure scheme to provide high data security and ensure the privacy of the patients' data. For secure communication, we applied a SIMON block cipher algorithm on sensed data, by the IoT sensor network. For improving the privacy of healthcare data among individuals, we implemented the share generation model. The share generation is done by optimal user selection (using TLBO algorithm), and the CRT technique shares the generated copy of every ciphertext. The outcomes demonstrated that the presented algorithm could optimize the number of users and enhance data privacy accuracy in the cloud. Furthermore, its execution time shows better performance than the other cipher algorithms and share generation model. The optimal CRT depicts maximum security level as 65–95% for several blocks compared to other techniques. For future investigations, we will study the detailed implementation of the algorithms with different measures by using innovative data encryption methods with the hybrid optimization approach. This will be pertinent to various applications in cloud data security under threats/attacks condition.

References

1. Alagar V, Alsaig A, Ormandjiva O, Wan K (2018) Context-based security and privacy for healthcare IoT. In: 2018 IEEE international conference on smart internet of things (SmartIoT). IEEE, pp 122–128

2. Ammar M, Russello G, andCrispo B (2018) Internet of things: a survey on the security of IoT frameworks. Journal of Information Security and Applications 38:8–27

3. Avudaiappan T, Balasubramanian R, Pandiyan SS, Saravanan M, Lakshmanaprabu SK, Shankar K (2018) Medical image security using dual encryption with oppositional based optimization algorithm. J Med Syst 42(11):208

4. Banerjee M, Lee J, Choo KKR (2018) A blockchain future for internet of things security: a position paper. Digital Communications and Networks 4(3):149–160

5. Beaulieu R, Treatman-Clark S, Shors D, Weeks B, Smith J, Wingers L (2015) The SIMON and SPECK lightweight block ciphers. In: 2015 52nd ACM/EDAC/IEEE design automation conference (DAC). IEEE, pp 1–6

6. Bhoyar P, Dhok SB, Deshmukh RB (2018) Hardware implementation of secure and lightweight Simeck32/64 cipher for IEEE 802.15. 4 transceiver. AEU Int J Electron Commun 90:147–154

7. Bi S, Gross WJ (2008) The mixed-radix Chinese remainder theorem and its applications to residue comparison. IEEE Trans Comput 57(12):1624–1632

8. Chaudhury S, Paul D, Mukherjee R, Haldar S (2017) Internet of thing based healthcare monitoring system. In: Industrial automation and electromechanical engineering conference (IEMECON), 2017 8th annual. IEEE, pp 346–349

9. Das AK, Zeadally S, He D (2018) Taxonomy and analysis of security protocols for internet of things. Futur Gener Comput Syst 89:110–125

10. El-hajj M, Chamoun M, Fadlallah A, Serhrouchni A (2017) Analysis of authentication techniques in internet of things (IoT). In: Cyber security in networking conference (CSNet), 2017 1st. IEEE, pp 1–3

11. Elhoseny M, Shankar K, Lakshmanaprabu SK, Maseleno A, Arunkumar N (2018) Hybrid optimization with cryptography encryption for medical image security in internet of things. Neural Comput & Applic:1–15

12. Haqaf H, Koyuncu M (2018) Understanding key skills for information security managers. Int J Inf Manag 43:165–172

13. Hossain M, Islam SR, Ali F, Kwak KS, Hasan R (2018) An internet of things-based health prescription assistant and its security system design. Futur Gener Comput Syst 82:422–439

14. Huang CD, Behara RS, Goo J (2014) Optimal information security investment in a healthcare information exchange: an economic analysis. Decis Support Syst 61:1–11

15. Jagdeo SM, Umbarkar AJ, Sheth PD (2018) Teaching–learning-based optimization on Hadoop. In: Soft computing: theories and applications (pp. 251–263). Springer, Singapore, pp 1–13

16. Leloglu E (2017) A review of security concerns in internet of things. Journal of Communications and Computer Engineering 5(1):121–137

17. Martínez-Caro E, Cegarra-Navarro JG, García-Pérez A, Fait M (2018) Healthcare service evolution towards the internet of things: an end-user perspective. Technol Forecast Soc Chang:1–9

18. Moosavi SR, Gia TN, Nigussie E, Rahmani AM, Virtanen S, Tenhunen H, Isoaho J (2016) End-to-end security scheme for mobility enabled healthcare internet of things. Futur Gener Comput Syst 64:108–124

19. Risqi YS, Yohanes S, Windarta S (2015) Fixed point attack in PGV-5 scheme using SIMON algorithm. Procedia Computer Science 72:292–299

20. Rizk-Allah RM, Hassanien AE, Bhattacharyya S (2018) Chaotic crow search algorithm for fractional optimization problems. Appl Soft Comput:1–39

21. Sfar AR, Natalizio E, Challal Y, Chtourou Z (2018) A roadmap for security challenges in the internet of things. Digital Communications and Networks 4(2):118–137

22. Sha K, Wei W, Yang TA, Wang Z, Shi W (2018) On security challenges and open issues in internet of things. Futur Gener Comput Syst 83:326–337

23. Shankar K, Elhoseny M, Kumar RS, Lakshmanaprabu SK, Yuan X (2018) Secret image sharing scheme with encrypted shadow images using optimal homomorphic encryption technique. J Ambient Intell Humaniz Comput:1–13

24. Sharma P, Sundaram S, Sharma M, Sharma A, Gupta D (2018) Diagnosis of Parkinson's disease using modified grey wolf optimization. Cogn Syst Res:1–24

25. Steinbart PJ, Raschke RL, Gal G, Dilla WN (2018) The influence of a good relationship between the internal audit and information security functions on information security outcomes. Acc Organ Soc:1–15

26. Tao H, Bhuiyan MZA, Abdalla AN, Hassan MM, Zain JM, Hayajneh T (2018) Secured data collection with hardware-based ciphers for IoT-based healthcare. IEEE Internet Things J:1–10

27. Ullah A, Sehr I, Akbar M, Ning H (2018) FoG assisted secure De-duplicated data dissemination in smart healthcare IoT. In: 2018 IEEE international conference on smart internet of things (SmartIoT). IEEE, pp 166–171

28. Usman M, Ahmed I, Aslam MI, Khan S, Shah UA (2017) Sit: a lightweight encryption algorithm for secure internet of things. arXiv preprint arXiv:1704.08688

29. Williams PA, McCauley V (2016) Always connected: the security challenges of the healthcare internet of things. In: Internet of things (WF-IoT), 2016 IEEE 3rd world forum on. IEEE, pp 30–35

30. Yehia L, Khedr A, Darwish A (2015) Hybrid security techniques for internet of things healthcare applications. Advances in Internet of Things 5(03):21

Publisher's note Springer Nature remains neutral with regard to jurisdictional claims in published maps and institutional affiliations.

S.Sheeba Rani is a faculty of Electrical and Electronics Engineering at Sri Krishna College of Engineering and Technology, Coimbatore, Tamil Nadu, India. She has completed her under graduation in Instrumentation and Control Engineering and post-graduation in Embedded Systems Technologies from College of Engineering, Anna University Chennai. She has also secured a post graduate in Business Administration from Madras University. She has been conferred doctorate in Embedded Systems Engineering Education from National Institute of Technical Teacher Training and Research, Chennai. She has authored more than 50 scientific publications and 5 books. She is a noted key note speaker in Embedded Systems and Outcome based Education in Engineering Education domain. Her research interests are Bio medics, Internet of things and Curriculum development.

Jafar A. Alzubi received a B.Sc(Hons) in Electrical Engineering, majoring Electronics and Communications from the University of Engineering and Technology, Lahore, Pakistan in 2001. In 2005 received M.Sc. (Hons) in Electrical and Computer Engineering from New York Institute of Technology, New York, USA. Between 2005 and 2008, he became a full time lecturer in the School of Engineering at Al-Balqa Appiled University – Jordan. In 2008, He joined the Wireless Communications Research Laboratory at Swansea University - UK, completed his PhD in Advanced Telecommunications Engineering in June 2012. He is now an associate professor at Computer Engineering department, Al-Balqa Applied University - Jordan. His research interests include and focuses on Elliptic curves

cryptography and cryptosystems, classifications and detection of web scams, using Algebraic-Geometric theory in channel coding for wireless networks. As part of his research, he designed the first regular and first irregular block turbo codes using Algebraic Geometry codes and investigated their performance across various computer and wireless networks. Currently he is visiting associate professor at Wake Forest University - USA.

LAKSHMANAPRABU S.K. is a senior research fellow and he is currently pursuing his Ph.D. degree in multivariable process control in the Department of Electronics and Instrumentation Engineering of B.S. Abdur Rahman Crescent Institute of Science and Technology. He completed his Bachelor of Engineering (B.E.) degree in Electronics and Instrumentation Engineering from the R.M.K. Engineering College, Chennai in the year 2009. He did his Masters in M.E. Industrial Engineering from Sudharsan Engineering College, Pudukkottai, Tamilnadu in the year 2011. He received National Fellowship from University Grand Commission, Govt. of India, Delhi, for doing his Ph.D. degree for the Year of 2013–2018. His area of interests includes Multivariable Control, Evolutionary Algorithm, Fuzzy Logic Control, Artificial Intelligence, Internet of Things, Model Based Development and Hardware in the loop Testing.

Deepak Gupta has completed B.Tech. from Guru Gobind Singh Indraprastha University, M.E. from Delhi College of Engineering and Ph.D. from Dr. APJ Abdul Kalam Technical University. He has published 24 text books on various topics of computer science & engineering with International Publishers, has edited 9 book published by Elsevier, Springer, Wiley and 49 research papers in various International Journals of repute.

R. Manikandan received his PhD from the SASTRA University, India. He received his Bachelor of Engineering and Master of Technology from Bharathidasan University and SASTRA University respectively. He is an enterprising personality has got high knowledge in the field of VLSI, Computational intelligence and Data Mining. He has got more than 60 papers in SCOPUS with SCIE indexed journals. Currently working as an Assistant professor in SASTRA Deemed University for the past 13 years. He has 19 years experience in teaching. He has attended more than 12 International and national Conferences. He has also served as reviewer to many high quality peer reviewed journals. His current research interests include data mining, big data analytics, VLSI Physical design, IoT and Health care applications.

Affiliations

S. Sheeba Rani[1] · Jafar A. Alzubi[2] · S. K. Lakshmanaprabu[3] · Deepak Gupta[4] · Ramachandran Manikandan[5]

[1] Sri Krishna College of Engineering and Technology, Coimbatore, India

[2] Al-Balqa Applied University, Salt 19117, Jordan

[3] B. S. Abdur Rahman Crescent Institute of Science and Technology, Chennai, India

[4] Maharaja Agrasen Institute of Technology, Delhi, India

[5] SASTRA Deemed University, Thanjavur, India

Preliminary Assessment for the Potential of Citrus Limetta Peel Waste for Bioethanol Production under Indian Conditions

Vinay Prabhakar, SK Singh

Department of Environmental Engineering, Delhi Technological University, Delhi, India

Abstract
Brazil is the top producer of citrus fruits in the world with 20 million tons annually while India stands 5th on the list with total production of 6,286,000 tonnes annually. Citrus limetta being the third most cultivated species of citrus after orange and lemon with 4,200,000 metric tonnes produce annually in the world. CLPW is pectin rich agro waste and can utilised for the production of bioethanol which can be used as a substitute for the conventional fuel as it is cleaner and cheaper fuel source. On overviewing different research work it can be concluded that fruit peel waste especially citrus fruit has a huge potential for bioethanol production rather discarded into the environment. The carbohydrates content of the solid waste can be determined by using Anthrone method. The fermentation is done in the bioreactor using the combination with the maximum reducing sugar yield and using *S. cerevisiae* as the microorganism. Dichromate method used for the analysis of ethanol production. The moisture content of waste was 80.59% of total weight. The average carbohydrates content of sample was found out to be 62.35% on wet weight whereas the ash content was 10.51% on dry weight basis. With increase in acid concentration there is decrease in reducing sugar yield and vice-versa. With increase in temperature there is increase in reducing sugar yield. It can also be concluded that reducing sugar yield was maximum at 150˚C and without acid. It can be also concluded that rather throwing the peel waste it can be used as a source of energy production. It can be also concluded that the method used for treatment of waste can be serve as a tool for waste management.

1. Introduction

  Human society produced waste materials as it is one of an inevitable part of their life. In ancient times, the waste generation was less and land area available for disposal are more make it very easy to dispose the waste. But, with industrialisation and urbanisation the waste generated are more and it is difficult to rely on land for disposal. There is a need of other treatment options for the wastes generated due to human activities. The per capita waste generation in India is around 0.37 kg/person/day[1]. The other treatment option available for waste treatment and disposal includes composting, incineration, land filling and production of different biofuels. The choice among them is based on different technical and economic factors.

According to an estimate by Food and Agriculture Organisation (FAO) the citrus fruit production around the world is around 115.6 million tons in 2011. It is one of the most abundant crops in the world. Brazil is the top producer of citrus fruits in the world with 20 million tons annually while India stands 5th on the list with total production of 6,286,000 tonnes annually. Citrus limetta being the third most cultivated species of citrus after orange and lemon with 4,200,000 metric tonnes produce annually in the world[2]. The distribution of citrus fruits types grown in the world is shown in figure 1. Around 57% of processed citrus limetta contributes to peel wastes[2].
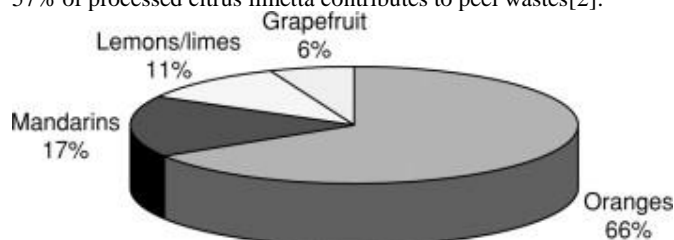

Fig. 1: Average Production Percentages of Main Types of Citrus Fruit Grown in the World

Citrus limetta peel waste (CLPW) unlike other citrus peel wastes (CPW) may be used for cattle feed[3]. However, due to unavailability of cost efficient process for treatment of CLPW a large amount of it is lost[4]. CLPW is pectin rich agro waste and can utilised for the production of bioethanol which can be used as a substitute for the conventional fuel as it is cleaner and cheaper fuel source[5].

Karimi and Karimi study on the ethanol production from kitchen and garden wastes and their residue left after for biogas production found

that the addition of fermentation biomass to the pre-treated solid significantly improved the bio methane production yield. They also found that after pre-treatment at 150 °C for 30 min and without detoxification, the maximum amounts of gasoline equivalent of 162.1 and 120.6 L were obtained with and without starch hydrolysis, respectively, where methane production yield was 157.4 mL/g VS and ethanol yields were 75.9% and 94.2%[6].

Kiran and Liu his study uses a fungal mash rich in hydrolytic enzymes produced from waste cake in-situ and applied it for the hydrolysis of mixed food wastes. Around 127 g/L glucose and 1.8 g/L free amino nitrogen act as a balanced nutrient stream produced from the enzymatic pre-treatment of food wastes using this fungal mash at 24 h. Also, using this solution as sole fermentation feedstock gives 58 g/L of ethanol corresponding to an ethanol yield of 0.5 g/g glucose was obtained within 32 h. It can be concluded from this study that the pre-treatment of mixed food wastes with the fungal mash produced is an effective option for food waste saccharification and bioethanol production[7].

Agro wastes like carrot peel, onion peel, potato peel and beetroot peel are put forward for saccharification process by *Penicillium sp.* for the hydrolysis followed by the fermentation using yeast *Saccharomyces cerevisiae* for the production of alcohol. They found that 14.52% ethanol was produced on 28th day from beetroot peel using dichromate method and 17.3% ethanol from same waste and time using Gas chromatography method for analysis[8].

Castro et. al. work on production of ethanol using three sweet sorghum cultivars. The fermentation by *Saccharomyces cerevisiae* and *Escherichia coli* followed pre-treatment of residual bagasse with dilute phosphoric acid steam explosion. They found that sugar concentration in the juice ranging from 140 to 170 g/L and almost complete conversion into ethanol by yeast. They also found that 27.5 g EtOH/L at enzyme concentrations of 11.5 FPU/gDW is produced. They also found that 10,600 L of ethanol per hectare was produced from the method they used[9].

The biofuels produced from agricultural waste such as ethanol and hydrogen is a renewable energy source. The maximum sugar production from pineapple peel is 34.03±1.30 g/L was obtained after 24 h of incubation time and maximum yield of ethanol using *S. cerevisiae* after 72h is 9.69g/L with no hydrogen production whereas using *E. aerogenes* ethanol and hydrogen production are 1.38g/L and 1,416mL/L after 72h and 12h cultivation respectively. But, when immobilized bacterial cell in matrix of loofah were used the biofuel production increased by 1.2-folds[10].

*Corresponding Author,
E-mail address: prabhakarvinay01@gmail.com, sksinghdce@gmail.com; Phone No.: +91-9891599903

Ethanol fermented from renewable sources for fuel or fuel additives are known as bio-ethanol. Many food crops have been specifically grown for the production of bio-ethanol in Nigeria. Itelima et. al. study on banana, plantain and pineapple peels for the production of bioethanol as these wastes are in abundance and do not interfere with food security were put forward for simultaneous saccharification and fermentation for 7days by co–culture of *Aspergillus niger* and *Saccharomyces cerevisiae*. They found that after 7 days of fermentation, pineapple peels had the highest biomass yield of 1.89 (OD), followed by banana peels 1.60 (OD), while plantain peels had the least 0.98 (OD). They also found that reducing sugar concentrations ranged between 0.27 – 0.94 mg/cm^3 for pineapple, 0.20 – 0.82 mg/cm^3 for banana and 0.16 – 0.45 mg/cm^3. They also found that optimal ethanol yields were 8.34% v/v, 7.45 % v/v and 3.98 % v/v for pineapple, banana and plantain peels respectively. They also conclude from the findings that pineapple and banana peels ethanol yields were significantly higher (P<0.05) than plantain peel ethanol yield. It can also be concluded that fruit wastes are no longer discarded into environment rather converted into the useful products like bioethanol which can serve as an alternative energy[11].

Santi et.al. uses orange peel waste (OPW) for conversion into bioethanol by consecutive acid-catalysed steam-explosion (ACSE), enzymatic saccharification and fermentation with *Saccharomyces cerevisiae*. They found that OPW pre-treated at 180°C for 150s yield the highest glucose solubilisation degree of around 56% at the end of the saccharification step and the maximum ethanol yield coefficient around 0.495g/g and productivity of 4.85g/L/h at the end of the 3rd repeated fermentation batch in shaken-flasks[12].

Boluda and Lopez have applied steam explosion and enzymatic hydrolysis for pre-treatment of Citrus limon L. peel wastes to obtain bioethanol, galacturonic acid and other co-products, such as d-limonene and citrus pulp pellets. They observed significant antimicrobial activity of lemon essential oils on *S. cerevisiae* at concentrations above 0.025%. They found that steam explosion pre-treatment reduces the residual content of essential oils below 0.025% and significantly decreases the hydrolytic enzyme requirements. They also found that ethanol production in excess of 60 L/1000 kg fresh lemon peel biomass can be produced[13].

Choi et. al. developed a novel approach for converting single-source CPW (i.e., orange, mandarin, grapefruit, lemon, or lime) or CPW in combination with other fruit waste (i.e., banana peel, apple pomace, and pear waste) to produce bioethanol. They used two in-house enzymes produced from *Avicel* and CPW and were tested with fruit waste at 12-15% (w/v) solid loading. They observed rate of enzymatic conversion of fruit waste to fermentable sugars were approximately 90% for all feed-stocks after 48 h. They also designed a d-limonene removal column (LRC) for successfully removal of inhibitor from the fruit waste. They also found that ethanol concentration is 14.4 to 29.5 g/L and yield is 90.2 to 93.1% when using LRC coupled with an immobilized cell reactor (ICR) which is 12-fold greater than products from ICR fermentation alone[14].

Citrus-processing industries generate every year huge amounts of wastes and citrus peel waste alone accounts for almost 50% of the wet fruit mass. Citrus waste is of immense economic value as it contains an abundance of various flavonoids, carotenoids, dietary fiber, sugars, polyphenols, essential oils, and ascorbic acid, as well as considerable amounts of some trace elements. Citrus waste also contains high levels of sugars suitable for fermentation for bioethanol production. However, compounds such as D-limonene must be removed for efficient bioethanol production[15].

On overviewing different research work it can be concluded that fruit peel waste especially citrus fruit has a huge potential for bioethanol production rather discarded into the environment. The main focus of this study was to produce bioethanol from citrus limetta peel waste. The specific objective of the study were to optimize the factors mainly temperature and acid concentration for hydrolysis of CLPW to obtain the kinetics of bioethanol production and calculating the theoretical bioethanol potential of Delhi.

2. Methodology

The waste i.e. citrus limetta peel commonly known as mousambi was collected from the fruit juice vendor outside the campus gate. It is followed by shredding of waste which is the size reduction technique for solid waste. In our study for shredding mixer grinder was used and the sample was put in air tight container and stored at 4°C for further analysis i.e. Characterisation of Waste and Acid Hydrolysis followed by Estimation of Reducing Sugars for knowing the potential of waste to produce bioethanol. Characterisation of waste includes estimation of moisture content, ash content and carbohydrates content using the standard methods. Carbohydrates content was estimated using spectrophotometer by anthrone method at 630 nm wavelength. Acid Hydrolysis is done by using different concentration of acid at different temperature (130°C to 150°C). The reducing sugar yield was analysed by DNS method using spectrophotometer at 540 nm wavelength with acid hydrolysed supernatant. Some statistical analysis like Principal Component Analysis (PCA) and Factor Analysis (FA) are applied for interpreting the results obtained from acid hydrolysis and reducing sugars yield. The maximum reducing sugars yield is further used for fermentation.

3. Results and Discussions

3.1 Characteristics of Sample

The sample was analysed for moisture content, ash content and carbohydrates as described in the previous chapter. As per the analysis carried out, the moisture content was 80.59% of total weight. The average carbohydrates content of sample was found out to be 62.35% on wet weight whereas the ash content was 10.51% on dry weight basis. The composition of 62.35% total carbohydrate shows the enormous potential for ethanol conversion. The carbohydrate content is less than the carbohydrate content in a study by Khatiwada was 72.62%[16]. The only difference was that they used organic portion of kitchen waste and in our study instead of kitchen waste citrus limetta peel waste was used.

3.2 Acid Hydrolysis and Estimation of Reducing Sugar in the Sample

As mentioned in the methodology acid hydrolysis is done with different concentration of acid ranging from 0 to 10% at different temperature ranging from 130 to 150°C. It was found that the reducing sugar concentration at 0% acid concentration and 150°C has maximum value i.e. 110.13 ppm. The combination of acid and temperature which has highest reducing sugar yield will be used for the fermentation. In our study, it can be recommended to use the sample with no acid at 150°C hydrolysed sample for fermentation process. The variation of reducing sugar yield with acid and temperature is shown in the figure 2.

3.3 Effect of Acid on Reducing Sugar Yield

It can be seen from figure 2 that with increase in acid concentration there is decrease in reducing sugar yield and vice-versa.

3.4 Effect of Temperature on Reducing Sugar Yield

It can be seen from figure 2 that with increase in temperature there is increase in reducing sugar yield.
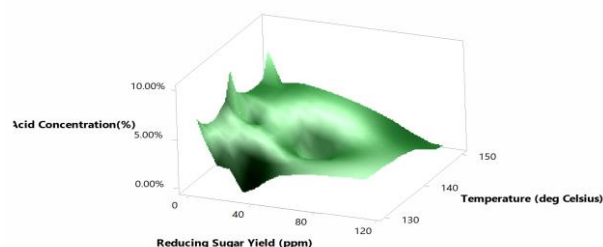
Fig. 2 Variation of Reducing Sugar Yield with Acid Concentration and Temperature

3.5 Statistical Analysis for Acid Hydrolysis and Reducing Sugar Estimation

The statistical tools like principal component analysis (PCA) and factor analysis (FA) had been applied for the result obtained for acid hydrolysis followed by reducing sugar estimation. The figure 3 and 4 shows the PCA and FA of the result obtained respectively. It can be found from the PCA that the first two principal components have eigenvalues greater than 1 and these two components explain 89.8%

of the variation in the data. Also, it can be seen that first component has large positive association with reducing sugar yield and second and third components have large negative association with temperature. There is negligible association of acid based on the PCA analysis. So, it is recommended to use distilled water for the hydrolysis of waste. It can be found from the FA that first factor has variance greater than 1 and the percentage of variability explained by factor 1, 2 and 3 are 56.5%, 33.3% and 10.2% respectively. Together, all the three factors explain 100% variation in the data.

Principal Component Analysis: Acid Concentration(%), ... r Yield (ppm)

Eigenanalysis of the Correlation Matrix

Eigenvalue	1.6938	1.0000	0.3062
Proportion	0.565	0.333	0.102
Cumulative	0.565	0.898	1.000

Eigenvectors

Variable	PC1	PC2	PC3
Acid Concentration(%)	-0.687	-0.238	0.687
Temperature (deg Celsius)	0.168	-0.971	-0.168
Reducing Sugar Yield (ppm)	0.707	0.000	0.707

Fig. 3 Principal Component Analysis (PCA) of Results Obtained

Factor Analysis: Acid Concentration(%), Temperature ... ar Yield (ppm)

Principal Component Factor Analysis of the Correlation Matrix

Unrotated Factor Loadings and Communalities

Variable	Factor1	Factor2	Factor3	Communality
Acid Concentration(%)	-0.894	-0.238	0.380	1.000
Temperature (deg Celsius)	0.219	-0.971	-0.093	1.000
Reducing Sugar Yield (ppm)	0.920	0.000	0.391	1.000
Variance	1.6938	1.0000	0.3062	3.0000
% Var	0.565	0.333	0.102	1.000

Factor Score Coefficients

Variable	Factor1	Factor2	Factor3
Acid Concentration(%)	-0.528	-0.238	1.241
Temperature (deg Celsius)	0.129	-0.971	-0.304
Reducing Sugar Yield (ppm)	0.543	0.000	1.278

Fig. 4 Factor Analysis (FA) of Results Obtained

4. Conclusions

It can be concluded that the citrus limetta peel waste have the potential for bioethanol production as it contain 62.35% of total carbohydrates. It can also be concluded that reducing sugar yield was maximum at 150˚C and without acid. It can be also concluded that maximum sugar yield of the waste with combination of acid and temperature will be used for fermentation using S. cerevisiae for the production of bioethanol. It can also be concluded that keeping in mind about the sustainability the use of simple hydrolysis with distilled water rather than acid hydrolysis is used for preparing the final sample for the fermentation as the less consumption of acid is done. It can be also concluded that rather throwing the peel waste it can be used as a source of energy production. It can be also concluded that the method used for treatment of waste can be serve as a tool for waste management.

References

[1]   RK Annepu. Sustainable Solid Waste Management in India, 2012.

[2]   E González-Molina, R Domínguez-Perles, DA Moreno, C García-Viguera. Natural bioactive compounds of Citrus limon for food and health, Journal of Pharmaceutical and Biomedical Analysis. 2010.

[3]   F Talebnia, M Pourbafrani, M Lundin, MJ Taherzadeh, Optimization study of citrus wastes saccharification by dilute-acid hydrolysis, BioResources, 2008.

[4]   M Boluda-Aguilar, L García-Vidal, FdP González-Castañeda, A López-Gómez. Mandarin peel wastes pretreatment with steam explosion for bioethanol production, Bioresour. Technolgy, 2010.

[5]   E Molnár, N Nemestóthy, K Bélafi-Bakó. Utilisation of bipolar electrodialysis for recovery of galacturonic acid, Desalination, 2010.

[6]   S Karimi, K Karimi. Efficient ethanol production from kitchen and garden wastes and biogas from the residues, J. Clean. Prod., 2018.

[7]   E Uçkun Kiran, Y Liu. Bioethanol production from mixed food waste by an effective enzymatic pretreatment, Fuel, 2015.

[8]   I Mushimiyimana, P Tallapragada. Bioethanol production from agro wastes by acid hydrolysis and fermentation process, J. Sci. Ind. Res. (India)., 2016.

[9]   E Castro et al. Potential for ethanol production from different sorghum cultivars, Ind. Crops Prod., 2017.

[10]   A Choonut, M Saejong, K Sangkharak. The production of ethanol and hydrogen from pineapple peel by Saccharomyces cerevisiae and Enterobacter aerogenes, in Energy Procedia, 2014.

[11]   J Itelima, F Onwuliri, E Onwuliri, I Onyimba, S Oforji. Bio-Ethanol Production from Banana, Plantain and Pineapple Peels by Simultaneous Saccharification and Fermentation Process, Int. J. Environ. Sci. Dev., 2013.

[12]   G Santi et al. Orange peel pretreatment in a novel lab-scale direct steam-injection apparatus for ethanol production, Biomass and Bioenergy, 2014.

[13]   M Boluda-Aguilar, A López-Gómez. Production of bioethanol by fermentation of lemon (Citrus limon L.) peel wastes pretreated with steam explosion, Ind. Crops Prod., 2013.

[14]   IS Choi, YG Lee, SK Khanal, BJ Park, HJ Bae. A low-energy, cost-effective approach to fruit and citrus peel waste processing for bioethanol production, Appl. Energy, 2015.

[15]   K Sharma, N Mahato, MH Cho, YR Lee. Converting citrus wastes into value-added products: Economic and environmently friendly approaches, Nutrition. 2017.

[16]   NR Khatiwada. Production of Ethanol from municipal solid waste of India and Nepal, December, 2017.

SNAP-BATNET: Cascading Author Profiling and Social Network Graphs for Suicide Ideation Detection on Social Media

Rohan Mishra[*]
Delhi Technological University
rohan.mishra1997@gmail.com

Pradyumna Prakhar Sinha[*]
Delhi Technological University
pradyumna_bt2k15@dtu.ac.in

Ramit Sawhney
Netaji Subhas Institute of Technology
ramits.co@nsit.net.in

Debanjan Mahata
Bloomberg
dmahata@bloomberg.net

Puneet Mathur
MIDAS, IIIT-Delhi
pmathur3k6@gmail.com

Rajiv Ratn Shah
MIDAS, IIIT-Delhi
rajivratn@iiitd.ac.in

Abstract

Suicide is a leading cause of death among youth, and the use of social media to detect suicidal ideation is an active line of research. While it has been established that these users share a common set of properties, the current state-of-the-art approaches utilize only text-based (stylistic and semantic) cues. We contend that the use of information from networks in the form of condensed social graph embeddings and author profiling using features from historical data can be combined with an existing set of features to improve the performance. To that end, we experiment on a manually annotated dataset of tweets created using a three-phase strategy and propose SNAP-BATNET, a deep learning based model to extract text-based features and a novel Feature Stacking approach to combine other community-based information such as historical author profiling and graph embeddings that outperform the current state-of-the-art. We conduct a comprehensive quantitative analysis with baselines, both generic and specific, that presents the case for SNAP-BATNET, along with an error analysis that highlights the limitations and challenges faced paving the way to the future of AI-based suicide ideation detection.

1 Introduction

Suicide is among the top three causes of death among youth worldwide. According to a WHO report[1], almost one million people die from suicide annually and 20 times more people attempt suicide. Therefore, suicide causes a global mortality rate of 16 per 100,000, and there is one attempt every 3 seconds on average (Radhakrishnan and Andrade, 2012). Moreover, the effect of it on friends and family members are often devastating (E. Clark and D. Goldney, 2000). What compounds the issue is that while it is preventable and, early detection is crucial in effective treatment, there is a lot of social stigma related to it which prevents people from disclosing their thoughts and seeking professional help. It has been found that people suffering from suicidal ideation make use of social media networks to share information about their mental health online (Park et al., 2012) with many having disclosed their suicidal thoughts and plans (Prieto et al., 2014). Therefore it is a pressing issue to be able to utilize the signals available on social media in order to identify individuals who suffer from *suicide ideation* in an automated manner and offer them the required help and treatment.

There exists an active field of research in the field of suicidal ideation detection (O'Dea et al., 2015; Sawhney et al., 2018a) that are able to extract meaningful patterns of behavior from users of social media in order to predict suicidal behavior. These have utilized the information presented in the text of the posts that were shared and utilized both traditional as well as deep learning methods. A rich body of literature exists to show the influence of social interactions of at-risk individuals for their effective detection and treatment. However, to the best of our knowledge, no advances have been made to include information from social engagement, ego networks and other user attributes

---

[*] Denotes equal contribution.
[1] https://www.who.int/mental_health/prevention/suicide/suicideprevent/

which we hypothesize would help us in being able to detect suicidal behavior better. Since the interaction of a person with their social surrounding in the form of author profiling from historical tweets and social graph based information can give us a plethora of information about their mental health (Luxton et al., 2012), we explore the usage of author profiling and other features to detect the presence of suicide ideation in tweets better.

Our contributions to the field are as follows -

1. Creation of a significantly large manually annotated dataset for detection of patterns in suicidal behavior in social media along with historical tweet data and social network graphs which will be made publicly available after anonymization keeping all ethical considerations in mind.

2. Proposing *SNAP-BATNET (Social Network Author Profiling - BiLSTM Attention NETwork)*, a feature stacking based architecture that uses novel handcrafted features: *author profiling, historical stylistic features, social network graph embeddings* and *tweet metadata* with an ablation study for validation.

3. Conducted an extensive quantitative comparison with several traditional and state-of-the-art baselines along with an in-depth error analysis to highlight the challenges faced.

2 Related Work

2.1 Suicidal Ideation Detection

There have been certain advances in the usage of social media to automatically detect cases of suicidal ideation in the past (Sawhney et al., 2018a; De Choudhury et al., 2013; Benton et al., 2017). Cavazos-Rehg et al. (2016) performed a content-based analysis on a small number of depression related tweets to derive certain qualitative insights into the behavior of users displaying suicidal behavior but did not propose any automated solution for the task of detection. Sawhney et al. (2018a) prepared a manually annotated dataset of tweets and proposed a set of features to be used to improve classifier performance but included only text-based features which limits the performance of the classifiers. De Choudhury et al. (2013) developed a crowd-sourced set of patients diagnosed with Major Depressive Disorder(MDD) and used their social media posting through the course of a

year to establish a set of signals to help predict depression before its onset. Benton et al. (2017) utilized a novel multitask learning framework to predict atypical mental health conditions with a scope of predicting suicidal behavior but included only text-based features for their multi-task framework.

Furthermore, there have been several forays into tweet classification that utilize a similar set of signals for other applications such as detection of abuse, cyberbullying and hate speech (Mathur et al., 2018b), (Mathur et al., 2018a). Waseem and Hovy (2016) used a public dataset and used a collection of features to show the usefulness of gender-based and location-based information in improving the effectiveness of classifiers. Gambäck and Sikdar (2017) developed a CNN model that used both character n-grams and word2vec features in order to improve the classifier performance greatly. Badjatiya et al. (2017) made use of the same benchmarking dataset, provided a set of baselines and used a combination of randomly initialized embeddings along with LSTM and Gradient Boosting Decision Trees to achieve state of the art performance.

2.2 Author Profiling

The inclusion of author based information has been explored in some tasks related to natural language processing. Waseem and Hovy (2016) utilized gender and location-based information along with text-based features to achieve superior performance. Johannsen et al. (2015) used similar features for syntactic parsing. While it is accepted that such demographic features may improve performance, it is often not possible to extract such features from social media websites like Twitter since this information is often unavailable and unreliable. This has spawned an exciting line of research that makes use of a social graph of interaction between users to derive information about the user. Applications extract information about each user by representing each user as a node in a social graph and creating low dimensional representations usually induced by neural architecture (Grover and Leskovec, 2016; Qiu et al., 2018).

The application of such graph-based features overcomes the limitation caused by unavailability. Mishra et al. (2018); Qian et al. (2018) use such social graph based features to gain considerable improvement in the task of abuse detection. Tasks like sarcasm detection also gain improvement by

using such features(Amir et al., 2016).

3 Data

The unavailability of a public dataset for performing benchmark tests, motivated us to develop our own dataset of considerable size in order to validate our hypothesis. We would like to make our dataset, lexicon, and embeddings public to the research community after making it anonymous and keeping all ethical considerations in mind to improve AI-based suicide prevention and analysis[2].

The dataset generation was a two-phase process: (i) A lexicon of suicidal phrases was generated (ii) Tweets were scraped using the lexicon and, historic tweets and social engagement data was gathered for each of the users.

3.1 Developing a Lexicon of Suicidal Phrases

In order to scrape tweets to create the dataset, a lexicon of phrases which could indicate suicidal ideation was created. The top posts, most of which are much larger than tweets, were scraped from three different forums which have an abundance of posts with suicidal ideation. These are *r/suicidalthoughts* [3] (top 100), *r/suicidewatch*[4](top 100) and *takethislife.com* [5] (top 200). Pytextrank [6] is a python module which implements a ranking model for text processing (Mihalcea and Tarau, 2004). This was used to rank and gather the list of the most prominent phrases from these posts. A manual filtering pass was also done to remove posts with little or no suicidal ideation information. The resulting list had 143 phrases such as *hit life, think suicide, wanting to die, suicide times, last day, feel pain point, alternate life, time to go, beautiful suicide, hate life*. Furthermore, the lexicon was extended by using the lexicon shared in (Sawhney et al., 2018a).

3.2 Data Collection

Collecting tweets: For each phrase in the curated lexicon, tweets were scraped using the Twitter REST API[7]. A total of 48,887 tweets were

---

[2]https://github.com/ramitsawhney27/NAACLSRW19Suicide
[3]https://www.reddit.com/r/suicidalthoughts/
[4]https://www.reddit.com/r/SuicideWatch/
[5]https://www.takethislife.com
[6]https://pypi.org/project/pytextrank/
[7]https://developer.twitter.com/en/docs.html

tweet_id	text
hashtags	user_mentions
user_id	retweet_count
favorite_count	

Table 1: Dataset fields.

Graph Type	Edge Represents	Sparsity (10⁻⁵)	Avg Degree
quotes	A quoted B	0.570	0.185
mentions	A mentioned B	2.780	0.905
repliedTo	A replied to B	1.755	0.571
follower	A follows B	1.587	0.516

Table 2: Graph comparisons(A and B represent users along an edge in the graph).

obtained. Furthermore, retweets and non-English language tweets were removed. A manual check was done to remove the tweets (around 3000) which were trivially non-suicidal. The final dataset has 34,306 tweets. Each tweet in the dataset is described by the fields given in Table 1.

Data for Author Profiling: For the 34,306 tweets in the dataset, there are 32,558 unique users. For each of these users, the tweet timeline (previous 100 tweets or as many available) was scraped. Texts from historical tweets were combined for each of the users to generate the historical corpus for author profiling.

Social Graphs: The engagement between the users from the dataset was captured in the form of social graphs where the users were represented as vertices and edges denoted the relationships. Table 2 shows the different graphs constructed corresponding to four different relationships and also the statistical comparisons between them.

For the *Follower Graph*, follower lists were scraped for each of the users while for the other three graphs, tweets from the dataset and the historical collection were crawled through.

3.3 Data Annotation

Two annotators, who are students in clinical psychology adept in using social media on a daily basis, were provided with the guidelines to label the tweets as used in (Sawhney et al., 2018b). The guidelines were based on the following classification system -

1. **Suicidal intent present**

   - Posts where suicide plan and/or previous attempts are discussed.

- Text conveys a serious display of suicidal ideation.
- Posts where suicide risk is not conditional unless some event is a clear risk factor eg:depression, bullying, etc.
- Tone of text is sombre and not flippant.

2. **Suicidal intent absent**

- Posts emphasizing on suicide related news or information.
- Posts containing no reasonable evidence that the risk of suicide is present; includes posts containing song lyrics, etc.
- Condolences and awareness posts.

An acceptable Cohen's Kappa score was found between the two annotations (**0.72**). In cases of ambiguity in labeling or conflicts in merging, the default class 0 (non-suicidal) was assigned. The resulting dataset had 3984 suicidal tweets (12% of the entire dataset).

4 Methodology

The overall methodology is split into three phases: *preprocessing of data, extraction of features* and finally *evaluation of models and feature sets.*

4.1 Preprocessing

Due to the unstructured format of the text used in social media, a set of filters were employed to reduce the noise while not losing useful information.

1. A tweet-tokenizer was used [8] to parse the tweet and replace every username mentions, hashtags, and urls with <mention>, <hashtag>and <url>respectively.

2. The tokenized text then underwent stopword removal and was used as an input to Word-Net Lemmatizer provided by nltk(Bird and Loper, 2004).

3. Using Lancaster Stemmer, provided by nltk(Bird and Loper, 2004) stemmed text was also generated to be used as inputs for some feature extraction methods.

4.2 Feature Extraction

The features extracted from the data set can be broadly classified into four types: *Text-based features, tweet metadata features, User Historical tweets features and Social Graph-based features.*

---

[8]https://pypi.org/project/tweet-preprocessor/

Text Based Features

- *TF-IDF*: Term Frequency-Inverse Document Frequency was used with the unigrams and bigrams from the stemmed text, using a total of 2000 features chosen by the tf-idf scores across the training dataset. The tf-idf scores were l2 normalized.

- *POS*: Parts of Speech counts for each lemmatized text using The Penn Tree Bank(Marcus et al., 1993) from the Averaged Perceptron Tagger in nltk is used to extract 34 features.

- *GloVe Embeddings*: The word embeddings for each word present in the pre-trained GloVe embeddings trained on Twitter (Pennington et al., 2014) were extracted, and for each tweet, the average of these is taken.

- *NRC Emotion*: The NRC Emotion Lexicon (Mohammad and Turney, 2013) is a publicly available lexicon that contains commonly occurring words along with their affect category (anger, fear, anticipation, trust, surprise, sadness, joy, or disgust) and two polarities (negative or positive). The score along these 10 features was computed for each tweet.

- *LDA*: Topic Modelling using the probability distribution over the most commonly occurring 100 topics was used as a feature for each tweet. LDA features were extracted by using scikit-learn's Latent Dirichlet Allocation module (Pedregosa et al., 2011). Only those tokens were considered which occurred at least 10 times in the entire corpus.

Tweet Metadata Features: The count of hashtags, mentions, URLs, and emojis along with the retweet count and favorite count of every tweet was extracted and used as a feature to gain information about the tweets response by the authors environment.

User Historical tweets: To gain information about the behavior of the author and their stylistic choices, a collection of their tweets were preprocessed, and stylistic and semantic features such as the averaged GloVe embeddings, NRC sentiment scores and Parts of Speech counts were extracted.

Social Graph Features: Grover and Leskovec (2016) describe an algorithm *node2vec* for converting nodes in a graph (weighted or unweighted) into feature representations.This method has been

employed by Mishra et al. (2018) in the task of abuse detection in tweets. *node2vec* vectors were generated for each of the graphs as introduced in Section 3.2.

5   Baselines

A set of baselines that reflect the current state-of-the-art approaches in short text classification were established. These include methods that use traditional learning algorithms as well as deep learning based models.

- **Character n-gram + Logistic Regression**: Character n-gram with Logistic Regression in the range (1,4) has often been used effectively for classification and works as a strong baseline (Waseem and Hovy, 2016; Badjatiya et al., 2017; Mishra et al., 2018).

- **Bag of Words + GloVe + GBDT**: A Bag of Words(BoW) corpus was generated with unigram and bigram features, the averaged pretrained GloVe embeddings were then used on a Gradient Boosting Decision Tree which incrementally builds in stage-wise fashion. It is used as a baseline in (Badjatiya et al., 2017).

- **GloVe + CNN**: A CNN architecture inspired from (Kim, 2014; Badjatiya et al., 2017) was used with filter sizes (3,4,5).

- **GloVe + LSTM**: An LSTM with 50 cells was used along with dropout layers ($p = 0.25$ and 0.5, preceding and following, respectively).

- **ELMo**: Tensorflow Hub [9] was used to get ELMo(Peters et al., 2018) embeddings which are known to have an excellent performance in several fields including sentiment analysis and text classification.

- **USE** - The Universal Sentence Encoder (Cer et al., 2018) encodes text into high dimensional vectors that can be used for tasks like text classification, semantic similarity, and clustering. Tensorflow Hub was used to get sentence encoding. Each tweet was converted encoded onto a dense 512 feature space.

- **Sawhney C-LSTM**: We replicated the C-LSTM architecture used in (Sawhney et al.,

---

2018a) which uses CNN to capture local features of phrases and RNN to capture global and temporal sentence semantics.

- **R-CNN**: Recurrent Convolutional Neural Networks as proposed by (Lai et al., 2015) make use of a recurrent structure to capture contextual information as far as possible when learning word representations.

6   Methodology: SNAP-BATNET

6.1   Graph Embeddings

As discussed in the previous sections, social graphs were constructed for author profiling which could capture demographic features and improve the performance of the classifier. Four such weighted and undirected graphs were constructed: *Follower Graph, Mentions Graph, RepliedTo Graph* and *Quotes Graph*. All the self-loops were removed from the graphs, as they do not contribute to suicide-related communication features.

To obtain the author profiles, the nodes in the graphs were converted into feature representation using *node2vec* (Grover and Leskovec, 2016). *node2vec* works on the lines of word2vec and determines the context of the nodes by looking into their neighborhoods in the graph. It constructs a fixed number of random walks of constant length for each of the nodes to define the neighborhood of the nodes. The random walks are governed by the parameters *p (return parameter)* and *q (in-out parameter)* which have the ability to fluctuate the sampling between a depth-first strategy and a breadth-first strategy.

node2vec by itself does not generate embeddings for solitary nodes which comprised about 2/3rd of the total nodes. As per the empirical rule of normal distribution, 99.73% of the values lie within three standard deviations of the mean. To isolate the solitary nodes from the remaining ones, a random vector was generated three standard deviations away from the mean and was assigned to them.

Embeddings were generated for both weighted and unweighted graphs and were individually studied for the classification task. The number of dimensions and the number of epochs was set to 200 and 10 respectively. A stratified 5-fold grid search was carried out on the hyperparameters - *p, q, walk-length, window-size*. It was found that the default values for p and q(1 and 1) along with

Combination	F1	AP
Follower+Mentions (CG)	0.808	0.203
Follower+RepliedTo (CG)	0.806	0.196
Mentions+RepliedTo (CG)	0.803	0.197
Follower+Mentions + RepliedTo (CG)	0.807	0.201
Follower+Mentions + RepliedTo (CE)	**0.849**	**0.268**

Table 3: Graph combination results(CG-Combining graphs, CE-Combining embeddings) with weighted F1 and area under precision recall curve.

the combination of walk length 10 and window-size 5 performed best. This performance of short walks can be attributed to the sparse nature of the graphs. It was determined that unweighted graphs performed better and were used for generating combined social graph embeddings.

Combining Graph Embeddings: *Quotes Graph* was discarded from any further study owing to its individual performance in contrast with the other graphs. Its poor performance can be attributed to its statistics as given in the table 2. The rest of the graphs were combined followed two methods: by combining graphs or by combining embeddings using a deep learning approach. The resulting embeddings were trained using a Balanced Random Forest classifier. These results are shown in Table 3.

For generating these combined embeddings, a deep learning model as shown in Figure 1 was designed to be trained on the dataset. After the training, the concatenation layer was picked up as the embedding for the combination, and this was generated for all the users. These embeddings were then used in an LR classifier and a balanced random forest classifier. The results from the balanced random forest classifier were superior and were further used for feature stacking as mentioned in Section 6.2. *SNAP-BATNET* uses Follower, Mention and RepliedTo embeddings combined using the deep learning approach to generate social graph based features.

6.2 Feature Stacking

The competing systems make use of the text based features for classification. To leverage the availability of different kinds of information in form of tweet metadata, historical author profiling and social graph based embeddings so as to overcome the unavailability of a predefined lexico-semantic pattern in the text, methods of combining infor-
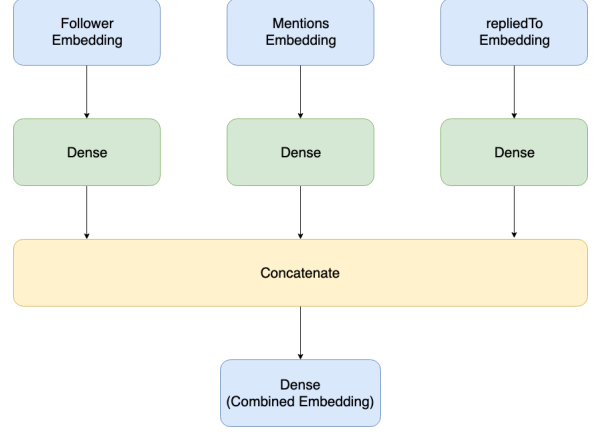

Figure 1: Combining graph embeddings.
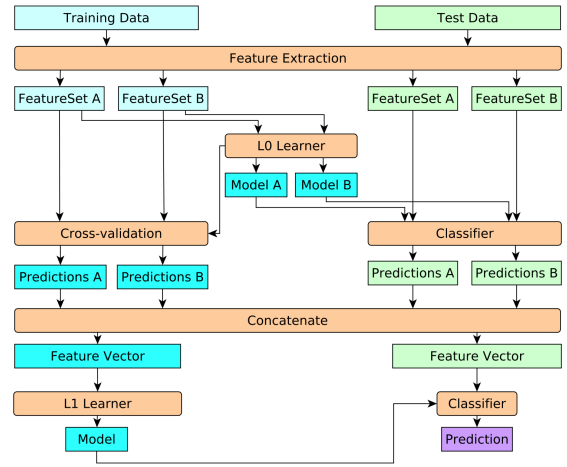
Figure 2: Feature Stacking: A meta-learning approach (figure taken from (Lui, 2012)).

mation were explored. While tweet metadata is sparse, social graph based embeddings are dense in nature.

Initially, concatenation was used, and several models were tried by performing ablation studies. It was observed that the performance of the classifiers did not change significantly and in some cases deteriorated as features were concatenated. Therefore, it was reasoned that the feature sets should be combined in a way that would have the ability to join them related to their relative importance and also allow learning of non-linear relationships between them. Instead of using concatenation which proved to be ineffective or relative weighing, which is cumbersome, we used a meta learning approach inspired from (Lui, 2012).

One major difference between (Lui, 2012) and our approach is that while it uses Logistic Regression as weak learner for each feature set, different weak learners depending on the feature set or

Model	F1	AP	F1	AP	F1	AP	F1	AP
	Text Based		+ Tweet Metadata		+ Author Profiling		+ Graph	
FeatStackLR	.891	.641	.893	.640	.894	.643	.896	.671
Char ngram+ LR	.892	.646	.910	.653	.912	.647	**.915**	**.679**
BoWV+GloVe+GBDT	.897	.567	.896	.534	.897	.542	.899	.584
GloVe+CNN	.908	.619	.910	.619	.910	.623	.913	.644
GloVe+LSTM	.908	.612	.906	.613	.907	.617	.910	.642
USE	.915	.669	.916	.667	.916	.666	.914	.663
ELMo	.913	.650	.894	.629	.909	.629	.911	.623
Sawhney-C-LSTM	.915	.662	.915	.662	.916	.661	.912	.687
RCNN	.921	.704	.919	.705	.920	.706	.923	.726
SNAP-BATNET	.923	.709	.925	.707	.925	.708	**.926**	**.726**

Table 4: Results with weighted F1 and area under precision recall curve.

baseline models were employed in our approach. The weak learners were chosen by using grid search over { *Logistic Regression, Balanced Random Forest Classifier, SVM* }. For each of the baselines, features from tweet metadata, historical author profiling, and social graph embeddings were combined using Feature Stacking. Logistic Regression was used as L1 learner since stacked LR is theoretically closer to a neural network and can help introduce non-linearity between the features (Dreiseitl and Ohno-Machado, 2002).

Our model *SNAP-BATNET* uses feature stacking with different L0 learners to combine the feature sets pertaining to text-based information(BiLSTM+Attention), tweet metadata information(Logistic Regression), historical author profiling(Logistic Regression) and social graph embeddings(Balanced Random Forest Classifier). Furthermore, a simple architecture(*FeatStackLR*) is proposed that uses Logistic Regression as both L0 and L1 learners. An ablation study of the hand-crafted feature sets was carried out using *FeatStackLR*, which is shown in Table 5. The addition of GloVe based embedding leads to an improvement in results as these embeddings encode semantic information that is missing from statistical features.

7 Experiments and Results

7.1 Experimental Setup

All the experiments were conducted with a train-test split of 0.2. The hyperparameters for each learner were calculated by using a 5-fold stratified cross-validation grid search. The CNN and

Features	F1	AP
TF-IDF + EMB + POS + LDA + NRC	**0.891**	**0.641**
TF-IDF + EMB + POS + LDA	0.891	0.640
TF-IDF + EMB +POS	0.890	0.641
TF-IDF + EMB	0.890	0.641
TF - IDF	0.888	0.618

Table 5: Ablation study (measured using weighted F1 score and area under Precision-Recall curve).

LSTM architectures used 200-dimensional GloVe embeddings pre-trained on Twitter corpus using the Adam optimizer and were run for 10 epochs. The models were implemented in Keras with a Tensorflow Backend. In CNN and LSTM models, 0.1 of the training data was held out as validation data to prevent the model from overfitting. Each baseline model uses Feature Stacking and is used as a L0 learner to extract text-based features to be combined with other feature sets such as tweet metadata, historical author profiling and finally social graph embeddings.

7.2 Results

Zhang and Luo (2018) describe the lacunae of reporting metrics such as micro F1, Precision or Recall provided in cases of highly imbalanced datasets such as Abuse Detection. In order to properly gauge the ability of a system to detect suicidal ideation from tweets, we report the F1, Precision and Recall scores on a per class basis in Table 4. The results in Table 6 include the weighted F1 Score along with the area under the

Models and Classes		Text Based			+ Metadata			+ Author Profiling			+ Graph		
		P	R	F	P	R	F	P	R	F	P	R	F
FeatStackLR	0	.97	.89	.93	.97	.90	.93	.97	.90	.93	.97	.90	.93
	1	.47	.75	.57	.47	.74	.58	.47	.76	.58	.48	.77	.59
Char n-gram +LR	0	.97	.89	.93	.95	.94	.95	.95	.94	.95	.96	.94	.95
	1	.47	.77	.58	.57	.63	.60	.58	.63	.60	**.59**	**.66**	**.62**
BoWV + GloVe + GBDT	0	.92	.98	.95	.94	.94	.94	.94	.94	.94	.95	.94	.94
	1	.71	.32	.44	.52	.53	.52	.52	.53	.53	.52	.58	.55
GloVe +CNN	0	.94	.97	.95	.95	.96	.95	.95	.96	.95	.95	.96	.95
	1	.64	.47	.55	.60	.55	.57	.61	.54	.57	.62	.56	.59
GloVe +LSTM	0	.94	.97	.95	.95	.94	.95	.95	.94	.95	.95	.95	.95
	1	.65	.46	.54	.56	.59	.58	.56	.59	.58	.58	.60	.59
Universal Sentence Encoder	0	.94	.97	.95	.96	.94	.95	.96	.94	.95	.96	.94	.95
	1	.65	.54	.59	.58	.68	.63	.59	.66	.63	.57	.69	.62
ELMo	0	.94	.98	.96	.97	.90	.93	.94	.97	.95	.96	.94	.95
	1	.70	.46	.56	.48	.73	.58	.64	.48	.55	.57	.64	.60
Sawhney- C-LSTM	0	.94	.98	.96	.94	.96	.95	.94	.97	.96	.96	.93	.95
	1	.70	.48	.57	.64	.56	.59	.67	.53	.59	.55	.72	.63
RCNN	0	.95	.96	.96	.96	.95	.95	.96	.95	.95	.96	.96	.96
	1	.65	.62	.63	.62	.66	.64	.61	.66	.64	.64	.66	.65
SNAP-BATNET	0	.95	.97	.96	.95	.97	.96	.95	.97	.96	.95	.96	.96
	1	.71	.55	.62	.69	.60	.64	.68	.61	.64	**.68**	**.62**	**.65**

Table 6: Results with precision, recall and F1 score on a per class basis.

Precision-Recall Curve.

It was observed that adding features such as social graph embeddings, historical author profiling, and tweet metadata led to a considerable improvement in the performance of the classifiers since each feature set encodes a different kind of information that gives the resulting models more adept at the task of classification. As per our hypothesis, the addition of social graph embeddings led to significant improvement in performance across all baseline models. There was an increase in the recall value which is desirable because the reduction of false negatives was more important than the reduction of false positives. Among the traditional classifiers, character n-gram with Logistic Regression performed the best. Moreover, the use of LSTMs in the model such as Sawhney-C-LSTM, RCNN, and SNAP-BATNET improved the classifier performance. This can be reasoned by the effectiveness of LSTM in capturing long term dependencies. Among all the deep learning models, SNAP-BATNET, when combined with all other feature sets using Feature Stacking, performed the best outperforming the current state-of-the-art, i.e., Sawhney-C-LSTM.

7.3 Error Analysis

Here we go through some examples posed challenges to highlight limitations and future scope.

1. **Subtle indication**: "*Death gives meaning to life*" contains subtle indications of suicidal behavior but caused ambiguity between annotators and was not detected by the model.

2. **Sarcasm**: "*I want to f**king kill myself lol xD* " is one of the several examples where the frivolity of the tweet couldn't be determined.

3. **Quotes and Lyrics**: "*Better off Dead S̃leeping With Sirens; I'm as mad, and I'm not going to take this anymore!*" are song lyrics and movie dialogues which the annotators were able to identify but the model could not as it lacked real-world knowledge.

8 Conclusion

This paper explores the use of information from the behavior of users on social media by using features such as text-based stylistic features in combination with historical tweets based profiling and social graph based embeddings. We develop a

manually annotated dataset on detection of suicidal ideation in tweets, a set of handcrafted features were extracted which were utilized by a set of traditional and state of the art deep learning based models and a quantitative comparison was carried out which validated the hypothesis of the effectiveness of social graph based features and author profiling in suicidal behavior detection with our proposed SNAP-BATNET model, particularly in improving recall. An extensive error analysis and comparison with baselines presents the case for our methodology.

In the future, this work can be extended by exploiting multi-modalities in the data in the form of images, videos, and hyperlinks. Multi-modal approaches have extensively been used for various tasks like predicting social media popularity (Meghawat et al., 2018; Shah and Zimmermann, 2017). Another interesting aspect would be to adapt the pipeline described in this paper to different problems like identifying mentions of personal intake of medicine in social media (Mahata et al., 2018b,a).

References

Silvio Amir, Byron C Wallace, Hao Lyu, and Paula Carvalho Mário J Silva. 2016. Modelling context with user embeddings for sarcasm detection in social media. *arXiv preprint arXiv:1607.00976*.

Pinkesh Badjatiya, Shashank Gupta, Manish Gupta, and Vasudeva Varma. 2017. Deep learning for hate speech detection in tweets. In *Proceedings of the 26th International Conference on World Wide Web Companion*, pages 759–760. International World Wide Web Conferences Steering Committee.

Adrian Benton, Margaret Mitchell, and Dirk Hovy. 2017. Multi-task learning for mental health using social media text. *arXiv preprint arXiv:1712.03538*.

Steven Bird and Edward Loper. 2004. Nltk: the natural language toolkit. In *Proceedings of the ACL 2004 on Interactive poster and demonstration sessions*, page 31. Association for Computational Linguistics.

Patricia A Cavazos-Rehg, Melissa J Krauss, Shaina Sowles, Sarah Connolly, Carlos Rosas, Meghana Bharadwaj, and Laura J Bierut. 2016. A content analysis of depression-related tweets. *Computers in human behavior*, 54:351–357.

Daniel Cer, Yinfei Yang, Sheng-yi Kong, Nan Hua, Nicole Limtiaco, Rhomni St John, Noah Constant, Mario Guajardo-Cespedes, Steve Yuan, Chris Tar, et al. 2018. Universal sentence encoder. *arXiv preprint arXiv:1803.11175*.

Munmun De Choudhury, Michael Gamon, Scott Counts, and Eric Horvitz. 2013. Predicting depression via social media. *ICWSM*, 13:1–10.

Stephan Dreiseitl and Lucila Ohno-Machado. 2002. Logistic regression and artificial neural network classification models: a methodology review. *Journal of biomedical informatics*, 35(5-6):352–359.

Sheila E. Clark and Robert D. Goldney. 2000. The impact of suicide on relatives and friends. *The international handbook of suicide and attempted suicide*, pages 467–484.

Björn Gambäck and Utpal Kumar Sikdar. 2017. Using convolutional neural networks to classify hate-speech. In *Proceedings of the First Workshop on Abusive Language Online*, pages 85–90.

Aditya Grover and Jure Leskovec. 2016. node2vec: Scalable feature learning for networks. In *Proceedings of the 22nd ACM SIGKDD international conference on Knowledge discovery and data mining*, pages 855–864. ACM.

Anders Johannsen, Dirk Hovy, and Anders Søgaard. 2015. Cross-lingual syntactic variation over age and gender. In *Proceedings of the Nineteenth Conference on Computational Natural Language Learning*, pages 103–112.

Yoon Kim. 2014. Convolutional neural networks for sentence classification. *arXiv preprint arXiv:1408.5882*.

Siwei Lai, Liheng Xu, Kang Liu, and Jun Zhao. 2015. Recurrent convolutional neural networks for text classification. In *AAAI*, volume 333, pages 2267–2273.

Marco Lui. 2012. Feature stacking for sentence classification in evidence-based medicine. In *Proceedings of the Australasian Language Technology Association Workshop 2012*, pages 134–138.

David D Luxton, Jennifer D June, and Jonathan M Fairall. 2012. Social media and suicide: a public health perspective. *American journal of public health*, 102(S2):S195–S200.

Debanjan Mahata, Jasper Friedrichs, Rajiv Ratn Shah, and Jing Jiang. 2018a. Detecting personal intake of medicine from twitter. *IEEE Intelligent Systems*, 33(4):87–95.

Debanjan Mahata, Jasper Friedrichs, Rajiv Ratn Shah, et al. 2018b. # phramacovigilance-exploring deep learning techniques for identifying mentions of medication intake from twitter. *arXiv preprint arXiv:1805.06375*.

Mitchell P Marcus, Mary Ann Marcinkiewicz, and Beatrice Santorini. 1993. Building a large annotated corpus of english: The penn treebank. *Computational linguistics*, 19(2):313–330.

Puneet Mathur, Ramit Sawhney, Meghna Ayyar, and Rajiv Shah. 2018a. Did you offend me? classification of offensive tweets in hinglish language. In *Proceedings of the 2nd Workshop on Abusive Language Online (ALW2)*, pages 138–148.

Puneet Mathur, Rajiv Shah, Ramit Sawhney, and Debanjan Mahata. 2018b. Detecting offensive tweets in hindi-english code-switched language. In *Proceedings of the Sixth International Workshop on Natural Language Processing for Social Media*, pages 18–26.

Mayank Meghawat, Satyendra Yadav, Debanjan Mahata, Yifang Yin, Rajiv Ratn Shah, and Roger Zimmermann. 2018. A multimodal approach to predict social media popularity. In *2018 IEEE Conference on Multimedia Information Processing and Retrieval (MIPR)*, pages 190–195. IEEE.

Rada Mihalcea and Paul Tarau. 2004. Textrank: Bringing order into text. In *Proceedings of the 2004 conference on empirical methods in natural language processing*.

Pushkar Mishra, Marco Del Tredici, Helen Yannakoudakis, and Ekaterina Shutova. 2018. Author profiling for abuse detection. In *Proceedings of the 27th International Conference on Computational Linguistics*, pages 1088–1098.

Saif M Mohammad and Peter D Turney. 2013. Nrc emotion lexicon. *National Research Council, Canada*.

Bridianne O'Dea, Stephen Wan, Philip J Batterham, Alison L Calear, Cecile Paris, and Helen Christensen. 2015. Detecting suicidality on twitter. *Internet Interventions*, 2(2):183–188.

Minsu Park, Chiyoung Cha, and Meeyoung Cha. 2012. Depressive moods of users portrayed in twitter. In *Proceedings of the ACM SIGKDD Workshop on healthcare informatics (HI-KDD)*, volume 2012, pages 1–8. ACM New York, NY.

Fabian Pedregosa, Gaël Varoquaux, Alexandre Gramfort, Vincent Michel, Bertrand Thirion, Olivier Grisel, Mathieu Blondel, Peter Prettenhofer, Ron Weiss, Vincent Dubourg, et al. 2011. Scikit-learn: Machine learning in python. *Journal of machine learning research*, 12(Oct):2825–2830.

Jeffrey Pennington, Richard Socher, and Christopher Manning. 2014. Glove: Global vectors for word representation. In *Proceedings of the 2014 conference on empirical methods in natural language processing (EMNLP)*, pages 1532–1543.

Matthew E. Peters, Mark Neumann, Mohit Iyyer, Matt Gardner, Christopher Clark, Kenton Lee, and Luke Zettlemoyer. 2018. Deep contextualized word representations. In *Proc. of NAACL*.

Víctor M Prieto, Sergio Matos, Manuel Alvarez, Fidel Cacheda, and José Luís Oliveira. 2014. Twitter: a good place to detect health conditions. *PloS one*, 9(1):e86191.

Jing Qian, Mai ElSherief, Elizabeth M Belding, and William Yang Wang. 2018. Leveraging intra-user and inter-user representation learning for automated hate speech detection. *arXiv preprint arXiv:1804.03124*.

Jiezhong Qiu, Yuxiao Dong, Hao Ma, Jian Li, Kuansan Wang, and Jie Tang. 2018. Network embedding as matrix factorization: Unifying deepwalk, line, pte, and node2vec. In *Proceedings of the Eleventh ACM International Conference on Web Search and Data Mining*, pages 459–467. ACM.

Rajiv Radhakrishnan and Chittaranjan Andrade. 2012. Suicide: an indian perspective. *Indian journal of psychiatry*, 54(4):304.

Ramit Sawhney, Prachi Manchanda, Puneet Mathur, Rajiv Shah, and Raj Singh. 2018a. Exploring and learning suicidal ideation connotations on social media with deep learning. In *Proceedings of the 9th Workshop on Computational Approaches to Subjectivity, Sentiment and Social Media Analysis*, pages 167–175.

Ramit Sawhney, Prachi Manchanda, Raj Singh, and Swati Aggarwal. 2018b. A computational approach to feature extraction for identification of suicidal ideation in tweets. In *Proceedings of ACL 2018, Student Research Workshop*, pages 91–98.

Rajiv Shah and Roger Zimmermann. 2017. *Multimodal analysis of user-generated multimedia content*. Springer.

Zeerak Waseem and Dirk Hovy. 2016. Hateful symbols or hateful people? predictive features for hate speech detection on twitter. In *Proceedings of the NAACL student research workshop*, pages 88–93.

Ziqi Zhang and Lei Luo. 2018. Hate speech detection: A solved problem? the challenging case of long tail on twitter. *arXiv preprint arXiv:1803.03662*.

Study of the influence of friction stir processing on tungsten inert gas welding of different aluminum alloy

Husain Mehdi[1] · R. S. Mishra[1]

Abstract

Tungsten inert gas welding is the most commonly used process for joining of aluminum alloy, which are highly demanded in aerospace application. In this process coarse grain structure, micro crack and porosity was obtained due to persisting thermal conditions when the fusion zone start to solidify. The formation of these defects on the weld region will result in reduction of weld strength about to half the parent material. To avoid these defects the top surface of gas tungsten arc welding are processed using friction stir processing up to certain depth from the top of the welds. Friction stir processing destroyed the coarse grain dendritic structure in the tungsten welded joint, because of change in grains refinement and microstructure significantly improved the hardness of the friction stir processing (FSP) weld over the base metal and TIG weld. In this study, we compared the experimental result of TIG, FSW and (TIG + FSP) welded joint. Coarse grain structure was observed in TIG welding and fine grain structure was observed in FSP process. In addition very fine grain structure we observed in stir zone due to the effect of intense plastic deformation and temperature during TIG + FSP.

Keywords Tensile strength · Microstructure analysis · Micro-hardness · Friction stir welding

1 Introduction

Friction stir welding (FSW) is a new technique of joint similar and dissimilar materials and it is environmental friendly and energy efficient [1, 2]. The friction stir welding has been successfully used to produce joint in Mg-alloy, Al-alloy, Ti-Alloy and other alloy [3–7]. Comparison between TIG and FSW technique with a long established one the friction stir welding shown the advantages to tungsten inert welding. The used material Al-6082-T6 makes high claims to these techniques due to the problem of pore formation and hot cracks [8]. Another problem is the loss of strength and hardness caused by the microstructural instability in the heat affected zone (HAZ) [9].

In the recent year, FSW has been a research focus instead of TIG welding. Comparison to other welding process, FSW is versatile for magnesium alloy, aluminum alloy, copper alloy, steel and dissimilar alloy [10–15]. It is widely used for Al–Zn and Al–Cu series which have a poor

performance [16–21]. The carbon migration takes place in dissimilar welded joint subjected to thermal loading at temperature of 625°. The micro-hardness and ultimate tensile strength of welded joint increase by increasing the pre-stress [22–24].

There are several techniques applied such as heat treatment process, gas tungsten arc welding (TIG), arc melting and mechanical deformation process to modify the material properties in order to improve the joint properties. However these methods are not efficient and some of those are not applicable for using welded joints, where the joint strength is highly required. In recent year, friction stir welding becomes a prominent welding process for joining of aluminum alloy [1]. The joining of aluminum alloy magnesium alloy can be easily weld by FSW process, moreover, it is also suitable for joining of dissimilar material [25–31]. Friction stir welding involves a cylindrical rotating tool of consumable or non-consumable material that plunges between the two plates and moves, stir and bounded

between them. The heat is produced during FSW process and generation of thermo-mechanical conditions develops a heterogeneous fine grained microstructure across the weld seam [32]. The stirred zone materials to soften without melting of parent material due to heat generated by the process of adiabatic heat and mechanical mixing with in the material [33]. The mechanical properties of FSW joint are mainly dependent on chemical composition and processing parameters of alloying element. The microstructural analysis of FSW joints shows the formation of new grain size in the weld zone with different amount of heat input by controlling the processing parameter [34–37].

The coarse grain structure, micro-cracks and porosity are obtained in TIG welding due to the unremitting thermal conditions. Forming these defects on the weld zone will result in a reduction in weld strength. In this work, to avoid these defects, a friction stir processing is used to destroy the coarse-grained dendritic structure in the tungsten welded joint and very fine grain structure was observed in stir zone to the effect of intense plastic deformation and temperature during TIG + FSP.

2 Materials and method

2.1 Selection parameter for TIG welding

When TIG welding is applied, rust, paint, dirt oil and other contamination must be removed from the welded material surface. The welding properties is also depended on the electrode condition, arc length, travel speed, current polarity on weld shape, shielding gas coverage and angle of the torch. The welding parameter ranges taken into account for welding arc welding current of 120–180 amp gas flow rate of 15 L/min and welding speed of 90–105 mm/min.

2.2 Selection parameter for FSW

After TIG welding on aluminum alloy, friction stir welding was applied on TIG welded joint. FSW involve plastic deformation and complex movement. FSW processing parameter such as welding speed, tool rotation and axial force on the welding characteristics. Weld were made by joining of two plates ($200 \times 60 \times 7$ mm) workpiece were clamped on the machine tool.

2.3 Experimental procedure

The aluminum alloy used in this study in the form of plates with the dimension of ($200 \times 60 \times 7$ mm). The plates were cleaned with the help of acetone to remove the oil the oil and dirt etc. and steel wire brush was used to remove the oxide layer. During TIG welding. The optimized welding parameter such as welding current of 120 amp, a voltage of 20 V and the welding speed of 34 mm/min and argon shielding are used. Before friction stir welding the GTAW weld reinforcement are removed by machining it and flattened the weld bead with its substrate sides for applying better friction stir processing, after marching of GTAW weld, FSP was applying at the transverse speed of 1.1 mm/sec, target depth of 2 mm, rotational speed of 1200 rpm and vertical force of 8000 kg applied over the weld during FSP. The cylindrical tool was used during FSP of EN31 with pin length of 2 mm. The pin and shoulder diameter of FSP tool were 6 mm and 18 mm respectively [39].

3 Results and discussions

3.1 Tensile strength

The ultimate tensile strength of welded joint of Al-6083-T6 and Al-2024 has been investigated by using of TIG, FSW and (TIG + FSP) welding process at different process parameter as shown in Fig. 1. The average tensile strength and their corresponding percentage elongation as shown in Tables 1 and 2 for TIG and FSW respectively. In each condition three specimen were tested. The chemical composition for Al-6083-T651 and Al-2024 as shown in Tables 3 and 4. The minimum ultimate tensile strength of 204.23 MPa was obtained at 160 amp current in TIG welding, whereas
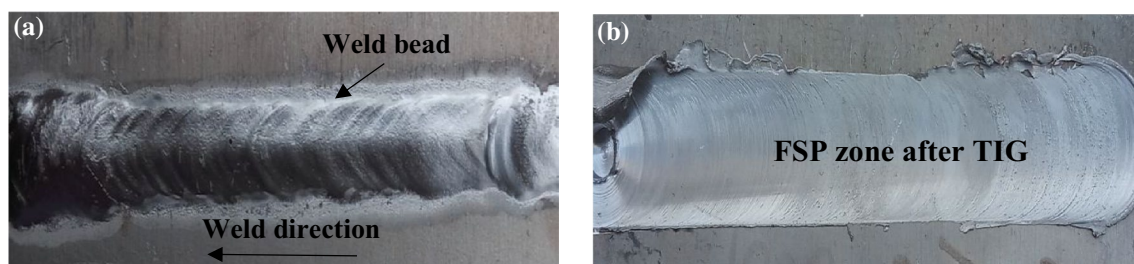

Fig. 1 Weld bead formation and quality of weld, **a** TIG welding, **b** TIG + FSP

Table 1 Processing parameter of TIG welding [38]

Specimen designation	Current (amp)	Gas flow rate (l/min)	Tensile strength (MPa)	Microhardness (HV)	Percentage elongation	Impact toughness
B$_1$	120	15	165	49	3.53	6
B$_2$	140	15	204	57	4.52	8
B$_3$	160	15	186	54	4.21	5
B$_4$	180	15	173	49	4.11	4

Table 2 Processing parameter of friction stir welding [38]

Exp. no.	Tool speed (rpm)	Welding speed (mm/min)	Axial force (KN)	Tensile strength (MPa)	Percentage elongation	Micro-hardness (HV)	Impact toughness
1	300	25	6	202	5.4	52	15
2	700	25	6	221	6.4	55	19
3	500	15	6	229	6.3	58	15
4	500	35	6	244	7.8	60	18
5	500	25	4	234	5.8	57	16
6	500	25	8	250	6.7	55	20
7	500	25	6	265	7.1	65	24

Table 3 Chemical composition of Al-6082-T651 [38]

Si	Cu	Fe	Mg	Mn	Zn	Cr	Ti	Al
0.7–1.3	0.1	0.5	0.6–1.2	0.4–1.0	0.2	0.25	0.2	Balance

Table 4 Chemical composition of Al-2024 [39]

| Si	Cu	Fe	Mg	Mn	Zn	Cr	Ti	Al
0.5	3.9	0.48	1.45	0.58	0.24	0.09	0.148	Balance

maximum ultimate tensile strength of 223.65 MPa at tool rotation of 500 rpm, welding speed of 25 mm/min and axial force of 6KN was obtained in FSW process. The strength of both at GTAW and GTAW + FSP welds are lower than the parent material as shown in Figs. 2 and 3. The strength of TIG weld and TIG + FSP, however TIG + FSP joint showed better performance and its elongation is higher than the TIG welds. The ductility of the TIG + FSP welds are better than the TIG welds due to absence of porosity and other defects and improved microstructure characteristics.

3.2 Micro-hardness

In this study, 2 mm thick cold rolled annealed and 6 mm thick hot rolled plate Al–Mg–Mn–Sc–Zr alloy were examined to study the effect of FSW and tungsten inert gas welding process on the microstructure and mechanical properties of welded joints as shown in Table 5.

Figure 4 shows the micro-hardness of FSW and TIG welded joint for cold rolled annealed and hot rolled
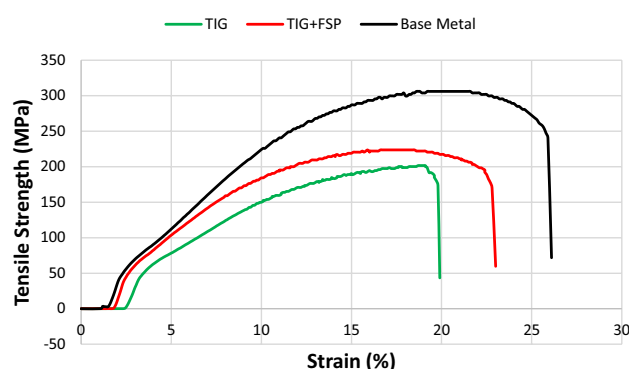
Fig. 2 Comparison of stress strain diagram of Al-2024 for base metal, TIG and TIG + FSP

aluminum alloy plate. The micro-hardness value for both the welding processes are low at the center of welded joint and the microhardness of the welded joint higher than the base material [43]. For hot rolled and cold rolled plate,
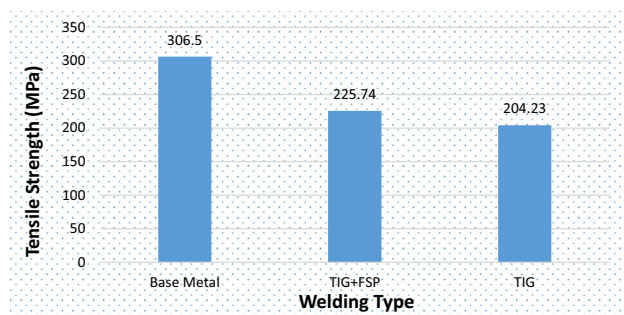
Fig. 3 Comparison of tensile strength of Al-2024 for two different welding process TIG and TIG + FSP

Table 5 Tensile mechanical properties of base metal and welded joints [43]

Sample	Tensile strength (MPa)	Yield strength (MPa)	Elongation (%)
Hot rolled plate			
Base plate	411	290	19.6
FSW joint	380	239	12.5
TIG joint	344	227	9.5
Cold rolled plate			
Base plate	423	322	20.7
FSW joint	391	257	10.9
TIG joint	365	246	10.2

the micro-hardness at FSW center is higher than the TIG weld center and the yield point stress of aluminum alloy is directly proportional to its hardness [46]. The distribution of micro-hardness is consistent with the result that tensile test sample of friction stir welding all broke at the weld center (Table 6).

The hardness values of the TIG welds HAZ region exhibits higher hardness over the HAZ of the TIG + FSP joint. The distance away from the weld center towards unaffected

Table 6 Mechanical properties of Al-6082-T651 [38]

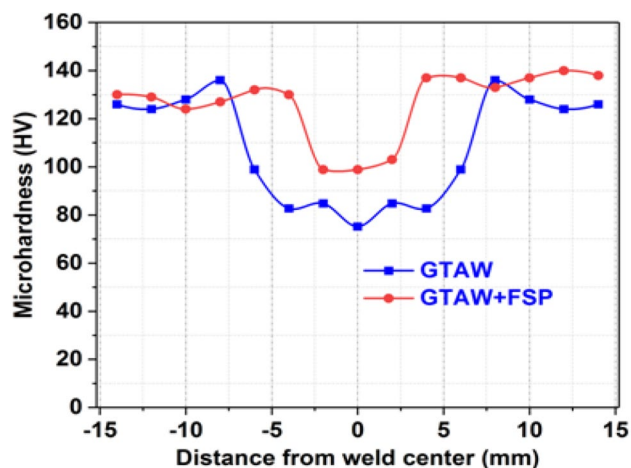| Ultimate tensile strength (MPa)	Yield strength (MPa)	Percentage elongation	Hardness (HV)
312–322	260	10–13	94

Fig. 5 Microhardness of welded joint at two different welding processes TIG and TIG + FSP [39]

base metal, the HAZ region after the TMAZ, in this zone the joints temperature is comparatively low and at this low temperatures, this zone experienced to induce a kind of ageing, hence it's resulted in an enhancement of mechanical properties. As a matter of fact, the microhardness of TIG + FSP joints as shown in Fig. 5 clearly indicates the lowest hardness value are related to the TMAZ region and stir zone, while the hardness of HAZ region are slightly higher compared to the even un affected base metal. As seen from the microstructures and modified microstructure of the TIG + FSP weld of fine grain structure over the TIG coarse grain structure, the hardness distribution directly indicates the evidence of improved microstructural characteristics and mechanical properties of the TIG + FSP weld [39].
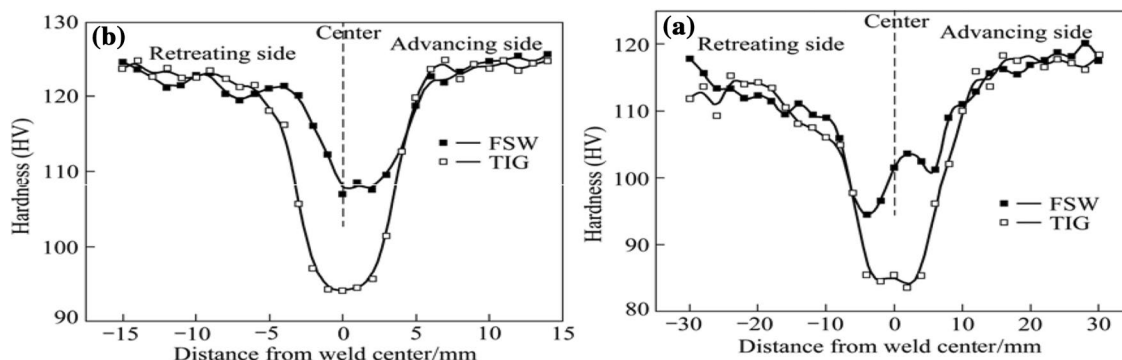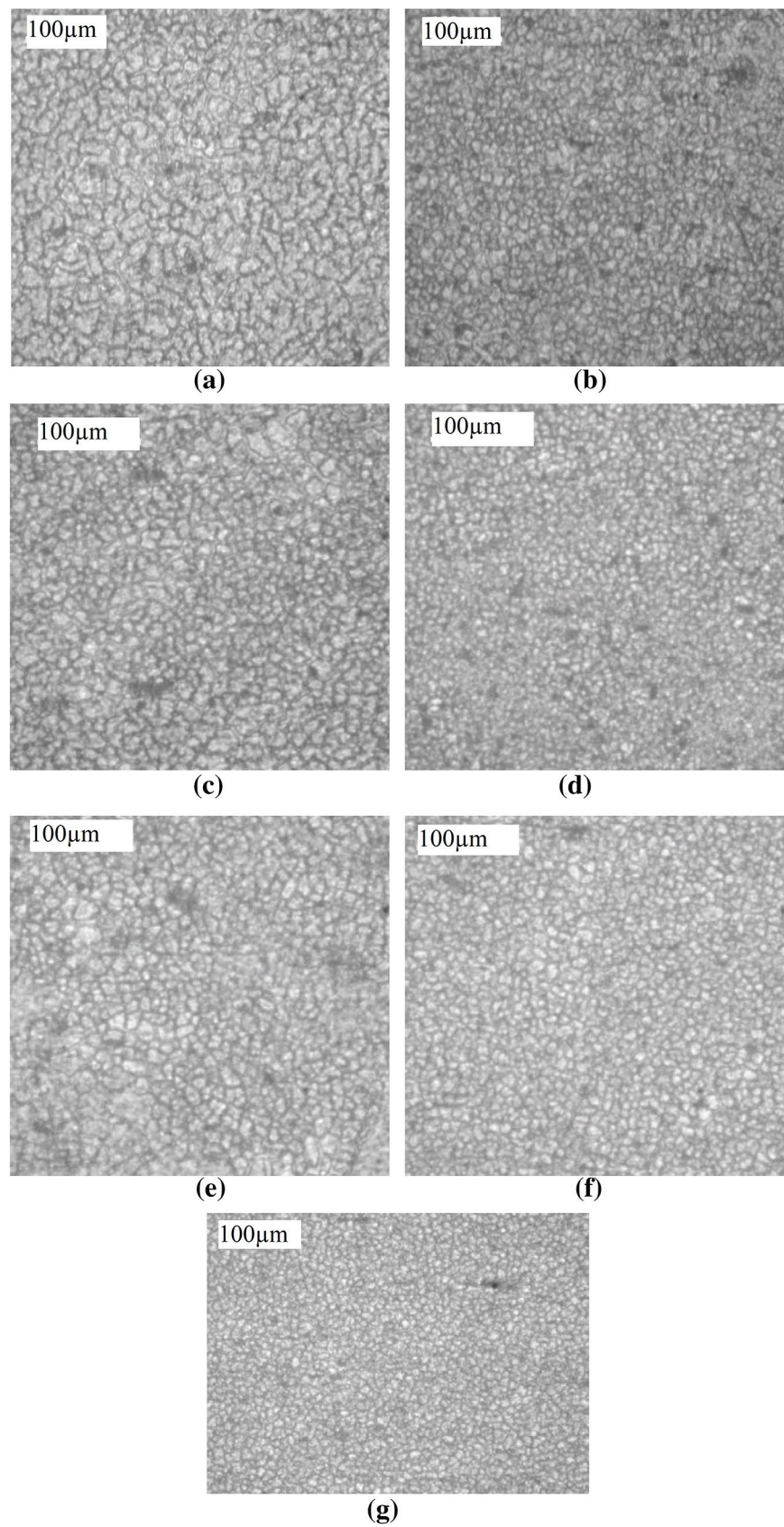

Fig. 4 Microhardness of the welded joint, **a** cold rolled annealed plate, **b** hot rolled plate [43]

Fig. 6 Optical micrograph of FSW for Al-alloy specimen from the experiment No 1 to 7 (at ×100) [38]
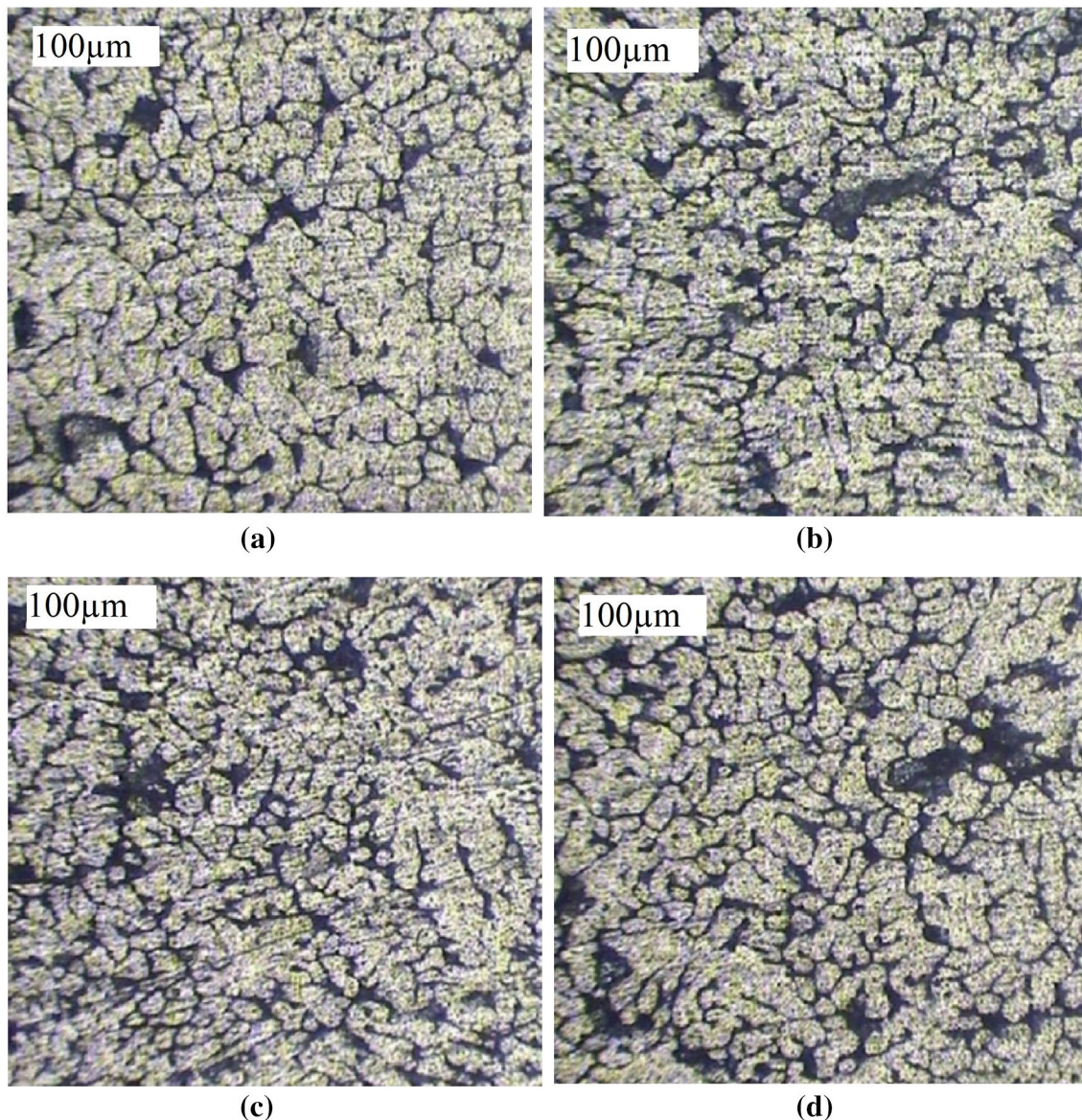
Fig. 7 Optical micrograph of TIG welded joint at different current, **a** 120 amp, **b** 140 amp, **c** 160 amp, **d** 180 amp

3.3 Microstructure analysis of TIG, FSW and (TIG + FSP)

3.3.1 Optical micrograph of FSW and TIG welded joints

Figures 6 and 7 illustrate the optical micrograph of FSW and TIG welded joints. The microstructure of the FSW joint, the weld region of FSW contain equiaxed and finer grain structure and TIG welded shows the elongated and coarse grain structure. The distribution of precipitates were different in TIG and FSW welded joint [40–42]. Due to equiaxed and finer grain structure in FSW and dendrite structure in TIG welded joint and the tensile strength of FSW joint was higher than the TIG welded joint.

During the welding process, the temperature at TIG weld center was higher than the FSW weld nugget zone, and the temperature at TIG weld center was higher than melting point of the alloy. Figure 8a–d, shows the optical microstructure of TIG welded joint. It shows the weld center of cold rolled annealed and hot rolled plate exhibits cast structure and the grain sixe of TIG welded joint of hot rolled plate, there are a few short feathery or pine tree structure (Fig. 8a), the boundary of semi-molten zone and heat affected zone (HAZ) is obvious (Fig. 8b), and there is very thin layer of equiaxed grains between the semi fused zone and the heat affected zone, the equiaxed and smaller than the grain structure of fused zone and HAZ as shown in Fig. (8c) [43].
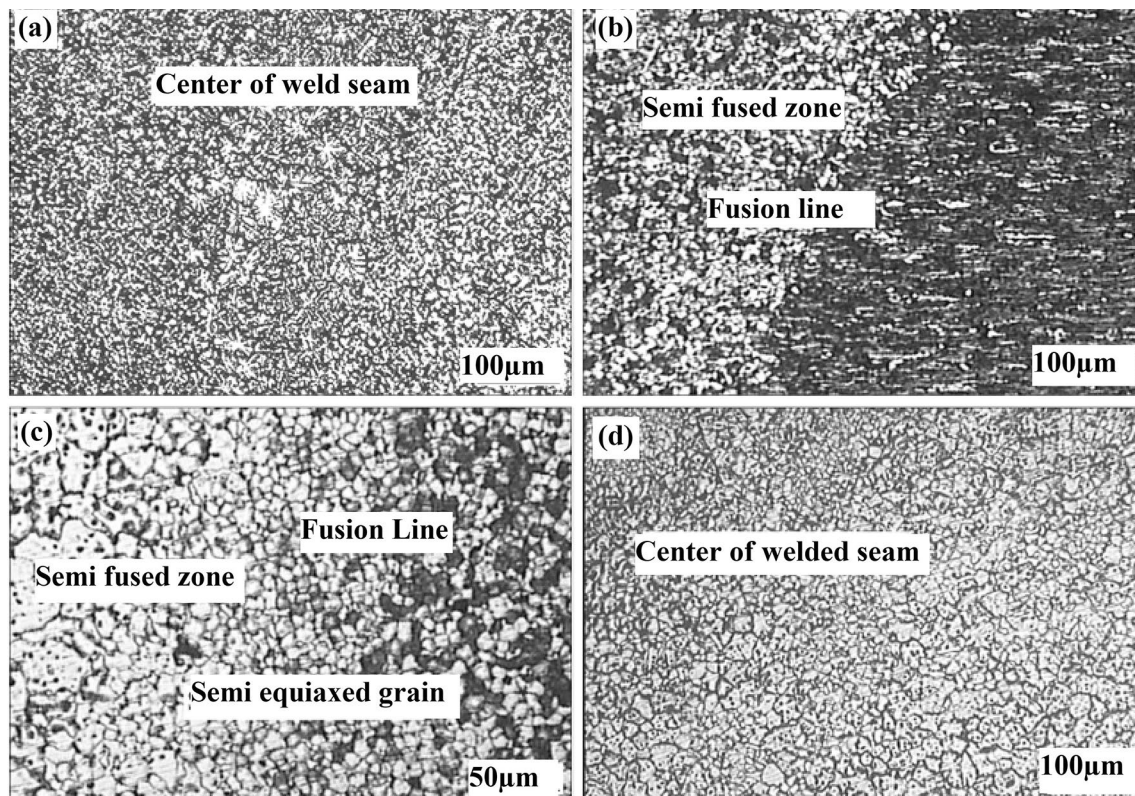
Fig. 8 Optical micrograph of TIG welded joint **a**–**c** hot rolled plate, **d** cold rolled plate [43]
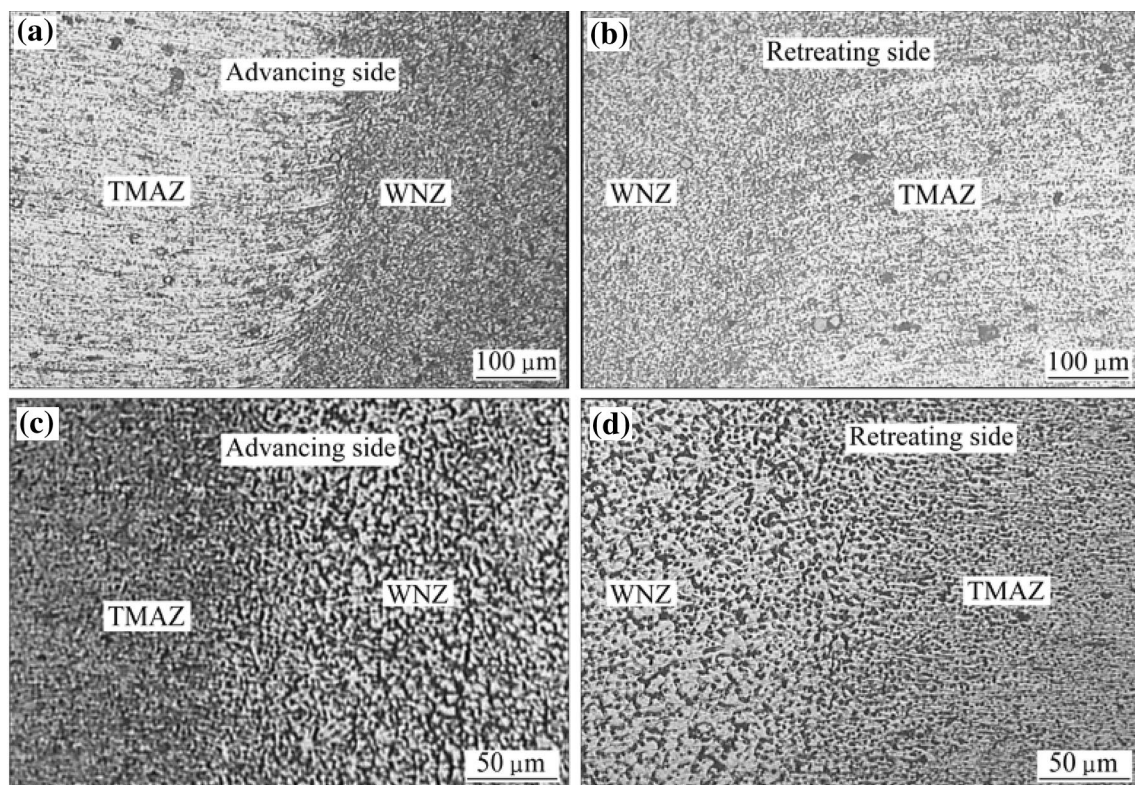

Fig. 9 Optical microstructure of friction stir welded joint, **a** advancing side of hot rolled plate, **b** retreating side of hot rolled plate, **c** advancing side of cold rolled plate, **d** retreating side of cold rolled plate [43]
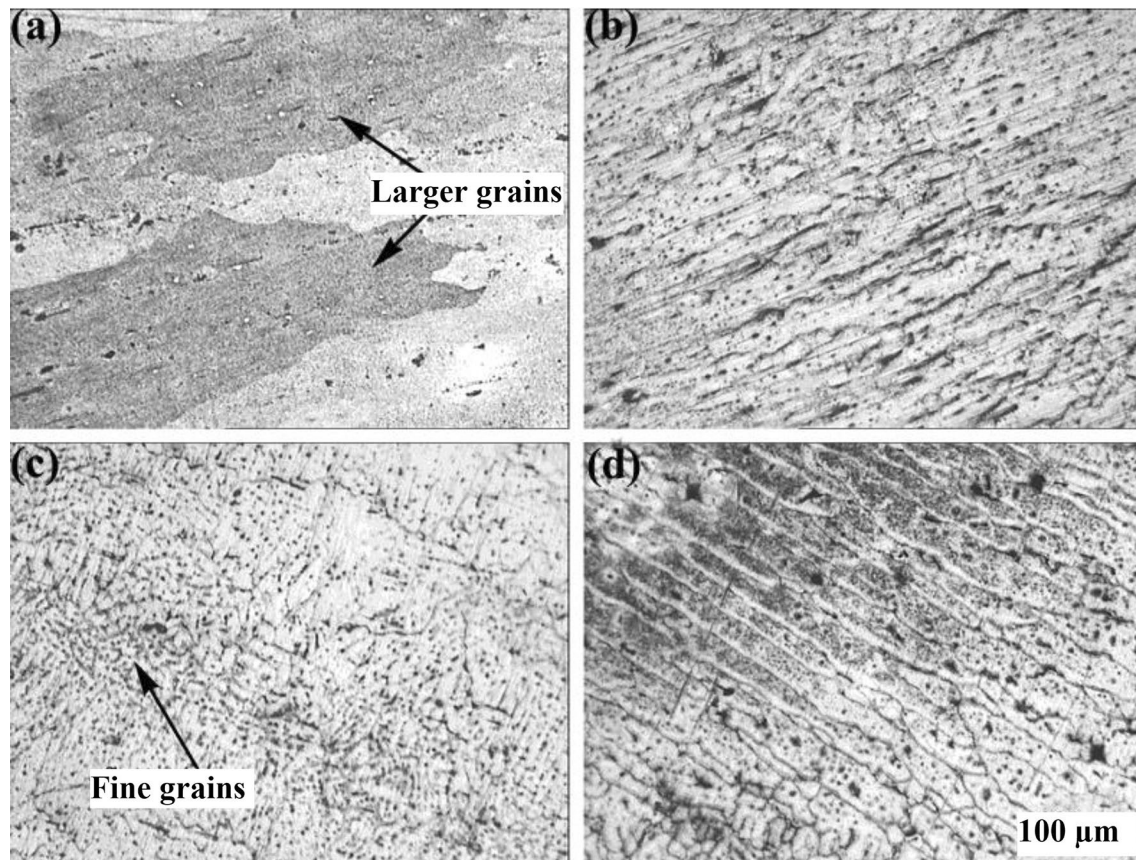
Fig. 10 Microstructure of the TIG welded joint at various zone, **a** parent material, **b** HAZ, **c** fusion zone, **d** partially melted zone [39]

Figure 9 shows the two kinds of welded joint thermo-mechanically zone (TMAZ) and the weld nugget zone (WNZ). The microstructure of weld nugget zone in cold rolled annealed and hot rolled plate were crushed by the strong stirring effect of rotating tool. Because of temperature at weld nugget zone was very high, the dynamic recrystallization takes place small and uniform equiaxed grains emerge at weld nugget zone. The thermo-mechanically zone is weaker heating affected zone than weld nugget zone but stronger than HAZ. The boundary at retreating side is vague and at advancing side is obvious [43]. The relative rate between rotating pin and base metal reached a peak in advancing side and it was the lowest in the retreating side. The stain degree and rate were greater in the advancing side, and the distortion of fibrous microstructure in the advancing side is more severe than that in retreating side [44], which brought the asymmetry of micro-hardness distribution.

Figure 10 shows a microstructure of the TIG weld with the formation of different zone [39]. The grain size of the base metal is completely modified after welding process, and a columnar epitaxial grains can be clearly seen from the HAZ and partly melted zone (PMZ), which are formed at high temperature adjacent to fusion zone. In this zone, the precipitates which are parent hardened experience a heat treated of over ageing that can cause to phase formation, resulting in deteriorating the mechanical properties of weld [38–40]. It is observed that the microstructure of HAZ and partly melted zone contain coarse and grown epitaxial dendritic grains of α-aluminum and θ-phase [45]. The grown dendritic grains are caused due to the cooling and solidification rate of the weld pool and presence of Mg and other element in the eutectic phase. The presence of insufficient amount of Mg in weld metal resulted in the formation of weak precipitates and not enough to form intermetallic compounds. The zone of the weldments exhibited the micro crack in the grain boundaries where the precipitates and rich in concentration and wider gap between dendrites led to defect formation.

The new approach of using friction stir welding over the TIG welds resulted in a significant improvements in the weld zone. In TIG welding, there are still the presence of porosities in the weld zone, which resulted in the carefully understanding of various spruces of these contaminants to identify the cause and take the necessary actions to get rid of porosities as shown in Fig. 11 [39]. The defect
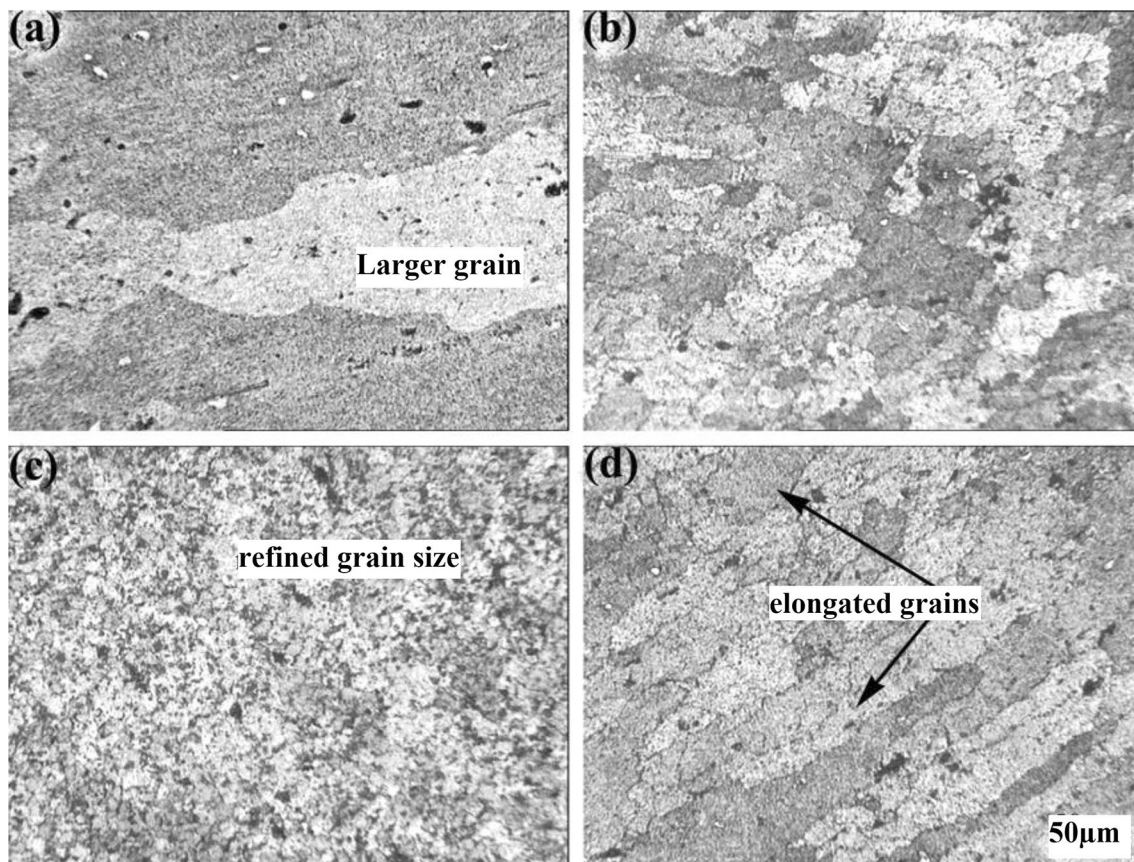
Fig. 11 Microstructure of (TIG + FSP) welds at various zone, **a** base material, **b** HAZ, **c** stir zone, **d** thermo-mechanically affected zone)

free microstructure with the refines grain sizes in the weld zone are depicted in Fig. 11. In this fig, it is found that than course and grown dendritic structure are completely modified in the HAZ and TMAZ. It may be due to the breaking of the dendrites and precipitates completely and refined than into a new shape formation as shown the (TIG + FSP) weld microstructure. The grain size of the stir zone is much finer that the TIG fusion zone, there is no evidence of porosity in the weld zone. The small pits also hard to find the TIG + FSP welds and complete defect free weld are achieved. On the other hand, it is worth to mention that the tool motion induces the greater stresses thus resulted in fine grain structure formation, which can allow a partial recovery of the weld metal strength properties and this effect can be seen only on weld nugget [32].

4 Conclusions

A new approach of TIG + FSP process can improve the microstructure and mechanical properties of TIG welded joint. In this study, to avoid coarse grain structure, porosity and micro-crack, friction stir processing is used after Tungsten inert gas welding. FSP is used to destroy the

coarse-grained dendritic structure in the tungsten welded joint and very fine grain structure was observed in stir zone to the effect of intense plastic deformation and temperature during TIG + FSP. The microstructure and mechanical properties of TIG welded joint and TIG + FSP welded joints were studied to understand the behavior of grain structure of both processes. The following conclusions are made during this study.

- The defect and porosity found in TIG weld can completely eliminated by using friction stir processing.
- The friction stir processing over TIG weld completely modified the mechanical and microstructure properties of TIG welded joint.
- The micro-hardness of the TIG + FSP weld is higher than the TIG weld due to fine grain structure in TIG + FSP welds.
- The ultimate tensile strength and elongation of welded joint of (TIG + FSP) are higher than those of TIG and FSW joints, the strength of TIG, FSW and (TIG + FSW) are lower than the parent material.
- The weld nugget zone of friction stir welding and the molten zone of TIG welding are the weakest zone of the welded joints.

Compliance with ethical standards

References

1. Thomas WM, Nicholas ED, Needham JC, Murch MG, Templesmith P, Dawes CJ (1991) Friction stir butt welding: PCT/GB92/02203 [P]
2. Mishra RS, Ma ZY (2005) Friction stir welding and processing. Mater Sci Eng R 50(1–2):1–78
3. Nandan R, Debroy T, Bhadeshia HKDH (2008) Recent advances in friction-stir welding: process, weldment structure and properties. Prog Mater Sci 53(6):980–1023
4. Fonda RW, Knipling KE (2010) Texture development in near—α Ti friction stir welds. Acta Mater 58(19):6452–6463
5. Zhou L, Liu HJ, Liu P, Liu QW (2009) The stir zone microstructure and its formation mechanism in Ti–6Al–4V friction stir welds. Scr Mater 61(6):596–599
6. Wu LH, Wang D, Xiao BL, Ma ZY (2014) Microstructural evolution of the thermomechanically affected zone in a Ti–6Al–4V friction stir welded joint. Scr Mater 78–79:17–20
7. Zhang Y, Sato YS, Kokawa H, Park SHC, Hirano S (2008) Microstructural characteristics and mechanical properties of Ti–6Al–4V friction stir welds. Mater Sci Eng, A 485(1–2):448–455
8. Miyazaki M, Nishio K, Katoh M, Mauake S, Kerr W (1990) Quantitative investigation of heat affected zone cracking in aluminum alloy 6061. Weld Res Suppl 69(9):362–371
9. Malin V (1995) Studey of metallurgical phenomena in the HAZ of 6061-T6 aluminum welded joints. Weld Res Suppl 74:305–318
10. Esparza JA, Dvis WC, Trillo AE, Murr LE (2002) Friction stir welding of magnesium alloy AZ31B. J Mater Sci Lett 21(12):917–920
11. Meran C (2006) The joint properties of brass plates by friction stir welding. Mater Des 27(9):719–726
12. Leitao C, Leal RM, Rodrigues DM, Loureiro A, Vilaca P (2009) Mechanical behaviour of similar and dissimilar AA5182-H111 and AA6016-T4 thin friction stir welds. Mater Des 30(1):101–108
13. Satoy S, Yamanoi H, Kokawa H, Furuhara T (2007) Microstructural evolution of ultrahigh carbon steel during friction stir welding. Scr Mater 57(6):557–560
14. Kwon YJ, Shigematsu I, Saito N (2008) Dissimilar friction stir welding between magnesium and aluminum alloys. Mater Lett 62(23):3827–3829
15. Christian BF, Murray WM, Mike C (2010) Evolution of microstructure and mechanical properties in naturally aged 7050 and 7075 Al friction stir welds. Mater Sci Eng, A 527(9):2233–2240
16. Li Y, Trillo EA, Murr LE (2000) Friction-stir welding of aluminum alloy 2024 to silver. J Mater Sci Lett 19(12):1047–1051
17. Peel M, Steuwer A, Preuss M, Withers PJ (2003) Microstructure, mechanical properties and residual stresses as a function of welding speed in aluminium AA5083 friction stir welds. Acta Mater 51(16):4791–4801
18. Genevois C, Deschamps A, Denquin A, Doisneau-Coottignies B (2005) Quantitative investigation of precipitation and mechanical behaviour for AA2024 friction stir welds. Acta Mater 53(8):2447–2458
19. Rhodes CG, Mahoney MW, Spurling RA, Bampton C (1997) Effect of friction stir welding on microstructure of 7075 aluminum. Scr Mater 36(1):69–75
20. Mahoney MW, Rhodes CG, Flintoff JG, Bingel WH, Spurling RA (1998) Properties of friction stir welded 7075-T651 aluminum. Metall Mater Trans A 29(7):1955–1964
21. Cavaliere P, Cabibbo M, Panella F, Squillace A (2009) 2198 Al-Li plates joined by friction stir welding: mechanical and microstructural behavior. Mater Des 30(9):3622–3631
22. Saini M, Arora N, Pandey C, Mehdi H (2014) Mechanical properties of bimetallic weld joint between SA 516 Grade 65 carbon steel and SS 304 L for steam generator application. Int J Res Eng Technol 3(7):39–42
23. Saini M, Arora N, Pandey C, Mehdi H (2014) Preliminary studies on thermal cycling of reactor pressure vessel steel. Int J Mech Eng 4(2):51–58
24. Mehdi H, Gaurav S, Kumar T, Sharma P (2017) Mechanical characterization of SA-508Gr3 and SS-304L steel weldments. Int J Adv Prod Ind Eng 2(1):41–46
25. Cheepu M, Ashfaq M, Muthupandi V (2017) A new approach for using interlayer and analysis of the friction welding of titanium to stainless steel. Trans Indian Inst Met 70:2591–2600. https://doi.org/10.1007/s12666017-1114-x21
26. Muralimohan CH, Ashfaq M, Ashiri R, Muthupandi V, Sivaprasad K (2016) Analysis and characterization of the role of Ni interlayer in the friction welding of titanium and 304 austenitic stainless steel. Metall Mater Trans A 47:347–359
27. Cheepu MM, Muthupandi V, Loganathan S (2012) Friction welding of titanium to 304 stainless steel with electroplated nickel interlayer. Mater Sci Forum 710:620–625
28. Muralimohan CH, Muthupandi V, Sivaprasad K (2014) Properties of friction welding titanium-stainless steel joints with a nickel interlayer. Proc Mater Sci 5:1120–1129
29. Cheepu M, Muthupandi V, Che WS (2018) Improving mechanical properties of dissimilar material friction welds. Appl Mech Mater 877:157–162. https://doi.org/10.4028/www.scientific.net/AMM.877.157
30. Muralimohan CH, Muthupandi V (2013) Friction welding of type 304 stainless steel to CP titanium using nickel interlayer. Adv Mater Res 794:351–357
31. Cheepu M, Haribabu S, Ramachandraiah T, Srinivas B, Venkateswarulu D, Karna S, Alapati S, Che WS (2018) Fabrication and analysis of accumulative roll bonding process between magnesium and aluminum multi-layers. Appl Mech Mater 877:183–189. https://doi.org/10.4028/www.scientific.net/AMM.877.183
32. Sutton MA, Yang B, Reynolds AP, Taylor R (2002) Microstructural studies of friction stir welds in 2024-T3 aluminum. Mater Sci Eng, A 323:160–166
33. Mishra RS, Ma ZY (2005) Friction stir welding and processing. J Mater Sci Eng 50:1–78
34. Mehdi H, Mishra RS (2016) Mechanical properties and microstructure studies in friction stir welding (FSW) joints of dissimilar alloy—a review. J Achiev Mater Manuf Eng 77(1):31–40
35. Mehdi H, Mishra RS (2017) Influences of process parameter and microstructural studies in friction stir welding of different alloys: a review. Int J Adv Prod Ind Eng 509:55–62
36. Mehdi H, Mishra RS (2017) Mechanical and microstructure characterization of friction stir welding for dissimilar alloy—a review. Int J Res Eng Innov 1(5):57–67
37. Mehdi H, Mishra RS (2018) Analysis of material flow and heat transfer in reverse dual rotation friction stir welding: a review. Int J Steel Struct. https://doi.org/10.1007/s13296-018-0131-x
38. Singh G, Kang AS, Singh K, Singh J (2017) Experimental comparison of friction stir welding process and TIG welding process for 6082-T6 aluminium alloy. In: 5th international conference of materials processing and characterization (ICMPC 2016), proceedings, vol 4, pp 3590–3600
39. Deviredd K, Devuri V, Cheepu M, Kumar BK (2018) Analysis of the influence of friction stir processing on gas tungsten arc welding of 2024 aluminum alloy weld zone. Int J Mech Prod Eng Res Dev 8(1):243–252

40. Koteswara Rao SR, Madhusudhan Reddy G, Prasad Rao K (2008) Effects of thermo-mechanical treatments on mechanical properties of AA 2219 gas tungsten arc welds. J Mater Process Technol 202:283–289

41. Malarvizhi S, Balasubramanian V (2011) Fatigue crack growth resistance of gas tungsten arc, electron beam and friction stir welded joints of AA2219 aluminium alloy. Mater Des 32(3):1205–1214

42. Khan NZ, Khan ZA, Siddiquee AN (2015) Effect of shoulder diameter to pin diameter (D/d) ratio on tensile strength of friction stir welded 6063 aluminium alloy. Mater Today Proc 2:1450–1457

43. Zhen-Bo He, Yong-Yi Peng, Zhi-Min Yin, Xue-Feng Lei (2011) Comparison of FSW and TIG welded joints in Al–Mg–Mn–Sc–Zr alloy plates. Trans Noferrous Met Soc China 21:1685–1691

44. Hua Zhang, Lin San-Bao Wu, Lin Feng Ji-Cai (2004) The weld nugget formation of friction stir welded AZ31 magnesium alloy and its affecting factors. J Aeronaut Mater 24(6):610

45. Cieslak BA, Zdunek J, Mizera J (2016) Evolution of microstructure and precipitates in 2xxx aluminum alloy after severe plastic deformation. IOP Conf Ser Mater Sci Eng 123:1–4

46. Yutaka SS, Kokawa H (2001) Distribution of tensile property and microstructure in friction stir weld of 6063 aluminum. Metall Mater Trans A 32(12):3023–3031

Publisher's Note Springer Nature remains neutral with regard to jurisdictional claims in published maps and institutional affiliations.

THE SHARP BOUNDS OF THE SECOND AND THIRD HANKEL DETERMINANTS FOR THE CLASS $\mathcal{SL}^*$

SHAGUN BANGA AND S. SIVAPRASAD KUMAR

ABSTRACT. The aim of the present paper is to obtain the sharp bounds of the Hankel determinants $H_2(3)$ and $H_3(1)$ for the well known class $\mathcal{SL}^*$ of starlike functions associated with the right lemniscate of Bernoulli. Further for $n = 3$, we find the sharp bound of the Zalcman functional for the class $\mathcal{SL}^*$. In addition, a couple of interesting results of $\mathcal{SL}^*$ is appended at the end.

1. INTRODUCTION

Let $\mathcal{A}$ be the class of analytic functions $f(z) = z + \sum_{n=2}^{\infty} a_n z^n$, defined in the open unit disk Δ. The subclass $\mathcal{S}$ of $\mathcal{A}$ consists of univalent functions. We say, f is subordinate to g, denoted by $f \prec g$, if there exists a Schwartz function ω with $\omega(0) = 0$ and $|\omega(z)| < 1$ such that $f(z) = g(\omega(z))$, where f and g are analytic functions. For each $n \geq 2$, Zalcman conjectured the following coefficient inequality for the class $\mathcal{S}$:

$$|a_n^2 - a_{2n-1}| \leq (n-1)^2. \tag{1.1}$$

The above inequality also implies the Bieberbach conjecture $|a_n| \leq n$ (see [4]). Consider the class $\mathcal{SL}^*$ [24], given by

$$\mathcal{SL}^* := \left\{ f \in \mathcal{A} : \frac{zf'(z)}{f(z)} \prec \sqrt{1+z}, \quad z \in \Delta \right\}.$$

It is evident that if $\omega = zf'(z)/f(z)$, then the analytic characterization of the functions in $\mathcal{SL}^*$, is given by $|\omega^2 - 1| < 1$, which in fact is the interior of the right loop of the lemniscate of Bernoulli, with the boundary equation $\gamma_1 : (u^2 + v^2)^2 - 2(u^2 - v^2) = 0$. In 2009, Sokół [22] obtained the sharp bounds for a_2, a_3 and a_4 of functions in the class $\mathcal{SL}^*$, further it is conjectured that $|a_{n+1}| \leq 1/2n$ whenever $n \geq 1$, with the extremal function f satisfying $zf'(z)/f(z) = \sqrt{1+z^n}$. Later, Shelly Verma [20] gave the proof for the sharp estimate of the fifth coefficient with the extremal function for $\mathcal{SL}^*$ using the characterization of positive real part functions in terms of certain positive semi-definite Hermitian form. Sokół [23] also dealt the radius problems for the class $\mathcal{SL}^*$. Recently, Ali *et al.* [2] have examined the radius of starlikeness associated with the lemniscate of Bernoulli. Some differential subordination results associated with lemniscate of Bernoulli is studied in [1,13].

The qth Hankel determinant for a function $f \in \mathcal{A}$, where q, $n \in \mathbb{N}$ is defined as follows:

$$H_q(n) := \begin{vmatrix} a_n & a_{n+1} & \cdots & a_{n+q-1} \\ a_{n+1} & a_{n+2} & \cdots & a_{n+q} \\ \vdots & \vdots & \ddots & \vdots \\ a_{n+q-1} & a_{n+q} & \cdots & a_{n+2q-2} \end{vmatrix}. \tag{1.2}$$

This has been initially studied in [19]. This determinant has also been considered by several authors. It also plays an important role in the study of singularities (see [5]). Noor [18] studied the

rate of growth of $H_q(n)$ as $n \to \infty$ for functions in $\mathcal{S}$ with bounded boundary. The computation of the upper bound of $|H_q(n)|$ for several subclasses of $\mathcal{S}$ has always been a trendy problem in the field of geoemtric function theory. Hayami and Owa [7] determined the second Hankel determinant $H_2(n)$ ($n = 1, 2, \ldots$) for functions f satisfying $\mathrm{Re}(f(z)/z) > \alpha$ or $\mathrm{Re}\, f'(z) > \alpha$ ($0 \le \alpha < 1$). Recently, Zaprawa [26] obtained the upper bound of $|H_2(n)|$ for the class T of typically real functions. Note that the Hankel determinant $H_2(1) := a_3 - a_2^2$ coincides with the famous Fekete-Szegö functional. In the year 1983, Bieberbach [6] estimated the bound of $|H_2(1)|$ for the class $\mathcal{S}$. The generalization of Fekete-Szegö functional is given by $a_3 - \mu a_2^2$, where μ is either real or complex. The computation for the bound of $|H_2(2)|$, where $H_2(2) := a_2 a_4 - a_3^2$ requires the formulae of p_2 and p_3 [17] in terms of p_1, where $p_i's$ are the coefficients of the functions in the Carathéodory class $\mathcal{P}$, defined by:

$$p(z) = 1 + \sum_{n=1}^{\infty} p_n z^n \ (z \in \Delta),$$

with $\mathrm{Re}\, p(z) > 0$ in Δ. Recently, many authors have estimated the bound of $|H_2(2)|$ (see [3, 7–9, 16]). Recall that the second Hankel determinant is given by

$$H_2(3) = \begin{vmatrix} a_3 & a_4 \\ a_4 & a_5 \end{vmatrix} = a_3 a_5 - a_4^2. \tag{1.3}$$

Zaprawa [28] investigated the Hankel determinant $H_2(3)$ for several classes of univalent functions. The estimate of the upper bound of the third order Hankel determinant, which is given by

$$H_3(1) = \begin{vmatrix} a_1 & a_2 & a_3 \\ a_2 & a_3 & a_4 \\ a_3 & a_4 & a_5 \end{vmatrix} = a_3(a_2 a_4 - a_3^2) - a_4(a_4 - a_2 a_3) + a_5(a_3 - a_2^2), \tag{1.4}$$

requires the sharp bounds of the initial coefficients (a_2, a_3, a_4 and a_5), Fekete-Szegö functional, second Hankel determinant $H_2(2)$ and the quantity $|a_4 - a_2 a_3| =: L$. Using triangle inequality in (1.4), the upper bound of $|H_3(1)|$ can be obtained as follows:

$$|H_3(1)| \le |a_3||H_2(2)| + |a_4||L| + |a_5||H_2(1)|,$$

(see [12, 21, 25, 27]). Note that this computation does not yield sharp bound for $H_3(1)$. It is pertinent to know that the computation of $|H_3(1)|$ and $|H_2(3)|$ is tedious if we desire to obtain the sharp bound. For the class $\mathcal{SL}^*$, Raza and Malik [21] obtained the sharp bounds of $|H_2(1)|$ and $|H_2(2)|$ and the upper bound of $|H_3(1)|$. Thus, the sharp estimate of $|H_3(1)|$ for $\mathcal{SL}^*$ until now is an open problem. The study of the bound for third Hankel determinant has become an interesting problem only after the well known formula of expressing p_4 in terms of p_1 which was recently obtained in [14], which yields the sharp results in most of the cases. Kwon et al. [15] improved the estimate of the third Hankel determinant for starlike functions. Recently, Kowalczyk et al. [10] obtained the sharp bound of $|H_3(1)|$ for the class $T(\alpha) := \{f \in \mathcal{A} : \mathrm{Re}(f(z)/z) > \alpha, \alpha \in [0, 1)\}$ and in [11] establish the sharp bound of the same for the class of convex functions. Zaprawa [26] estimated the sharp bound of $|H_2(3)|$ for the class of typically real functions. Note that these are the only three (as per the knowlegde of the authors) sharp bounds of $|H_2(3)|$ and $|H_3(1)|$ proved for any subclass of analytic functions till date.

For the class $\mathcal{SL}^*$, the known upper bound for $|H_3(1)|$ is $\frac{43}{576}$ (see [21]), whereas in this paper, we obtain a sharp estimate for the same which is equal to $\frac{1}{36}$. Further, we find the sharp bound of the second Hankel determinant $H_2(3)$ for the class $\mathcal{SL}^*$. Also, we estimate the sharp bound of the quantity $|a_3^2 - a_5|$ for the class $\mathcal{SL}^*$, which is the Zalcman functional, given in (1.1), when $n = 3$. In the last section, we establish few results pertaining to the sufficient condition for the functions in $\mathcal{S}$ to belong to the class $\mathcal{SL}^*$.

The following lemmas are required for the formulae of p_2, p_3 [17] and p_4 [14] in order to establish our main results.

Lemma 1.1. *Let* $p \in \mathcal{P}$ *and of the form* $1 + \sum\limits_{n=1}^{\infty} p_n z^n$. *Then*

$$2p_2 = p_1^2 + \gamma(4 - p_1^2), \tag{1.5}$$

$$4p_3 = p_1^3 + 2p_1(4 - p_1^2)\gamma - p_1(4 - p_1^2)\gamma^2 + 2(4 - p_1^2)(1 - |\gamma|^2)\eta \tag{1.6}$$

and

$$\begin{aligned} 8p_4 =& p_1^4 + (4 - p_1^2)\gamma(p_1^2(\gamma^2 - 3\gamma + 3) + 4\gamma) \\ & - 4(4 - p_1^2)(1 - |\gamma|^2)(p_1(\gamma - 1)\eta + \overline{\gamma}\eta^2 - (1 - |\eta|^2)\rho), \end{aligned} \tag{1.7}$$

for some ρ, γ *and* η *such that* $|\rho| \leq 1$, $|\gamma| \leq 1$ *and* $|\eta| \leq 1$.

Lemma 1.2. *[20] Let* a, b, c *and* d *satisfy the inequalities* $0 < c < 1$, $0 < d < 1$ *and*

$$8d(1 - d)((cb - 2a)^2 + (c(d + c) - b)^2) + c(1 - c)(b - 2dc)^2 \leq 4c^2(1 - c)^2 d(1 - d).$$

If $p \in \mathcal{P}$, *then*

$$|ap_1^4 + dp_2^2 + 2cp_1p_3 - (3/2)bp_1^2p_2 - p_4| \leq 2.$$

2. Main Results

We proceed with the following theorem.

Theorem 2.1. *If* $f \in \mathcal{SL}^*$. *Then we have*

$$|H_3(1)| \leq 1/36. \tag{2.1}$$

The bound is sharp.

Proof. Let $f \in \mathcal{SL}^*$ then from [20, p. 509], we have

$$a_2 = \frac{p_1}{4}, \quad a_3 = \frac{1}{8}p_2 - \frac{3}{64}p_1^2, \quad a_4 = \frac{1}{12}p_3 - \frac{7}{96}p_1p_2 + \frac{13}{768}p_1^3 \tag{2.2}$$

and

$$a_5 = -\frac{1}{16}\left(\frac{49}{384}p_1^4 - \frac{17}{24}p_1^2p_2 + \frac{1}{2}p_2^2 + \frac{11}{12}p_1p_3 - p_4\right). \tag{2.3}$$

On simplifying the equation (1.4), we get

$$H_3(1) = 2a_2a_3a_4 - a_3^3 - a_4^2 + a_3a_5 - a_2^2a_5. \tag{2.4}$$

Since the class $\mathcal{P}$ is invariant under the rotation, the value of p_1 lies in the interval $[0, 2]$. Let $p := p_1$ and substituting the above values of $a_i's$ in (2.4), we have

$$\begin{aligned} H_3(1) =& \frac{1}{2359296}\left(689p^6 - 3368p^4p_2 + 3520p^3p_3 + 24064pp_2p_3 + 3008p^2p_2^2\right. \\ & \left. - 16128p^2p_4 - 13824p_2^3 - 16384p_3^2 + 18432p_2p_4\right). \end{aligned}$$

Using the equalities (1.5)-(1.7) and upon simplification, we arrive at

$$H_3(1) = \frac{1}{2359296}\left(\nu_1(p, \gamma) + \nu_2(p, \gamma)\eta + \nu_3(p, \gamma)\eta^2 + \psi(p, \gamma, \eta)\rho\right).$$

Where ρ, η, $\gamma \in \overline{\Delta}$,

$$\nu_1(p,\gamma) := 29p^6 + (4-p^2)((4-p^2)(944p^2\gamma^2 - 640p^2\gamma^3 - 2304\gamma^3 + 128p^2\gamma^4)$$
$$- 116p^4\gamma + 752p^4\gamma^2 - 3456p^2\gamma^2 - 864p^4\gamma^3),$$
$$\nu_2(p,\gamma) := (4-p^2)(1-|\gamma|^2)\left(224p^3 + 3456p^3\gamma + (4-p^2)(2432p\gamma - 512p\gamma^2)\right),$$
$$\nu_3(p,\gamma) := (4-p^2)(1-|\gamma|^2)\left((4-p^2)(4096 - 512|\gamma|^2) + 3456p^2\overline{\gamma}\right),$$
$$\psi(p,\gamma,\eta) := (4-p^2)(1-|\gamma|^2)(1-|\eta|^2)\left(-3456p^2 + 4608\gamma(4-p^2)\right).$$

Further, by taking $x := |\gamma|$, $y := |\eta|$ and using the fact $|\rho| \le 1$, we have

$$|H_3(1)| \le \frac{1}{2359296}\left(|\nu_1(p,\gamma)| + |\nu_2(p,\gamma)|y + |\nu_3(p,\gamma)|y^2 + |\psi(p,\gamma,\eta)|\right)$$
$$\le G(p,x,y),$$

where

$$G(p,x,y) := \frac{1}{2359296}\left(g_1(p,x) + g_2(p,x)y + g_3(p,x)y^2 + g_4(p,x)(1-y^2)\right) \qquad (2.5)$$

with

$$g_1(p,x) := 29p^6 + (4-p^2)((4-p^2)(944p^2x^2 + 640p^2x^3 + 2304x^3 + 128p^2x^4)$$
$$+ 116p^4x + 752p^4x^2 + 3456p^2x^2 + 864p^4x^3),$$
$$g_2(p,x) := (4-p^2)(1-x^2)(224p^3 + (4-p^2)(2432px + 512px^2) + 3456p^3x),$$
$$g_3(p,x) := (4-p^2)(1-x^2)((4-p^2)(4096 + 512x^2) + 3456p^2x),$$
$$g_4(p,x) := (4-p^2)(1-x^2)(3456p^2 + 4608x(4-p^2)).$$

Now we need to maximize $G(p,x,y)$ in the closed cuboid $S : [0,2] \times [0,1] \times [0,1]$. We establish this by finding the maximum values in the interior of the six faces, on the twelve edges and in the interior of S.

I. First we proceed with interior points of S. Let $(p,x,y) \in (0,2)\times(0,1)\times(0,1)$. In an attempt to find the points where the maximum value is attained in the interior of S, we partially differentiate equation (2.5) with respect to y and on algebraic simplification, we get

$$\frac{\partial G}{\partial y} = \frac{1}{73728}(4-p^2)(1-x^2)(8y(x-1)(4(4-p^2)(x-8) + 27p^2)$$
$$+ p(4x(4-p^2)(19+4x) + p^2(7+108x))).$$

Now $\frac{\partial G}{\partial y} = 0$ yields

$$y = \frac{p(4x(4-p^2)(19+4x) + p^2(7+108x))}{4(x-1)(4(4-p^2)(8-x) - 27p^2)} =: y_0.$$

For the existence of the critical points, y_0 should lie in the interval $(0,1)$, which is possible only when

$$p^3(7+108x) + 4px(4-p^2)(19+4x) + 32(1-x)(8-x)(4-p^2) < 216p^2(1-x) \qquad (2.6)$$

and

$$27p^2 > 4(4-p^2)(8-x). \qquad (2.7)$$

Now, we find the solutions satisfying both the inequalities (2.6) and (2.7) for the existence of critical points. Let $g(x) := 16(8-x)/(59-4x)$, which is decreasing function of x as $g'(x)$ is negative for $x \in (0,1)$. Hence $\min g(x)_{(x=1)} = 112/55$. Thus from equation (2.7), we can conclude that $p > 1$ for all $x \in (0,1)$. But for $p \ge 1$, the inequality (2.6) does not hold as it is not difficult to see

that $7p^3 \geq 216p^2(1-x)$ for all x. This shows that there does not exist any solution satisfying both the inequalities (2.6) and (2.7). Hence the function G has no critical point in $(0,2) \times (0,1) \times (0,1)$.

II. Here we consider the interior of all the six faces of the cuboid S.

On the face $p = 0$, $G(p,x,y)$ reduces to

$$h_1(x,y) := G(0,x,y) = \frac{2(1-x^2)(y^2(x-1)(x-8)+9x)+9x^3}{576}, \quad x,y \in (0,1). \qquad (2.8)$$

We note that h_1 has no critical point in $(0,1) \times (0,1)$ since

$$\frac{\partial h_1}{\partial y} = \frac{y(1-x^2)(x-1)(x-8)}{144} \neq 0, \quad x,y \in (0,1). \qquad (2.9)$$

On the face $p = 2$, $G(p,x,y)$ reduces to

$$G(2,x,y) = \frac{29}{36864}, \quad x,y \in (0,1). \qquad (2.10)$$

On the face $x = 0$, $G(p,x,y)$ reduces to $G(p,0,y)$, given by

$$h_2(p,y) := \frac{128y^2(512-364p^2+59p^4)+224p^3y(4-p^2)+13824p^2-3456p^4+29p^6}{2359296}, \qquad (2.11)$$

where $p \in (0,2)$ and $y \in (0,1)$. We solve $\frac{\partial h_2}{\partial y} = 0$ and $\frac{\partial h_2}{\partial p} = 0$ to determine the points where the maxima occur. On solving $\frac{\partial h_2}{\partial y} = 0$, we get

$$y = -\frac{7p^3}{8(128-59p^2)} =: y_1. \qquad (2.12)$$

For the given range of y, we should have $y_1 \in (0,1)$, which is possible only if $p > p_0$, $p_0 \approx 1.47292$. A computation shows that $\frac{\partial h_2}{\partial p} = 0$ implies

$$256y^2(-182+59p^2) - 112y(-12p+5p^3) + 87p^4 - 6912p^2 + 13824 = 0. \qquad (2.13)$$

Substituting equation (2.12) in equation (2.13) and upon simplification, we get

$$75497472 - 107347968p^2 + 51265024p^4 - 8426096p^6 + 95167p^8 = 0. \qquad (2.14)$$

A numerical computation shows that the solution of (2.14) in the interval $(0,2)$ is $p \approx 1.39732$. Thus h_2 has no critical point in $(0,2) \times (0,1)$.

On the face $x = 1$, $G(p,x,y)$ reduces to

$$h_3(p,y) := G(p,1,y) = \frac{36864 + 22784p^2 - 7920p^4 + 9p^6}{2359296}, \quad p \in (0,2). \qquad (2.15)$$

Solving $\frac{\partial h_3}{\partial p} = 0$, we get a critical point at $p =: p_0 \approx 1.2008$. A Simple calculation shows that h_3 attains its maximum value ≈ 0.0225817 at p_0.

On the face $y = 0$, $G(p,x,y)$ reduces to

$$h_4(p,x) := G(p,x,0) = \frac{1}{2359296}\Big(29p^6 + (4-p^2)((4-p^2)(944p^2x^2 + 640p^2x^3 - 2304x^3 \\ + 128p^2x^4 + 4608x) + 116p^4x + 752p^4x^2 + 864p^4x^3 + 3456p^2x^2)\Big).$$

A computation shows that

$$\frac{\partial h_4}{\partial x} = \frac{1}{2359296}\Bigg((8192p^2 - 576p^4 + 512p^6)x^3 + (30720p^2 - 4992p^4 - 672p^6)x^2$$
$$+ (30208p^2 - 9088p^4 + 384p^6)x + 73728 - 36864p^2 + 5072p^4 - 116p^6 \Bigg).$$

and

$$\frac{\partial h_4}{\partial p} = \frac{1}{2359296}\Bigg((4096p - 4096p^3 + 768p^5)x^4 + (3840p - 6656p^3 - 1344p^5)x^3$$
$$+ (30208p - 18176p^3 + 1152p^5)x^2 + (-73728p + 20288p^3 - 696p^5)x$$
$$+ 1344p - 13824p^3 + 174p^5 \Bigg).$$

A numerical computation shows that there does not exist any solution for the system of equations $\frac{\partial h_4}{\partial x} = 0$ and $\frac{\partial h_4}{\partial p} = 0$ in $(0,2) \times (0,1)$.

On the face $y = 1$, $G(p, x, y)$ reduces to

$$G(p, x, 1) = \frac{1}{2359296}\Bigg(29p^6 + (4 - p^2)(116p^4x + 752p^4x^2 + 3456p^2x^2 + 864p^4x^3$$
$$+ (1 - x^2)(224p^3 + 3456p^2x + 3456p^3x) + (4 - p^2)((1 - x^2)(2432px$$
$$+ 512px^2 + 4096 + 512x^2) + 944p^2x^2 + 640p^2x^3 + 2304x^3 + 128p^2x^4)) \Bigg)$$
$$=: h_6(p, x).$$

Proceeding on the similar lines as in the previous case for face $y = 0$, again there is no solution for the system of equations $\frac{\partial h_6}{\partial x} = 0$ and $\frac{\partial h_6}{\partial p} = 0$ in $(0,2) \times (0,1)$.

III. Now we calculate the maximum values achieved by $G(p, x, y)$ on the edges of the cuboid S. Considering the equation (2.11), we have $G(p, 0, 0) =: s_1(p) = (29p^6 - 3456p^4 + 13824p^2)/2359296$. It is easy to verify that the function $s_1'(p) = 0$ for $p =: \lambda_0 = 0$ and $p =: \lambda_1 \approx 1.43285$ in the interval $[0, 2]$. We observe that λ_0 is the point of minima and the maximum value of $s_1(p)$ is ≈ 0.00596162, which is attained at λ_1. Hence

$$G(p, 0, 0) \le 0.00596162, \quad p \in [0, 2].$$

Evaluating the equation (2.11) at $y = 1$, we obtain $G(p, 0, 1) = s_2(p) := (65536 - 32768p^2 + 896p^3 + 4096p^4 - 224p^5 + 29p^6)/2359296$. It is easy to verify that $s_2'(p)$ is decreasing function in $[0, 2]$ and hence attains its maximum value at $p = 0$.Thus

$$G(p, 0, 1) \le \frac{1}{36}, \quad p \in [0, 2].$$

In view of the equation (2.11) and by straightforward computation the maximum value of $G(0, 0, y)$ is attained at $y = 1$. This implies

$$G(0, 0, y) \le \frac{1}{36}, \quad y \in [0, 1].$$

As the equation (2.15) is independent of x, we have $G(p, 1, 1) = G(p, 1, 0) = s_3(p) := (9p^6 - 7920p^4 + 22784p^2 + 36864)/2359296$. Now, $s_3'(p) = 45568p - 31680p^3 + 54p^5 = 0$ for $p =: \lambda_2 = 0$ and $p =: \lambda_3 \approx 1.2008$ in the interval $[0, 2]$, where λ_2 is a point of minima and $s_3(p)$ attains its maximum value at λ_3. We can conclude that

$$G(p, 1, 1) = G(p, 1, 0) \le 0.0225817, \quad p \in [0, 2].$$

Substituting $p = 0$ in equation (2.15), we obtain $G(0, 1, y) = 1/64$. The Equation (2.10) is independent of all the variables p, x and y. Thus the value of $G(p, x, y)$ on the edges $p = 2$, $x = 1$; $p = 2$, $x = 0$; $p = 2$, $y = 0$ and $p = 2$, $y = 1$, respectively, is given by

$$G(2, 1, y) = G(2, 0, y) = G(2, x, 0) = G(2, x, 1) = 29/36864, x, y \in [0, 1].$$

Equation (2.11), yields $G(0, 0, y) = y^2/36$. A simple computation shows that

$$G(0, 0, y) \leq \frac{1}{36}, \quad y \in [0, 1].$$

Using equation (2.8), we get $G(0, x, 1) =: s_4(x) = (16 - 4x^2 + 9x^3 - 2x^4)/576$. A simple computation shows that the function s_4 is decreasing in $[0, 1]$ and hence attains its maximum value at $x = 0$. Thus

$$G(0, x, 1) \leq \frac{1}{36}, \quad x \in [0, 1].$$

Once again, by using the equation (2.8), we get $G(0, x, 0) = s_5'(x) := -(x^2 - 2)/64$. Performing a simple calculation, we get $s_5'(x) = 0$ for $x =: x_0 = \sqrt{2}/\sqrt{3}$ and for $0 \leq x < x_0$, s_5 is an increasing function and for $x_0 < x \leq 1$, it's a decreasing function. Thus, it attains maximum value at x_0. Hence

$$G(0, x, 0) \leq 0.0170103, \quad x \in [0, 1].$$

In view of the cases I-III, the inequality (2.1) holds. Let the function $f : \Delta \to \mathbb{C}$ be as follows

$$f(z) = z \exp\left(\int_0^z \frac{\sqrt{1 + t^3} - 1}{t} dt\right) = z + \frac{z^4}{6} + \cdots. \tag{2.16}$$

The sharpness of the bound $|H_3(1)|$ is justified by the extremal function f given by (2.16), which belongs to the class $\mathcal{SL}^*$. For this function f, we have $a_2 = a_3 = a_5 = 0$ and $a_4 = 1/6$, which clearly shows that $|H_3(1)| = 1/36$ using equation (2.4). This completes the proof. ∎

We now estimate the bound for the Hankel determinant $H_2(3)$.

Theorem 2.2. *Let $f \in \mathcal{SL}^*$. Then we have*

$$|H_2(3)| \leq \frac{1}{36}. \tag{2.17}$$

The result is sharp.

Proof. We proceed here on the similar lines as in the proof of Theorem 2.1. Now, substituting the equalities (2.2)-(2.3) in (1.3) and with the assumption $p_1 =: p \in [0, 2]$, we get

$$H_2(3) = \frac{1}{1179648}\left(103p^6 - 712p^4 p_2 - 4608p_2^3 + 1984p^2 p_2^2 + 5888pp_2 p_3\right.$$
$$\left. - 160p^3 p_3 - 8192p_3^2 - 3456p^2 p_4 + 9216p_2 p_4\right). \tag{2.18}$$

Using the equalities (1.5)-(1.7) and simplifying the terms in the expression (2.18), we get

$$H_2(3) = \frac{1}{1179648}\left(\zeta_1(p, \gamma) + \zeta_2(p, \gamma)\eta + \zeta_3(p, \gamma)\eta^2 + \xi(p, \gamma, \eta)\rho\right),$$

where ρ, η and $\gamma \in \overline{\Delta}$,

$$\zeta_1(p, \gamma) := -5p^6 + 4p^2\gamma(4 - p^2)(-p^2 - 20(4 - p^2)\gamma - 26p^2\gamma + 144\gamma + 36p^2\gamma^2$$
$$+ 16\gamma^2(4 - p^2) + 40\gamma^2(4 - p^2)),$$
$$\zeta_2(p, \gamma) := 16p(4 - p^2)(1 - |\gamma|^2)(-5p^2 - 36p^2\gamma - 16\gamma^2(4 - p^2) - 20\gamma(4 - p^2)),$$
$$\zeta_3(p, \gamma) := 64(4 - p^2)(1 - |\gamma|^2)(-4(4 - p^2)(8 + \gamma^2) - 9p^2\gamma),$$
$$\xi(p, \gamma, \eta) := 576(4 - p^2)(1 - |\gamma|^2)(1 - |\eta|^2)(p^2 + 4\gamma(4 - p^2)).$$

By taking $x := |\gamma|$, $y := |\eta|$ and using the fact $|\rho| \leq 1$, we get

$$|H_2(3)| \leq \frac{1}{1179648}\left(|\zeta_1(p, \gamma)| + |\zeta_2(p, \gamma)|y + |\zeta_3(p, \gamma)|y^2 + |\xi(p, \gamma, \eta)|\right)$$
$$\leq F(p, x, y),$$

where

$$F(p, x, y) := \frac{1}{1179648}\left(q_1(p, x) + q_2(p, x)y + q_3(p, x)y^2 + q_4(p, x)(1 - y^2)\right) \qquad (2.19)$$

with

$$q_1(p, x) := 5p^6 + 4p^2x(4 - p^2)(p^2 + 20(4 - p^2)x + 26p^2x + 144x + 36p^2x^2$$
$$+ 16x^3(4 - p^2) + 40x^2(4 - p^2)),$$
$$q_2(p, x) := 16p(4 - p^2)(1 - x^2)(5p^2 + 36p^2x + 16x^2(4 - p^2) + 20x(4 - p^2)),$$
$$q_3(p, x) := 64(4 - p^2)(1 - x^2)(4(4 - p^2)(8 + x^2) + 9p^2x),$$
$$q_4(p, x) := 576(4 - p^2)(1 - x^2)(p^2 + 4x(4 - p^2)).$$

In order to complete the proof, we need to maximize the function $F(p, x, y)$ in the closed cuboid $T : [0, 2] \times [0, 1] \times [0, 1]$. For this, we find the maximum values of F in T by considering all the twelve edges, interior of the six faces and in the interior of T.

I. We proceed with interior points of T. Let us assume $(p, x, y) \in (0, 2) \times (0, 1) \times (0, 1)$. To determine the points where the maximum value occur in the interior of T, we partially differentiate equation (2.19) with respect to y and we get

$$\frac{\partial F}{\partial y} = \frac{1}{73728}(4 - p^2)(1 - x^2)(8y(x - 1)(4(4 - p^2)(x - 8) + 9p^2)$$
$$+ p(4x(4 - p^2)(5 + 4x) + p^2(5 + 36x))).$$

Now, $\frac{\partial F}{\partial y} = 0$ yields

$$y = \frac{p(4x(4 - p^2)(5 + 4x) + p^2(5 + 36x))}{8(x - 1)(4(4 - p^2)(8 - x) - 9p^2} =: y_1.$$

Now, y_1 should lie in the interval $(0, 1)$ for the existence of the critical points. Thus, we have

$$p^3(5 + 36x) + 4px(4 - p^2)(5 + 4x) + 32(1 - x)(8 - x)(4 - p^2) < 72p^2(1 - x) \qquad (2.20)$$

and

$$4(4 - p^2)(8 - x) < 9p^2. \qquad (2.21)$$

We try to find the solutions satisfying both the inequalities (2.20) and (2.21). Let us assume $g(x) := 16(8 - x)/(41 - 4x)$, which is decreasing function of x due to the fact that $g'(x)$ is negative for $x \in (0, 1)$. Therefore $\min r(x)_{(x=1)} = 112/37$. This implies $p > 1$ for all $x \in (0, 1)$ using equation (2.21). But for $p \geq 1$, the inequality (2.20) does not hold as $5p^3 \geq 72p^2(1 - x)$ for all x. Thus we can conclude that there does not exist any solution satisfying (2.20) and (2.21). Thus

function F has no critical point in $(0, 2) \times (0, 1) \times (0, 1)$.

II. Now, we consider the interior of all the six faces of the cuboid T.

On the face $p = 0$,

$$k_1(x, y) := F(0, x, y) = \frac{1 - x^2}{288}\left(y^2(x - 1)(x - 8) + 9x\right), \quad x, y \in (0, 1). \tag{2.22}$$

A simple calculation shows that $\partial k_1/\partial y = \partial h_1/\partial y$. Thus equation (2.9) implies k_1 has no critical point in $(0, 1) \times (0, 1)$.

On the face $p = 2$,

$$F(2, x, y) = \frac{5}{18432}, \quad x, y \in (0, 1). \tag{2.23}$$

On the face $x = 0$,

$$k_2(p, y) := F(p, 0, y) = \frac{64y^2(512 - 292p^2 + 41p^4) + 80p^3y(4 - p^2) + 2304p^2 - 576p^4 + 5p^6}{1179648}, \tag{2.24}$$

$p \in (0, 2)$ and $y \in (0, 1)$. On solving $\frac{\partial k_2}{\partial y} = 0$, we get

$$y = \frac{5p^3}{8(41p^2 - 128)} =: y_1. \tag{2.25}$$

For the given range of y, y_1 should lie in the interval $(0, 1)$, which holds only if $p > p_0$, $p_0 \approx 1.7669$. The computation shows that $\frac{\partial k_3}{\partial p} = 0$ implies

$$y^2(5248p^2 - 18688) + 40y(12p - 50p^3) + 2304 - 1152p^2 + 15p^4 = 0. \tag{2.26}$$

Let $p > p_0$ and substituting equation (2.25) in equation (2.26) and performing lengthy computation, we get

$$1048576 - 1196032p^2 + 449216p^4 - 57582p^6 + 615p^8 = 0. \tag{2.27}$$

The numerical computation shows that the solution of (2.27) for $p \in (0, 2)$ is $p =: p_0 \approx 1.35957$. Thus k_2 has no critical point in $(0, 2) \times (0, 1)$.

On the face $x = 1$,

$$k_3(p) := F(p, 1, y) = \frac{7168p^2 - 2000p^4 + 57p^6}{1179648}, \quad p \in (0, 2). \tag{2.28}$$

To attain maximum value of k_3, we solve $\partial k_3/\partial p = 0$ and get critical point at $p =: p_0 \approx 1.39838$. Simple calculation shows that k_3 attains its maximum value ≈ 0.00576045 at p_0.

On the face $y = 0$,

$$F(p, x, 0) = \frac{1}{1179648}\Bigg(5p^6 + (4 - p^2)((4 - p^2)(2304x(1 - x^2) + 80p^2x^2$$
$$+ 160p^2x^3 + 64p^2x^4) + 4p^4x + 576p^2x^2 + 104p^4x^2$$
$$+ 144p^4x^3 + 576p^2(1 - x^2)) =: k_4(p, x).$$

A complex computation shows that

$$\frac{\partial k_4}{\partial p} = \frac{1}{589824}\Bigg(2304p - 1152p^3 + 15p^5 + (-18432p + 4640p^3 - 12p^5)x$$
$$+ (1280p - 448p^3 - 72p^5)x^2 + (20992p - 6016p^3 + 48p^5)x^3$$
$$+ (1024p - 1024p^3 + 192p^5)x^4\Bigg)$$

and

$$\frac{\partial k_4}{\partial x} = \frac{1}{294912}\bigg((p^2 - 4)((-256p^2 + 64p^4)x^3 + (6912 - 2208p^2 + 12p^4)x^2$$
$$+ (-160p^2 - 12p^4)x - 2304 + 576p^2 - p^4)\bigg).$$

The numerical computation shows that there does not exist any solution for the system of equations $\frac{\partial k_5}{\partial p} = 0$ and $\frac{\partial k_5}{\partial x} = 0$ in $(0, 2) \times (0, 1)$.

On the face $y = 1$,

$$F(p, x, 1) = \frac{1}{1179648}\bigg(5p^6 + (4 - p^2)((4 - p^2)(80p^2x^2 + 64p^2x^4 + 160p^2x^3$$
$$+ (1 - x^2)(256px^2 + 320px + 256(8 + x^2))) + 4p^4x + 104p^4x^2$$
$$+ 576p^2x^2 + 144p^4x^3 + (1 - x^2)(80p^3 + 576p^3x + 576p^2x)) \bigg) =: k_5(p, x).$$

Proceeding on the similar lines as in the previous case on the face $y = 0$, again, the system of equations $\partial k_5/\partial p = 0$ and $\partial k_5/\partial x = 0$ have no solution in $(0, 2) \times (0, 1)$.

III. We now consider the maximum values attained by $F(p, x, y)$ on the edges of the cuboid T: In view of the equation (2.24), we have $F(p, 0, 0) = l_1(p) := 5p^6 - 576p^4 + 2304p^2)/1179648$. It is easy to compute that $l_1'(p) = 0$ for $p =: \lambda_0 = 0$ and $p =: \lambda_1 \approx 1.43351$ in the interval $[0, 2]$, where λ_0 is the point of minima and λ_1 is the point of maxima. Hence

$$F(p, 0, 0) \leq 0.00198843, \quad p \in [0, 2].$$

Again, considering the equation (2.24), we obtain $F(p, 0, 1) = l_2(p) := (32768 - 16384p^2 + 320p^3 + 2048p^4 - 80p^5 + 5p^6)/1179648$. Now, we note that l_2 is decreasing function in $[0, 2]$ and hence attains its maximum value at $p = 0$. Thus,

$$F(p, 0, 0) \leq \frac{1}{36}, \quad p \in [0, 2].$$

Now, we observe that the equation (2.28) does not depend on the value of y, hence we get $F(p, 1, 1) = F(p, 1, 0) = l_3(p) := (7168p^2 - 2000p^4 + 57p^6)/1179648$. It is easy to verify that the function l_3 has two critical points at $p = 0$ and $p =: \lambda_2 \approx 1.39838$ in the interval $[0, 2]$, where the maximum value is attained at λ_2. Thus

$$F(p, 0, 0) = F(p, 1, 0) \leq 0.0057645, \quad p \in [0, 2].$$

On substituting $p = 0$ in (2.28), we get $F(0, 1, y) = 0$. In view of equation (2.23), which is independent of all the variables p, x and y, the value of $F(p, x, y)$ on the edges $p = 2, x = 0; p = 2, x = 1; p = 2, y = 0$ and $p = 2, y = 1$, respectively, is given by

$$F(2, 0, y) = F(2, 1, y) = F(2, x, 0) = F(2, x, 1) = 5/18432, \quad x, y \in [0, 1].$$

Evaluating equation (2.24) at $p = 0$, we get $F(0, 0, y) = l_4(y) := y^2/36$. It is easy to verify that l_4 is an increasing function of y and hence attains maximum value at $y = 1$ in $[0, 1]$. Thus

$$F(0, 0, y) \leq \frac{1}{36}, \quad y \in [0, 1].$$

Using equation (2.22), we get $F(0, x, 1) = l_5(x) := (8 - 7x^2 - x^4)/288$. Since l_5 is decreasing function in $[0, 1]$, it attains maximum value at $x = 0$. Thus

$$F(0, x, 1) \leq \frac{1}{36}, \quad x \in [0, 1].$$

Substituting $y = 0$ in equation (2.22), we obtain $F(0, x, 0) = l_6(x) := x(1 - x^2)/32$. A simple calculation shows that the function $l_6'(x) = 0$ at $x =: x_0 = \sqrt{3}/3$ and it is increasing in $(0, x_0)$ and decreasing in $(x_0, 1)$. Hence it attains the maximum value at $x = x_0$. Thus we conclude

$$F(0, x, 0) \leq \sqrt{3}/144, \quad x \in [0, 1].$$

Taking into account all the cases I-III, the inequality (2.17) holds. For the function given in (2.16), which belongs to the class $\mathcal{SL}^*$, $a_3 = a_5 = 0$ and $a_4 = 1/6$. Thus $|H_2(3)| = 1/36$ for this function, which also proves the result is sharp. This completes the proof. ∎

We note that for $n = 2$, the exprssion on the left of the inequality (1.1) reduces to the famous Fekete-Szegö functional. In the following theorem we obtain the Zalcman coefficient inequality for $n = 3$ for the class $\mathcal{SL}^*$.

Theorem 2.3. *Let $f \in \mathcal{SL}^*$. Then*

$$|a_3^2 - a_5| \leq \frac{1}{8}.$$

The estimate is sharp.

Proof. Using equation (2.2) and (2.3), we get

$$a_3^2 - a_5 = \frac{125}{12288}p_1^4 - \frac{43}{768}p_1^2 p_2 + \frac{3}{64}p_2^2 + \frac{11}{192}p_1 p_3 - \frac{1}{16}p_4. \tag{2.29}$$

Applying Lemma 1.2 with $a = 125/768$, $b = 43/72$, $c = 11/24$ and $d = 3/4$ in the equation (2.29), we get

$$|a_3^2 - a_5| \leq \frac{1}{8}.$$

Let the function $f : \Delta \to \mathbb{C}$, be defined as follows:

$$f(z) = z \exp\left(\int_0^z \frac{\sqrt{1 + t^4} - 1}{t} dt\right) = z + \frac{z^5}{8} + \cdots. \tag{2.30}$$

The equality holds for the function given in (2.30), which belong to $\mathcal{SL}^*$ as $a_3 = 0$ and $a_5 = 1/8$, which contributes to the sharpness of the inequality. This completes the proof. ∎

3. Further Results

Let f and g be analytic functions of the form, respectively

$$f(z) = z + \sum_{n=2}^{\infty} a_n z^n \quad \text{and} \quad g(z) = z + \sum_{n=2}^{\infty} b_n z^n.$$

Then the Hadamard product (or convolution) of $f(z)$ and $g(z)$ is defined by

$$(f * g)(z) = z + \sum_{n=2}^{\infty} a_n b_n z^n.$$

Now, we derive the necessary and sufficient condition for a function $f \in \mathcal{S}$ to belong to the class $\mathcal{SL}^*$ in the following theorem, involving the convolution concept.

Theorem 3.1. *A function $f \in \mathcal{S}$ is in the class $\mathcal{SL}^*$ if and only if*

$$\frac{1}{z}(f * H_t(z)) \neq 0, \quad (z \in \Delta) \tag{3.1}$$

where

$$H_t(z) = \frac{z}{(1 - z)(1 - S(t))}\left(\frac{1}{1 - z} - S(t)\right)$$

and

$$S(t) = \sqrt{t} + i\left(\pm\sqrt{\sqrt{1+4t} - (t+1)}\right), \quad (0 < t < 2).$$

Proof. Define $p(z) = zf'(z)/f(z)$. As we know $p(0) = 1$, to prove the result, it suffices to show that $f \in \mathcal{SL}^*$ if and only if $p(z) \notin \gamma_1$, where

$$\gamma_1 = \{(u^2 + v^2)^2 - 2(u^2 - v^2) = 0\}.$$

By taking $u^2 = t$, we can give the parametric representation of the curve γ_1 as follows

$$S(t) = \sqrt{t} + i\left(\pm\sqrt{\sqrt{1+4t} - (t+1)}\right), \quad (0 < t < 2).$$

For $f \in \mathcal{S}$, we have

$$\frac{z}{(1-z)^2} * f(z) = zf'(z) \quad \text{and} \quad \frac{z}{1-z} * f(z) = f(z). \tag{3.2}$$

Using the above equations (3.1) and (3.2), we get

$$\frac{1}{z}(f * H_t(z)) = \frac{f(z)}{z(1 - S(t))}\left(\frac{zf'(z)}{f(z)} - S(t)\right) \neq 0,$$

which clearly shows that $zf'(z)/f(z) \neq S(t)$. Hence $1/(z(f * H_t(z))) \neq 0$ if and only if $p(z) \notin \gamma_1$ if and only if $f \in \mathcal{SL}^*$. ∎

Theorem 3.2. *The function*

$$\Theta(z) = \frac{z}{1 - \alpha z}, \quad (z \in \Delta)$$

belongs to the class $\mathcal{SL}^*$ if $|\alpha| \leq 1/4$.

Proof. By the definition of the class $\mathcal{SL}^*$, it suffices to show that the following inequality holds for the given range of α.

$$\left|\left(\frac{1}{1 - \alpha z}\right)^2 - 1\right| < 1. \tag{3.3}$$

The above inequality (3.3) holds
whenever

$$|2\alpha z - \alpha^2 z^2| < 1 + |\alpha z|^2 - 2Re(\alpha z),$$

which in turn holds if

$$2|\alpha z| \leq 1 - 2|\alpha z|,$$

which holds if

$$|\alpha| \leq \frac{1}{4}.$$

Hence the function $\Theta(z) \in \mathcal{SL}^*$. ∎

References

[1] R. M. Ali, N. E. Cho and V. Ravichandran, Differential subordination for functions associated with the lemniscate of Bernoulli, Taiwanese J. Math. **16** (2012), no. 3, 1017–1026.

[2] R. M. Ali, N. K. Jain and V. Ravichandran, Radii of starlikeness associated with the lemniscate of Bernoulli and the left-half plane, Appl. Math. Comput. **218** (2012), no. 11, 6557–6565.

[3] D. Bansal, Upper bound of second Hankel determinant for a new class of analytic functions, Appl. Math. Lett. **26** (2013), no. 1, 103–107.

[4] J. E. Brown and A. Tsao, On the Zalcman conjecture for starlike and typically real functions, Math. Z. **191** (1986), no. 3, 467–474.

[5] P. Dienes, *The Taylor series: an introduction to the theory of functions of a complex variable*, Dover Publications, Inc., New York, 1957.

[6] A. W. Goodman, *Univalent Functions*, Mariner, Tampa, Florida, 1983

[7] T. Hayami and S. Owa, Generalized Hankel determinant for certain classes, Int. J. Math. Anal. (Ruse) **4** (2010), no. 49-52, 2573–2585.

[8] W. K. Hayman, On the second Hankel determinant of mean univalent functions, Proc. London Math. Soc. (3) **18** (1968), 77–94.

[9] A. Janteng, S. A. Halim and M. Darus, Hankel determinant for starlike and convex functions, Int. J. Math. Anal. (Ruse) **1** (2007), no. 13-16, 619–625.

[10] B. Kowalczyk, A. Lecko, M. Lecko and Y. J. Sim, The sharp bound of the third Hankel determinant for some classes of analytic functions, Bull. Korean Math. Soc. **55** (2018), no. 6, 1859–1868.

[11] B. Kowalczyk, A. Lecko and Y. J. Sim, The sharp bound for the Hankel determinant of the third kind for convex functions, Bull. Aust. Math. Soc. **97** (2018), no. 3, 435–445.

[12] D. V. Krishna, B. Venkateswarlu and T. RamReddy, Third Hankel determinant for bounded turning functions of order alpha, J. Nigerian Math. Soc. **34** (2015), no. 2, 121–127.

[13] S. S. Kumar, V. Kumar, V. Ravichandran and N. E. Cho, Sufficient conditions for starlike functions associated with the lemniscate of Bernoulli, J. Inequal. Appl. **2013**, 2013:176, 13 pp.

[14] O. S. Kwon, A. Lecko and Y. J. Sim, On the fourth coefficient of functions in the Carathéodory class, Comput. Methods Funct. Theory **18** (2018), no. 2, 307–314.

[15] O. S. Kwon, A. Lecko and Y. J. Sim, The bound of the Hankel determinant of the third kind for starlike functions, Bull. Malays. Math. Sci. Soc. **42** (2019), no. 2, 767–780.

[16] S. K. Lee, V. Ravichandran and S. Supramaniam, Bounds for the second Hankel determinant of certain univalent functions, J. Inequal. Appl. **2013**, 2013:281, 17 pp.

[17] R. J. Libera and E. J. Złotkiewicz, Early coefficients of the inverse of a regular convex function, Proc. Amer. Math. Soc. **85** (1982), no. 2, 225–230.

[18] K. I. Noor, Hankel determinant problem for the class of functions with bounded boundary rotation, Rev. Roumaine Math. Pures Appl. **28** (1983), no. 8, 731–739.

[19] C. Pommerenke, On the coefficients and Hankel determinants of univalent functions, J. London Math. Soc. **41** (1966), 111–122.

[20] V. Ravichandran and S. Verma, Bound for the fifth coefficient of certain starlike functions, C. R. Math. Acad. Sci. Paris **353** (2015), no. 6, 505–510.

[21] M. Raza and S. N. Malik, Upper bound of the third Hankel determinant for a class of analytic functions related with lemniscate of Bernoulli, J. Inequal. Appl. **2013**, 2013:412, 8 pp.

[22] J. Sokół, Coefficient estimates in a class of strongly starlike functions, Kyungpook Math. J. **49** (2009), no. 2, 349–353.

[23] J. Sokół, Radius problems in the class $\mathcal{SL}^*$, Appl. Math. Comput. **214** (2009), no. 2, 569–573.

[24] J. Sokół and J. Stankiewicz, Radius of convexity of some subclasses of strongly starlike functions, Zeszyty Nauk. Politech. Rzeszowskiej Mat. No. 19 (1996), 101–105.

[25] T. V. Sudharsan, S. P. Vijayalaksmi, B. A. Sthephen, Third Hankel determinant for a subclass of analytic functions, Malaya J. Math. **2** (2014), no. 4, 438-444.

[26] P. Zaprawa, Second Hankel determinants for the class of typically real functions, Abstr. Appl. Anal. **2016**, Art. ID 3792367, 7 pp.

[27] P. Zaprawa, Third Hankel determinants for subclasses of univalent functions, Mediterr. J. Math. **14** (2017), no. 1, Art. 19, 10 pp.

[28] P. Zaprawa, On Hankel determinant $H_2(3)$ for univalent functions, Results Math. **73** (2018), no. 3, Art. 89, 12 pp.

Department of Applied Mathematics, Delhi Technological University, Delhi–110042, India
E-mail address: shagun05banga@gmail.com

Department of Applied Mathematics, Delhi Technological University, Delhi–110042, India
E-mail address: spkumar@dce.ac.in

Toward Zero Energy: Active and passive design strategies to achieve net zero Energy Building

Shambalid Ahady, Nirendra Dev, Anubha Mandal

Department of Civil engineering, Delhi Technological University, Delhi, 110042, India

Abstract

Buildings are found to be an essential part of the needed transition towards energy sustainability. In the past few years, there have been growing interests in net zero energy buildings (NZEB) adapted worldwide. The minimized energy demand and airtightness of a passive house and the low energy buildings have provided in the past a step forward to the energy efficiency goal and the net-zero energy building. Implementation of proven energy efficiency technologies offers the world the fastest, most economical, and most environmentally benign way to alleviate threats.

This paper will discuss Net Zero Energy Building definition and design strategies targeting for energy efficiency and environmental sustainability. The literature shows that to improve the integrated performance of the building and to achieve the goal of energy efficient and NZEB, appropriate active and passive design strategies should utilize. Also, energy demand should reduce to a minimum, through energy efficient building designs, leaving only a fraction of the energy required to be covered by renewable energy generation.

1. Introduction

Building are found to be an essential part of the needed transition towards energy sustainability [1]. Also, buildings are one of the leading consumers of energy and considerable producers of greenhouse gases (GHG) [2]. Increased rate of infrastructure development has led to higher consumption of energy. The consumption of energy by the building sector is continuously increasing because construction rate of buildings is faster than diminishing rate Moreover, buildings are responsible for more than forty percent of global energy use and production of a third of global greenhouse gas emissions, in developed as well as developing nations [3].

The impact of global warming, increase of energy demand and use of electrical energy are obliging international communities to propose future targets to deal with this threat, mainly through public awareness, new regulations and other useful measures [4]. In construction sector energy is consumed during Manufacturing of Building component and Material (embodied energy), Transport of these material from plant to site (grey energy), construction of the building (induced energy), operation of the building (operational energy) and demolition of the building (recycling of building parts) [5].

To overcome these problems, Governments must take the lead by prioritizing the building sector in their national climate change strategies and putting in place some building blocks [2]. Reducing emissions from buildings will bring multiple benefits to both, the economy regarding growth in GDP and to the society by providing better houses and access to clean energy and water [6]. NZEB is a radical approach to the mitigation of the energy demand in the buildings sector [7]. This concept proposed in the literature as an evolution of very energy-efficient buildings, and it requires building with zero energy balance on an annual basis [2].

The United States of America and Canada implemented ZEB strategies and achieved the NZEB goal through the construction of several Commercial and residential Zero Net Energy Buildings. Furthermore, the European Energy Performance of Buildings Directive 2010 (EPBD) requires all new buildings to be nearly Zero Energy Buildings (NZEB) by 31st December 2020 and all buildings acquired by public bodies by 31st December 2018 [8]. The European Union aims at drastic reductions in domestic greenhouse gas emissions by 80% in 2050 compared to the level in 1990[9].

This study aims to review various policies and studies that have been conducted to minimize current global climate problems through the implementation of NZEB. In addition to it, this paper discusses ZEB definitions, identifies ZEB strategies applied in different regions and gives an overview of the significant challenges of ZEB design.

*Corresponding Author,
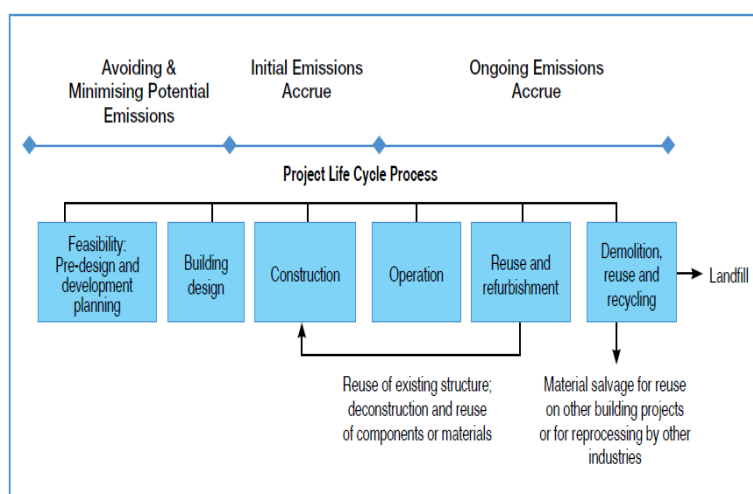E-mail address: shambalidahady_phd2k18@dtu.ac.in

Fig. 1: Life Cycle Phases of Buildings {Source :Garaham,P.(2013)[6]}

1.1 Net Zero Energy Building A ZEB does not have a clear and distinctive definition but its defined in several ways depending on the metric, boundary and the project goals [8.] A good net zero energy building definition should first encourage energy efficiency, and then use renewable energy sources available on site[7]. Summary of ZEBs definition has shown in table (1) . The U.S. Department of Energy (DOE) by National Institute of Building Sciences (Institute) established definitions for zero energy buildings which are as [10]-

1.2 Zero Energy Building (ZEB)

The Net Zero Energy building is an energy-efficient building which, the annual delivered energy is less or equal to the on-site exported renewable energy. On-site renewable energy includes any renewable energy generated within the site boundary whereas the exported energy is On-site renewable energy supplied via the site boundary and used outside the site boundary.

1.3 Zero Energy Campus

It is an energy-efficient campus where, on a source energy basis, the actual annual delivered energy is less or equal to the on-site renewable exported energy. Source Energy is the algebraic sum of site energy and energy consumed during extraction, processing, and transport of primary fuels.

1.4 Zero Energy Portfolio

An energy-efficient portfolio where, the actual annual delivered energy, on a source energy basis is less or equal to the on-site exported renewable energy.

Table 1:ZEB Definitions [Source: Torcellini, Pless and Deru, 2006]

Definition	Pluses	Minuses	Other Issues
Site ZEB	• Easy to implement • Verifiable through on-site measurements • Conservative approach to achieving ZEB • Easy for building a community to understand and communicate. • Patronize energy efficient building designs.	• Need more PV export to offset natural gas. • Does not consider all utility cost (can have a low load factor) • Not able to equate fuel types • Does not account for non-energy differences between fuel type (supply availability, pollution)	
Source ZEB	• Able to equate energy of fuel types used at the site. • A better model for impact on the national energy system. • Easier Zero energy building to reach	• does not account for non-energy differences between fuel types • source calculation too broad • source energy use accounting and fuel switching can have a great impact than efficiency technologies. • It does not consider all energy costs(can have a low load factor).	• Require to develop the site to source conversion factors which require a significant amount of information to define.
Cost ZEB	• Allows for demand positively control. • Verifiable from utility bills. • It is easy to implement.	• It may not reflect impact to the national grid for demand since the generation of excess Photovoltaic could be more valuable for reducing demand with on-site storage than exporting to the grid. • Highly volatile energy rates make for difficult tracking over time. • Requires net metering agreements such that exported electricity can offset energy and non-energy charges.	• Net metering is not well established often with capacity limits and at buyback rates lower than retail rates. • Offsetting monthly service, and infrastructure charges, required going beyond ZEB.
Emission ZEB	• A better model for green power. • Account for non-energy differences between fuel type (pollution, greenhouse gases). • Easier ZEB to reach.		• Need appropriate emission factor.

1.5 Zero Energy Community

An energy-efficient community where, on a source energy basis, the actual annual delivered energy is less or equal to the on-site exported renewable energy. Kurnitski .et al. stated that Net zero energy requirement has the exact performance level of 0 kWh/m² primary energy. An NZEB is a grid-connected building with high energy performance which aims towards balancing energy use such that the primary energy feed-in to the grid equals the primary energy delivered to NZEB from energy networks. Therefore, an NZEB produces energy when conditions are suitable, and uses delivered energy during rest of the time [11].

As per European ZEB definition, a nZEB should take into account the climate, building geometry, and usage conditions as follows :9

1.5.1 Geometry

Building geometry does not seem to be a striking argument for differences in energy requirements (e.g., in kWh/m2 per year) for the new buildings the requirements should be independent of geometry. On the other hand, for the existing building stock, geometry aspects should be further analyzed in order to avoid additional unfair burdening of the building owners.

1.5.2 Usage

All residential buildings should meet the same requirements as they typically have the same usage patterns. Non-residential buildings with a similar usage pattern as residential buildings may still have the same requirements as residential buildings. The other non-residential buildings should have classified in a few categories as possible (following the main criteria of indoor temperature, internal heat gains, required ventilation, and so forth) and should have particular energy performance requirements.

2. Net Zero Energy Building- Strategies

There are various ways to achieve Net Zero Energy balance in a building by incurring rational spending. Prevailing industry perceives

the concept of zero energy to cost prohibitive and suitable only for large budgets; however, there is a mounting record that zero energy building has achieved within typical construction budgets [12].

Griffith, B. et al. [13] of NREL figured out that early prioritization of energy performance goal and integrated design could be used to achieve significant energy savings. In the same context, Griffith et al. estimated the portion of the commercial sector that could achieve zero energy with varying levels of energy savings relative to the minimum requirements of ASHRAE 90.1.2004 [13,14].

The first cost-effective strategy for net-zero energy is to maximize the reduction in energy demand and simultaneously produce renewable energy on-site to meet the future requirement[15].

This approach simplifies the design process and optimizes the potential of renewable energy technologies on any building initiative.

3. Passive Strategies

3.1 Reduce Energy Demand

Passive strategies include all the strategies that do not require energy for operation. Effectual employment of these strategies can provide buildings with low energy consumption. Typically, low-energy buildings will comprise a high level of insulation, energy efficient windows, high level of airtightness and natural/mechanical ventilation with efficient heat recovery to reduce heating/cooling needs [9.] Building energy demand can be reduced through Passive strategy by better architectural design and energy saving techniques.

3.2 Building design and architecture

Designing sustainable NZEB necessitates a delicate balance between energy generation/ consumption and social/environmental impact. Building architecture includes the exterior façade as well as structural elements. In addition to it, building orientation, massing, and layout can be designed to reduce building thermal loads without increasing construction costs [12]. Building layout planning, site planning,

natural lighting, and ventilation are the most critical parameters that can have a high impact on the energy consumption of the building.

3.3 Building orientation

A building must be oriented in a way to take maximum advantage of natural light and prevailing winds while simultaneously reducing the need for artificial systems. For instance, a rectangular floor plan works best for passive solar design, with the long (east-west) axis of the house oriented within 10 degrees of true south [16]. Similarly, a two-story compact house is better than a single-story house since its exterior building envelope is smaller per unit size of floor space [1]. Choi et al. [17] concluded that electricity consumption of plate-type buildings is lower than tower-type buildings. However, gas consumption of plate type buildings is much higher. Furthermore, from the perspective of a building's living type, mixed-use buildings generate more CO_2 than the general residential buildings. At the same time, buildings with a simpler geometry tend to utilize lesser energy than the buildings with complicated geometry. Hence, for new buildings, differences in geometry do not seem to be a striking argument for differences in energy requirements (e.g., in kWh/m^2 per year) and the requirements should, therefore, be independent of geometry [9].

3.4 Natural daylighting

Generally, lighting systems utilize 30%-40% of a building's total energy consumption, thereby, making it a prime concern for net-zero energy discussions. National Renewable Energy Laboratory's (NREL's) proved that in net zero energy design, lighting systems in office facility should consume not more than 10% and less than 6% of the total building load when a data center or other equipment-heavy spaces are included [9].

Window arrangement is a crucial factor in determining daylight in the building. Tuning the window-to-wall ratio is one of the most effective strategies. Extra glazing adds material cost and increases HVAC system size without adding any benefit. Generally, net-zero projects have insulation values well beyond code. Daylighting should achieve in such a way that it reduces air infiltration through the use of a continuous air barrier to ensure the best performance under the design assumptions[15].Therefore, the literature suggests employing layers of light for basic ambient light levels through daylight while providing occupants with additional lighting options to meet their needs.

Successful slashing facility lighting in the building can be achieved through the following goals in early project planning :18

3.4.1 By Setting the Maximum Lighting Power Density goal

Lighting Power Density (LPD) is the electrical load of lighting per area lit, measured in watts per square foot. Overlit spaces (i.e., LPD too high), lead to wastage of energy as well as potential occupant discomfort.

3.4.2 By Setting a Daylight Sufficiency Goal

It specifies the amount of daylight needed to provide adequate light to perform typical tasks appropriate to each space, without additional electric lighting. It measures in lumens or foot-candles. It provides the appropriate balance between too little daylight (resulting in eyestrain or unnecessary electric light usage) and too much (resulting in excess glare or heat) to perform most tasks in the space.

3.5 Natural ventilation

The basic principle in a tropical climate is to have rooms allowing air to blow through, by having opposite exterior facades with a porosity higher than 20%[19].

A case study carried out by Shan.R. et al.[20] in severe cold climate in China shows that building energy performance is mostly influenced by climate. According to his research, the annual total building energy consumption was much smaller than a traditional office building given almost no cooling or lighting load for the SGZEB. He also suggested that the mechanical ventilation load was significantly reduced by applying natural ventilation strategies. Simulation result provided by Energy Plus which shows that the annual energy consumption (195505 kBtu or 57297 kWh), is contributed mostly by the heating load in the extremely cold winter time [20].

It is possible to recycle the air at a rate of 40 to 100 vol/h with interior speeds of 1 m.s-1 for wind speeds of approximately 2 m.s-119.

As stated by Gard [19], few architectural innovations such as interior blinds, wall lights, using air fans, improved management and intelligent dimensioning of the building systems and it is possible to create a building which uses a third of the energy of a standard building with an additional cost of 2% 19.The natural Airflow design of a building is shown in figure 2.
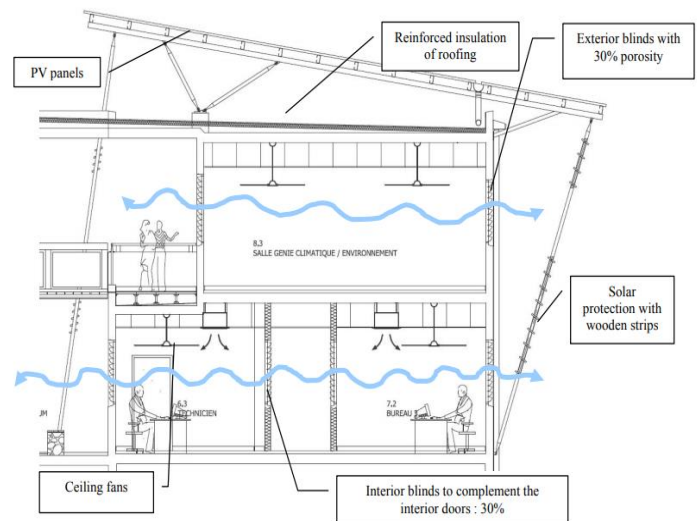

Fig.2: Technical solution for the thermal and airflow design of the building [Source: Gard, F.et.al. 2006]

4.Passive Energy Conservation Techniques

4.1 Building Envelop

Building Envelope is an essential component of NZE design, especially for buildings with large heating loads. An energy efficient building must be tightly insulated and carefully constructed to prevent air infiltration and heat transfer through the building envelope. Thermal zoning and ventilation setback can yield energy savings up to 23% when troops are deployed 21.

insulation is the primary material in the thermal control system. The thermal resistance of the installed insulation as quantified by the R-values. Achieving high R-values is a necessary part of any high-performance enclosure design strategy. Pettit,B.et.al.2015 presented design R-values of the insulation for the net zero residential test facility which is shown in table (2)22.

Table 2: Insulation R-Values by component [Source:Pettit,B.et.al.NIST.2015]

	Sub-Slab	Fdn Wall	Ext Wall	Windows	Roof
Prescriptive 2012 IECC nominal R-value[m2.K/W (ft2.h.°F/Btu)]	1.8 (10)	1.8 (10)	3.5 (20)	0.5 (2.8)	6.7 (38)
NZERTF nominal R-value m2.K/W (ft2.h.°F/Btu)]	1.8 (10)	4.1 (23)	7.9 (45)	0.9 (5.2)	12.7 (72)

Climatic conditions influences building envelope design23.Kolokotsa, D.et.al.(2018) investigated design and energy technologies of a zero energy school in Greece and analyzed energy performance of the zero energy building and showed a significant 68% reduction of the energy demand by improvement of the indoor thermal comfort through the zero energy building design24.

Thermal mass plays a dominant role in the design of passive solar houses by allowing for more heat to be captured and modulating heat distribution thereby enabling less temperature swings in the house. The optimal amount of thermal mass required depends on the amount of glazing and mass location. Mass heated indirectly by warm air from the living space is reported to require roughly four times more area as the same mass in direct sun to provide the same thermal effect 16. New building material production methods lead to better control of heat and mass flux by the building envelope including foundation, roof, walls, doors, windows 25.

To determine the quantity of thick mass, Chiras,D. (2002) suggested using three glass-to-mass ratios 16:

a. South-facing windows stretching beyond 7% of floor space requires an additional 5.5 m2 of uncovered and sunlit floor mass.
b. In case the mass is not in direct contact with the sunlight, but in the same room, an additional 40 m2 of mass is required per additional square meter of south-facing glazing above 7%.

Therefore, the optimal amount of glazing depends on the total heated floor area, total thermal mass, and other design parameters 16. A study carried out by Bajc,T.et al. (2015) on the impact analysis of the building energy demand of a passive house with the Trombe wall considering the Belgrade weather showed that the trombe wall increased the cooling demand in summer and efficient heating energy-saving in winter 26.The most cost-effective steps toward a reduction in a building's energy consumption can occur during the design process. Griffith, B.et al. NREL (2006) recommended strategies for the design of NZEB with controlled cost and highlighted action is summarized in table 3 [13.]

Table (3): NZEB cost effective design strategies
[Source: Griffith, B.et al. NREL (2006)]

Design strategies				
Audience	**Integrate simple and passive strategies**	**Consider life-cycle cost impacts**	**Allow for cost tradeoffs across disciplines**	**Leverage value added benefits**
Architects and Design Engineers	• Leverage orientation, massing, and layout to reduce thermal loads without increasing cost. • Integrate efficiency strategies with the building envelope and structure. • Avoid unnecessary control and moving components. • Consider strategies that minimize the need for ongoing calibration.	• Use energy modeling and life cycle analysis to identify integrated design packages that are favorable long-term investments. • Consider long-term maintenance requirements when comparing strategies. • Monitor and evaluate the operational performance of past design to provide insight into reliability, maintenance, and other operational consideration. • Evaluate efficiency investments using an avoided cost of renewables metric.	• Right- size HVAC systems to account for the load reductions provided by other efficiency strategies. • Leverage cost saving from HVAC system capacity reduction to invest in other improved efficiency packages. • Use energy modeling early and often to evaluate interactions between building systems and design choices and maximize cost tradeoff benefits.	• Document and emphasize non-energy benefits (comfort, aesthetics, productivity, flexibility, etc) of effective strategies to secure decision-maker buy-in. • Align efficiency strategies with the organizational mission to increase the willingness of decision-makers to sign off on emerging or un-conventional strategies.
Owners and developers	• Communicate maintenance capabilities and operational priorities to the design team.	• Explore robust long-term investment options before screening by the first cost.	• Reconsider typical discipline- centric budget allocations to enable fluid cost tradeoffs.	• Consider the values of efficiency strategies beyond energy cost saving.
Contractors and subcontractors	• Identify opportunities for reducing the first cost with a simplified construction.	• Inform team members of construction considerations that can affect life-cycle cost.	• Inform team members if options involve tradeoffs between material and installation costs.	• Communicate value-added benefits related to construction processes.

Design strategies (continue)		
Audience	**Maximize use of modular design strategies**	**Size Glazing area for Daylighting, Views, and efficiency**	**Consider alternative financing for higher cost systems**
Architects and Design Engineers	• Leverage the replicability of modular elements to reduce design and construction costs. • Standardize building construction (punched windows, exterior wall panels and so forth) to reduce cost through economies of scale. • Use modular elements to increase space efficiency and reduce footprints.	• Size glazing area to balance daylighting, thermal performance and architectural amenities. →First specify the amount of daylighting glazing necessary for the projects daylighting goals. →Then identify key opportunities for implementing view glazing that improves the interior environment while minimizing thermal gains. →Limit east and west facing glazing to the extent possible.	• Consider leveraging alternative financing to take advantage of tax deductions, credits, and local utility rebates that are available to third-party commercial entities. • Take advantage of demand-side rebate programs provided by local utilities to help defray the cost of efficiency investments. • Consider a PPA for renewable energy systems if adequate funds cannot be freed through other cost-saving strategies. • When direct purchase and financing options are both feasible, evaluate

	• Reinvest space efficiency cost saving into efficiency strategies. • Leverage modular floor plans to simplify mechanical and electrical system design.	→Eliminate unnecessary glazing to decrease overall envelope costs and improve thermal	the life cycle cost, mission impacts, and other value added for each scenario.
Owners and developers	• Encourage designers and construction contractors to pursue innovatively, cost-saving modular design and construction strategies.	• Recognize that glazing has a wide range of implications beyond aesthetic and that careful design can optimize benefits.	• Provide input during evaluations of how alternative investment scenarios align with owner goals and constraints.
Contractors and subcontractors	• Identify opportunities to modularize specific building constructions.	• Communicate energy performance implications of glazing constructions (e. g. thermal breaks in frames).	• Relay to owners any construction cost considerations, such as system sizing or construction schedule.

4.2 Design of Energy Efficient Lighting

A standard building has lighting from three 4x18W installations, giving a total power of 216 W and a rate of 11W/m² 19. In areas having grid electricity, energy efficient lighting design can be achieved by replacing incandescent light bulbs with compact fluorescent bulbs, which last four times longer and use one-quarter of the electricity 27.

Stated by Della Cava et al.2004 that the official efficiency standard for lighting energy in new buildings in China, sets mandatory limits on wattage per m2 and recommends using natural daylight and controlling the use of electric lighting 28.

5. Produce Unmet Energy Demand –Active Strategy

The active strategies mainly represent ways to reduce building energy consumption through energy production.

5.1 Renewable energy

The term renewable energy refers to energy which flows naturally through the environment on a continual basis 29. Renewable energy sources are a necessity for achieving NZEB and beyond 9. Renewables are the second largest contributor to global electricity production. RE accounted for 23.8% of world generation in 2016 29. The global production of renewable sources in 2016, such as solar PV, wind, solar thermal, geothermal, kept on expanding at a fast pace (+31.1%, +14.2%, +3.2%, +4.0%, respectively) but still accounted for less than 2% of global primary energy production together 30.

In selecting a renewable-energy technologies for a building, the site-capacity from the energy model can be used for determining energy sources which will be able to meet the demands of the building within the constraints of the site, budget, timeline, and performance goals. The most common renewable systems are Photovoltaics, Wind power, Geothermal systems, Hydroelectric power, and Biomass 9.

• The photovoltaic systems convert sunlight directly into electricity using the PV effect through which light causes matter to emit electrons.The photovoltaic technology generates electricity on a completely different physical basis than either conventional generation or other kinds of renewable energy generation 31.

• For existing infrastructure, the PV can be easily installed economically. The solar panels can produce the equivalent of 2.5 times the building's energy use 19.

• Ground-based or roof-mounted wind turbines can be a potential source of renewable energy in the areas having high wind velocities. Cao et al. (2017) evaluated the wind power resource around the 1000-meter scale of mega-tall buildings and showed that the technical performance of the wind turbine system was seen to be the best when at distances of 300 and 200 m from the ground, and when the building orientation is north and south 32.

• Geothermal systems harness the power of underground heat. They are expensive at small scale and are not an option on most sites. Geothermal energy is most useful when it occurs in the hydrothermal form: springs of hot pressurized water or steam known as aquifers. High-velocity steam made from exploiting geothermal energy by converting water to highly pressurized steam is used to create electricity 31.

• Bioenergy or biomass is the energy recovered from biomass that is from the chemical bonds formed via photosynthesis in the living matte.it is a single most significant source of energy in the developing countries providing 35% of total primary energy supply 33.

The primary source of biomass fuels is wood also, sources of biomass includes animal residues, agricultural residues, urban refuse, sewage sludge, industrial waste, and energy crops 31.

5.2 Hydroelectric power

The power of falling water – has been used by human civilization for centuries to carry out mechanical work milling, grinding, or merely irrigating agricultural lands. Hydroelectric installations are characterized as either small or in the large scale. Schemes with 10 MW and less are small scales and those of installed capacity of more than 10 MW are usually consider ed to be large scale 31, hydro provided 2.5% of global production in 2016.

To support and operate renewable energy technologies and for better RE management, backup systems required and it should fully installed and commissioned 34. Table (4) shows a summary of technologies used in NZEB.

Source: Maria, K and virot, L.(2013) 35

Table 4: Main technologies for use in ZEBs

	Proven and stabilized technologies	**Still developing technologies**	**Technologies on the horizon**
Thermal insulation	Low conductivity materials	Reflective roofs, green roofs, exploring new material for thermal insulation	Smart, reflective roofs, cool colored paints(with IR reflective pigments), exploring new materials for thermal insulation (nanomaterials), highly insulation façade systems
Windows	Multi-layer windows Low-e-grazing Gas-filled air gaps Thermal break frames	Glazings with dynamic properties(e. g. electrochromic)	BIPV glazings, solar glazing, solar curtain walls

IJARI

Lighting	CFL, LED, daylight harvest through transparent envelope	CFL, LED, intelligent, dynamic and light-re-directing facades with automated lighting controls	Intelligent, dynamic and light-redirecting façades combined with automated lighting controls, intelligent natural daylighting distributing systems
Heating and	Condensing gas boilers Biomass boilers High EER chillers Heat pumps(ground and air source)	Micro-combined heat and power	Solar combined heat, cooling, and power, thermally activated heat pump (HP), thermoelectric cooling, frostless HP, distributed refrigeration/ water-source HP
Ventilation	Mixed mode natural and mechanical with heat recovery (HR), night cooling, stack effect ventilation	Hybrid ventilation systems with automatic controls displacement ventilation	Heat recovery widows personalized ventilation
Renewable technologies	Thermal solar, biomass heating, PV systems, PV thermal solar systems, air solar collectors	PV system (increased efficiency) BIPV systems, wind turbines(WT) and micro WT	BIPV systems, WT, and micro
Building energy management systems	Sensors, energy control (zone cooling and heating) and monitoring systems	monitoring and control systems running on IP communication infrastructure	Improved management systems with grid/ consumer supply-demand integration

6. Conclusions

A significant rise in the water level of oceans and precipitation changes in the desert are visible changes brought due to the impact on climate. Climate change has all the necessary ingredients to prove to be a global threat.

The literature demonstrated that environmental sustainability can be achieved through designing sustainable and energy efficient buildings by the help of NZEB technologies.Since, the energy consumption, especially in the building sectors associated with climate change therefore, focusing on energy efficiency in buildings must allow to meet goals for reduction of greenhouse gas emission. for that, the energy efficient buildings would be an immediate option for a Secure, Clean, and Healthy Future.

In order to design an NZEB, a professional, having expertise in energy and comfort must involve to the design team at the earliest phase of the design process. A design team must consist of experts in building Physics, architects and Mechanical engineers so that they work concurrently toward this approach to achieve NZEBs.

Many research has been conducted in the area of ZEB for past few decades, yet only a few zero-energy buildings (ZEBs) exist limiting mostly to USA, Canada and a few European and Asian countries, which shows that there are many socio-economic factors which are hindering the design, construction and operation of NZEBs. Primarily, the energy demand for new buildings is higher than the old buildings, and most of this energy tends to get waste due to inappropriate architectural design which shows that architects have to modify their approach and follow the ZEBs strategies to obtain better services with lower energy need. Simultaneously, mechanical engineers must change their conventional approach of building oversizing plants and systems and must look into the economic as well as environmental concerns of the design.

References

[1]. PFG Bancll, ADPeacock. Energy efficient new housing. The UK reaches for sustainability, Building Research & Information. 35(4), 2007, 426.

[2]. P De Wilde, D Coley.The implications of a changing climate for buildings. Build Environ.55, 2012, 1-7.

[3]. UNEP-DTIE Sustainable Consumption & Production Branch. Buildings and Climate Change.Summary for Decision Makers. United Nations Environment Program. 2009.

[4]. IEA. Energy performance certification of buildings: A policy tool to improve energy efficiency. Paris:OECD/IEA, 2010.

[5]. UNEP. Buildings and climate change. summary for decision makers. United Nation Environment Program, sustainable building and climate initiative 2009, 10-11.

[6]. P Graham. Building Ecology: First Principles for a Sustainable Built Environment Blackwell, Oxford, UK 2003.

[7]. P Torcellini, S Pless, M Deru, D Crawley. Zero Energy Buildings: A Critical Look at the Definition, National Renewable Energy Laboratory (NREL), Pasific Grove, CA, 2006.

[8]. European Parliament. Energy performance of buildings (recast)', Official Journal of the European Union, 53, 2010, L153/1–L153/35

[9]. T Boermans. Principles for nearly zero energy building, Buildings Performance Institute Europe and Danish Building Research Institute, 2011.

[10]. National Institute of Building Science. A Common Definition for Zero Energy Buildings U.S. Department of Energy, 2015 .

[11]. J Kurnitski, F Allard, D Braham, G Goeders. How to define nearly net zero energy buildings. Rehva proposal for uniformed national implementation of EPBD recast, 2011.

[12]. National renewable energy laboratory. Cost control strategies for zero energy buildings. High performance design and construction on a budget. 2014, NREL/BR-5500-62752

[13]. B Griffith, P Torcellini, N Long, D Crawley, J Ryan. Assessment of the Technical Potential for Achieving Zero-Energy Commercial Buildings. National Renewable Energy Laboratory. California NREL/CP-550-42144, 2006.

[14]. ASHRAE. 2004. ANSI/ASHRAE/IESNA Standard 90.1. Energy Standard for Buildings Except Low-Rise Residential Buildings, Atlanta, GA, 2004

[15]. AIA continuing education, Sustainable design. Net zero energy design and the living building challenge, 2016, 48.

[16]. D Chiras. The Solar House: Passive Heating and Cooling. White River Junction, VT: Chelsea Green Publishing, 2002.

[17]. IY Choi, SH Cho, JT Kim. Energy consumption characteristics of high-rise apartment buildings according to building shape and mixed-use development.46, 2012, 123–131.

[18]. GSA. Office of Federal High Performance Green Buildings saving energy through lighting and daylighting strategies.https://www.gsa.gov/about-us/organization/office-of-governmentwide-policy/office-of-federal-highperformance-buildings/resource-library/energy-water/the-fort-carson-energy-research-project.

[19]. F Garde, A Bastide, D Bentaleb, AH Fakra, F Ottenwelter. The construction of a zero energy building in Reunion island. Presentation of a new approach to the design studies. IASTED. MSO, Modelling, Simulation and Optimisation. , 2006,1-8.

[20]. R Shan, M Carol, S Tiemao. Design Strategies for a Net Zero Energy Building in Severe Cold Climate: A Case Study for China.   https://www.researchgate.net/publication/293816833, 2016.

[21]. GSA. Strategies to achieve net zero energy. The fort carson energy research project General Services Administration. GSA, 2014.

[22]. B Pettit, C Gates, A Fanney, M Healy. Design Challenges of the NIST Net Zero Energy Residential Test Facility. National Institute of Standards and Technology (NIST). Technical Note 1847, 2015, 25.

[23]. L Yang, JC Lam, CL Tsang. Energy performance of building envelopes in different climate zones in China. Appl Energy, 85, 2008, 800-817.

[24]. D Kolokotsa, V Vagias, L Fytraki, K Oungrinis. Energy analysis of zero energy schools: the case study of child's asylum in Greece. Advances in Building Energy Research, 2018, 11.

[25]. S Hoque. Net Zero Energy Homes: An Evaluation of Two Homes in the Northeastern United States. Journal of Green Building, 5(2), 2010, 85.

[26]. T Bajc, MN Todorovi´c, J Svorcan. CFD analyses for passive house with Trombe wall and impact to energy demand. Energy Build. 98, 2015, 39-44.

[27]. L Richard, Ottinger. Energy Efficiency: The Best Immediate Option for a Secure, Clean, and Healthy Future, Strategic Planning for Energy and the Environment, 2010, 28.

[28]. MF DellaCava, S Weil, P DuPont, SR Na Phuket, S Constantine, JE McMahon. Ministry of Construction Gazette N° 247. 2000 30(2), 2004, 43

[29]. International Energy Agency. Renerable information. IEA. Renewable information: overview 2018, 5.

[30]. International Energy Agency. World energy balance. IEA: overview edition, 2018, 3.

[31]. T Jackson. Renewable energy sources. Center for environmental strategy, University of surrey. United Kingdom, 2000.

[32]. J Cao, X Man, J Liu, L Liu, T Shui. Preliminary assessment of the wind power resource around the thousand-meter scale megatall building. Energy Build, 142, 2017, 62–71.

[33]. WEC. New Renewable Energy Resources. A guide to the future, World Energy Council, Kogan Page, London, 1994

[34]. Department of Housing, Planning and Local Government of Ireland. Conservation of Fuel and Energy Buildings other than Dwellings, Building Regulations. part L, 2017, 17.

[35]. K Maria, L Virota. Recent progress on net zero energy buildings. Advances in building energy research, 2018, 158.